GSAOI
CONCEPTUAL DESIGN REVIEW DOCUMENTATION

VOL. 2

Submitted to the International Gemini Project Office
under
AURA Contract No. 9414257-GEM00304

Research School of Astronomy and Astrophysics
Australian National University
Canberra, Australia

August 20-21, 2002

This page is left blank intentionally.

TECHNICAL REVIEW

GSAOI
Conceptual Design Review Document

Research School of Astronomy and Astrophysics
Australian National University
Canberra, Australia

August 20-21, 2002

This page is left blank intentionally.

Table of Contents

This page is left blank intentionally.

List of Acronyms

A&G	Acquisition and Guidance
AC	Alternating Current
ADC	Analog-to-Digital Converter
ADU	Analog-to-Digital Unit
ALU	Arithmetic Logic Unit
AO	Adaptive Optics
AR	Anti-Reflection
ASIC	Application Specific Integrated Circuit
BBAR	Broad-Band Anti-Reflection
BSP	Board Support Package
BW	Band Width
CAD	Command Action Directive
CAR	Command Action Response
CASPIR	Cryogenic Array Spectrometer/Imager
CC	Components Controller
CCD	Charge Coupled Device
CDS	Correlated Double Sampling
CICADA	Computerized Instrument Control And Data Acquisition
CICS	Core Instrument Control System
CMOS	Complementary Metal Oxide Silicon
CPU	Central Processing Unit
CWS	Cold Work Surface
DAC	Digital-to-Analog Converter
DC	Detector Controller
DCS	Detector Control System
DHS	Data Handling System
DIO	Digital Input-Output
DMA	Direct Memory Access
DSP	Digital Signal Processor
EPICS	Experimental Physics and Industrial Control System
ESO	European Southern Observatory
FEA	Finite Element Analysis
FCAL	Fiber Channel Arbitrated Loop
FET	Field-Effect Transistor
FIFO	First-In-First-Out
FITS	Flexible Image Transport System
FPDP	Front Panel Data Port
FPGA	Field Programmable Gate Array
FPRD	Functional and Performance Requirements Document
FWHM	Full Width at Half Maximum
GCAL	Gemini Calibration Unit
GIRMOS	Gemini Infrared Multi-Object Spectrograph
GSAOI	Gemini South Adaptive Optics Imager
H2RG	HAWAII-2RG
HAWAII	HgCdTe Astronomical Wide Area Infrared Imager
ICD	Interface Control Document
ICS	Instrument Control System
IfA	Institute for Astronomy
IFU	Integral Field Unit
IMP	Interprocess Message Passing
IOC	Input-Output Controller

IR	InfraRed
IRCS	Infrared Camera and Spectrograph
IRTF	Infrared Telescope Facility
IS	Instrument Sequencer
ISS	Instrument Support Structure
ISAAC	Infrared Spectrometer And Array Camera
LAN	Local Area Network
LED	Light Emitting Diode
LVDS	Low Voltage Differential Serial
MBE	Molecular Beam Epitaxy
MCAO	Multi-Conjugate Adaptive Optics
MCS	Mechanisms Control System
MUX	Multiplexer
NDR	Non Destructive Read
NGST	Next Generation Space Telescope
NIC	Network Interface Card
NICI	Near-Infrared Coronograph Imager
NIFS	Near-infrared Integral-Field Spectrograph
NIRI	Near-InfraRed Imager
NIRSPEC	Near-Infrared Spectrograph
OCS	Observatory Control System
ODGW	On-Detector Guide Window
OIWFS	On-Instrument Wave-Front Sensor
PACE	Producible Alternative to CdTe for Epitaxy
PC	Personal Computer
PCB	Printed Circuit Board
PCI	Peripheral Component Interface
PGA	Pin Grid Array
PID	Proportional, Integral, and Differential
PMC	PCI Mezzanine Card
PPC	Power PC
PSF	Point Spread Function
QLD	Quick Look Display
RAM	Random Access Memory
RMS	Root Mean Square
ROI	Regions of Interest
RSAA	Research School of Astronomy and Astrophysics
SALSA	Safe Aircraft Localization and Satellite Acquisition
SAD	Status and Alarm Database
SBC	Single Board Computer
SDSU	San Diego State University
SIR	Status Information Record
SNL	State Notation Language
SRAM	Static Random Access Memory
SSB	Sensor Support Board
STL	Standard Template Library
TCP/IP	Transmission Control Protocol/Internet Protocol
TCS	Temperature Control System
TMA	Three Mirror Anastigmat
TTL	Transistor-Transistor Logic
UAE	Universal Application Environment
USCSI	Ultra Small Computer Systems Interface
VLT	Very Large Telescope
VME	Versa Module Europe
WCS	World Coordinate System

WFC3	Wide Field Camera 3
WFI	Wide Field Imager

This page is left blank intentionally.

1 Overview

This overview summarizes the contents of Volume 2 of the Gemini South Adaptive Optics Imager (GSAOI) Conceptual Design Review Documentation.

1.1 Design Priorities

GSAOI will be used predominantly for faint broad-band near-infrared imaging. These observations will be background limited (§3.1.3.2 of Vol. 1). The signal-to-noise ratio achieved under this condition is given by

$$SNR = \frac{pTi_{obj}}{\left(pTi_{sky}\right)^{1/2}} = \frac{p^{1/2}T^{1/2}i_{obj}}{i_{sky}^{1/2}}$$

where T is the integration time, i_{obj} is the object photo-current per pixel, i_{sky} is the background photo-current per pixel, and p is the number of object pixels summed. For fixed integration time and fixed point spread function (PSF) set by the Multi-Conjugate Adaptive Optics (MCAO) performance, the signal-to-noise ratio achieved is a function only of the throughput of the optical system:

$$SNR \propto \frac{i_{obj}}{i_{sky}^{1/2}} = \frac{N_{obj}}{N_{sky}^{1/2}} \tau_{atm}^{1/2} \tau_{tel}^{1/2} \tau_{aos}^{1/2} \tau_{ima}^{1/2} Q^{1/2}$$

where N_{obj} is the number of object photons above the Earth's atmosphere, N_{sky} is the (equivalent) number of sky photons above the Earth's atmosphere, τ_{atm} is the transmission of the Earth's atmosphere, τ_{tel} is the transmission of the telescope, τ_{aos} is the MCAO transmission, τ_{ima} is the transmission of the GSAOI imager, and Q is the imager detector quantum efficiency.

The imager transmission is the only performance parameter that is within the power of the instrument designer to optimize. Maximizing the imager transmission has been the prime objective of the GSAOI Conceptual Design Study and is the primary parameter on which the imager design should be assessed.

The second design priority is gaining access to GSAOI at the telescope as soon as possible. The baseline design is conservative. Low risk choices have been made that will not incur long or unforeseen development times. Options are given in some cases for higher risk alternatives that offer greater functionality but with protracted deliver.

1.2 Technical Implementation

The Research School of Astronomy and Astrophysics (RSAA) will fast-track development of GSAOI by re-using many of the designs already developed for the Gemini Near-InfraRed Imager (NIRI) by the Institute for Astronomy (IfA) of the University of Hawaii. GSAOI will be mounted in a duplicate of the NIRI cryostat and use the same On-Instrument Wave-Front Sensor (OIWFS) detector system. The instrument will use the same mechanism encoding architecture used in NIRI and will use the same cryogenic stepper motors adopted for NIRI. This commonality of mechanical designs means that the NIRI mechanism control system hardware and temperature control system hardware can also be duplicated for GSAOI with minimal change. The EPICS Instrument Sequencer (IS), Components Controller (CC), and engineering interface software developed for NIRI and the CC and Detector Controller (DC) for the OIWFS will also be re-used for GSAOI with only minor modification. This same approach has been successfully adopted by RSAA in the development of the Near-infrared Integral-Field Spectrograph (NIFS) where it has clearly led to significant savings in schedule and budget.

The NIFS integration frame will be duplicated for GSAOI. This uses a minor modification of the NIRI integration frame to allow it to fit within the Gemini elevator.

The GSAOI imager Detector Controller software will be an evolution of the similar code already written for the NIFS HAWAII-2 detector.

GL Scientific will design and manufacture the GSAOI imager detector focal plane assembly in consultation with the RSAA. GL Scientific designs will be tested by Don Hall as part of his NGST detector development. RSAA have worked with GL Scientific in developing a similar focal plane assembly for their Wide Field Imager 8k×8k CCD mosaic camera. GL Scientific will share the development cost over four groups initially. They are responsible for manufacturing all HAWAII-2RG focal-plane assemblies ordered through Rockwell.

RSAA will bring new resources to the GSAOI project with AUSPACE, a Canberra-based aerospace company, assisting with the design and construction of the OIWFS. Prime Optics, in Queensland, designed the NIFS camera optics and have been involved in developing the GSAOI optical design. They will continue in this role.

1.3 Systems Design

The GSAOI system is shown in Figure 2. The main mechanical subsystems are the imager, the OIWFS, and the cryostat. GSAOI will be a facility instrument that meets all the requirements that this implies. Duplication of the NIRI/NIFS cryostat and integration frame guarantees to a large extent that GSAOI will meet volume, mass, and moment requirements.

GSAOI will be controlled through EPICS commands from the Observatory Control System (OCS) in a similar way to NIRI/NIFS. The GSAOI Detector Controller software interfaces to the Detector Control System (DCS) hardware that then interfaces to the imager detector. The Components Controller software interfaces to the Mechanisms Control System (MCS) hardware and the Temperature Control System (TCS) hardware. These in turn interface to motors and Hall-effect-sensor encoders, and heaters and temperature sensors, respectively, in the cryostat.

The OIWFS DCS interfaces to OIWFS DC software in the Acquisition and Guidance (A&G) Input-Output Controller (IOC). This OIWFS DC software is a Gemini responsibility. The OIWFS DCS also interfaces to the OIWFS detector. The OIWFS CC software interfaces to the GSAOI MCS to control OIWFS mechanisms.

So far, this is standard Gemini architecture.

GSAOI extends standard Gemini architecture in the following ways:

- An On-Detector Guide Window (ODGW) will be implemented to permit tip-tilt monitoring directly on the imager detector. This ODGW will interface with the imager DCS, which in turn interfaces to the GSAOI DC software. The ODGW will be controlled from the A&G IOC, so a command interface must exist for this purpose between the A&G IOC and the GSAOI DC software. ODGW image data will be passed to the A&G IOC, so a data interface must exist for this purpose between the A&G IOC and the GSAOI DC software.

- GSAOI will contain convex and concave defocus lenses that will be used to record out-of-focus images with the imager detector from which wave-front phase errors will be derived. The MCAO deformable mirror DM0 will be configured to null these wave-front errors. An interface must exist between MCAO and the instrument operator so that a description of these wave-front errors can be input to the MCAO system.

- GSAOI will contain a fast cold shutter that will block the imager beam in the event of poor adaptive-optics (AO) correction or laser shutdown as directed by the MCAO SALSA system. An interface must exist between MCAO and the GSAOI Instrument Sequencer so that MCAO can command this shutter to open and close. An interface must also exist between the GSAOI IS and the GSAOI DC so that the actual integration time can be accurately determined and recorded.

1.4 Optical Design

1.4.1 Imager

The baseline imager optical design is intentionally minimal. *It delivers the highest possible sensitivity, so that the demanding science goals can be addressed to the greatest extent practicable*. The design uses the minimum number of optical surfaces consistent with excellent image quality. This maximizes throughput. The design delivers excellent image quality with an expected RMS wave-front error of 46 nm, which is within the wave-front error of 65 nm allocated to the science instrument in the MCAO system budget. *This ensures that GSAOI will not overly degrade the high Strehl ratio achieved by MCAO*. The optical design has low distortion that is insignificant compared to the asymmetric distortion of the MCAO optics. *This adds no impediment to high precision astrometry over that imposed by MCAO.*

The baseline imager design is reproduced in Figure 1. It is a refractive system consisting of a CaF_2 field lens, a CaF_2 telephoto lens and a CaF_2/MgO doublet collimator that produces a 25 mm diameter pupil image in collimated light at a cold stop. A MgO/CaF_2 doublet camera and CaF_2 telephoto lens then reimage the focal plane onto the imager detector. Two filter wheels are located in collimated space ahead of the cold stop.

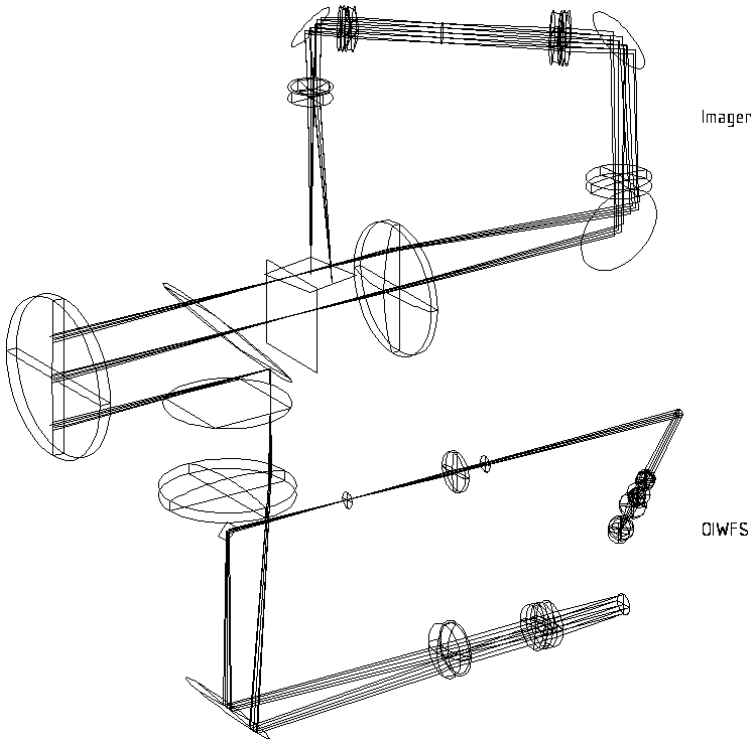

Figure 1: Folded layout of the baseline optics showing both the imager and the OIWFS.

The key strengths of the design are:

- The excellent chromatic correction so there is no need for active focus adjustment between pass bands.
- The location of the filters in collimated space so that filters of different optical thickness do not cause defocus.
- The excellent ghost image performance due to the diverging chief rays in the camera.

The potential drawbacks of the design are:

- The non-telecentric off-axis beams on to the detector cause a weak in-focus ghost image due to the detector substrate. The ghost image is displaced by up to four pixels radially from the primary image, depending on field position. This ghost is discussed in §3.5.5.1. We believe that its intensity will be acceptably low, and that the additional complexity of designs that avoid it is unwarranted and counter to the goal of maximizing throughput.

- MgO is an excellent chromatic match with CaF_2, and the RSAA Optical Workshop has successfully manufactured lenses from MgO for a previous near-infrared camera. However, MgO may be difficult to procure in the required sizes, cryogenic refractive index data are not available, and it is a cubic crystal that may imprint a "square" figure error on the surface. MgO procurement is discussed in §3.15. One supplier has been identified who currently can supply optical blanks. Their willingness to do so in the future is unknown. Avenues for measuring MgO cryogenic refractive indices are discussed in §3.8.1. This remains problematic. The effect of figure errors on the wave-front error budget is discussed in §3.5.4.4. This is shown to be negligible, based on a new technique that was used to refigure a test lens for this study.

Several design variants have been developed that address the possible drawbacks of the baseline design:

- A similar design using a ZnSe field lens and BaF_2 and fused silica collimator and camera lenses has been developed very recently. This design addresses the MgO procurement and cryogenic refractive index concerns. The design delivers similar optical performance to the baseline design. Cryogenic refractive index data are available for each material. Janos has experience in manufacturing and AR coating large ZnSe lenses. The RSAA Optical Workshop has experience in manufacturing BaF_2 and fused silica lenses (for NIFS and other applications) and can AR coat these materials in Australia. This is a viable alternative to the baseline design. Detailed tolerancing and ghost image analysis are yet to be performed on this design variant.

- A design with telecentric beams on to the detector is presented in §3.5.1.4. This design avoids the detector substrate ghost. An additional lens is included near the detector to force telecentricity. The extra lens degrades throughput, and the enforced telecentricity degrades overall image quality. The telecentric output introduces additional ghost images; the very thing it is intended to reduce. The design has not been progressed as far as other variants because of these unattractive features.

1.4.2 OIWFS

An OIWFS guide star is required for every GSAOI observation to track slow focus changes due to variations in the height of the atmospheric sodium layer. The OIWFS will also be used to monitor image motion due to slow flexure and fast atmospheric tip-tilt variations when the ODGW is not used. Maximizing OIWFS guide star availability directly maximizes the scientific scope of the instrument. However, the short development time set so that GSAOI is available on a time scale commensurate with MCAO dictates that a low-risk approach be adopted.

The baseline OIWFS design is also shown in Figure 1. It is a compromise between OIWFS field size and simplicity of implementation. The square 85″×85″ imager field passes directly to the imager. The remainder of the circular 120″ diameter MCAO field is passed to the OIWFS. Thus the OIWFS guide star must be located in one of the four "crescent" regions outside the imager field. The MCAO exit pupil is reimaged at a steerable mirror that directs the guide star beam to an intermediate focus at the OIWFS aperture wheel. The beam passing through the aperture forms a pupil on a four-facetted Shack-Hartmann prism, which causes four images of the OIWFS guide star to be formed at the OIWFS detector. Image translation is derived from the mean position of the four images. Focus is derived from the separations of perpendicular image pairs.

The final image scale is 0.065″/pixel. This was found to be optimal in OIWFS centroiding simulations (§3.4 of Vol. 1). This is partly because diffraction at the Shack-Hartmann prism broadens the image point spread function by a factor of ~ 2 relative to the imager (as shown in Figure 15 of Vol. 1).

The baseline OIWFS has excellent image quality. However, one features of the design is a possible concern:

- Guide stars are acquired in this design in the same way as they are in NIRI. Significant schedule and risk reductions are achieved by adopting this simple and proven approach. However, the restricted OIWFS acquisition field will make guide star selection more problematic. We view this as an acceptable compromise in order to achieve the short delivery time required of GSAOI.

We briefly consider an alternative OIWFS feed design using a cryogenic probe in §8.6 of Appendix A to address these potential concerns. In our view, a robotic probe is a high-risk alternative that significantly increases the complexity of the instrument, extends its schedule, and compromises the imager performance. We do not recommend this approach.

1.5 Mechanical Design

1.5.1 Cryostat

The mechanical design for GSAOI reuses the NIRI/NIFS cryostat. RSAA have pioneered this approach in the construction of NIFS. The manufacture of the NIFS duplicate cryostat is now completed, and RSAA is well placed to produce another duplicate.

Several modifications to the NIFS design are required by parts obsolescence. The principal change is that the Cool Power 130 cryocoolers used in NIRI/NIFS are no longer manufactured. A suitable alternative has been identified (§4.3.2). This will require minor modifications to the cryocooler mounting arrangement. The thermal load on the cryostat will be similar to NIRI/NIFS and the new cryocoolers have similar power to the NIRI/NIFS cryocoolers, so the cool down and warm up times and the equilibrium cryostat temperature will be similar to those of NIRI/NIFS.

Several modifications to the NIFS design are necessitated by the different application. The cryostat window for GSAOI is larger than for NIRI/NIFS and will be made from silica, rather than CaF_2, because of its greater strength and the absence of a need to operate beyond 2.5 μm. This change will be accommodated by altering the window housing (§4.3.6). The drive for the mechanism that operates the environmental cover over the cryostat window will also be changed to a direct current motor and gearbox to improve its reliability (§4.3.5). Various cable ports will also be relocated because of the different arrangement of internal components.

The major change to the NIRI/NIFS internal arrangement is to locate the imager on the opposite side of the cryostat to NIRI/NIFS (§4.4). The NIRI cryostat is a hexagonal cylinder with a central hexagonal plate (the cold work surface plate; CWS plate). This plate supports the science instrument on one side and the OIWFS on the other. In NIRI/NIFS, a mirror reflects the science field from the window side of the CWS plate to the science instrument that is mounted on the opposite side of the CWS plate. The fold mirror is close to focus, so the f/16 beam footprint is small in NIRI/NIFS, and would be even smaller in the f/34 MCAO beam. The GSAOI imager is located on the window side of the CWS plate to avoid adding this unnecessary reflection to the imager optical path. This significantly lowers the risk associated with achieving the required optical performance.

1.5.2 Imager

The imager optics are mounted within and on an optable similar to that used for the NIRI/NIFS OIWFS. This optable also serves to stiffen the CWS plate in the same way that the OIWFS optable does in NIRI/NIFS. The optable will be machined from a single aluminum block, so changes in detail from

NIRI/NIFS can be readily incorporated. A light-weight photon shield will enclose components on the outer optable surface to exclude stray radiation.

The imager lenses will be mounted in bores in the same way they are in the NIFS camera. Lenses will be constrained axially by spring-loading them against conical seats that are arranged to make tangential contact with the adjacent spherical lens surface. Paired lenses will be separated by precision glass spacer rings having faces ground to match those of the adjacent lens surfaces. Lenses will be constrained radially by precision fits within close fitting housing bores. Tolerances will be arranged to produce near-zero clearance at the cryogenic operating temperature.

Achieving the required lens centering accuracy in a folded optical system is seen as a significant challenge. Lenses will be accurately mounted within their housing cells. Lens cells will be fixed in orientation and axial position, but adjustable in radial position. Fold mirrors will be fixed in position, but adjustable in surface orientation by means of three-point kinematic mounts. In turn, each mirror will be adjusted to square the reflected optical axis to the following lens cell, and each lens cell will be adjusted to center it on the reflected axis.

The GSAOI imager contains a focal plane wheel, two filter wheels, a fast shutter, and a utility wheel. Each wheel will be mounted on angular contact bearings using slight preload. The drive systems will be via the same cryogenic stepper motors used in NIRI/NIFS with two-stage spur gear trains. A friction brake on the wheel will prevent wheel motion once set. The wheel positions will be encoded with the same Hall-effect-sensor design used in NIRI/NIFS. This allows duplication of the NIRI/NIFS Mechanisms Control System and Components Controller software. The fast shutter will use a rotating blade driven by a stepper motor.

The imager detector is located close to the CWS plate and mounted from it. Access to the imager detector is gained from the OIWFS side of the cryostat. This is undesirable from a maintenance point of view. However, the arrangement is stiff and the thermal and electrical connections to the detector assembly can be made conveniently, once access has been gained to the OIWFS side of the cryostat.

1.5.3 OIWFS

The OIWFS will be located on the opposite side of the CWS plate to the NIRI/NIFS OIWFS. The beam is folded by four coplanar mirror segments immediately below the cryostat window on the imager side of the CWS plate. The OIWFS components are mounted within and on an optable similar in concept, but not shape, to the NIRI/NIFS OIWFS optable. OIWFS lenses will be mounted in the same way as the imager lenses, and the aperture and filter wheels will use the same drive and encoding philosophy.

The major new development in the GSAOI OIWFS is the steerable mirror mechanism (§4.5.4). The NIRI OIWFS gimbal mirror mechanism will not be duplicated because the GSAOI steerable mirror is required to act over a larger angular range than the NIRI/NIFS gimbal mirror (due to the slower MCAO beam), and we have concerns about the flexure properties of the NIRI/NIFS gimbal mirror. Our solution is to devise a steerable mirror with a three-point actuator system that is similar in concept to the mount designed by RSAA for the tip-tilt secondary mirror on its 2.3 m telescope at Siding Spring Observatory. The three-point actuator system maintains mirror orientation under changing gravity vector and provides the required setting accuracy and angular range using proven concepts.

1.6 Detector Control Systems

GSAOI will use two Detector Control Systems; one for the imager and one for the OIWFS.

1.6.1 Imager Detector Control System

The GSAOI imager will use a 2×2 mosaic of Rockwell 2040×2040 pixel HAWAII-2RG HgCdTe/CdZnTe Molecular Beam Epitaxy (MBE) detectors. GL Scientific will be sub-contracted to design and fabricate the focal plane assembly, and to mount and align the four detectors in this focal plane assembly. RSAA have

worked with GL Scientific previously in a similar way. RSAA will interact closely with Gerry Luppino to ensure that the design for the focal plane assembly meets RSAA requirements. RSAA will collaborate with Don Hall of IfA on the design, optimization, and characterization of the GSAOI imager detector system.

Two imager detector controller designs plus a readout speed upgrade option are presented.

The first controller design is based on a SDSU-2 controller (§5.2.5), which communicates via a 12.5 Mpixel/s fiber-optic link to a standard Gemini IOC. This is proven technology with which RSAA and Gemini have much experience. It is a low risk, cost-effective solution. Each HAWAII-2RG detector will be read out through its four 100 kHz output amplifiers at the slightly faster speed of 200 kHz. The associated read noise is expected to be ~ 10*√2 = 14 e. The pixel time will be 5 μs and the single-read frame time will be 5 s. This result in a correlated double sample (CDS) readout time of 10 s. Detector biases will be provide by a custom RSAA low-noise and high-stability bias board. Detector amplifier output loads will be provide by a custom RSAA output load board.

The second detector controller option is based on four Rockwell Application Specific Integrated Circuits ASICs (§5.2.6). This technology is under development at Rockwell for the Next Generation Space Telescope (NGST). The development time scale may be incompatible with GSAOI. The design uses four ASICs mounted on the focal plane assembly motherboard. The baseline design assumes the NGST detector packaging specified in the Gemini contract with Rockwell. This uses a 65-pin Nanonics connector on the detector package. This limits the device to its four-output modes. The four ASICs replace the SDSU-2 controller in the alternative design. They supply all bias and clock voltages and all necessary video channels. The data are digitized with on-chip ADCs and transmitted via a Low Voltage Differential Serial (LVDS) link to a custom ASIC communications board mounted outside the cryostat. The ASIC communication board produces all supply voltages need to operate the ASICs and implements a 12.5 Mpixel/s fiber-optic communications link to a PMC board in the DC IOC. The design of the communications link will be based on the SDSU-2 communications link design. The overall design will deliver similar performance to the SDSU-2 design, but is expected to be more robust because the ASICs are mounted in close proximity to the detectors. Adverse interaction between the ASICs and the detectors is unquantified, and a major risk with this approach.

The SDSU-2 and ASIC detector controller designs are conservative in order to comply with the requirement for a fast-track instrument. A faster readout speed option is also presented that increases telescope utilization efficiency for short exposure times. In this option, the ASIC detector controller design is upgraded to read out the imager detector in ~ 2.7 s (CDS) using 32 amplifiers per detector at 100 kHz using the 100 kHz slow readout mode of the HAWAII-2RG multiplexer (§5.2.7). The design improves the duty cycle for 60 s integration times from 84% to 96% and for 120 s integration times from 92% to 98%. Viability of the design depends on the availability of a 32-channel HAWAII-2RG detector package and requires variations to the Gemini/Rockwell detector contract. The costs for adopting the upgrade are higher risk, increased complexity of the communication paths, ASIC motherboard, and detector wiring, and a longer time required for detector characterization.

Transferring the imager data from the DC IOC to the Gemini Data Handling System (DHS) is identified as a bottleneck. This cannot be addressed without either modification to the Gemini DHS, which we understand will not happen in the short term, or the addition of an expensive local disk to the DC IOC, which we see as unwarranted and incompatible with a fast-tracked instrument.

1.6.2 OIWFS Detector Control System

Large schedule and cost savings are achieved by duplicating the NIRI/NIFS OIWFS DCS. This is what we will do.

Modern alternatives to the HAWAII-1 detector used in the NIRI/NIFS OIWFSs were considered, but none offers features that significantly improve on the performance of the NIRI/NIFS OIWFSs.

The GSAOI OIWFS DCS will be duplicated from the NIFS DCS that is currently being assembled by the University of Hawaii. RSAA will do this work for the GSAOI OIWFS DCS. One quadrant of a HAWAII-1 detector will be operational. The four OIWFS images will be positioned in one corner of the quadrant near the output amplifier. Acquisition fields of 40×40 pixels and 80×80 pixels will be available, as with NIRI/NIFS. These fields are asymmetric about the optical axis (because only one detector quadrant is operational), and each object in the acquisition field will produce four adjacent images (because the Shack-Hartmann prism is fixed). These are viewed as acceptable compromises in order to reduce OIWFS development time and maintain OIWFS stability, respectively.

1.7 Instrument Control System

GSAOI will use a duplicate of the NIRI/NIFS Instrument Control System (ICS) to control mechanisms and temperatures. The NIRI ICS has been successfully duplicated at RSAA for NIFS. RSAA could begin work on a further duplicate for GSAOI immediately.

Only minor modifications to the NIFS design are required to produce the GSAOI ICS:

- Minor changes are required to some circuit boards to accommodate GSAOI differences. The Sensor Support Boards (SSBs) will incorporate two more channels to accommodate the GSAOI sensor configuration.
- GSAOI will use two more stepper motors than NIFS. This is easily accommodated using the existing Phytron Backplane. The stepper motor driver used to control the NIFS environmental cover will control the GSAOI fast shutter motor. The environmental cover will be controlled using a DC servo motor driven by digital I/O from the VME crate.
- Different cryocoolers will be used. However, the control of these cryocoolers will be similar to the NIRI/NIFS cryocoolers so no major modifications are foreseen.

1.8 Control Software

GSAOI will use duplicates of the NIRI/NIFS Engineering Interface, Instrument Sequencer, Components Controller, OIWFS Components Controller, and OIWFS Detector Controller software with only minor modifications. The GSAOI imager Detector Controller will be based on the NIFS spectrograph DC that controls a HAWAII-2 detector. This will require some modification to accommodate the larger data frames of the mosaic detector and to handle the On-Detector Guide Window.

The minor changes required to the NIFS IS, CC, and OIWFS CC software are:

- Addition of one new mechanism type to the imager CC.
- Addition of separate aperture wheel control to the OIWFS CC. The NIRI/NIFS OIWFS uses one wheel for combined apertures and filters.
- Modification of the OIWFS steerable mirror control to accommodate the three-actuator design. NIRI/NIFS uses a two-axis gimbal mirror.

The OIWFS DC software is a Gemini responsibility, but will be identical to the NIRI/NIFS software because the OIWFS DCS is identical.

The GSAOI DC software is a multi-task design that interfaces to the Gemini EPICS environment using the thin-layer approach adopted for NIFS. The control software required to operate the detector mosaic is written in conventional C/C++ code while the EPICS architecture is used for just parameter and status database handling. Specialist tasks in the design handle control, detector readout, data pre-processing, and then final data transfer to the DHS. These operations are performed in parallel where appropriate to maximize throughput. This architecture is essentially the same as that used for NIFS. Different hardware with higher throughput will be used to handle the larger data volumes involved.

The requirement to use ODGWs is new for GSAOI. Small regions on each of the four HAWAII-2RG detectors will be read out at 100 Hz and the data will be sent to the A&G System using reflective memory and the Gemini Synchro Bus. This guide mode will be in operation before a full detector readout begins, during an exposure, and after the last detector readout of an observation completes. It will be paused when an actual detector readout is underway. The detector controller interface code running on the DC IOC will divert the stream of pixels from the ODGW to the reflective memory sub-system.

Also new for the GSAOI DC software is support for the Gemini *Pause* and *Continue* sequences. These will be used to operate the imager fast shutter, so code will be written to accurately compute exposure time when the fast shutter has been used.

The advantages of the RSAA software design are:

- **Low-cost:** The IS, imager CC, and OIWFS CC use the successful NIFS software. This means that the cost of development for these systems is low. (excluding management, meetings, and commissioning, savings of ~ 600 hr of effort are estimated, compared with the effort expended on the NIFS IS, CC, and OIWFS software).
- **Experience:** RSAA software developers have experience working in the Gemini software environment, including working with EPICS, CICS, VxWorks, UAE, and the DHS. (savings of ~ 300 hr are estimated, compared with time spent becoming accustomed to these systems for NIFS).
- **Proven solution:** By using the IS, imager CC, and OIWFS CC of NIFS and NIRI, the software will have been well tested. We also plan to reuse the NIRI/NIFS OIWFS DC software package.
- **Heritage:** Use of the RSAA *Camera* and *Controller* classes for the DC software takes advantage of code that has had many years of development and testing. (excluding management, meetings, and commissioning, savings of ~ 800 hr of effort are estimated for the GSAOI DC software, compared with effort expended on the NIFS DC software).
- **Parallel development and testing:** Re-using the NIFS DC software components in the CICADA environment will allow us to develop software early on in the project life-cycle, before any hardware is ready. The CICADA package can also be used for parallel detector testing, just as has been done for NIFS.
- **Simplicity:** Re-using the thin-layer EPICS approach adopted for NIFS with software that is already debugged and tested will simplify the EPICS integration.
- **Performance:** The parallel aspects of the DC software architecture coupled with appropriate choice of hardware components in the DC IOC enable the system throughput to be maximized. In addition, use of the Gemini Synchro Bus to transfer ODGW data to the A&G system will be deterministic and fast.

1.9 Summary

In summary, the RSAA design for GSAOI will deliver excellent image quality with high throughput and high stability on a time scale commensurate with MCAO commissioning. These attributes will ensure that the Gemini community gains the maximum scientific return from their investment in MCAO and GSAOI.

2 Systems Design

2.1 Introduction

GSAOI is a complex instrument comprised of various subsystems that must work together. It is also a Gemini facility instrument that must interface to the Gemini environment in a defined way.

The manner in which the top-level GSAOI subsystems interact with each other and with the Gemini environment is described in this chapter.

2.2 Subsystem Interfaces

The interfaces between the GSAOI instrument subsystems and the Gemini environment are shown in Figure 2.

The main mechanical subsystems are the GSAOI imager, OIWFS, and cryostat. The imager contains the focal plane wheel, filter wheel, fast shutter, utility wheel, and imager detector subsystems. The OIWFS contains the steerable mirror, aperture wheel, filter wheel, and OIWFS detector subsystems. The cryostat contains the cryocooler, environmental cover, cold work surface (CWS) plate, and pressure gauge subsystems.

Control of these subsystems normally originates from the Gemini Observatory Control System (OCS). Software commands are received by the GSAOI Instrument Sequencer (IS) and passed to either the Components Controller (CC) or Detector Controller (DC) software. The CC interfaces to the Mechanisms Control System (MCS) hardware and to the Temperature Control System (TCS) hardware. The DC interfaces to the Detector Control System (DCS) hardware.

The MCS interfaces to each of the GSAOI mechanism subsystems in the imager, OIWFS, and cryostat.

The TCS drives the cryocoolers, controls the temperatures of the imager detector, the OIWFS detector, and the CWS plate, and monitors the cryostat vacuum pressure. It also monitors various temperature sensors attached to the CWS plate and controls cool down and warm up functions.

The DCS interfaces to the imager detector.

On-Detector Guide Window data are passed from the DCS via the DC software to the Gemini Acquisition and Guidance (A&G) system. The A&G system is responsible for centroiding the image and initiating tip-tilt and focus correction.

A separate control path exists for the OIWFS. Software commands originating from the Gemini OCS are received by the A&G system and passed to the OIWFS IS. This passes OIWFS mechanism commands to the OIWFS CC and OIWFS detector commands to the OIWFS DC. The OIWFS IS and DC are Gemini responsibilities. The OIWFS CC is a GSAOI responsibility.

The OIWFS CC interfaces with the GSAOI MCS hardware.

The OIWFS DC interfaces with the OIWFS DCS hardware, which then interfaces to the OIWFS detector.

The MCAO system interfaces with the GSAOI IS via software commands to activate the imager fast shutter.

GSAOI also interfaces with MCAO to configure the static form of deformable mirror DM0. This is shown in Figure 2 as an interface from the imager utility wheel that houses the defocusing system to the MCAO.

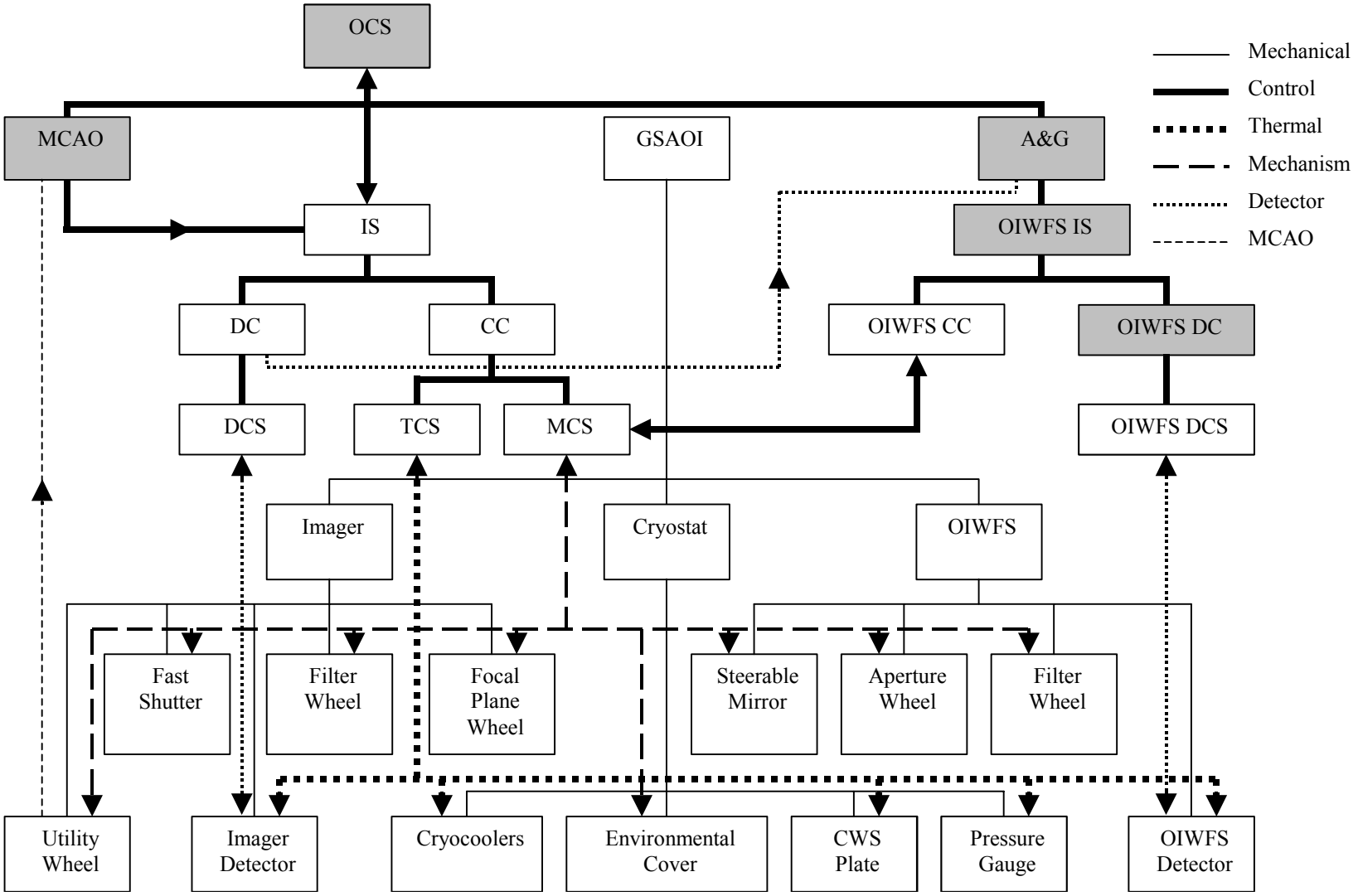

Figure 2: GSAOI subsystem interface schematic. Shaded boxes are Gemini responsibilities.

2.3 Environmental Heat Load

The GSAOI design meets the Gemini environmental heat load requirement. The maximum acceptable heat load that can be conducted into the instrument body is 50 W and the maximum acceptable heat load that can be convected into the dome is 50 W. The heat generated by the cryocoolers is excluded from this budget. The majority of the heat-generating electronic components will be mounted inside the two cooled thermal enclosures. The two items that need to be mounted on the cryostat are the imager SDSU-2 detector controller and the OIWFS SDSU-2 detector controller. These detector controllers generate ~ 45 W each and will be bolted to the cryostat. Both will be water cooled so only a small fraction of this heat will be dissipated at the cryostat.

2.4 Mass Budget

The GSAOI design meets the Gemini instrument mass requirement of 2000 kg. The mass budget for GSAOI is presented in Table 1.

Table 1: GSAOI Mass Budget

Item	Mass [kg]	Source
ISS Interface Plate	187	Mechanical Desktop Solid Model
Main Frame (and partial ballast)	500	Estimate
Cryostat Vacuum Jacket	265	Mechanical Desktop Solid Model
OIWFS (including optable and radiation shield)	125	Mechanical Desktop Solid Model (estimate)
CWS and Support Trusses	58	Mechanical Desktop Solid Model
Imager (including optable and radiation shield)	170	Mechanical Desktop Solid Model (estimate)
Detector Controllers (2 of)	15	Estimate
Thermal Enclosures (2 of)	330	From Gemini ICD
Detector Controller Power Supplies (2 of)	23	Estimate
IOC (2 of)	40	Estimate
ICS Stepper Motor Drive Frame	20	Estimate
ICS Sensor Interface Frame	10	Estimate
ICS Temperature Controllers (3 of)	15	Estimate
ICS Temperature Control Hardware	20	Estimate
Cabling and Hoses	50	Estimate
Miscellaneous	40	Estimate
Subtotal	**1868**	
Ballast	132	
Total	**2000**	

2.5 Center of Gravity Budget

The GSAOI design meets the Gemini center of gravity requirement; ballast weights will be used to give GSAOI the same center of gravity as NIRI.

2.6 Instrument Volume

The GSAOI design meets the Gemini instrument volume requirement; it will occupy the same space envelope as NIRI.

2.7 Optical Image Quality Budget

GSAOI will produce an optical wave-front error of 46 nm RMS, which is less than the instrument allocation of 65 nm RMS. The optical image quality budget is presented in §3.5.4.4

2.8 Throughput Budget

The GSAOI design meets the requirement of > 25% system throughput, excluding MCAO. The throughput budget is presented in §3.5.6.

2.9 Emissivity Budget

The GSAOI design meets the requirement of an effective instrumental emissivity of < 1% at wavelengths > 2.2 μm (see §3.11) and an instrumental photon background less than one half of the detector dark current (see §3.14).

2.10 Mechanical Flexure Performance

GSAOI will use an OIWFS guide star to provide closed-loop tracking and flexure correction. It is then necessary only to control open-loop mechanical flexure between the OIWFS detector and the science detector.

The mechanical flexure performance is discussed in §4.7. GSAOI will perform well within the 0.1 pixels per hour requirement of Gemini.

Image translation will be monitored directly on the imager detector when a sufficiently bright ODGW guide star is available. This eliminated differential flexure between the imager and OIWFS detectors.

2.11 Thermal Enclosure Space Allocation

GSAOI will use two thermal enclosures. The Instrument Control System (ICS) consists of the Mechanism Control System and the Temperature Control System. It will be located in one thermal enclosure. The Detector Control System (DCS) will be located in the other thermal enclosure. The DCS consists of the DCS IOC, the imager detector controller power supply, the imager detector controller PMC interface board, the imager detector temperature controller, and the OIWFS detector controller power.

The components layouts for the ICS thermal enclosure and the DCS thermal enclosure are shown in Figure 3 and Figure 4.

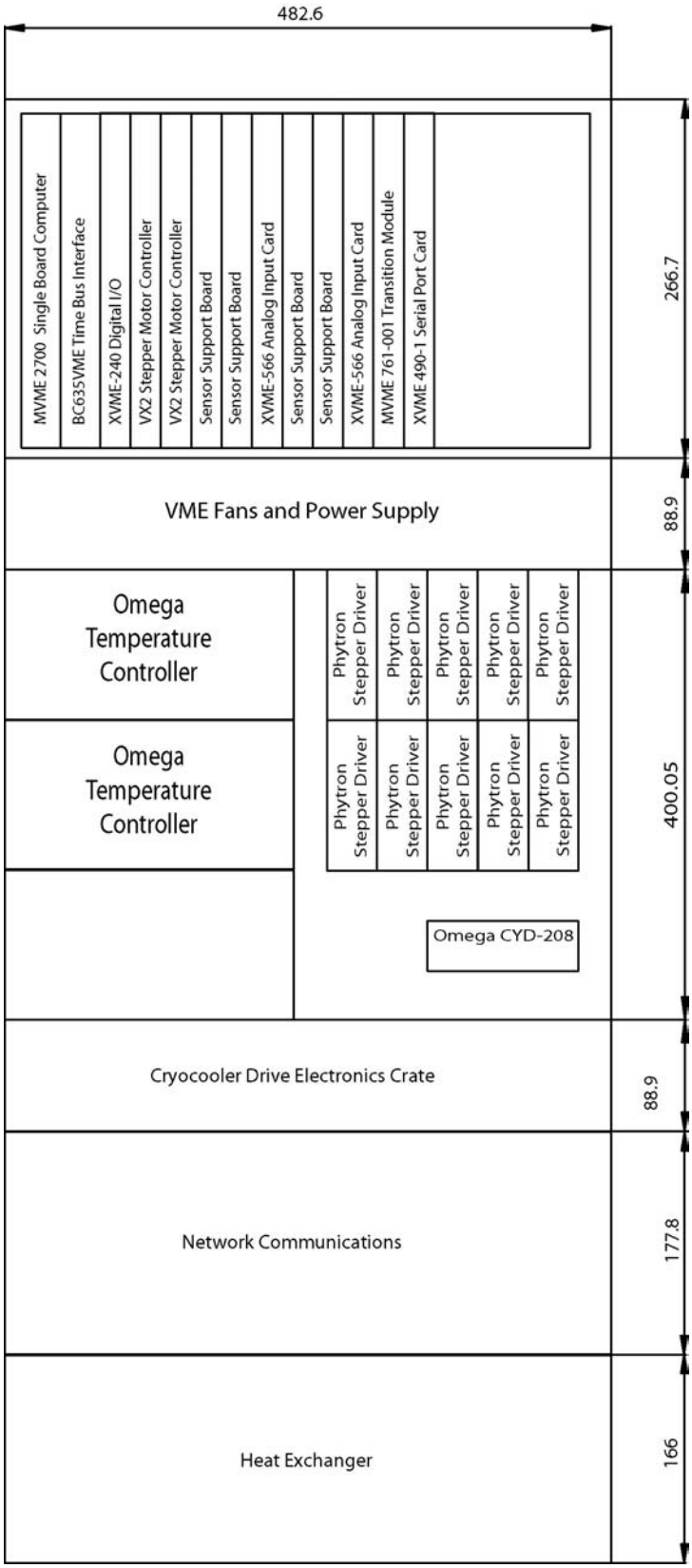

Figure 3: ICS thermal enclosure layout.

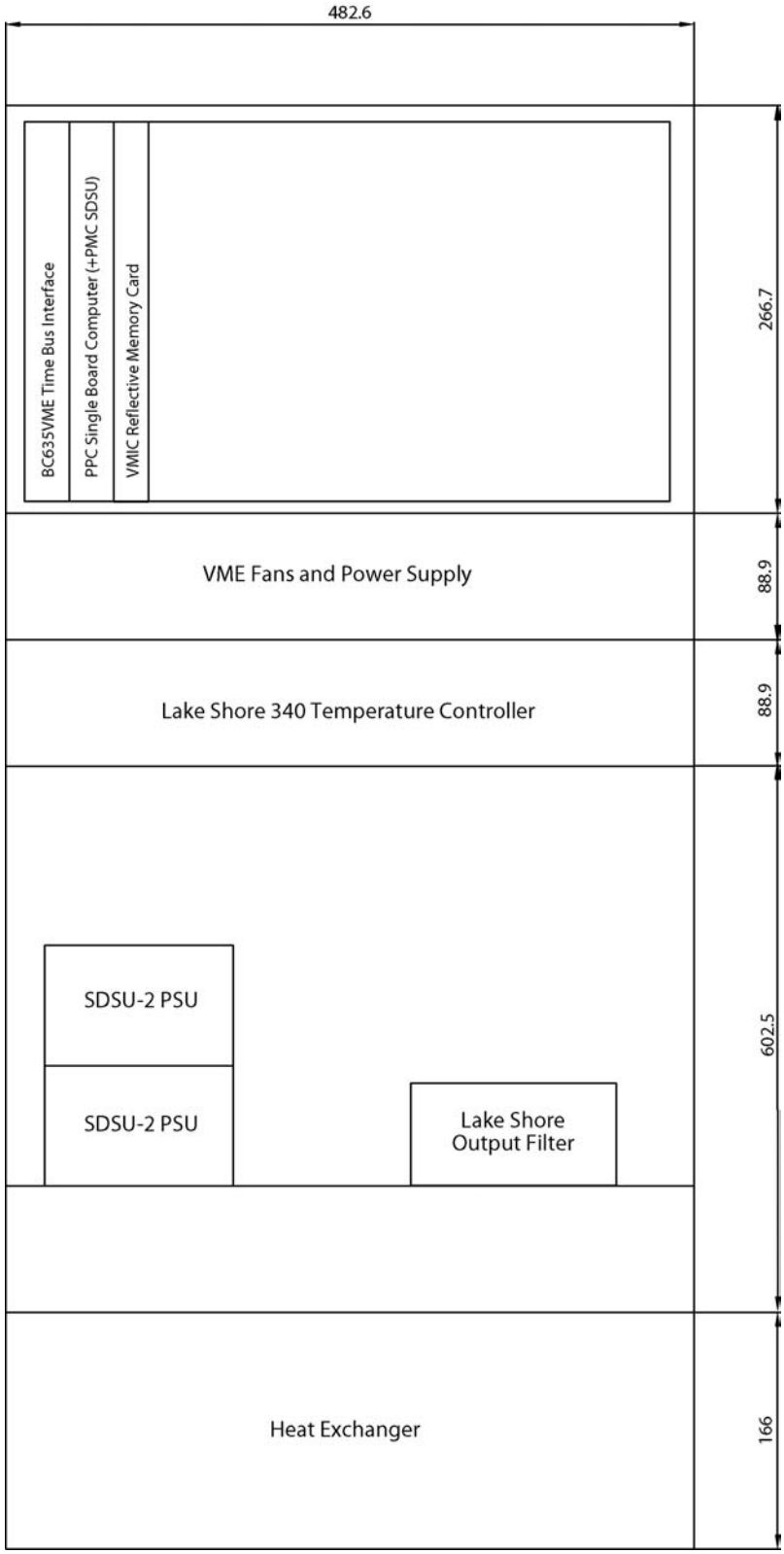

Figure 4: DCS thermal enclosure layout.

2.12 Electrical Power Budget

The estimated power requirements for the ICS thermal enclosure are shown in Table 3. Power requirements for the DCS thermal enclosure are shown in Table 4. These power requirements are based upon manufacturer's data sheets and are conservative. Actual measurements on the NIFS ICS thermal enclosure (equivalent to the GSAOI ICS thermal enclosure) show power consumptions of 770 VA during normal operation and 810 VA during accelerated warm up.

Table 3: ICS Thermal Enclosure Power Requirements.

Component	**Power (W)**
VME Rack:	
MVME 2700 Single Board Computer	23
BC635VME Time Bus Interface	9
XVME-566 A/D Card (×2)	42
Oregon VX2 Stepper Controller (×2)	24
XVME-240 DIO Card	8
XVME-490 Serial Card	7
Sensor Support Board (×4)	20
VME Fans & Power Supply	50
Thermal Control:	
Omega CYC321-01 Controller (×2)	130
Lambda ZUP-60 Power Supply	40
Pacific Scientific Stepper Drivers (×2)	50
Lambda FE-500 Power Supply (×2)	150
Mechanism Stepper Motor Control Total	150
Network Communications:	
Cisco Switch	240
Annex 2000 Terminal Server	100
Total ICS Thermal Enclosure	**1043**

Table 4: DCS Thermal Enclosure Power Requirements.

Component	Power (W)
VME Rack:	
BC635VME Time Bus Interface	9
PPC Single Board Computer	20
PMC SDSU Interface Card	10
VMIC Reflective Memory Card	6
VME Fans & Power Supply	50
Cabinet:	
Lakeshore 340 Controller	190
SDSU-2 Power Supply (×2)	80
Total DCS Thermal Enclosure	**365**

2.13 Handling Equipment

2.13.1 Test Area and Lifting Equipment

The entire GSAOI instrument will be integrated and tested in the RSAA workshop assembly room at Mt. Stromlo Observatory. The assembly area floor space measures ~ 5000×4600 mm and has a ceiling clearance to an overhead I-beam of ~ 4600 mm. The I-beam is suitable for lifting a 3 tonne mass and is fitted with twin chain hoists. Access to the room is via high double doors that are 1600 mm wide. This is wide enough to pass all GSAOI components including the integration frame. The overhead I-beam is high enough to allow full tilt tests to be performed on the assembled instrument. The thermal enclosures and their support frames will be added to the integration frame once it is in the room. The same facilities are currently being used to assemble NIFS.

Trolleys for handling GSAOI mechanical subsystems are described in §4.9.

2.13.2 Clean Room Trolleys, Hoist, and Beam

The GSAOI optical system and cryostat will be assembled in a clean room environment using anti-static precautions. A 150 kg rope hoist is fitted to the ceiling of the RSAA clean room. Small, purpose-built lifting systems will be used to lift GSAOI sections during assembly.

Two flatbed trolleys are available to transport the vacuum jacket sections to and from the clean room. These two trolleys have a 500 kg load capacity and measure ~ 1000 mm square.

The same procedures have been used to assemble NIFS.

2.14 Calibration Requirements

GSAOI imager frames will require bias subtraction, dark frame subtraction, flat fielding, correction for geometrical distortion, and flux calibration. GSAOI will use twilight sky frames, dome flats, or continuum lamps in the Gemini Calibration Unit (GCAL) for flat field calibration.

GSAOI OIWFS frames will require bias subtraction and possibly flat fielding. Continuum lamps in GCAL will be used to record OIWFS flat-field frames. The Observatory Control System is responsible for scheduling these exposures.

2.14.1 Imager Bias Frames

Bias frames are needed to determine the electrical offsets for each detector pixel. The GSAOI imager will include blocked positions in the focal plane wheel, filter wheels, and utility wheel. These will prevent external light reaching the imager detector. Bias frames will be recorded using the minimum possible exposure time (~ 5 s). Zero length exposures are not possible due to the readout architecture.

2.14.2 OIWFS Bias Frames

The GSAOI OIWFS will include a blocked position in its aperture wheel. This will be use to record OIWFS bias frames. These will be recorded using the minimum possible exposure time (~ 5 s).

2.14.3 Imager Dark Frames

Dark frames are used to remove the signal component due to spontaneously generated charge and background light from within the cryostat that does not scale in the same way as light entering from outside the cryostat. Imager dark frames will be recorded using the blocked positions in the imager focal plane wheel, filter wheels, and utility wheel.

2.14.4 Flat-Field Frames

Throughput variations and pixel-to-pixel quantum efficiency and gain variations cause pixel-to-pixel signal variations in response to uniform illumination. The GSAOI imager and OIWFS will use continuum lamps in GCAL for flat-field calibration. GCAL flats will use the near-infrared diffuser in GCAL. The lamp intensities have been specified for NIRI. The pixel scale of GSAOI is similar to the high-resolution mode of NIRI, so the GCAL lamp intensity should also suit GSAOI.

The beam from GCAL is injected below MCAO, so flat-field frames obtained in this way do not allow for throughput variations within MCAO. Large-scale sensitivity variations can be calibrated using exposures of the twilight sky or the dome interior.

2.14.5 Geometric Distortion

Exposures of astrometric star fields will be used to parameterize and remove geometrical distortion in imager frames. The distortion within each detector frame and the relative locations on the sky of the four detectors will both need to be determined.

2.14.6 Flux Calibration

Measurements of stellar flux standards will be used for absolute flux calibration of GSAOI images. Suitable flux standards will be drawn from lists of photometric standard stars. As noted in §3.1.3.1 of Vol. 1, it will be necessary to use a 512×512 pixel sub-region of the imager detector read out in 0.3 s to record unsaturated images of the brightest of the Persson et al. (1998, AJ, 116, 2475) faint photometric standards.

2.14.7 Non-Common-Path Phase Errors

Non-common-path wave-front phase errors will exist between MCAO and GSAOI. The wave-front error will be measured by recording defocussed images on either side of focus of artificial stars generated by MCAO (see §3.3 of Vol. 1). A convex and a concave defocus lens will be mounted in the utility wheel to produce these images. Gemini has already sent RSAA a copy of the program *ExtraFocal* (Laplacian Optics Inc.) for analyzing these images. This program outputs coefficients of low-order Zernike polynomials characterizing the wave-front shape. These will be converted into deformable mirror actuator offsets that will be input to the MCAO system to null the wave-front error.

2.15 Differential Atmospheric Refraction

2.15.1 Wavelength Dependence

Atmospheric refraction alters the apparent position of an object by an amount dependent on zenith distance and wavelength. The dominant effect for GSAOI is the differential refraction caused by the finite width of the wavelength bands passed by the filters. The MCAO atmospheric dispersion corrector is designed to correct this effect. The maximum value likely to be encountered occurs at a zenith distance of 60º. This value is listed in Table 5 for the major broad-band filters that will be used with GSAOI. The diffraction full width at half maximum on Gemini South at the central wavelength of each filter is also listed in the table. A comparison of these diameters shows that it will be necessary to use the MCAO atmospheric dispersion corrector for observations with the *Z*, *J*, and probably *H* filters, but that differential refraction will not significantly smear diffraction-limited images observed with the *K* filter.

Table 5: Wavelength-Dependent Differential Atmospheric Refraction at 60º Zenith Distance

Filter	Differential Refraction (″)	Diffraction FWHM (″)
Z	0.154	0.032
J	0.077	0.040
H	0.049	0.053
K	0.026	0.070

2.15.2 Field Dependence

A secondary effect is differential refraction between the tracking center and other objects in the field. The tracking center will effectively be the location of the primary tip-tilt guide star. We assume that this coincides with the field center. Figure 5 plots the differential refraction between this tracking center and an object located in a diagonal corner of the imager detector (there is only a weak wavelength dependence in this value). This effect produces an image displacement (i.e., distortion) of ~ 2 pixels at a zenith distance of 60º. The MCAO atmospheric dispersion corrector does not correct this. Consequently, astrometric observations should be restricted to zenith distances less than ~ 45º.

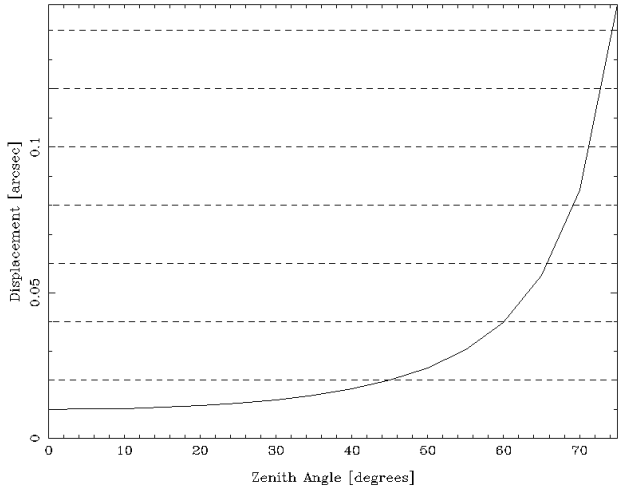

Figure 5: Differential refraction between field center and field edge as a function of zenith distance. The 0.02″ wide GSAOI pixels are indicated by dashed lines.

2.15.3 Guiding Implications

GSAOI can use its OIWFS to define the primary tracking center. The OIWFS will monitor its guide star at a position that is offset from the imager field center. The Telescope Control System will have to offset the OIWFS steerable mirror between long exposures to correct for differential refraction between the OIWFS and the imager field center.

2.16 Risk Analysis

A summary of the major risks associated with the GSAOI project is presented in Table 6. Each risk has been assigned an estimate of its impact on the scientific performance of GSAOI and a risk level. High-level risks that impact severely on science performance will be addressed with highest priority. A statement on how each risk will be mitigated is also included in Table 6.

Table 6: GSAOI Risk Mitigation Strategy

Item	Area of Concern	Science Impact	Risk Level	Risk Mitigation Plan
1	Science:			
1.1	Imager Sensitivity	HIGH	MEDIUM	Imager performance has been modeled and the impact of reduced sensitivity has been assessed in developing the science drivers.
1.2, 2.2	Guide Star Availability	HIGH	LOW	Guide star availability has been assessed in developing the science drivers. Many science drivers can choose fields near suitable guide stars. The OIWFS has been designed to be as sensitive as practicable in a fast-tracked instrument. However, OIWFS guide field has been sacrificed in order to simplify the OIWFS design.
2	Optical:			
2.1	Non-Telecentric Output	MEDIUM	MEDIUM	The excellent chromatic correction of the imager optics will be maintained to ensure that no wavelength dependent scale change occurs. The potential detector ghost is unavoidable.
2.3	Material Availability	MEDIUM	HIGH	Develop design variants using other optical materials in case MgO is not available on a suitable timescale.
2.4	Cryogenic Refractive Index Data	MEDIUM	HIGH	Attempt to make contact with groups who may be able to measure refractive indices. If this fails, adopt a design variant that uses materials with known cryogenic data.
2.5	Lens Manufacture	MEDIUM	LOW	Lens manufacture will be assigned ample lead time so that it is not on the critical path. An interferometer will be purchased for the RSAA Optical Workshop to ensure that surface figure can be measured to the required accuracy.

Item	Area of Concern	Science Impact	Risk Level	Risk Mitigation Plan
2.6	Doublet Lens Gap Precision	MEDIUM	LOW	The optical design will be revised to increase the glass-spacer thicknesses and improve their manufacturability. Doublet lenses and their glass spacers will be manufactured early to ensure that delays do not affect schedule.
2.7, 3.1	Lens Mounting Safety	MEDIUM	MEDIUM	Ample lens mounting tolerances will be allowed and mounts will be checked before lenses are installed. The mounting technique will be demonstrated for the NIFS spectrograph camera before it is used for GSAOI.
2.8	Throughput	HIGH	MEDIUM	Lens and mirror coatings will be obtained from experienced suppliers who are most likely to deliver the designed performance.
2.9	Filter Cost and Availability	HIGH	MEDIUM	Filter suppliers will be contacted early in the design phase. Attempts will be made to establish a new filter consortium to reduce costs and to encourage filter suppliers to commit to the filter manufacture. The lead time in producing the necessary filters is still a concern. Some filters may arrive after GSAOI is commissioned.
3	Mechanical:			
3.3	Steerable Mirror Development	MEDIUM	LOW	The steerable mirror mechanism will be designed by the Project Engineer and manufactured early so that it can be tested as soon as the GSAOI cryostat is available.
4	Detector:			
4.1	Detector Delivery	LOW	MEDIUM	Rockwell will be informed of delivery requirements. The imager DCS will be designed and manufactured before detector delivery based on experience at IfA with the NGST detectors.
4.2	Detector Damage	HIGH	LOW	Extreme precautions will be taken in handling and storing the device.
4.3	ODGW Performance	LOW	MEDIUM	The OIWFS will be treated as the primary source for monitoring image translation. It will be used in place of the ODGW if necessary.
4.4	Focal-Plane Assembly Delivery	LOW	MEDIUM	RSAA will work closely with Gerry Luppino in designing the focal plane assembly. RSAA will manufacture parts of the assembly if this proves necessary.

Item	Area of Concern	Science Impact	Risk Level	Risk Mitigation Plan
4.5	SDSU-2 Induced Bias Drift	LOW	LOW	A custom bias board will be used for the more sensitive H2RG biases. Reference pixels and reference channels will be sampled. Detector temperature will be controlled to the mK level. Experience gained in reaching higher performance levels for NIFS will be used in the DCS design.
4.6	ASICs Induced Bias Drift	LOW	MEDIUM	Performance of ASICs will be fully explored before deciding on this option. If chosen, the ASICs will be heat sunk to the detector housing to improve their thermal stability.
4.7	ASIC Performance	MEDIUM	HIGH	The development of the ASIC will be monitored and, through collaboration with IfA, early test data will be sought to determine the adequacy of ASICs to meet GSAOI requirements.
4.8	SDSU Controller Delivery	LOW	MEDIUM	The DCS will be developed with RSAA's CICADA software using a PCI interface before the PMC card will be required. Progress in testing of the Octal Channel video boards will be monitored and an order placed as soon as possible.
4.9	ASIC Microcontroller Code Development	LOW	LOW	Template microcontroller code will be obtained from Rockwell and from IfA. ASICs will only be adopted if all development issues are resolved.
4.10	Test Cryostat Development	LOW	LOW	Resources for a test cryostat will be indentified early. Duplication of Don Hall's system will be explored.
5	Software			
5.1	Staff Loss	LOW	LOW	This problem applies to several areas. The mitigation strategy is common. New staff are being involved in Gemini work so that the knowledge gained in developing NIFS and GSAOI is shared widely.
5.2	PMC Device Driver Development	LOW	MEDIUM	Initial DCS development will use a PCI interface and RSAA's CICADA software so that development of a PMC driver is not on the critical path. Availability of a driver from the MCAO group will be monitored. Driver development tools will be investigated.

3 Optical Design

3.1 Introduction

GSAOI is a diffraction-limited imager for the Gemini South telescope. It has an 85″ square field and includes an OIWFS to eliminate image motion and defocus. It will be used in conjunction with the MCAO system to achieve diffraction-limited performance over the whole field. GSAOI is only one component of the optical system, and so must contribute less than a prescribed amount to total image degradation. Accordingly, it has been allocated a wave-front error limit of 65 nm RMS. A distortion limit of 0.1% has also been specified.

The imager uses a 4080×4080 pixel detector array constructed as a mosaic of four 2040×2040 pixel buttable detectors with 18 μm square pixels. There is a gap of 2.5 mm between the detectors, so the complete detector surface is 76.2 mm square. The required image scale is 0.02″/pixel, and the angular field is therefore 84.7″ square. This neatly fits within the 120″ circular field delivered by the MCAO system.

The basic function of the imager is to re-image the MCAO field onto the detector at a suitable scale. In the process, it must form an image of the pupil on a cold stop to reject stray radiation, and provide suitable filtering. A facility to image the pupil onto the detector for diagnostic purposes is also provided.

Four optical systems have been considered for the imager, as described in §3.5. One of these has been adopted as the baseline design, and is described in detail. It is a refractive system with non-telecentric output that delivers good image quality through a minimum number of elements.

The basic function of the OIWFS is to capture a star image from within the MCAO field and use this to detect image motion and defocus. The possibility of using a movable probe to capture the star image has been investigated, but has not been adopted for the baseline system because of the need for extreme stability and rapid development. Instead, a field splitting mirror is proposed that feeds the unused crescent zones of the MCAO field to the OIWFS. This limits the available guide star field, but also eliminates vignetting of the imager field. The OIWFS design is discussed in §3.6.

For the OIWFS, a wave-front error limit of 120 nm RMS has been set to allow sufficiently accurate centroiding.

3.2 Cryostat Window Modification

The GSAOI cryostat will be a replica of the NIRI cryostat, except that the window will be modified to pass the larger GSAOI field. A clear aperture of at least 163 mm is required for the 120″ field at f/34. It is proposed that the window diameter be increased from 180 to 200 mm, and that the mount be modified to increase the clear aperture from 147 to 170 mm.

This modification can be made without any increase in the spatial envelope of the window port, and so it can be accommodated without changes to either the ISS interface plate or the window cleaning system.

The window material has been changed to fused silica because the extended wavelength range transmitted by calcium fluoride is not required for GSAOI, and fused silica is otherwise more suitable. The baseline optical design also makes use of slight convexity in the outer face of the window to assist with ghost image control.

3.3 Input Image Condition

The input image for GSAOI is delivered through the MCAO system. While this improves image quality, it also introduces considerable asymmetric field distortion and provides a severely tilted exit pupil image.

Correction of these aberrations in the imager would be difficult, and is not proposed. Rather, it is assumed that the optics of GSAOI will be designed for a perfect input image delivered from a perfect exit pupil, and image quality is assessed on that basis. The tilt of the exit pupil can be accommodated by tilting the cold stop, but poor imagery of the pupil onto the detector cannot be avoided.

3.4 General Layout

The layout of the baseline optical system is shown on Figure 6, including both the baseline version of the imager, and the OIWFS. In this trimetric view, the hexagonal cold work surface plate (not shown) lies in a horizontal plane between the imager and OIWFS, just below the cryostat window. The imager occupies the space above this plate, and the OIWFS occupies the space below.

The beam encounters a field splitter mirror immediately beyond the window. The inscribed square region of the field passes through a square hole in the mirror into the imager, while the remaining crescents from the circular input field are reflected through a hole in the CWS plate and into the OIWFS. A number of fold mirrors are required in both modules to accommodate them within the available cryostat space.

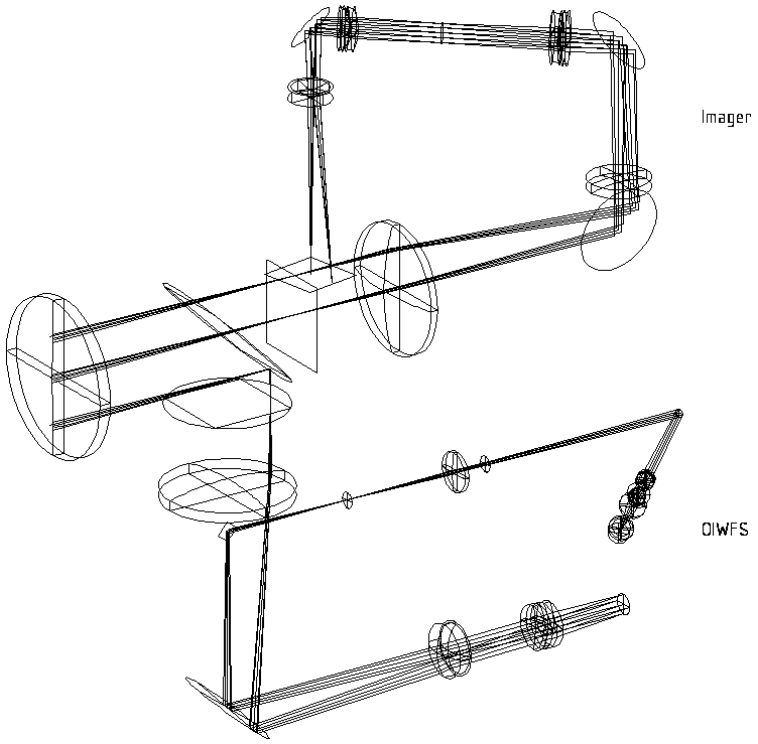

Figure 6: Folded layout of the baseline optics showing both the imager and the OIWFS.

3.5 Imager Design

The basic function of the imager is to re-image the MCAO field onto the detector at a scale of 0.02″/pixel. The detector pixels are 18 μm square and the focal length of the telescope and MCAO system is 262200 mm. The required magnification of the imager is therefore 0.708.

The imager must pass the full 85″ square field, and form a pupil image on a cold stop in the process. The beam is made roughly collimated at the pupil image, and so this region is also suitable for the placement of filters.

The input image is located 300 mm behind the ISS mounting surface. For design purposes, it is assumed to be free of aberrations.

Four basic optical systems have been considered for the imager. These comprise a TMA (three mirror anastigmat) reflective system, a hybrid system using an Offner relay, a refractive system with telecentric output, and a refractive system with non-telecentric output. The latter has been adopted as the baseline design. Within this, several variations have been devised that use different combinations of lens materials. That using calcium fluoride and magnesium oxide is favored.

3.5.1 Configuration Options

3.5.1.1 TMA System

A three mirror anastigmat is a possible configuration for the GSAOI imager optics. They have been used as the cameras for several 8-10 m telescope near-infrared spectrographs (ISAAC on the VLT, NIRSPEC on Keck, and IRCS on Subaru uses a four mirror anastigmat) and are being used in the Keck AO imager NIRC-2.

TMAs offer several advantages over refractive optical designs at near-infrared wavelengths:
- Mirror systems are intrinsically achromatic.
- They are intrinsically free from reflected ghost images.
- They have few surfaces and high throughput.
- They can handle wide fields.
- Any surface of revolution can be diamond machined as a metal mirror.

The disadvantages of TMAs are:
- They are difficult to design.
- They require tight alignment tolerances.
- They are expensive to manufacture.
- The diamond machining required for complex surfaces results in surface scatter.

The possibility of using TMAs as the collimator and camera for the imager is investigated analytically in Appendix A (§8.4). The conclusions are summarized as follows.

The three conic constants for the TMA surfaces can be chosen to eliminate three of the third-order aberrations (e.g., third-order spherical aberration, coma, and astigmatism). The geometry can be chosen to also eliminate field curvature using the Petzval condition.

This leaves distortion uncorrected. In principle, this can also be eliminated in a centered axial system by suitable choice of geometry. However, the options for doing so in the GSAOI imager optics are limited by the constraint of fitting the design within a duplicate NIRI/NIFS cryostat.

We might aim to cancel the asymmetric MCAO distortion in the GSAOI imager optics. However, the orientation of the MCAO system with respect to the cryostat is such that this requires a GSAOI TMA to be decentered perpendicular to the cryostat cold work surface plate. This is not a convenient geometry to implement. The result is a system combining two perpendicular asymmetric distortions that would be difficult to model and correct in practice.

All the TMA options investigated had severe distortion problems, and so no specific design is presented here. The option is rejected as being unsuitable for GSAOI.

3.5.1.2 Offner Relay System

An Offner relay (Offner 1975, Opt. Eng., 14, 130) is a simple symmetric reflective system that relays an image with unit magnification while forming a pupil image on an intermediate mirror that can act as a cold stop. It does not produce the scale change required for the GSAOI imager, but adding three lenses to the output beam can provide this. Such a system is shown in Figure 7. The optical performance of this design is excellent (Figure 8). Additional mirrors are required for packaging purposes, but it nevertheless has high throughput due to the low number of surfaces. Distortion is only 0.6 pixels (Figure 9), although it is asymmetric.

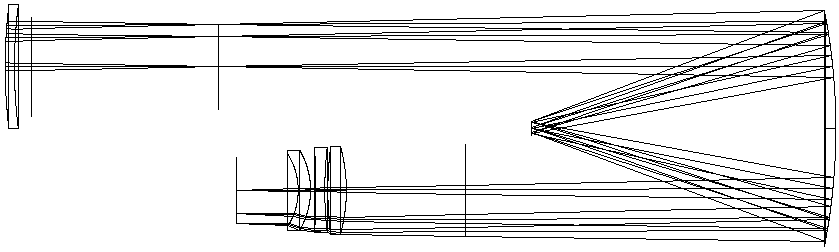

Figure 7: Optical layout for the Offner relay system.

The major shortcoming of this design is the need for 180 mm diameter filters in the f/33 output beam of the Offner. The cost and uniformity of such large filters are significant issues. More seriously, it would be very difficult to accommodate a suitable suite of such filters in the available cryostat space. There is also no convenient way of viewing the pupil image.

For these reasons, the Offner option is rejected.

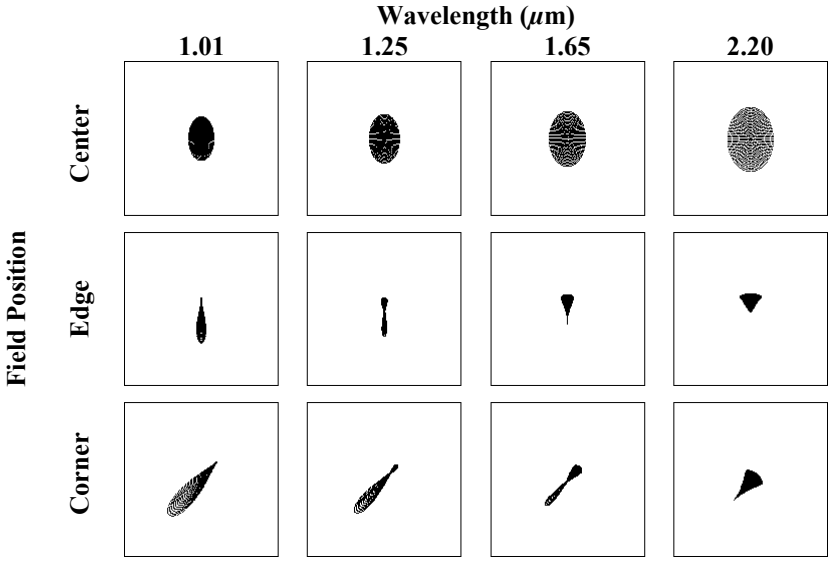

Figure 8: Spot diagrams for the Offner relay system. Boxes are 2 pixels square.

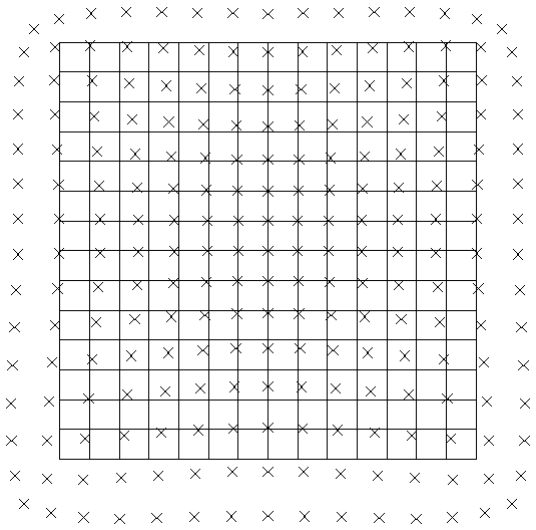

Figure 9: Grid distortion for the Offner relay system at a wavelength of 1.6 μm with deviations amplified by 1000. Maximum distortion is 0.6 pixels.

3.5.1.3 Refractive System with Non-Telecentric Output

A refractive optical system with non-telecentric output to the detector appears to be the most suitable option for the GSAOI imager. The layout of this is shown in Figure 10. This design features a minimum number of lenses, high throughput, excellent image quality, and low distortion (see §3.5.4). Pupil image quality is also reasonable in relation to that produced by the MCAO system.

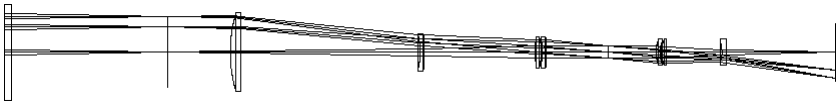

Figure 10: Optical layout for the non-telecentric output system.

In part, these characteristics have been achieved by accepting a non-telecentric output. The risks associated with this are that any focus instability is accompanied by scale instability, and that ghost images generated by internal reflection within the detector substrate become apparent because they are displaced slightly from the parent image (in proportion to field eccentricity). For the design presented, however, neither phenomenon appears to be significant.

The design is well-corrected over the entire wavelength range. As a result, no focus mechanism is required, and the system can therefore be designed for focus rigidity. Investigation of the substrate ghost (§3.5.5) indicates that it will not be significant.

This option is adopted as the baseline configuration. Its performance is examined in detail in subsequent sections.

In its preferred form, this system uses calcium fluoride and magnesium oxide as the materials in the achromatic pairs of both the collimator and camera. Three alternative forms of the non-telecentric design have been devised using:

- Barium fluoride and IRG2.
- Barium fluoride, lithium fluoride, and zinc selenide.
- Zinc selenide, fused silica, and barium fluoride.

All are feasible, and so provide options regarding cost, availability, and manufacturing characteristics. Comments on these options are as follows.

The baseline system using calcium fluoride and magnesium oxide is preferred because it has good performance, its geometry is well suited to folding within the available cryostat space, and the materials are available in blanks of the required size. There was some concern about the systematic surface irregularities in magnesium oxide, but subsequent investigation has discounted this (§3.5.4.4.2). The remaining concern is that cryogenic refractive index data is not available for magnesium oxide, and so measurement will be required during final design. There is a possibility that this could be problematic.

The system involving IRG2 is not preferred because this material would have to be manufactured to special order. Additionally, its refractive index is known to vary significantly from batch to batch, and so measurement would still be required.

The lithium fluoride option is considered the least desirable because it is well known for being difficult to work and the resulting surface geometry tends to be poor. In addition, the optical layout required more fold mirrors than the preferred system.

The system using zinc selenide, fused silica, and barium fluoride is regarded as the most feasible alternative to the preferred system. Its optical performance is slightly inferior, but it has no other problems. It has the advantage that cryogenic refractive index data are available.

3.5.1.4 Refractive System with Telecentric Output

A modified version of the baseline refractive system introduced in the foregoing section has been developed to provide telecentric output, as shown in Figure 11. This feature is achieved by adding a field lens near the detector. The field curvature that this introduces is then compensated by increasing the strength of negative lenses on both sides of the cold stop.

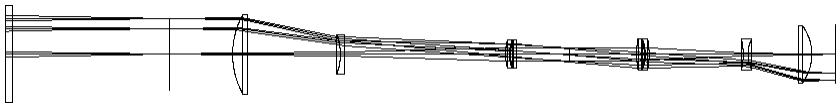

Figure 11: Optical layout for the telecentric output system.

In general, this design is compromised by the need to keep it short and so allow efficient folding within the available cryostat space.

Spot diagrams and distortion characteristics are shown in Figure 12 and Figure 13, respectively. Field imagery is not as good as that achieved by the non-telecentric system, but performance requirements are satisfied in this regard. In general, the design uses more severe surface curvature and is more stressed.

More seriously, however, pupil imagery is considerably degraded. Relative to the non-telecentric design, spherical aberration in the pupil image increases by a factor of 10, and chromatic aberration increases by a factor of 1.5. The radial aberration span at the edge of the pupil image is shown in Table 7 for both systems. The pupil image diameter in both cases is 25 mm.

The quality of the pupil image must be judged in relation to that delivered by the MCAO system. The radial aberration for this varies around the circumference of the pupil because the optics are asymmetrical, but a representative value is also included in Table 7 to allow comparison.

Table 7: Pupil Image Quality for the Two Refractive Imager Systems

Radial Aberration Span (mm)		Wavelength (μm)			
		0.85	**1.3**	**1.8**	**2.5**
System	**Telecentric**	-3.74	-2.81	-2.01	-0.73
	Non-Telecentric	-0.98	-0.38	0.13	0.96
	MCAO	1.0			

Clearly, the effectiveness of the cold stop in the telecentic output system would be reduced considerably. To correct this aberration, an aspheric surface could be used on the field lens, or better still, a doublet could be used in its place. Neither option is considered worthwhile.

This telecentric configuration is considered viable, but the non-telecentric version is preferred because it is simpler and has better performance.

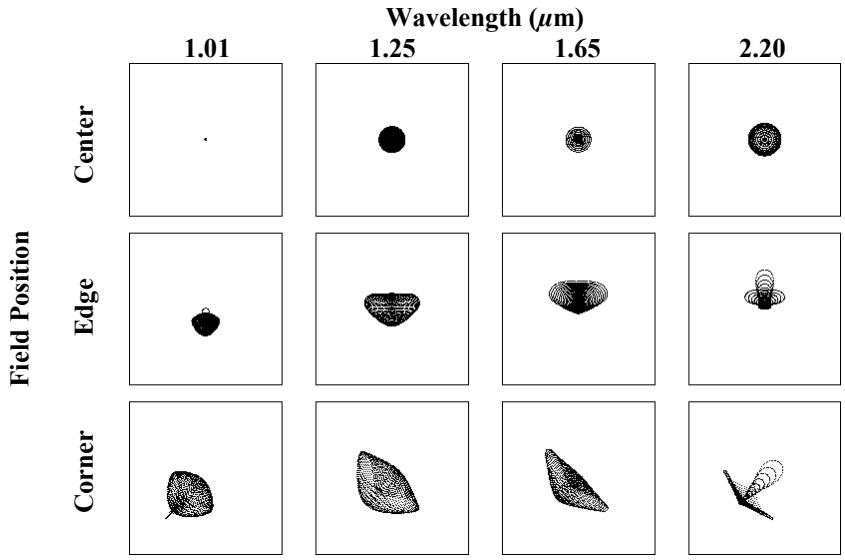

Figure 12: Spot diagrams for the telecentric output system. Boxes size is 2 pixels square.

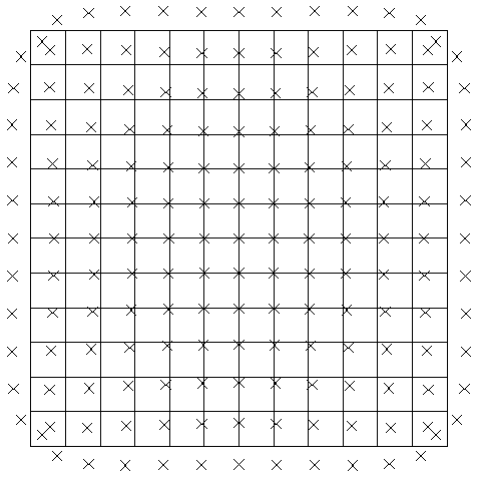

Figure 13: Grid distortion for the telecentric output system at a wavelength of 1.6 μm with deviations amplified by 1000. Maximum distortion is 0.2 pixels.

3.5.2 Baseline Configuration

The non-telecentric configuration introduced in §3.5.1.3 is adopted as the baseline design for further consideration.

3.5.3 Description

The folded layout of the baseline imager is shown in Figure 14. This clearly shows the non-telecentric output onto the detector. It is probably the simplest possible system for this application. Beyond the field lens, it uses just three lenses for both collimator and camera. In each case, one lens functions as a telephoto element, as is needed to shorten the system and so allow efficient folding within the available cryostat space.

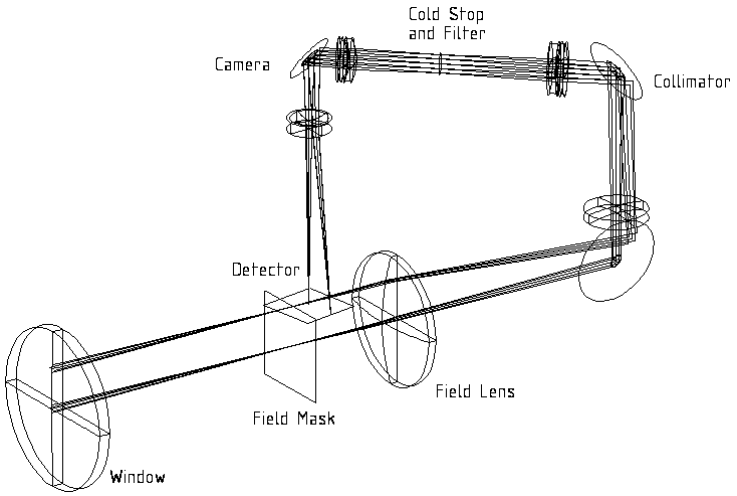

Figure 14: Folded layout of the baseline imager.

Apart from the window, it has a total of seven refractive elements. The collimator comprises a calcium fluoride field lens, a calcium fluoride telephoto lens, and a doublet of calcium fluoride and magnesium oxide near the cold stop. Likewise, the camera comprises a doublet of calcium fluoride and magnesium oxide, and a telephoto lens of calcium fluoride. The pupil image and cold stop are tilted, and have a diameter of ~ 25 mm.

The cryostat window is made from fused silica, and has a slightly convex outer surface to attenuate the otherwise serious ghost image produced by internal reflection.

The total length of the system from the cryostat window to the detector is ~ 1740 mm. The field lens has a diameter of 164 mm and a beam footprint of ~ 6 mm diameter. The two magnesium oxide lenses near the cold stop will require blank diameters of 70 mm, which is within the limits of availability. The filters will be placed in the collimated beam area before the cold stop and will require a clear aperture of ~ 44 mm.

Three fold mirrors are used to fit the layout within the available cryostat space. This arrangement results in the detector lying parallel to and near the CWS plate. This is desirable.

Detailed views of the collimator and camera are shown in Figure 15 and Figure 16, respectively.

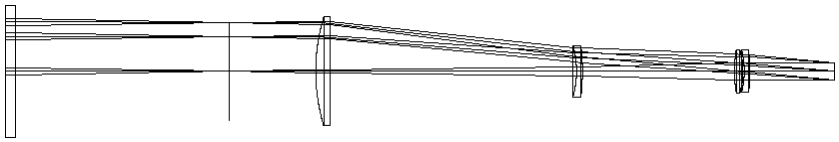

Figure 15: Imager collimator layout.

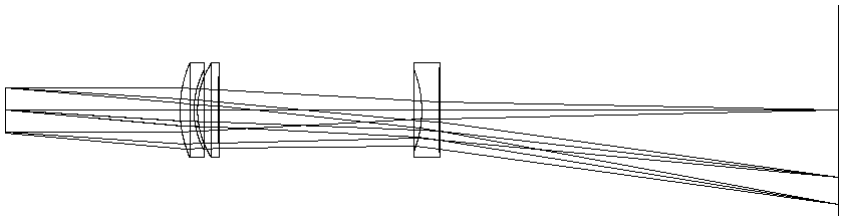

Figure 16: Imager camera layout.

The full optical prescription is presented in Appendix A (§8.9.1).

3.5.4 Image Quality

3.5.4.1 Spot Diagrams

The non-telecentric refractive design has excellent image quality, as shown in Figure 17. The box size corresponds to 2 detector pixels, and the plots are for a single focus setting across the full wavelenth range.

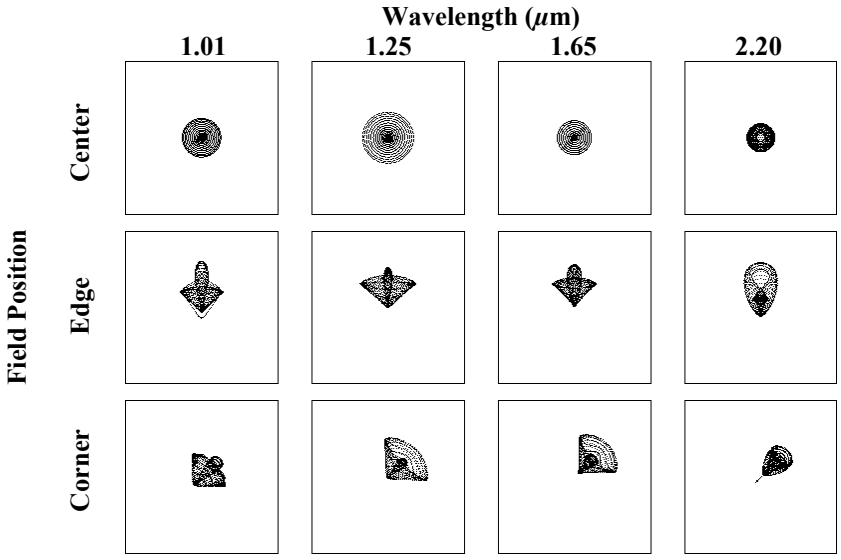

Figure 17: Spot diagrams for the baseline system. Boxes are 2 pixels square.

3.5.4.2 Distortion

The distortion values for the baseline non-telecentric system are excellent, as shown in Table 8. The grid displacements are shown in Figure 18, amplified by a factor of 1000. The maximum grid displacement is 0.2 pixels. The specified limit is 2 pixels.

Table 8: Distortion for the Baseline Imager at Various Wavelengths

Wavelength (μm)	Distortion (%)
1.01	0.0155
1.25	0.0133
1.65	0.0108
2.20	0.0079

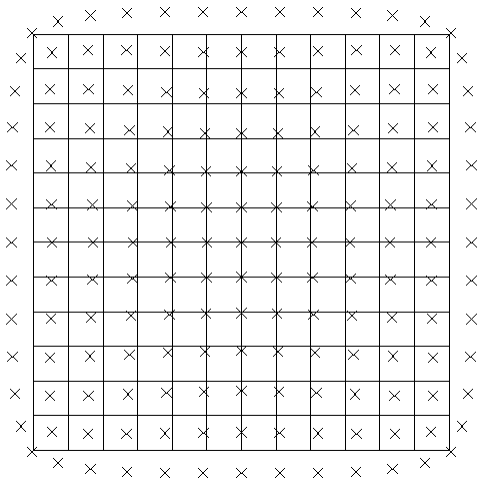

Figure 18: Grid distortion for the baseline system at a wavelength of 1.6 μm with deviations amplified by 1000. Maximum distortion is 0.2 pixels.

3.5.4.3 Wave-Front Error Limit

From the Functional and Performance Requirements Document (FPRD; see Vol. 3), clause REQ-OCD-0013, the total wave-front error introduced by the imager optical system will be < 65 nm RMS over the wavelength range 0.9–2.4 μm. This corresponds to an angular image blur of < 0.013″ RMS (see Appendix A, §8.2), and a Strehl ratio of > 0.94 at a wavelength of 1.6 μm.

3.5.4.4 Wave-Front Error Budget

The total wave-front error is made up of independent contributions from design imperfections, surface irregularities, component dimension errors, alignment errors, refractive index errors, and wave-front sensor errors. These effects are estimated and combined in this section.

3.5.4.4.1 Design Imperfections

Design imperfections have been determined by tracing rays from a perfect input image through the idealized optical system (including the cryostat window). The performance varies somewhat with field position and wavelength, as shown in Table 9. The wavelength values listed are the centers of the *Z*, *J*, *H*, and *K* bands. The "edge" and "corner" field positions have an angular eccentricity of 42″ and 60″, respectively.

Table 9: Wave-Front Errors at Various Field Positions and Wavelengths for the Idealized Design

Wave-Front Error (nm RMS)		Wavelength (μm)			
		1.01	**1.25**	**1.65**	**2.20**
Field Position	**Center**	10	13	5	14
	Edge	17	17	14	17
	Corner	16	18	15	10

A representative value for the whole field and wavelength range is determined by taking the RMS sum of all these values. That is

$$\sigma = 14 \text{ nm RMS}$$

3.5.4.4.2 Surface Irregularities

Surface irregularity, and the wave-front error it causes, has been estimated for all optical elements of the imager. It has been considered in two categories, namely that which is randomly distributed, and that which is systematically associated with the orientation of the crystal structure in magnesium oxide.

The randomly distributed irregularity is analyzed using the theory described in Appendix A (§8.2), assuming that it takes the form of astigmatism. If n is the refractive index of the material, d_{beam} is the diameter of the point-source beam footprint, d_{face} is the envelope diameter of the surface, and ε is the surface irregularity, then the wave-front error is

$$\sigma = \frac{n-1}{n}\left(\frac{d_{beam}}{d_{face}}\right)^2 \varepsilon$$

The results are shown in Table 10. The listing is of components rather than surfaces, and where relevant, double entries are used to specify the two surfaces of the component. The surface irregularity values are allocated from the range that is achievable in the Optical Workshop at RSAA in accordance with their sensitivity to the wave-front error. Combined effects are determined by summing in quadrature.

Table 10: Wave-Front Error Caused by Randomly Distributed Surface Irregularity

Component	Face Envelope Diameter (mm)	Point Source Beam Footprint Diameter (mm)	Refractive Index at 1.65 μm	Surface Irregularity (nm RMS)	Wave-Front Error (nm RMS)
Cryostat Window	200 / 200	10.5 / 10.2	1.44	32 / 32	0
Field Lens	164 / 164	4.1 / 4.5	1.43	32 / 32	0
Fold Mirror 1	110	17.5	-1	12	1
Collimator Lens 1	78 / 78	13.9 / 14.3	1.43	25 / 25	0
Fold Mirror 2	86	31.9	-1	13	3
Collimator Lens 2	66 / 66	25.3 / 25.2	1.43	25 / 25	2
Collimator Lens 3	58 / 64	25.0 / 25.2	1.71	25 / 25	3
Filter	44 / 44	25.2 / 25.2	1.44	19 / 19	2
Camera Lens 1	54 / 46	25.1 / 23.9	1.71	25 / 25	4
Camera Lens 2	54 / 54	24.0 / 23.2	1.43	25 / 25	2
Fold Mirror 3	64	27.3	-1	13	4
Camera Lens 3	46 / 54	10.1 / 9.8	1.43	25 / 25	0
Total (RSS)	-	-	-	-	**8**

Systematic surface irregularity occurs because crystals are anisotropic. The effect is analysed here using the theory developed in Appendix A (§8.2.1). It was derived only for magnesium oxide because experience at RSAA indicates that the effect is far less pronounced in the other crystal proposed for the baseline system, calcium fluoride. If d_{beam} is the diameter of the point source beam footprint and R is the radius of surface curvature, then the wave-front error resulting from the polishing technique used at RSAA is

$$\sigma = 14\left(\frac{d_{beam}}{R}\right)^2 \text{ nm RMS}$$

The results are shown in Table 11 for the two magnesium-oxide lenses in the system. For each lens, double entries are used to specify the parameters at the two lens surfaces. The wave-front error for each lens is determined as the arithmetic sum of the two surfaces effects because the surface irregularity is aligned.

Table 11: Wave-Front Error Caused by Systematic Surface Irregularity

Component	Point Source Beam Footprint Diameter (mm)	Radius of Surface Curvature (mm)	Wave-Front Error (nm RMS)
Collimator Lens 3	25.0 / 25.2	124 / 428	1
Camera Lens 1	25.1 / 23.9	68.6 / 49.2	5
Total (RSS)	-	-	**5**

Summing the random and systematic wave-front errors in quadrature gives the total due to surface irregularity as

$$\sigma = 9 \text{ nm RMS}$$

3.5.4.4.3 Component Dimension Errors

Dimension errors for the optical components of the imager are listed in Table 12, along with the resulting wave-front errors. The tolerances shown assume a high but achievable degree of precision using standard optical manufacturing methods.

Table 12: Wave-Front Error Caused by Component Dimension Errors

Component	Curvature Error ($\times 10^{-6}$ mm^{-1})	Thickness Error (mm)	Wedge (deg)	Wave-Front Error (nm RMS)
Cryostat Window	± 5 / ± 0.3	± 1	0.011	6
Field Lens	± 6 / ± 0.5	± 1	0.010	3
Fold Mirror 1	± 1	-	-	0
Collimator Lens 1	± 15 / ± 10	± 0.2	0.030	6
Fold Mirror 2	± 2	-	-	0
Collimator Lens 2	± 5 / ± 4	± 0.1	0.010	5
Collimator Lens 3	± 6 / ± 5	± 1	0.010	12
Filter	-	-	-	0
Camera Lens 1	± 2 / ± 2	± 0.05	0.003	14
Camera Lens 2	± 4 / ± 4	± 0.2	0.005	17
Fold Mirror 3	± 3	-	-	0
Camera Lens 3	± 14 / ± 4	± 0.15	0.020	10
Total (RSS)	**-**	**-**	**-**	**29**

3.5.4.4.4 Alignment Errors

It is proposed that the imager lenses be mounted in close fitting housings without internal adjustment. The mutual alignment of lenses that are grouped into common housings is then controlled by precision fits between lenses and bores.

Alignment of the imager system is made difficult by the presence of fold mirrors because the lenses do not share a common bore. It is proposed that the branches of the folded system be aligned by making the mirrors and lens housings adjustable in orientation.

Table 13 is compiled in accordance with these principles. The listings for eccentricity wedge and gap thickness account for mounting errors within the housings. Those for tilt, radial displacement, and axial displacement account for mounting errors between housings.

Eccentricity wedge results from clearance between the lens and housing, as explained in Appendix A (§8.3). The fit is arranged to provide a minimum clearance of zero, and so the maximum clearance is the quadrature sum of the lens and housing tolerances. If r_1 and r_2 are the curvature radii of the two lens surfaces, and d is the housing diameter, the maximum wedge angle is

$$\phi = 0.0042 d^{\frac{1}{3}} \left(\frac{1}{r_1} + \frac{1}{r_2} \right)$$

The gap thickness errors apply to the spacing between doublets, and assume that a floating spacer ring is used to control this.

The remaining alignment errors assume that the housings are aligned by fitting them with semi-reflective targets, which are bore-sighted with an alignment telescope. After adjustment, residual errors in tilt and radial displacement are largely due to errors in the fitment of the targets. Axial displacement errors are

larger, but also less important. Large tilt and displacement errors are accepted for the cryostat window because they have little effect, and because it is remote from the structure that supports the other optics.

Table 13: Wave-Front Error Caused by Alignment Errors

Component	Eccentricity Wedge (deg)	Gap Thickness Error (mm)	Tilt (deg)	Radial Displacement (mm)	Axial Displacement (mm)	Wave-Front Error (nm RMS)
Cryostat Window	0.000	-	0.030	1.00	± 1.00	4
Field Lens	0.005	-	0.005	0.08	± 0.10	1
Collimator Lens 1	0.004	-	0.009	0.06	± 0.10	3
Collimator Lens 2	0.013	± 0.05	0.010	0.06	± 0.10	10
Collimator Lens 3	0.006					
Camera Lens 1	0.005	± 0.02	0.011	0.05	± 0.10	23
Camera Lens 2	0.018					
Camera Lens 3	0.014	-	0.011	0.05	± 0.10	16
Total (RSS)	**-**	**-**	**-**	**-**	**-**	**30**

The merged cells in Table 13 indicate doublet groupings. The critical alignment errors are the eccentricity wedge and gap thickness for these doublets (especially that for the camera). To achieve the high precision required and listed for these, it is proposed that optically-polished glass spacer rings be used.

3.5.4.4.5 Refractive-Index Errors

Three refractive materials are used in the baseline design, namely fused silica, calcium fluoride, and magnesium oxide. For fused silica and calcium fluoride, refractive indices are known to five decimal places over the required wavelength and temperature ranges. Ray tracing shows that errors at this level have no significant effect on the aberrations of the system.

However, no refractive index data have been found for magnesium oxide at cryogenic temperatures. It is therefore proposed that a suitably equipped laboratory be contracted to measure the required values during final design. One such laboratory is operated by the Optical Sciences Center, University of Arizona. They have experience in this work, and report an uncertainty in their refractive index measurement of 0.00021 RMS. Conservatively assuming a refractive-index error of 0.0005 and an Abbe Number error of 0.25, the wave-front error for the imager is

$$\sigma = 7 \text{ nm RMS}.$$

3.5.4.4.6 Wave-Front-Sensor Errors

The OIWFS corrects both tip-tilt and defocus on the imager detector. It does this by splitting a pupil image into four segments using a Shack-Hartmann prism, and forming four corresponding images of a guide star. Tip-tilt and defocus are indicated by bulk and differential motion, respectively, of the image centroids.

The allowable centroiding error corresponds to a maximum tip-tilt error of 0.1 pixel, or 0.002″ (§3.6). This centroiding error also allows a maximum defocus of 0.002″. The combined error is taken to be ~ 0.003″ *max*, or ~ 0.001″ RMS. The relationship between angular aberration and wave-front error is discussed in Appendix A (§8.2). If the telescope aperture diameter is d_{tel} and the angular aberration is $\delta\gamma_{sky}$, then the wave-front error is

$$\sigma = \frac{1}{8} d_{tel} \delta\gamma_{sky}$$
$$= 5 \text{ nm RMS}$$

This very small effect suggests that the performance requirement specified for the OIWFS is unnecessarily severe.

3.5.4.4.7 Total Errors

The total wave-front error caused by the imager is estimated in Table 14. The resulting value of 46 nm RMS is less than the allowance of 65 nm RMS.

Table 14: Total Imager Wave-Front Error

Error Source	Wave-Front Error (nm RMS)
Design Defects	14
Surface Irregularities	9
Dimension Errors	29
Alignment Errors	30
Refractive-Index Errors	7
Wave-Front-Sensor Errors	5
Total (RSS)	**46**

3.5.5 Ghost Images

From the FPRD (see Vol. 3), clause REQ-OCD-0017, the intensity of ghost images generated by the imager optics must not be greater than 10^{-5} times that of the parent images. For the baseline optical system, the ghost image performance is remarkably good. In large part, this stems from the non-telecentric layout; reflections from the detector tend to be excluded from the system, and there are no optical elements close to the detector.

Significant ghost images are discussed as follows.

3.5.5.1 Detector Reflection Ghosts

Ghost images are formed by an even number of spurious reflections from optical surfaces. The surface reflectivity is small (typically ~ 2%), and so those ghosts produced by double reflections tend to dominate. Of these, the most important tend to involve a first reflection from the detector because it has relatively high reflectivity (estimated to be ~ 20%). The two most significant are discussed as follows.

A return reflection from the filter would produce strong ghosts if the filter were square to the optical axis. To avoid this, the filter is tilted by 3°.

A return reflection off the rear surface of the first collimator lens produces a roughly focused field image on the detector that has a single pixel intensity ratio of 6×10^{-6}. This is acceptably low, and in any case, it is excluded from all but the field center by the non-telecentric nature of the design.

3.5.5.2 Pupil Ghost

A ghost image of the pupil is formed on the detector by reflections from the convex surface of the first collimator lens and the flat surface of the field lens. It has an evenly illuminated diameter of 5.4 mm, but is fed only by the central 15″ (13.5 mm) of the field image. Its surface brightness is therefore 0.0025 times the

average brightness of the source field, which will be dominated by sky emission. The specification does not deal with pupil ghost intensity, but in any case this value is judged to be acceptable if only because the 5.4 mm diameter image is mostly lost in the 2.5 mm wide crossed gap between the four detectors.

3.5.5.3 Cryostat Window Ghost

The simplest form of cryostat window is a plane-parallel glass plate. Internal reflection within such a window, however, generates a ghost image of the focal plane that is axially displaced from the parent in proportion to the window thickness. Because this displacement is small, star image ghosts are only slightly out of focus and so have relatively high intensity.

Without corrective action, the single-pixel ghost intensity ratio for the imager would be 4×10^{-4}. This has been reduced to 4×10^{-8} by applying slight convex curvature the outer face of the window, so displacing the ghost image 80 mm from the input focal plane.

The optics of the imager take account for this slight window curvature. Any likely misalignment in the mounting of the window has been investigated and found to be insignificant (§3.5.4.4.4).

3.5.5.4 Filter Ghost

Filters are placed near the cold stop of the imager, where the beam is roughly collimated. Internal reflection within the filter produces a ghost image of the field. Ideally, the filter is a plane parallel element, and so the ghost image is harmlessly coincident with parent. Any wedge error within the filter, however, causes the ghost field to be displaced laterally from the parent field.

Assuming that the reflectivity of each surface of the filter is 2 %, the ghost intensity ratio will be 0.0004. According to filter supplier Barr Associates, a realistic wedge tolerance for the proposed filters is 10″. The maximum displacement between the ghost field and the parent field is then 4 pixels.

Little can be done to drastically reduce either the intensity or displacement of this ghost. Although the intensity ratio violates the specification, it is nevertheless judged to be acceptable because the displacement is small enough for the ghost to be lost within the parent. This is justified because the same conclusion is reached for the more severe case of the detector substrate ghost (§3.5.5.5), where the effect is investigated in depth.

3.5.5.5 Detector Substrate Ghost

The ghost image caused by reflection in the detector substrate has the potential to be a problem because the incident beam is not telecentric for the proposed optical system. A ghost image is also produced for a telecentic system, but it is then coincident with the parent, and because defocus is not significant, it is not offensive. For a non-telecentric system, however, the ghost is displaced radially from the parent in proportion to its field eccentricity, and so may become apparent.

Thus, the intensity ratio of this ghost image is independent of the optical design, but if it violates the specified requirement, it can still be acceptable in practice if the displacement is small enough for the ghost image to be lost within the parent image. In this respect, the simple intensity specification is invalid.

The GSAOI imager detector will be a mosaic of Rockwell HAWAII-2RG devices. These detectors use a 0.82 mm thick CdZnTe substrate (Cabelli, priv. comm.) in front of the HgCdTe detector material. The refractive index of this substrate material is uncertain, but is estimated to be ~ 3.29 at a wavelength of 1 μm and a temperature of 80 K (Appendix A, §8.5).

The displacement of the detector ghost is derived simply from the substrate thickness and refractive index, and the incident ray angle. The incident ray angle is 6.4º at the edge of the imager field so the chief ray passes through the detector substrate at an angle of ~ 1.9º. Consequently, a single internal reflection will

produce a ghost image with a radial displacement of 56 μm (3.1 pixels) from the primary image. The displacement is proportional to the field eccentricity, and reaches 4.4 pixels at the detector corners.

The ghost intensity cannot be estimated accurately, and so a conservative estimate is made as follows. The quantum efficiency of the detector is between 70 and 85%. Perhaps 10% of the light is reflected from the detector layer. The amount returned to the detector at the CdZnTe/vacuum interface is uncertain and depends on the characteristics of the anti-reflection (AR) coating. If there is no AR coating, ~ 28.5% would be internally reflected at the interface. The high quantum efficiency suggests that more like 10% is internally reflected. Of these photons, ~ 80% will be detected in the ghost image. The ghost intensity will then be ~ 0.1×0.1×0.8 = 0.008 of the primary intensity.

This ghost intensity ratio is considerably higher than the specified limit of 10^{-5}. It is therefore crucial to decide whether or not the ghost is lost within the AO-corrected PSF because of its small displacement. Simulated images (including the ghost) located near the detector edge are presented in Figure 19. These images suggest that the scientific impact of the detector ghost will be small, even on long exposures of bright stars.

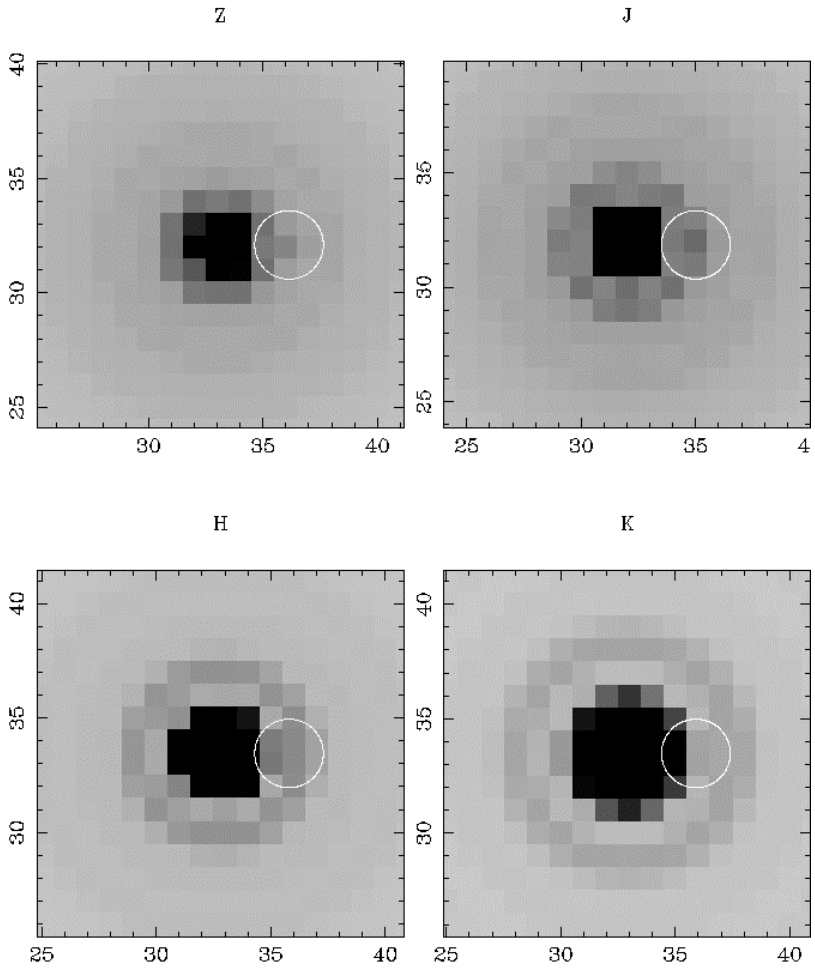

Figure 19: Simulated *Z*, *J*, *H*, and *K* images including the detector ghost at detector edge. The star is bright enough to just saturate the detector in 10 s. The images are for a total exposure time of 3600 s. The white circle indicates the position of the detector ghost.

Discussions with Rockwell indicate that reflection at the CdZnTe/HgCdTe interface may be more like 1-2%, rather than the 10% assumed above. This would probably make the ghost undetectable.

3.5.6 Throughput

The baseline imager optics were designed to achieve adequate image quality with the minimum number of surfaces in order to maximize throughput. The resulting throughput performance is shown in Table 15 for a range of wavelengths. All lenses and the cryostat window are assumed to be AR coated with a single layer of magnesium fluoride. All mirrors are assumed to be gold coated. Filter transmission is assumed to be 0.8, as specified by Barr Associates.

Table 15: Optical Throughput Budget for the Baseline Optical Design.

Transmission		Wavelength (μm)				
		1.00	**1.25**	**1.60**	**2.20**	**2.50**
Component	**Cryostat Window**	0.948	0.961	0.963	0.956	0.953
	Field Lens	0.949	0.958	0.960	0.955	0.953
	Fold Mirror 1	0.986	0.988	0.990	0.991	0.992
	Collimator Lens 1	0.949	0.958	0.960	0.955	0.953
	Fold Mirror 2	0.986	0.988	0.990	0.991	0.992
	Collimator Lens 2	0.949	0.958	0.960	0.955	0.953
	Collimator Lens 3	0.927	0.981	0.993	0.963	0.948
	Filter	0.8	0.8	0.8	0.8	0.8
	Camera Lens 1	0.927	0.981	0.993	0.963	0.948
	Camera Lens 2	0.949	0.958	0.960	0.955	0.953
	Fold Mirror 3	0.986	0.988	0.990	0.991	0.992
	Camera Lens 3	0.949	0.958	0.960	0.955	0.953
	Total	**0.481**	**0.576**	**0.601**	**0.548**	**0.526**

Figure 20 shows a plot of this transmission across the whole wavelength range, with and without AR coating.

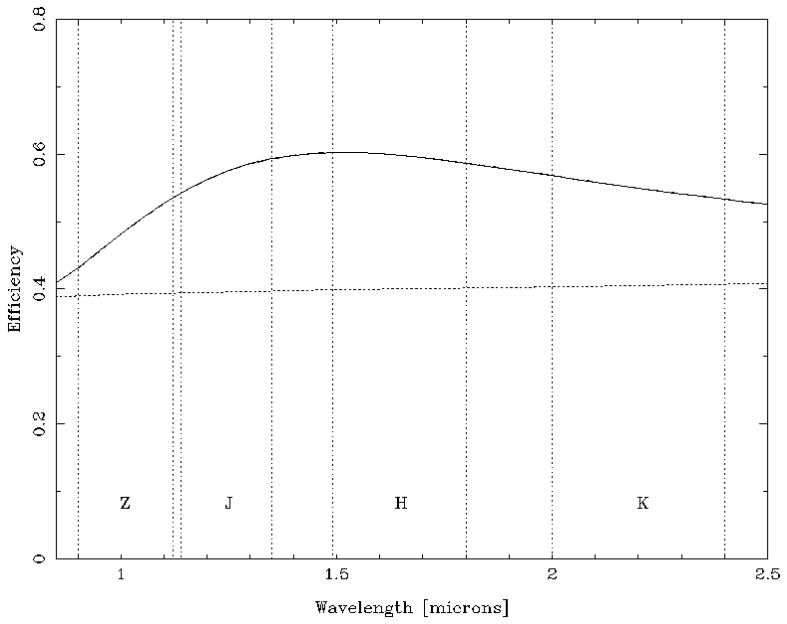

Figure 20: Transmission function for the baseline imager with AR coating (*solid*) and without AR coating (*dotted*). Standard photometric passbands are indicated.

The quantum efficiency of the detector is uncertain, and is not included in the above budgets. A HAWAII-1 or HAWAII-2 PACE detector has a quantum efficiency of ~ 60%. The quantum efficiency of the new MBE devices that GSAOI will use may be similar, but claims have been made that it is 85%.

3.5.7 Cold Stop Performance

The cold stop is located at the pupil image within the imager, and serves to exclude radiation emanating from outside the pupil. Its efficiency is therefore dependent on the quality of the pupil image on the cold stop. This image is aberrated by both the MCAO system and the collimator of the imager. The MCAO system also causes the pupil image to be tilted by 22.8°, but the performance effects of this are eliminated by likewise tilting the cold stop. The cold stop is therefore slightly elliptical.

Spot diagrams for this image are shown in Figure 21. They are images of points on the telescope secondary mirror, with the stop for this imaging process being the square field mask of the imager. The wavelength dependency arises entirely from the refractive collimator of the imager. The RMS blurring corresponds to 1.4% of the cold-stop diameter, or 0.35 mm.

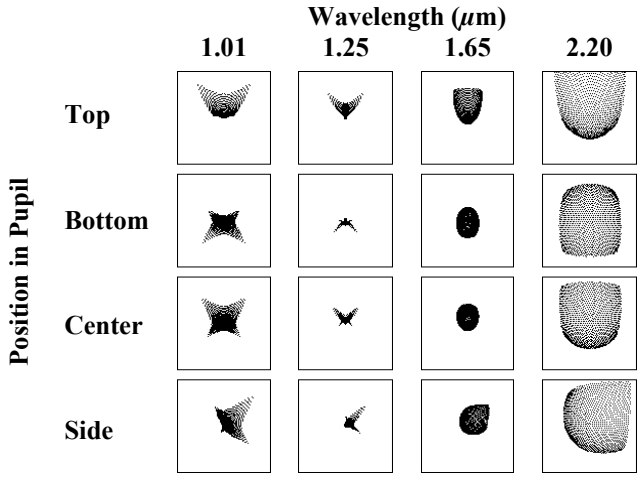

Figure 21: Spot diagrams for the pupil image on the tilted cold stop. Boxes are 2 mm square.

3.5.8 Pupil Viewer

The function of the pupil viewer is to image the cold stop, and the pupil image therein, onto the detector. It will be used both to align these two images, and to identify sources of extraneous background emission. The pupil image and cold stop should be mutually aligned to 0.5% of their diameter.

As discussed in §3.2 of Vol. 1, the diameter of the cold stop image is set to 3800 pixels (64 mm). This large size reduces the loss of the central detail in the detector mosaic gap, while still allowing images to be recorded with exposure times of a few minutes. The image resolution is not as fine as can be delivered by this pixel scale.

The pupil-viewer mode is implemented in the non-telecentric refractive imager by inserting a group of three lenses into the camera section, as shown on Figure 23. The first two lenses are of calcium fluoride, and the third is of fused silica. The optical prescription is included in that listed for the imager (Appendix A, §8.9.1).

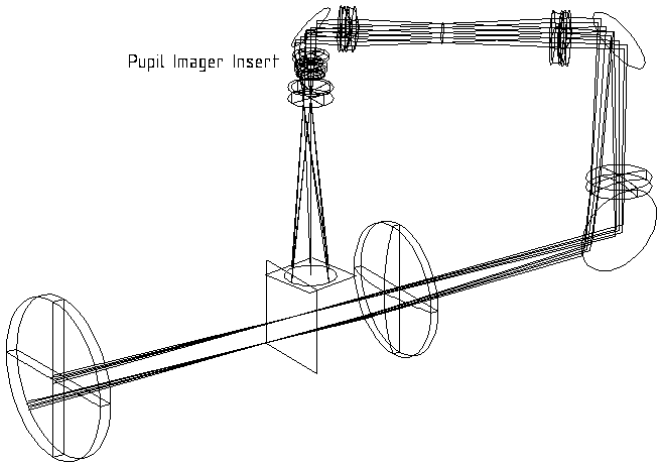

Figure 22: Imager with pupil-viewer lenses inserted.

Figure 23 shows the unfolded layout of the camera section alone, from cold stop to detector, with the pupil-viewer lenses inserted. The nominal pupil image diameter at the cold stop is 25 mm, but it is in fact tilted by 22.8° and therefore slightly elliptical (§3.5.7). The cold stop is likewise tilted and elliptical, and will be slightly oversized to accommodate aberration.

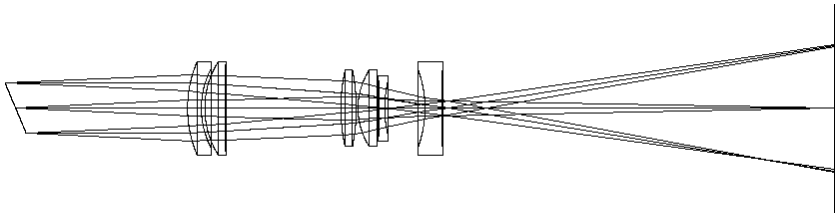

Figure 23: Camera with pupil-viewer lenses inserted.

The image quality delivered to the detector is limited mainly by the MCAO system (because it tilts the input fields) and the imager collimator, rather than by the pupil-viewer optics. The net performance is described in the following two sections, where the pupil for the imaging process is the square field mask of the imager. This performance is poor, but adequate for alignment purposes. By comparison, the diffraction limit for this imagery varies from 1.2 to 2.6 pixels over the wavelength range.

3.5.8.1 Pupil Image Quality

Spot diagrams for the pupil image are shown in Figure 24. The total RMS blur corresponds to 1.4% of the cold-stop diameter, or 54 pixels.

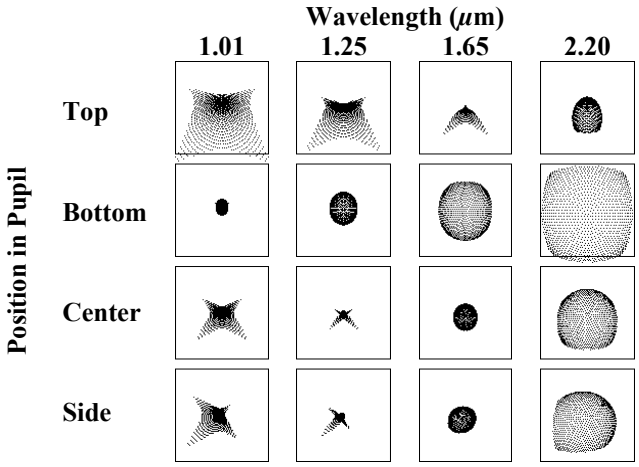

Figure 24: Spot diagrams for the pupil image on the detector. Boxes are 5 mm square.

3.5.8.2 Cold Stop Image Quality

Spot diagrams for the cold-stop image are shown in Figure 25. The total RMS blur corresponds to 0.85% of the cold-stop diameter, or 32 pixels.

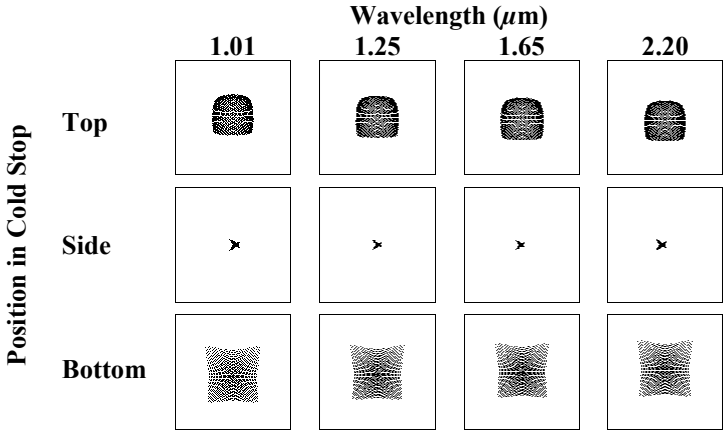

Figure 25: Spot diagrams for the cold-stop image on the detector. Boxes are 5 mm square.

3.5.9 Roddier Wave-Front Sensor System

Using techniques developed by Roddier (§3.3 of Vol. 1), wave-front aberrations can be measured at the detector by comparing images that are defocused in opposite directions. It is proposed that this facility be included in the imager so that aberrations introduced by the imager optics can be measured using the Roddier program, and then corrected by deforming the DM0 mirror in the MCAO system.

To achieve the required defocus, doublet lenses with positive and negative power will be alternately inserted into the imager at the same location used for the pupil-viewer lenses (Figure 22). All three lens modules will share the same carriage system. The layout of the two defocus arrangements is shown in Figure 26. For each, the lens materials are calcium fluoride and fused silica.

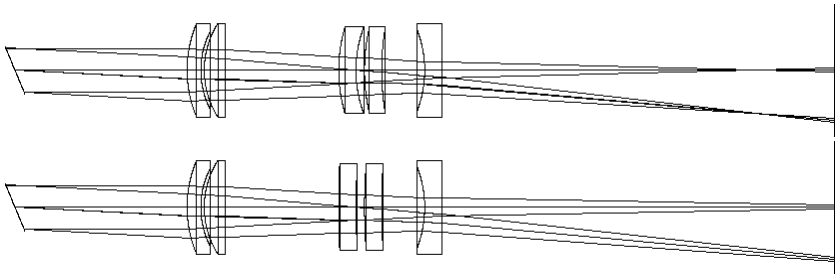

Figure 26: Camera layouts with the convex defocus lens (top) and concave defocus lens (bottom) inserted.

The illumination source for this imagery could be a star, and the imager optics could be characterized over the whole field by taking paired exposures for a range of star positions. To provide greater operational flexibility, however, it is proposed that the MCAO NGS source simulator be used instead. This generates a 5×5 array of 4 μm diameter fiber-optic sources with a separation of ~ 16.5″ referred to the sky. The rays shown in Figure 26 are for center and edge sources within this array.

The defocused spots are effectively images of the pupil formed through a pinhole camera. Wave-front errors manifest as geometrical distortion within that pupil image, and so cause variations in brightness. At any point in the pupil, the brightness difference between the retracted and extended images is a measure of wave-front curvature.

The defocus optics should be designed to produce pupil images of appropriate size. Larger image size increases spatial resolution but reduces sensitivity. The image size should therefore be set to the minimum that provides adequate resolution. For the proposed defocus optics, the pupil images have a diameter of 126 pixels. The two-pixel resolution of the system therefore corresponds to 127 mm at the 8 m diameter telescope primary mirror. The MCAO inter-actuator spacing maps to 500 mm at this surface, and so the resolution provided is adequate.

The criterion for judging the image quality of the defocus optics is that the blurring of the source images (displaced from the detector plane) should be small relative to the spatial resolution required of the process. This ensures adequately accurate registration between the retracted and extended pupil images. Spot diagrams are shown for the retracted and extended pupil images in Figure 27 and Figure 28, respectively, where the boxes correspond to the two-pixel spatial resolution. These show that the image quality is adequate.

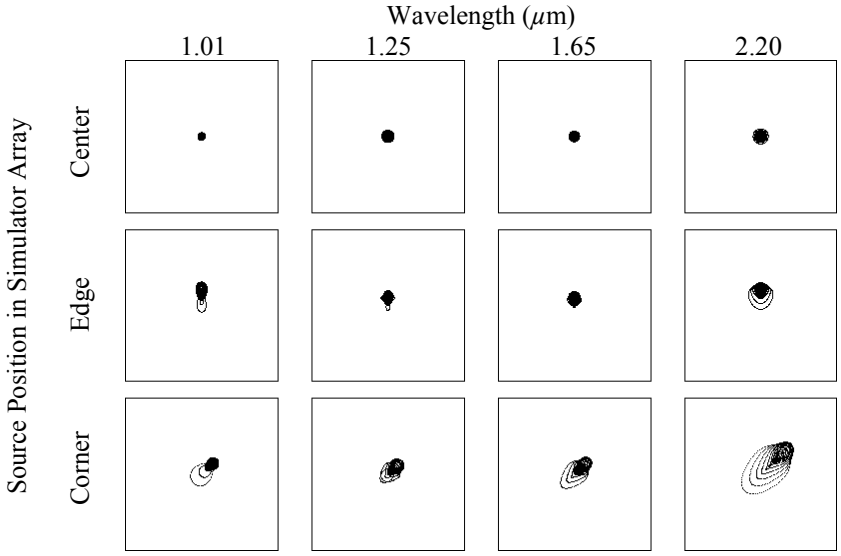

Figure 27: Spot diagrams for the retracted pupil images. Boxes are 2 pixels square.

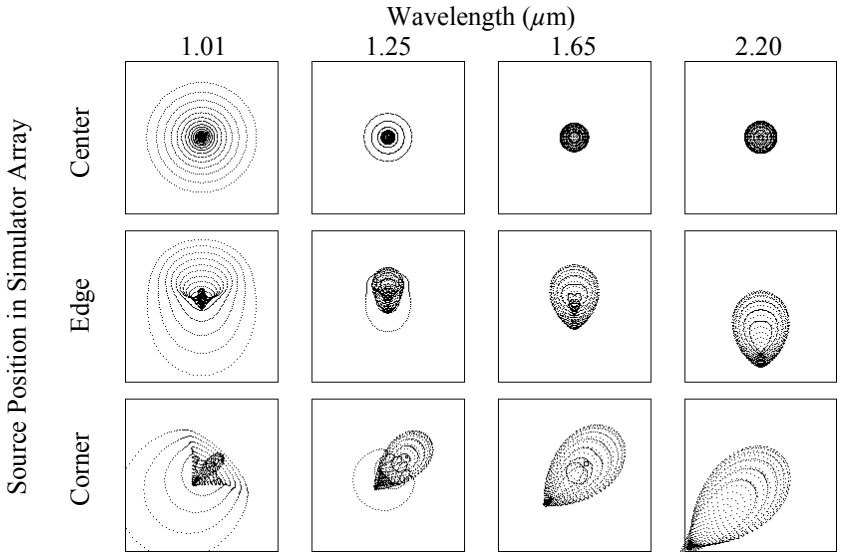

Figure 28: Spot diagrams for the extended pupil images. Boxes are 2 pixels square.

3.6 On-Instrument Wave-Front Sensor Design

The OIWFS is required to track slow flexure changes between the MCAO system and the imager detector and slow focus changes due to height variations in the atmospheric sodium layer. The OIWFS should also be able to perform fast tip-tilt and focus sensing when required to substitute for one of the MCAO tip-tilt/focus wave-front sensors. The OIWFS must operate at near-infrared wavelengths because the optical light has already been reflected to the MCAO wave-front sensors.

The necessity to track flexure changes for every object observed means that the availability of suitable OIWFS guide stars will be a strong constraint on the scientific scope of MCAO. For this reason, it is desirable that the OIWFS be able to select guide stars from the largest possible field.

Corrected image motion at the imager detector must not exceed 0.002" (0.1 imager pixels) over a period of one hour.

3.6.1 Guide Star Capture Options

Three possible methods of capturing guide stars have been considered. These are described as follows.

3.6.1.1 Pick-Off Probe

An articulated probe can be used to pick-off a guide star from anywhere within the MCAO field. Using two independently rotatable links mounted end-to-end with suitable mirrors and reimaging optics, the star image can be delivered to the fixed input aperture of the error sensing system. A detailed description of this arrangement is given in Appendix A, §8.6. A similar concept was investigated (but not constructed) by the Royal Observatory Edinburgh for the GIRMOS design study (Wright et al. 2000, SPIE, 4008, 729).

Such a system has the desirable feature that guide stars are available from anywhere within the MCAO field. Nevertheless, this option is not preferred because the stringent stability demands would be very difficult to satisfy, especially in circumstances where rapid development is required. It would also require the use of a powered window to provide telecentric input.

This conclusion is based on the specified requirement for 0.1-pixel image stability over periods of one hour. Some reconsideration of this may be warranted in the light of the error analysis presented in §3.5.4.4.6. This indicates that such a stability error corresponds to a wave-front error of only 5 nm RMS. The total allowable wave-front error is 65 nm RMS, and so the allowable stability error could be increased five fold before it would make a significant contribution to the total.

3.6.1.2 Spectral Beam Splitter

A selection of interchangeable dichroic beam splitters could be provided near the input focal plane so that pass bands not being used by the imager could be reflected to the OIWFS. Guide stars would then be available from the whole field, but with wavelength restrictions. This option was rejected because of limitations on dichroic efficiency and cut-off performance.

3.6.1.3 Spatial Field Splitter

A field splitting mirror can be placed near the input focal plane to feed the OIWFS. A rectangular hole in the mirror allows it to pass the 85″ square imager field, and reflect the unused crescent zones of the 120″ round MCAO field to the OIWFS, as shown in Figure 29.

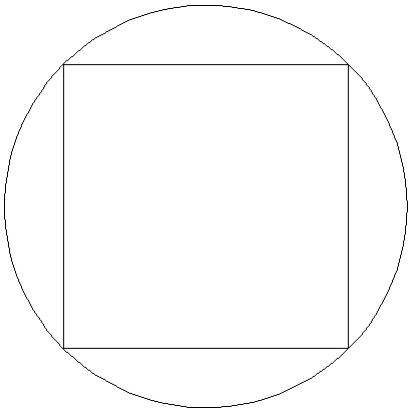

Figure 29: Field-splitting geometry for the imager and OIWFS. The central square field is passed to the imager.

With allowance for beam divergence away from focus, the OIWFS will receive unvignetted light from only 35% of the MCAO field. Nevertheless, this system is adopted because it is simple, able to provide the required image stability, and can be developed rapidly.

This arrangement will be adequate for most MCAO applications. The MCAO system requires that there are at least three optical tip-tilt stars within its field. An operational requirement of the OIWFS will therefore be to position the GSAOI imager field center so that the near-infrared light from one of these stars passes to the OIWFS, if no other OIWFS guide star is available.

3.6.2 Baseline Configuration

The spatial field splitter option is adopted as the baseline for further consideration. This system seriously restricts field coverage, but is rigid and can be developed rapidly. It is judged to be more compatible with the needs of the project, but the comments made about rigidity in §3.6.1.1 should be noted.

3.6.3 Description

The folded layout of the OIWFS is shown in Figure 30. Rays are drawn for a star that is outside the imager field. All such rays are intercepted by the field splitter, and reflected through a hole in the CWS plate into the OIWFS below. A field mask is located at the reflected focal plane just below the field splitter. A field lens forms a pupil image on the steerable mirror. The field lens is mounted just above the hole in the CWS plate. The optical prescription for this system is listed in Appendix A, §8.9.2.

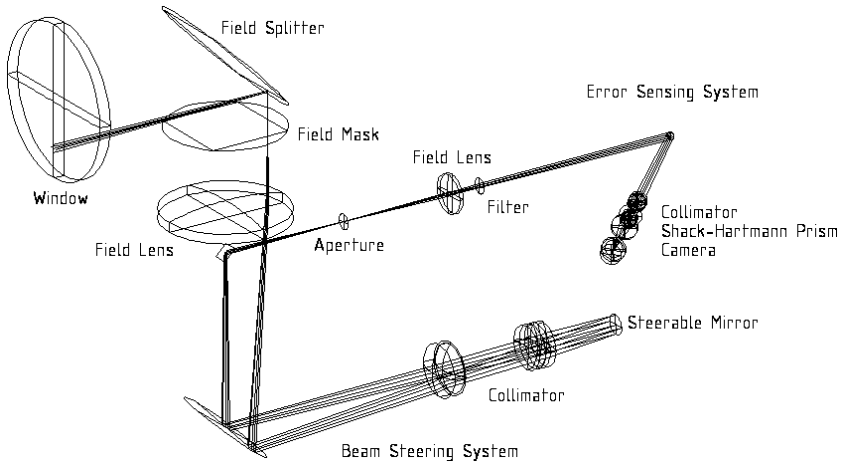

Figure 30: Folded layout of the OIWFS.

Beyond the field splitter, the OIWFS consists of two basic parts, namely, a beam steering system, and an error sensor system. These are described separately as follows.

3.6.3.1 Beam Steering System

The function of the beam steering system is to deliver a guide star image chosen from anywhere within the guide field to the entrance aperture of the error sensing system. It does this by relaying the guide field image to the error sensor system through a collimated pupil image cast on a beam steering mirror. The target star is selected by driving the mirror in tip and tilt.

Like the pick-off system discussed earlier, this system must be very stable in the guiding position, but this is more easily achieved with a tip-tilt mirror than with an articulated probe.

An unfolded layout of the beam steering system is shown in Figure 31. In this particular system, the relay optics are simplified by using the three collimator lenses in double-pass, thus avoiding the need for additional camera lenses. The return beam is then extracted from the input beam before it reaches the field lens by means of a small mirror mounted in the empty center zone of the input beam. The beam steering mirror is circularly symmetric about the optical axis.

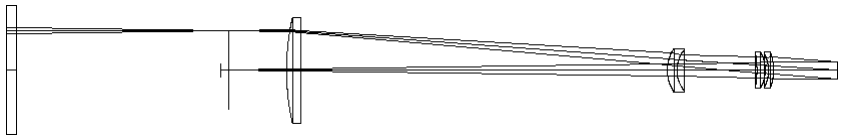

Figure 31: Unfolded layout of the beam steering system.

The field lens and the first two collimator lenses are made from calcium fluoride. The third collimator lens is of magnesium oxide. The effective focal length of the collimator is 858 mm, and that of the telescope and MCAO system is 262200 mm. The magnification at the beam steering mirror is therefore 306, and the beam diameter corresponding to an 8 m telescope aperture is 26 mm.

3.6.3.2 Error Sensing System

The error sensing system functions by relaying the selected guide star image to the detector through a collimated pupil image where the beam is split into four slightly deviated directions. Four slightly separated images are thereby formed on the detector. Guiding and focus errors are indicated by bulk and differential image motion, respectively.

Pupil splitting is achieved by means of a Shack-Hartmann prism with four differentially-sloped facets. The angular image separation provided is 0.52″. The image scale is set to the optimum value of 0.065″/pixel, as determined in §3.6.4. The detector has 18.5 μm square pixels.

An unfolded layout of the error sensing system is shown in Figure 32. The guide star image delivered by the beam steering system is at the right end. A set of interchangeable aperture masks is also located there. A set of filters (not shown) is located behind the field lens.

Figure 32: Unfolded layout of the error sensing system.

The field lens and two collimator lenses are of calcium fluoride, magnesium oxide, and calcium fluoride, respectively. The first and third camera lenses are of calcium fluoride, and the second and fourth are of magnesium oxide.

3.6.4 Image Scale

The corrected image motion on the imager detector must not exceed 0.1 pixels, or 0.002″ in a period of one hour. The pixel scale at the OIWFS detector must be set to achieve this performance with the faintest possible guide star. The optimum value has been determined by simulation, as described in §3.4 of Vol. 1.

The results presented there show that the centroiding accuracy depends on the diffraction-core size, and hence on the observation wavelength. The optimal pixel size is a compromise that is weighted towards longer wavelengths where MCAO will perform better.

Accordingly, the OIWFS image scale is chosen to be 0.065″/pixel.

The centroiding errors of the OIWFS limit the correction of both image movement and defocus on the imager detector. Both effects contribute to the wave-front error at the imager detector, and so are accounted for as wave-front sensor errors in the imager wave-front error budget (§3.5.4.4).

3.6.5 Image Quality

3.6.5.1 Spot Diagrams

The OIWFS has excellent image quality, as shown in Figure 33. The box size corresponds to 1 detector pixel, and the plots are for a single focus setting across the full wavelenth range.

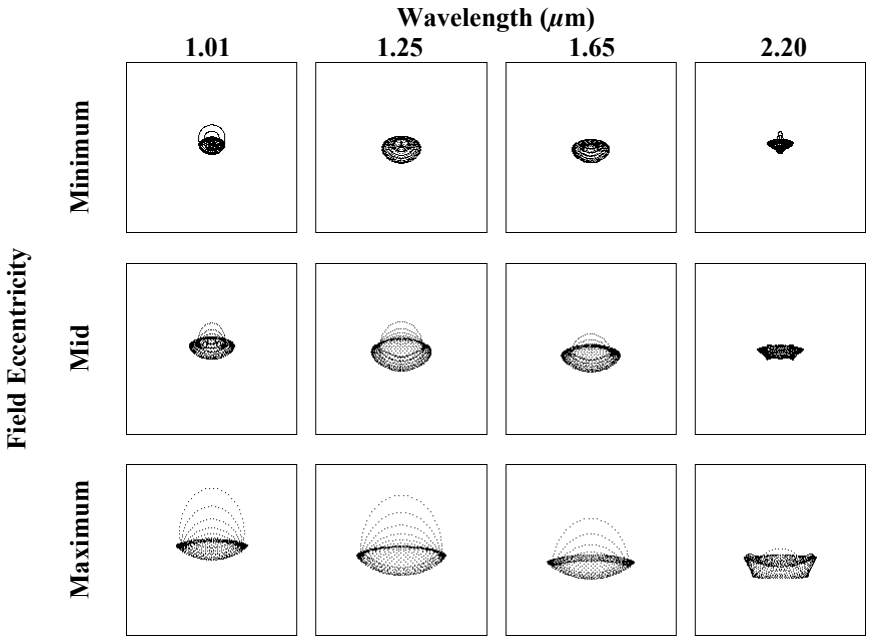

Figure 33: Spot diagrams for the OIWFS. Boxes are 1 pixel square.

3.6.5.2 Wave-Front Error Limit

From the FPRD (see Vol. 3), clause REQ-OCD-0028, the total wave-front error introduced by the OIWFS optical system will be < 120 nm RMS over the wavelength range 0.9–2.4 μm. This corresponds to an angular image blur of < 0.025″ RMS, and a Strehl ratio of > 0.80 at a wavelength of 1.6 μm.

3.6.5.3 Wave-Front Error Budget

3.6.5.3.1 Design Imperfections

Design imperfections have been determined by tracing rays from a perfect input image through the idealized optical system (including the cryostat window). The performance varies somewhat with field eccentricity and wavelength, as shown in Table 16. The wavelength values listed are the centers of the *Z*, *J*, *H*, and *K* bands. The "minimum", "mid", and "maximum" field eccentricities are 42″, 51″, and 60″, respectively.

Table 16: Wave-Front Errors at Various Field Positions and Wavelengths for the Idealized Design

Wave-Front Error (nm RMS)		Wavelength (μm)			
		1.01	**1.25**	**1.65**	**2.20**
Field Eccentricity	**Minimum**	12	23	22	15
	Mid	27	38	37	30
	Maximum	46	56	55	51

A representative value for the whole field and wavelength range is determined by taking the RMS sum of all these values. That is

$$\sigma = 37 \text{ nm RMS}.$$

3.6.5.3.2 Surface Irregularities

Surface irregularity, and the wave-front error it causes, has been estimated for all optical elements of the OIWFS. It has been considered in two categories, namely that which is randomly distributed, and that which is systematically associated with the orientation of the crystal structure in magnesium oxide.

The randomly distributed irregularity is analyzed using the theory described in Appendix A (§8.2), assuming that it takes the form of astigmatism. If n is the refractive index of the material, d_{beam} is the diameter of the point-source beam footprint, d_{face} is the envelope diameter of the surface, and ε is the surface irregularity, then the wave-front error is

$$\sigma = \frac{n-1}{n}\left(\frac{d_{beam}}{d_{face}}\right)^2 \varepsilon$$

The results are shown in Table 17. The listing is of components rather than surfaces, and where relevant, double entries are used to specify the two surfaces of the component. The surface irregularity values are allocated from the range that is achievable in the Optical Workshop at RSAA in accordance with their sensitivity to the wave-front error. For surfaces used in double-pass, the wave-front error is taken to be twice that for single-pass. Otherwise, the combined effects are determined by summing in quadrature.

Table 17: Wave-Front Error Caused by Randomly Distributed Surface Irregularity.

Component		Face Envelope Diameter (mm)	Point Source Beam Footprint Diameter (mm)	Refractive Index at 1.65 μm	Surface Irregularity (nm RMS)	Wave-Front Error (nm RMS)
Cryostat Window		200 / 200	10.5 / 10.2	1.44	32 / 32	0
Field Splitter Mirror		216	1.3	-1	32	0
Beam Steering System	Field Lens	164 / 164	3.2 / 3.5	1.43	25 / 25	0
	Fold Mirror 1	130	15.8	-1	6	0
	Collimator Lens 1	68 / 62	19.4 / 18.2	1.43	19 / 19	1
	Collimator Lens 2	56 / 56	24.2 / 25.2	1.43	19 / 19	3
	Collimator Lens 3	56 / 56	24.7 / 25.9	1.71	13 / 19	4
	Tip-Tilt Mirror	50	26	-1	6	3
	Fold Mirror 2	20	6.7	-1	13	3
Error Sensing System	Field Lens	50 / 50	4.2 / 4.2	1.43	25 / 25	0
	Filter	20 / 20	5.0 / 5.0	1.44	3 / 3	0
	Fold Mirror 3	20	10	-1	13	7
	Collimator Lens 1	16 / 22	12.9 / 13.5	1.71	13 / 19	5
	Collimator Lens 2	22 / 22	13.6 / 14.0	1.43	13 / 13	2
	Shack-Hartmann Prism	28 / 28	14.0 / 14.0	1.44	13 / 13	1
	Camera Lens 1	20 / 20	14.0 / 14.0	1.43	13 / 13	3
	Camera Lens 2	20 / 20	13.8 / 14.1	1.71	13 / 13	4
	Camera Lens 3	32 / 32	13.8 / 13.6	1.43	13 / 13	1
	Camera Lens 4	22 / 30	2.0 / 1.7	1.71	25 / 25	0
Total (RSS)		-	-	-	-	**12**

Systematic surface irregularity occurs because crystals are anisotropic. The effect is analysed here using the theory developed in Appendix A, §8.2.1. It was derived only for magnesium oxide because experience at RSAA indicates that the effect is far less pronounced in the other crystal proposed for the baseline system, calcium fluoride. If d_{beam} is the diameter of the point-source beam footprint and R is the radius of surface curvature, then the wave-front error resulting from the polishing technique used at RSAA is

$$\sigma = 14\left(\frac{d_{beam}}{R}\right)^2 \text{ nm RMS}$$

The results are shown in Table 18 for the four magnesium-oxide lenses in the system. For each lens, double entries are used to specify the parameters at the two lens surfaces. The wave-front error for each lens is determined as the arithmetic sum of the two surfaces effects because the surface irregularity is aligned. For the lens in the beam steering system, the double-pass error is taken to be twice that for a single-pass.

Table 18: Wave-Front Error Caused by Systematic Surface Irregularity.

Component		Point Source Beam Footprint Diameter (mm)	Radius of Surface Curvature (mm)	Wave-Front Error (nm RMS)
Beam Steering System	Collimator Lens 3	24.7 / 25.9	70.3 / 77.7	6
Error Sensing System	Collimator Lens 1	12.9 / 13.5	45.9 / 63.1	2
	Camera Lens 2	13.8 / 14.1	22.4 / 50.9	6
	Camera Lens 4	2.0 / 1.7	29.2 / 113.9	0
Total (RSS)		**-**	**-**	**9**

Summing the random and systematic wave-front errors in quadrature give the total due to surface irregularity as

$$\sigma = 15 \text{ nm RMS}.$$

3.6.5.3.3 Component Dimension Errors

Dimension errors for the optical components of the OIWFS are listed in Table 19, along with the resulting wave-front errors. The tolerances shown assume a high but achievable degree of precision using standard optical manufacturing methods.

Table 19: Wave-Front Error Caused by Component Dimension Errors.

Component		Curvature Error ($\times 10^{-6}$ mm^{-1})	Thickness Error (mm)	Wedge (deg)	Wave-Front Error (nm RMS)
Cryostat Window		± 5 / ± 0.3	± 1	0.011	6
Field Splitter Mirror		± 1	-	-	2
Beam Steering System	Field Lens	± 6 / 0.5	± 0.20	0.018	7
	Fold Mirror 1	± 1	-	-	5
	Collimator Lens 1	± 7 / ± 4	± 0.02	± 0.004	12
	Collimator Lens 2	± 6 / ± 5	± 0.05	± 0.010	8
	Collimator Lens 3	± 3 / ± 3	± 0.03	± 0.006	16
	Tip-Tilt Mirror	± 1	-	-	6
	Fold Mirror 2	± 4	-	-	8
Error Sensing System	Field Lens	± 8 / ± 5	0.30	± 0.050	4
	Fold Mirror 3	± 4	-	-	10
	Collimator Lens 1	± 24 / ± 15	± 0.20	± 0.026	12
	Collimator Lens 2	± 8 / ± 17	± 0.15	± 0.026	6
	Camera Lens 1	± 10 / ± 19	± 0.10	± 0.029	6
	Camera Lens 2	± 20 / ±19	± 0.05	± 0.022	11
	Camera Lens 3	± 3 / ± 11	± 0.10	± 0.018	6
	Camera Lens 4	± 35 / ± 8	± 0.10	± 0.057	6
Total (RSS)		**-**	**-**	**-**	**35**

3.6.5.3.4 Alignment Errors

It is proposed that the OIWFS lenses be mounted in close fitting housings without internal adjustment. The mutual alignment of lenses that are grouped into common housings is then controlled by precision fits between lenses and bores.

Alignment of the OIWFS system is made difficult by the presence of fold mirrors because the lenses do not share a common bore. It is proposed that the branches of the folded system be aligned by making the mirrors and lens housings adjustable in orientation.

Table 20 is compiled in accordance with these principles. The listings for eccentricity wedge and gap thickness account for mounting errors within the housings. Those for tilt, radial displacement, and axial displacement account for mounting errors between housings.

Eccentricity wedge results from clearance between the lens and housing, as explained in Appendix A, §8.3. The fit is arranged to provide a minimum clearance of zero, and so the maximum clearance is the quadrature sum of the lens and housing tolerances. If r_1 and r_2 are the curvature radii (mm) of the two lens surfaces, and d is the housing diameter (mm), the maximum wedge angle (rad) is

$$\phi = 0.0042 d^{\frac{1}{3}} \left(\frac{1}{r_1} + \frac{1}{r_2} \right)$$

The gap thickness errors apply to the spacing between doublets, and assume that a floating spacer ring is used to control this.

The remaining alignment errors assume that the housings are aligned by fitting them semi-reflective targets, and bore-sighted with an alignment telescope. After adjustment, residual errors in tilt and radial displacement are largely due to errors in the fitment of the targets. Axial displacement errors are larger, but also less important. Large tilt and displacement errors are accepted for the cryostat window because they have little effect, and because it is remote from the structure that supports the other optics.

Table 20: Wave-Front Error Caused by Alignment Errors.

Component		Eccentricity Wedge (deg)	Gap Thickness Error (mm)	Tilt (deg)	Radial Displacement (mm)	Axial Displacement (mm)	Wave-Front Error (nm RMS)
Cryostat Window		0.000	-	0.030	1.00	± 1.00	4
Beam Steering System	Field Lens	0.004	-	0.005	0.08	± 0.10	3
	Collimator Lens 1	0.004	-	0.010	0.06	± 0.10	23
	Collimator Lens 2	0.010	± 0.05	0.010	0.05	± 0.10	21
	Collimator Lens 3	0.001					
Error Sensing System	Field Lens	0.006	-	0.012	0.05	± 0.10	3
	Collimator Lens 1	0.004	± 0.05	0.020	0.04	± 0.10	5
	Collimator Lens 2	0.007					
	Camera Lens 1	0.028	± 0.05	0.022	0.04	± 0.10	24
	Camera Lens 2	0.016					
	Camera Lens 3	0.021	-	0.016	0.05	± 0.10	30
	Camera Lens 4	0.019	-	0.017	0.04	± 0.10	8
Total (RSS)		-	-	-	-	-	**51**

3.6.5.3.5 Refractive-Index Errors

Three refractive materials are used in the OIWFS design, namely fused silica, calcium fluoride, and magnesium oxide. For fused silica and calcium fluoride, refractive indices are known to five decimal places over the required wavelength and temperature ranges. Ray tracing shows that error at this level have no significant effect on the aberrations of the system.

However, no refractive index data has been found for magnesium oxide at cryogenic temperatures. It is therefore proposed that a suitably equipped laboratory be contracted to measure the required values during final design. One such laboratory is operated by the Optical Sciences Center, University of Arizona. They have experience in this work, and report an uncertainty in their refractive index measurement of 0.00021 RMS. Conservatively assuming a refractive-index error of 0.0005 and an Abbe Number error of 0.25, the wave-front error for the OIWFS is

$$\sigma = 7 \text{ nm RMS}.$$

3.6.5.3.6 Total Errors

The total wave-front error caused by the imager is estimated in Table 21. The resulting value of 74 nm RMS is less than the allowance of 120 nm RMS.

Table 21: Total OIWFS Wave-Front Error

Error Source	**Wave-Front Error (nm RMS)**
Design Defects	37
Surface Irregularities	15
Dimension Errors	35
Alignment Errors	51
Refractive-Index Errors	7
Total (RSS)	**74**

3.6.6 Throughput

The throughput of the OIWFS is shown in Table 22 for a range of wavelengths. All lenses and the cryostat window are assumed to be AR coated with a single layer of magnesium fluoride. All mirrors are assumed to be gold coated. Filter transmission is assumed to be 0.8, as specified by Barr Associates.

Table 22: Optical Throughput Budget for the OIWFS Optical Design

Transmission			Wavelength (μm)				
			1.00	1.25	1.60	2.20	2.50
Component	Cryostat Window		0.948	0.961	0.963	0.956	0.953
	Field Splitter Mirror		0.986	0.988	0.990	0.991	0.992
	Beam Steering System	Field Lens	0.949	0.958	0.960	0.955	0.953
		Fold Mirror 1	0.986	0.988	0.990	0.991	0.992
		Collimator Lens 1	0.949	0.958	0.960	0.955	0.953
		Collimator Lens 2	0.949	0.958	0.960	0.955	0.953
		Collimator Lens 3	0.927	0.981	0.993	0.963	0.948
		Fold Mirror	0.986	0.988	0.990	0.991	0.992
		Camera 1 Lens	0.927	0.981	0.990	0.991	0.992
		Camera 2 Lens	0.949	0.958	0.960	0.955	0.953
		Camera 3 Lens	0.949	0.958	0.960	0.955	0.953
		Tip-Tilt Mirror	0.986	0.988	0.990	0.991	0.992
		Fold Mirror 2	0.986	0.988	0.990	0.991	0.992
	Error Sensing System	Field Lens	0.949	0.958	0.960	0.955	0.953
		Filter	0.8	0.8	0.8	0.8	0.8
		Fold Mirror 3	0.986	0.988	0.990	0.991	0.992
		Collimator Lens 1	0.927	0.981	0.993	0.963	0.948
		Collimator Lens 2	0.949	0.958	0.960	0.955	0.953
		Shack-Hartmann Prism	0.948	0.961	0.963	0.956	0.953
		Camera Lens 1	0.949	0.958	0.960	0.955	0.953
		Camera Lens 2	0.927	0.981	0.993	0.963	0.948
		Camera Lens 3	0.949	0.958	0.960	0.955	0.953
		Camera Lens 4	0.927	0.981	0.993	0.963	0.948
	Total		**0.282**	**0.424**	**0.466**	**0.390**	**0.360**

Figure 34 shows a plot of this transmission across the whole wavelength range, with and without AR coating.

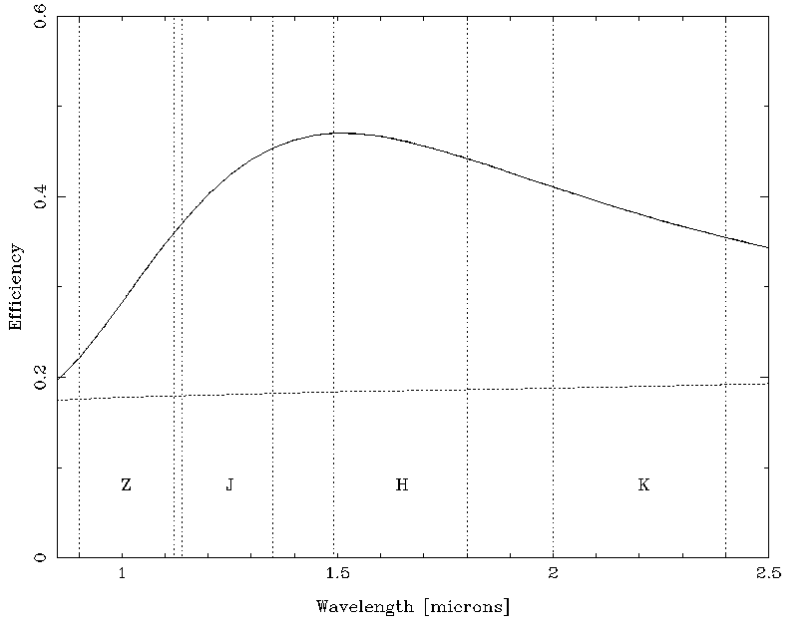

Figure 34: Transmission function for the OIWFS with AR coating (*solid*) and without AR coating (*dotted*). Standard photometric passbands are indicated.

3.7 Lens Mounting System

It is proposed that the lenses be mounted by inserting them into round holes and pressing them against conical seats with wave-washer springs, as shown in Figure 35. The cone is arranged to make tangential contact with the spherical lens surface. Diametral location is provided by means of a precision fit between lens and mount. The tolerancing is arranged so that the minimum clearance approaches zero at the cryogenic operating condition. The fit is loose at ambient temperature because the aluminum alloy housings contract more during cooling, so allowing easy assembly.

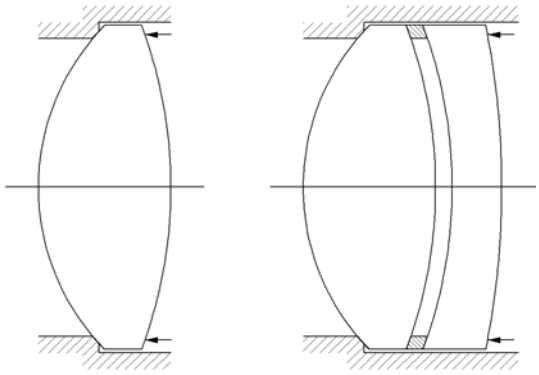

Figure 35: Lens mounting system.

Where lenses are mounted in pairs, a floating spacer is proposed, as shown in Figure 35. The tolerancing analyses for both the imager and OIWFS (§3.5.4.4 and §3.6.5.3) show that optical performance is extremely dependent on wedge errors in the gap between the lens pairs. To achieve the required precision it is proposed that the spacer be constructed as a glass meniscus lens having surfaces matched to those of the adjacent lenses, with the center removed to form a ring. The diametral clearance between the ring and housing will allow slight eccentricity of the ring, and so cause slight wedging of the lens gap, but analysis shows that this is not significant. Sensitivity to wedge error tends to be greatest where the gap is more nearly parallel, but then the wedge error is less sensitive to eccentricity.

The need to avoid interference between lenses and their mount under transient cooling conditions is considered in §3.8.2.1.

3.8 Cryogenic Compensation

GSAOI operates at cryogenic temperature, but is manufactured at laboratory temperature. Moving between these conditions causes two effects that must be accounted for in the design. Firstly, the refractive properties of the lens materials change. Secondly differential thermal strain within the instrument disturbs the optical layout. The design compensation required is described as follows.

3.8.1 Refractive Properties

All the optical design work done at this stage uses refractive indices applicable at ambient temperature. For the final design, cryogenic data would be used.

The refractive indices of most lens materials proposed for GSAOI are known over the wavelength and temperature range concerned. For each, this can be conveniently expressed as a Sellmeier 1 dispersion equation in the form

$$n = \sqrt{1 + \frac{K_1\lambda^2}{\lambda^2 - L_1} + \frac{K_2\lambda^2}{\lambda^2 - L_2} + \frac{K_3\lambda^2}{\lambda^2 - L_3}}$$

where K_1, K_2, and K_3 are polynomial functions of temperature, and L_1, L_2, and L_3 are constants. Typically, the data are accurate to five decimal places, which is more than adequate.

Beyond the warm cryostat window, the baseline non-telecentric system uses calcium fluoride and magnesium oxide. Good refractive index data are available for calcium fluoride, but not magnesium oxide. It is therefore proposed that a suitably equipped laboratory be contracted to measure the data for this material. It is anticipated that these measurements will have accuracy better than the 0.0005 assumed in the wave-front error budget (§3.5.4.4.5).

Three alternative forms of the non-telecentric design have been devised using

- Barium fluoride and IRG2.
- Barium fluoride, lithium fluoride and zinc selenide.
- Zinc selenide, fused silica, and barium fluoride.

All are feasible, and in the event of refractive index measurement being problematic, one of these designs could be used. The version using IRG2 could also be a problem in this regard, however, because its refractive index is known to vary significantly from batch to batch.

3.8.2 Thermal Strain

The cooled structural and optical materials used in GSAOI change size with temperature, as determined in Appendix A, §8.7. Thermal strain values are shown in Table 23 for the baseline materials at the expected operating temperature of 70 K with respect to 20 C.

Table 23: Thermal Strain Values

Material	Thermal Strain
Grade 6061 Aluminum Alloy	-0.00400
Calcium Fluoride	-0.00301
Magnesium Oxide	-0.00140

This thermal strain must be accounted for in two ways, described as follows.

3.8.2.1 Diametral Lens Location

The proposed lens mounting system is shown in Figure 35. The diametral clearance in these mounts is arranged to approach zero at the cryogenic operating temperature. The thermal strain in the aluminum alloy is higher than that in any of the lens materials proposed, and so a specific clearance can be provided at the manufacturing temperature to compensate for the differential strain. The minimum diametral clearance required to prevent interference when cooled is

$$\Delta d = \left(\varepsilon_{lens} - \varepsilon_{mount}\right)d$$

where ε is the thermal strain and d is the lens diameter.

During the cooling process there will be a transient temperature lag between the mount and the lens contained in it. To avoid lens damage, this temperature lag must never cause a transient interference condition to develop. This effect has been conservatively investigated in Appendix A, §8.8. For calcium

fluoride lenses there is a possibility of very slight interference, but this can be overcome by slightly increasing the clearance at ambient temperature. The resulting increase in lens location error is not significant.

The viability of this approach will soon be tested in NIFS. This instrument also uses calcium fluoride lenses in the same lens mounting system, and is more exposed to risk because the lenses are larger.

3.8.2.2 Axial Lens Location

The main structure of the cryostat is made from grade 6061 aluminum alloy. In this regard, the thermal strain is isotropic and a simple scale factor can be applied to provide compensation. Where lenses are involved, however, compensation is more complex.

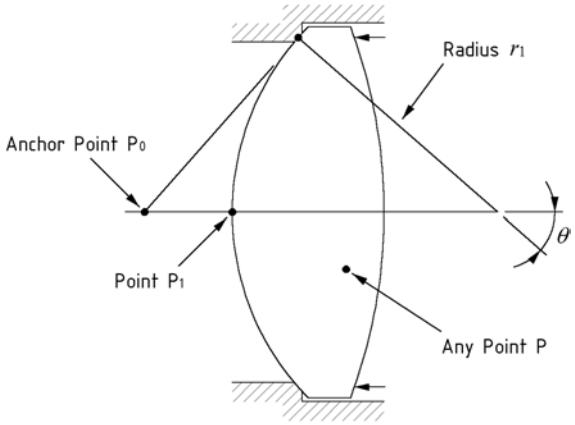

Figure 36: Positional compensation geometry for lenses.

The lens mounting method is shown in Figure 36. The anchor point, P_0, is the apex of the cone that is tangent to the lens at the circle where it contacts the mount. As temperature changes, this is the point where there is no relative movement between the lens and mount. The relative displacement between the lens and mount at any point, P, is the product of the distance $P_0 - P$ and the thermal strain difference $\varepsilon_{lens} - \varepsilon_{mount}$. At the vertex of the mounted lens surface, point P_1, it is

$$e_1 = r_1\left(\frac{1-\cos\theta}{\cos\theta}\right)\left(\varepsilon_{lens} - \varepsilon_{mount}\right)$$

This principle is applied to the cryogenic geometry to derive the ambient geometry.

3.9 Filter Selection

3.9.1 Imager

A suite of up to 28 interchangeable filters will be provided near the cold stop in the imager. They will use a fused silica substrate with a thickness of 3 mm and a clear aperture of 44 mm diameter. Surface parallelism will be < 10″, and wave-front error < 1/20th wave. They will be tilted by 3° to control ghost imaging.

The suite will include those listed in Table 24.

Table 24: Filter Suite for the Imager

Number	Description	λ_c (μm)	$\Delta\lambda$ (μm)
1	*Z*	1.010	0.220
2	*J*	1.250	0.180
3	*H*	1.650	0.290
4	*Ks*	2.145	0.310
5	*K*	2.200	0.330
6	*J* continuum	1.207	0.018
7	*H* continuum	1.570	0.024
8	CH_4 (short)	1.580	0.095
9	CH_4 (long)	1.690	0.101
10	*Ks* continuum	2.090	0.031
11	*Kl* continuum	2.270	0.034
12	He I 1.0830 μm	1.083	0.016
13	H I Pγ	1.094	0.016
14	H I Pβ	1.282	0.019
15	[Fe II] 1.644 μm	1.644	0.025
16	H_2O	1.996	0.050
17	H_2 1-0 S(1)	2.122	0.032
18	H I Brγ	2.166	0.032
19	H_2 2-1 S(1)	2.248	0.034
20	CO 2-0 (bh)	2.294	0.034
21	CO 3-1 (bh)	2.323	0.035
22	Blocked	…	…
23	Spare	…	…
24	Spare	…	…
25	Spare	…	…
26	Spare	…	…
27	Spare	…	…
28	Spare	…	…

3.9.2 OIWFS

A suite of 10 filters will be provided in the OIWFS, located near the field lens in the error sensing system. They will use a fused silica substrate with a thickness of 3 mm and a clear aperture of 20 mm diameter. The proposed suite is listed in Table 25.

Table 25: Filter Suite for the OIWFS

Number	Description	λ_c (μm)	$\Delta\lambda$ (μm)
1	Clear	...	...
2	*Z*	1.010	0.220
3	*J*	1.250	0.180
4	*H*	1.650	0.290
5	*Ks*	2.145	0.310
6	*K*	2.200	0.330
7	*ZJ*	1.120	0.440
8	*HK*	1.935	0.860
9	Blocked	…	…
10	Spare	…	…

3.10 Optical Coatings

3.10.1 Mirrors

The proposed coating material for all mirrors in the system is bare gold because it has excellent reflectivity over the required wavelength range, and it will not deteriorate in this environment. Freshly applied bare silver has even better reflectivity, but it deteriorates rapidly with even the limited exposure to atmosphere involved in this application. Special protected silver coatings, such as those available from Denton Vacuum, are a realistic alternative to bare gold, but the uncertainties involved make this unconvincing. Vapor deposition of gold, using an intermediate layer of chrome, is a proven technology.

The reflectivity of vapor-deposited gold is shown in Table 26 for a range of relevant wavelengths (R. N. Wilson, Reflecting Telescopes, Optics II, Table 6.1).

Table 26: Reflectivity of Freshly Evaporated Metals

Wavelength (μm)	Reflectivity (%)
0.9	98.4
1.0	98.6
1.5	99.0
2.0	99.1
3.0	99.3

3.10.2 Lenses

The refractive materials used in the baseline system are fused silica, calcium fluoride, and magnesium oxide. Single-layer AR coatings are proposed for all. Magnesium oxide has a relatively high refractive index (1.72 at these wavelengths), and so the option of using a special broad-band coating for it may be worthwhile. A BBAR coating from Janos is one such possibility.

3.11 Emissivity

GSAOI is required to have an instrument effective emissivity of less than 1% at a wavelength of 2.2 μm.

The cryostat window is the dominant contributor to the instrument effective emissivity. In the near-infrared, the absorption coefficient of IR-grade fused silica is $\sim 1\times10^{-5}$ cm^{-1} (Browder et al. 1991, Handbook of Infrared Optical Materials, ed. P. Klocek, p. 452). The emissivity of the 16 mm thick window is then $\sim 2\times10^{-5}$. Assuming that the contribution from other components in the cryostat is small, the instrument effective emissivity is ~ 0.002%.

A window cleaning system will be implemented to prevent dust collecting on the cryostat window.

3.12 Baffling

Baffling must be provided to prevent scattered light from reaching the detector. It is proposed to baffle the instrument chamber by partitioning it into many zones by means of thin blackened panels, with the beam being passed though holes with no more clearance than is necessary. The rational for this is that it forms large cavities with small apertures, and the entering radiation is widely spread to reduce flux, as for a blackbody cavity at low temperature. Baffles closely conforming to the beam are avoided where possible because stray light tends to be intercepted at grazing incidence, reflected, and contained within the beam space. The folded nature of the imager and OIWFS will require some close baffling between adjacent beams.

Detailed discussion of baffling is deferred to the mechanical engineering section (§4.4.1.11 and §4.5.7).

3.13 Blackening

Surfaces within the cooled chamber of the instrument should have high emissivity to suppress scattered radiation. Many proprietary infrared blacks are available for this purpose. For GSAOI, the plan is to use Aeroglaze Z306. It has an emissivity of ~ 0.9 at the wavelengths of interest, low out-gassing rates, and good mechanical adhesion properties.

3.14 Thermal Radiation

The imager chamber is almost a fully enclosed cavity held at a constant temperature, so the thermal radiation flux within it will be that of a black body. Analysis on this basis (§3.1.1.1.3 of Vol. 1) indicates that the imager temperature must be held below ~ 150 K to ensure that the total radiation flux remains significantly below the expected detector dark current. The NIRI cryostat is known to hold its instrument temperature at ~ 70 K, and so no problems are foreseen in this regard.

3.15 Lens Material Availability

All refractive materials employed in the baseline imager and OIWFS are available with delivery times of 2 to 4 months. The special IR grade of fused silica and the various sizes of single crystal calcium fluoride are readily available from a number of suppliers. Single-crystal magnesium-oxide blanks of suitable size (25-70 mm diameter) are more difficult to acquire, particularly in the larger sizes, but a potential supplier has been identified. A blank suitable for measuring cryogenic refractive index data should also be available.

An alternative design uses barium fluoride and IRG2 in place of calcium fluoride and magnesium oxide. If this were adopted, a special melt of the IRG2 material would have to be scheduled with Schott. No delivery time has been specified for this, but 12 months has been suggested.

Potential suppliers of the refractive materials used in the baseline optical system are listed in Table 27.

Table 27: Potential Suppliers of Refractive Materials for the Baseline System

Material	Suppliers
IR-Grade Fused Silica	Heraeus Amersil Corning
Single-Crystal Calcium Fluoride	Schott Lithotec Optovac
Single-Crystal Magnesium Oxide	Crystal GmbH

3.16 Lens Manufacture

Facilities and expertise required for the manufacture of all lenses and mirrors proposed are available at RSAA. Relevant experience has already been acquired. Polishing trials have recently been carried out on magnesium oxide to verify that the required tolerances can be achieved.

Companies such as Laserdyne and BAE within Australia can apply gold coating to mirrors and single-layer AR coatings. If needed, Janos could apply broad-band AR coatings in the USA.

3.17 Optical Design Risks

3.17.1 Non-Telecentric Output

The baseline imager system delivers a non-telecentric beam onto the detector. This has the potential to cause wavelength dependent scale changes if focus is wavelength dependent, and to create ghost image problems associated with reflections in the detector substrate (§3.5.5.5).

The proposed system has excellent chromatic correction and no focus adjustment is needed or provided. Investigation of the ghost image shows that it is almost completely lost in the parent image and is therefore likely to be undetectable. In any case, it is less prominent than unavoidable ghosts produced by reflections within the filters (§3.5.5.4). These risks are therefore judged to be low.

3.17.2 Guide Star Availability

The proposed OIWFS only has access to the crescent-shaped parts of the round MCAO field that are not delivered to the imager. This facilitates rigidity and rapid development, but may significantly restrict field coverage. The alternative of designing a movable probe would be possible but more difficult and time consuming.

Reconsideration of this decision may be warranted if this risk is serious, especially if the image stability requirement is relaxed as explained in §3.6.1.1.

3.17.3 Material Availability

Magnesium-oxide optical crystals can be difficult to obtain in blanks with a diameter of greater than 50 mm. The baseline optical design requires several blanks with diameters of up to 70 mm. Suitable blanks are currently available from one known supplier (§3.15), but future supply is not guaranteed.

One of the alternative variations to the baseline design substitutes IRG2. This is an obsolete material that is now only manufactured to order. Depending on demand at the time of order, this material could be unrealistically expensive.

Other variations have been presented (§3.5.1.3) that have no material supply problems, and so this risk is eliminated. The cost is a slight but acceptable reduction in optical quality.

3.17.4 Cryogenic Refractive Index Data

Cryogenic refractive-index data is not available for magnesium oxide, and if this material is adopted, the required data will have to be measured. Such a service is available, but it is a specialized process, and logistic problems may be encountered.

Similar measurement would also be required for one of the alternative materials, IRG2, because its refractive properties are known to vary from batch to batch.

Other variations have been presented (§3.5.1.3) that have no problems in this regard, and so this risk is eliminated for the imager. The cost is a slight but acceptable reduction in optical quality.

The proposed OIWFS also uses magnesium oxide, so a similar design revision could be required for this system as well.

3.17.5 Lens Manufacture

The manufacture of lenses from crystal materials presents special difficulties, and the stringent requirement for optical quality therefore makes this a concern. In particular, experience in the RSAA Optical Workshop has revealed that systematic surface irregularities are prominent in magnesium oxide. Polishing tests have

therefore been conducted to characterize this problem (Appendix A,§8.2.1), and the results applied to the error analysis. This indicates that the effect is acceptable, and so the risk is regarded as being low.

3.17.6 Doublet Lens Gap Precision

The wave-front error analysis shows the optical performance is critically dependent on achieving small wedge angles in the gap between lens doublets. Optically ground spacer rings are proposed for this purpose. This is a specialized technique that involves some risk in manufacture. Nevertheless, it has been used successfully at RSAA in the past.

3.17.7 Lens Mounting Safety

A simple and precise system of lens mounting is proposed (§3.7) that presents some risk of lens damage during cooling, particularly for the calcium fluoride elements. This risk will be dealt with by careful control of engineering tolerances.

The viability of this approach will soon be tested in NIFS. This instrument also uses calcium fluoride lenses in the same lens mounting system, and is more exposed to risk because the lenses are larger.

3.17.8 Throughput

An imager throughput of at least 60% is required to achieve the high sensitivities required to realize the science goals of GSAOI. Some science objectives may be unachievable if this sensitivity is inadequate.

3.17.9 Filter Cost and Availability

The cost estimates for filters presented in this proposal are based on recent consortium quotes from Barr Associates for similar filters. Barr Associates is likely to be the only available supplier. Costs are uncertain, and recent purchasing experience suggests that delivery time can be long for some filters. A basic set of filters will be available within the instrument construction schedule, but a full suite may not.

Delays would be minimized by commencing purchase negotiations as soon as possible.

4 Mechanical Design

4.1 Introduction

The GSAOI optics and detector will be mounted in a duplicate of the NIRI cryostat, illustrated in Figure 37. The NIRI cryostat consists of a hexagonal vacuum jacket in which is supported a central vertical cold-work-surface (CWS) plate that acts as an optical bench for both the imager and the OIWFS. Duplicates of the NIRI radiation shields and floating shields will be used. The GSAOI imager will replace the NIRI OIWFS, and the GSAOI OIWFS will replace the NIRI imager. A duplicate of the NIFS integration frame (i.e., space frame) will be used to carry the two thermal enclosures. This is similar to the NIRI integration frame, but has been modified to allow NIFS (and GSAOI) to fit within the Gemini service elevator without disassembling the instrument. The GSAOI cryostat and integration frame will be supported from the Instrument Support Structure (ISS) using a duplicate of the NIRI ISS interface plate.

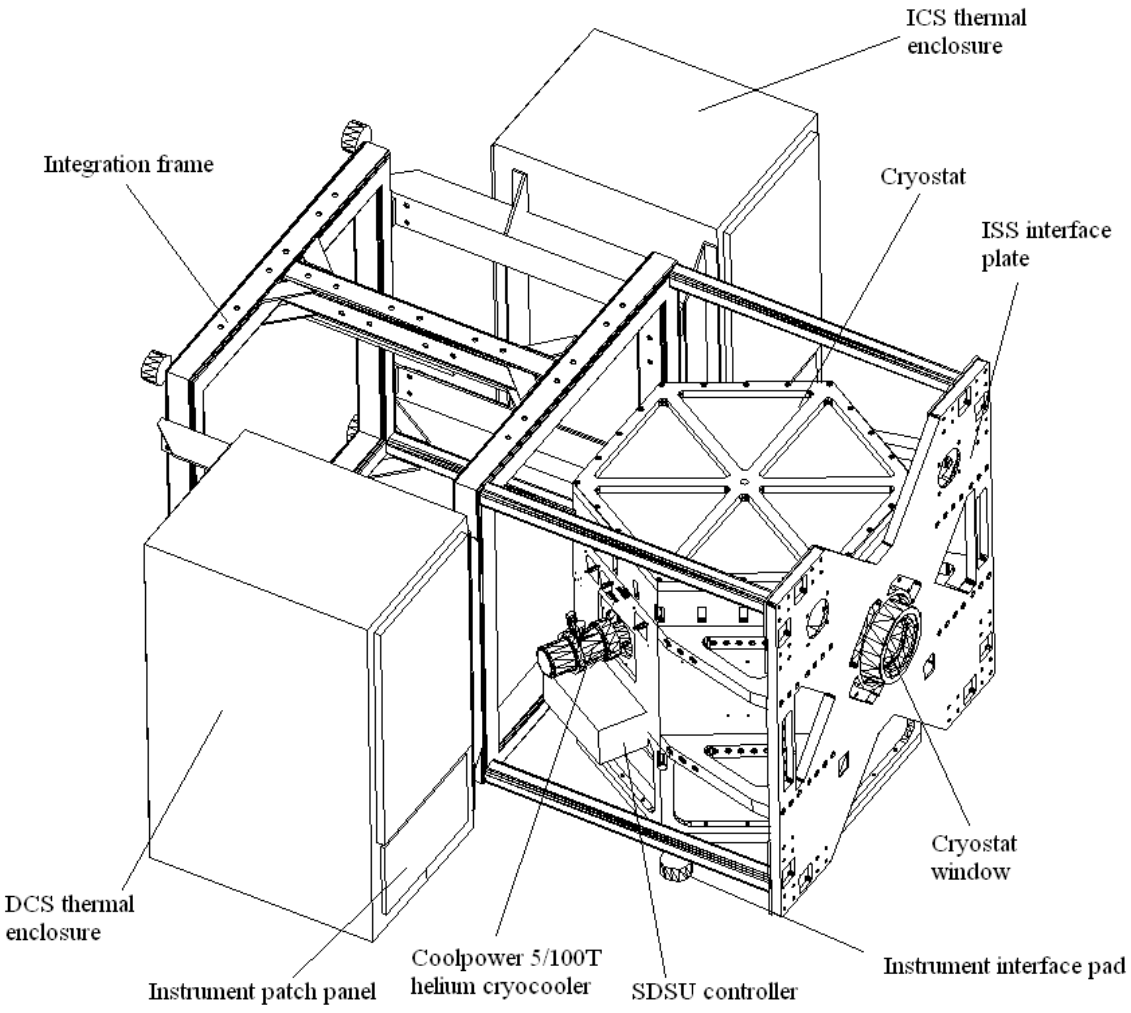

Figure 37: Complete GSAOI assembly ready for attachment to a side-looking port of the ISS.

4.2 External Components

4.2.1 ISS Interface Plate

Figure 38 shows an exploded view of the GSAOI ISS interface plate and vacuum jacket. The interface plate is at the top of the figure. The GSAOI cryostat and integration frame attach directly to the ISS interface plate. In this way, the ISS interface plate transfers the entire weight and bending moment of GSAOI to the ISS. The whole subsystem of the interface plate and its corner brackets will be duplicated for GSAOI.

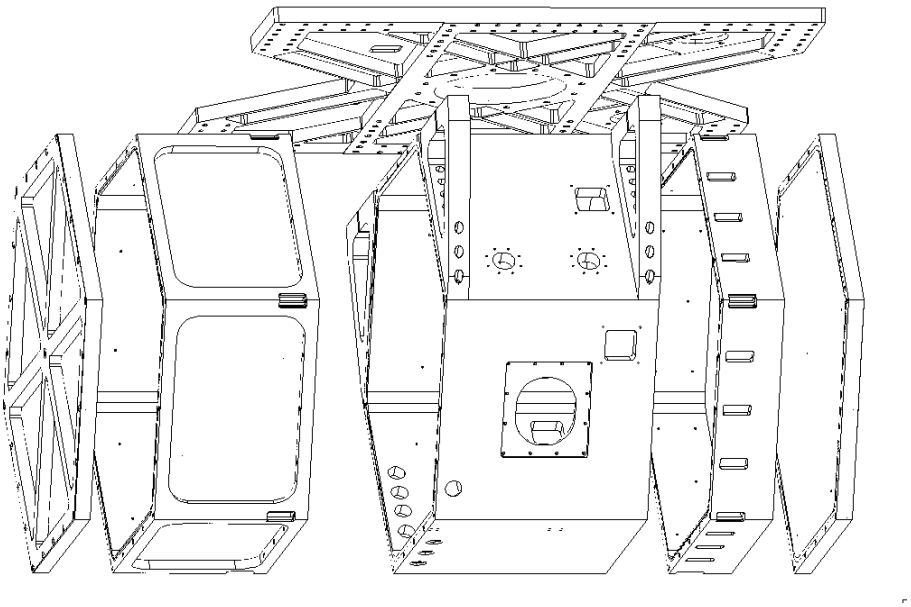

Figure 38: GSAOI ISS interface plate (*top*) and exploded view of the vacuum jacket.

4.2.2 Integration Frame

The GSAOI integration frame is a large welded frame measuring 1300×1300×2100 mm, shown in Figure 37. This frame is the largest GSAOI component and supports the ballast weights, thermal enclosures, cables and lines, and the interface to the Gemini instrument handling equipment (i.e., instrument trolley and instrument platform lift). The modified design adopted for NIFS will be duplicated. This allows the instrument to be transported in the Gemini service elevator without disassembly. All of the ballast, registration fittings to the instrument handling equipment, and support structure for the thermal enclosures will be duplicated from NIRI.

4.3 Cryostat Mechanical Design

4.3.1 Vacuum Jacket

The GSAOI vacuum jacket consists of three machined hexagonal forgings and two ribbed end plates, illustrated in Figure 38. It is a slightly modified copy of the NIRI vacuum jacket. These modifications include moving the O-rings from the vacuum jacket center section to the outer two sections to facilitate assembly, omitting the NIRI detector controller feed-through ports, adding ports and attachment points for the GSAOI detector controller, and adding lifting and trunnion attachment points for safe handling of the assembled cryostat. The same modifications have been made to the NIFS vacuum jacket. In addition, the positions of the vacuum sub-plates and through-holes for cables will be different due to the different

positions of the imager and OIWFS detectors. Outwardly, the GSAOI vacuum jacket will look little different from the NIRI and NIFS vacuum jackets.

4.3.2 Cryocoolers

NIRI and NIFS use two Leybold Coolpower 130 cryocoolers. However, production of these cryocoolers has ceased so they are nolonger available. They will be replaced with a different model developed by the same company, namely the Coolpower 5/100T. The refrigeration capacity of the new cryocoolers closely matches that of the Coolpower 130. The first stage has 100 W at 80 K compared to the 95 W of the 130 model, while the second stage has 7.5 W compared to 9 W. In addition, the manufacturer specifies that the cool down time for the first and the second stage to reach 80 K and 20 K, respectively, is 20 minutes. Despite the slightly lower cooling capacity of the second stage, the Coolpower 5/100T is considered to be an acceptable replacement for the Coolpower 130 since GSAOI does not need to reach as low a temperature as NIRI (because of the 2.5 μm detector cut-off).

Modifications will be required to the external cooler mounts, due to the adoption of a new cooler. The main modification will be to mount the two cryocoolers square to the vacuum jacket, rather than in-line as they are in NIFS and NIRI. This will require a slight shift of the cryocooler port towards the back of the cryostat to accommodate the new orientation. Rubber cryocooler vibration mounts will be used instead of the spring-loaded hinged structure used in NIRI/NIFS. This mounting method will achieve sufficient structural stiffness and absorb the majority of vibrations generated by the cryocooler stepper motors. We are confident that the new mounting method will result in a more compact and efficient design than that used in NIRI and NIFS. The rubber mounting system has been used successfully in the CASPIR imager on the RSAA 2.3 m telescope.

4.3.3 Cold-Work-Surface Plate

GSAOI retains the NIRI-designed CWS plate suspended on titanium trusses near the mid point of the cryostat.

4.3.4 Cold-Work-Surface Plate Cooling

NIRI has experienced some vibration coupling from the helium cryocoolers to the CWS plate. We have modified parts of the original NIRI design to make the cold strap links in NIFS more compliant, to reduce the number of cold surface interfaces, and to reduce the total number of parts in the cold strap assembly. A similar approach will be adopted for GSAOI, but taking into account the new cryocooler dimensions and mounting requirements.

Figure 39 shows the cold end of a Coolpower 5/100T helium cryocooler. Note that the cold strap assemblies use “S” shaped cold straps, and have copper conductor rings bolted directly to the flanges of the helium cryocoolers. Each cold strap is formed from 24 thin laminations. The laminations will be spaced with paper before bending to shape. When the paper is removed, the combined laminated strap will be compliant in all x, y, and z directions. The cold straps will connect the 1st stage of both cryocoolers to the CWS plate (60 K connection). The 2nd stage of one cryocooler connected to the 20 K tie point, which connects to the imager detector. The 2nd stage of the other cryocooler cools the cryostat getter, which will be a stack of charcoal-coated copper plates similar to the ones in NIRI/NIFS.

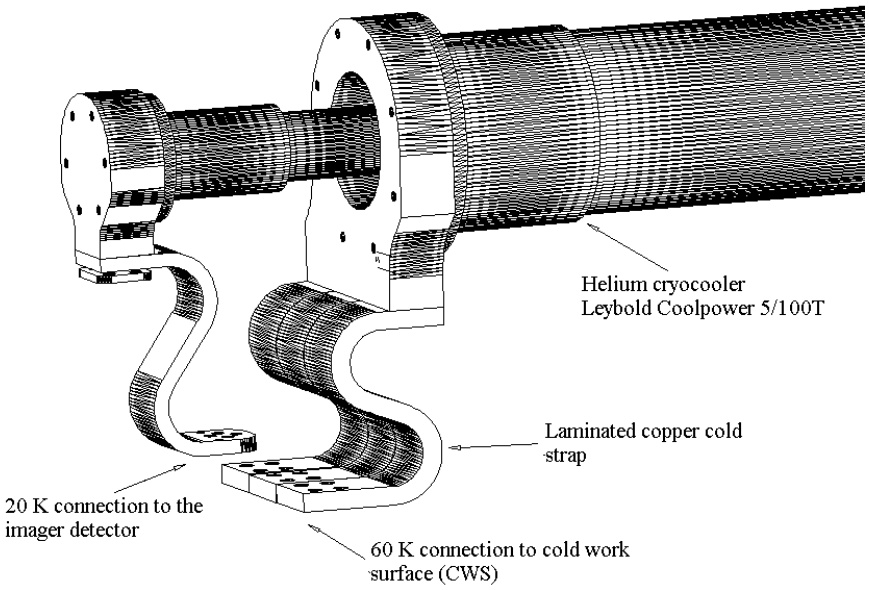

Figure 39: GSAOI helium cryocooler and CWS plate cold straps.

4.3.5 Environmental Cover

RSAA have recently assembled and tested a copy of the NIRI environmental cover for NIFS. We found that this design is deficient in two respects. Firstly, the motor drive system does not have enough power to drive the cover blades uphill against gravity. Secondly, power to the motor is not maintained in the open or closed positions so this allows the cover to drift to partly open or closed positions with changing gravity vectors while observing is in progress. The existing control system for the cover reads a switch at the end of the total travel of the two blades but does not automatically sense any drift and re-apply power to the motor to return the blades to the open or closed positions. The observer is not automatically notified that the blades may be vignetting the beam.

To overcome these problems, the stepper motor will be replaced with a DC gear motor, and the drive mechanism will be modified to accommodate this. The gear motor will incorporate a high reduction ratio gear head so that it will resist being back-driven by the load of the cover.

The existing software used to drive the stepper motor will be replaced with a device handler written to control a simple DC motor via two relays using a simple binary output record employing the existing XYCOM-240 digital I/O card. The existing limit switches will be used to sense the shutter limits and control the relays. This will free a stepper motor drive system in the Mechanisms Control System that will be use to drive the fast shutter (§4.4.1.7).

4.3.6 Cryostat Window

The cryostat window will be enlarged over that of NIRI/NIFS due to the larger scale of the MCAO field. A 237 mm diameter window mount will be necessary in order to accommodate a 200 mm diameter window, having a 170 mm diameter clear aperture (§3.2). The window material is also changed to IR-grade fused silica from the NIRI/NIFS calcium fluoride. This allows the thickness of the window to be reduced to 16 mm. Analysis shows that a 20:1 aspect ratio gives a comfortable stress margin for a silica vacuum window. The GSAOI window will have an aspect ratio of 12.5:1. A modified version of the NIRI/NIFS window input baffle tube will be used in GSAOI with this different window.

4.4 Imager Mechanical Design

4.4.1 Mechanical Design – Non-Telecentric Imager Layout

The main characteristic of the imager mechanical design is its location in the section of the cryostat occupied by the OIWFS in NIRI/NIFS. This location requires the minimum number of fold mirrors in the imager optical path, which maximizes the imager throughput. Furthermore, it avoids placing a fold mirror in the imager optical path near the MCAO focus. The beam footprint on such a mirror would be small so coating imperfections would be a risk that is avoided in the adopted arrangement.

The positions of the mechanical elements of the imager are shown in Figure 40 and Figure 41.

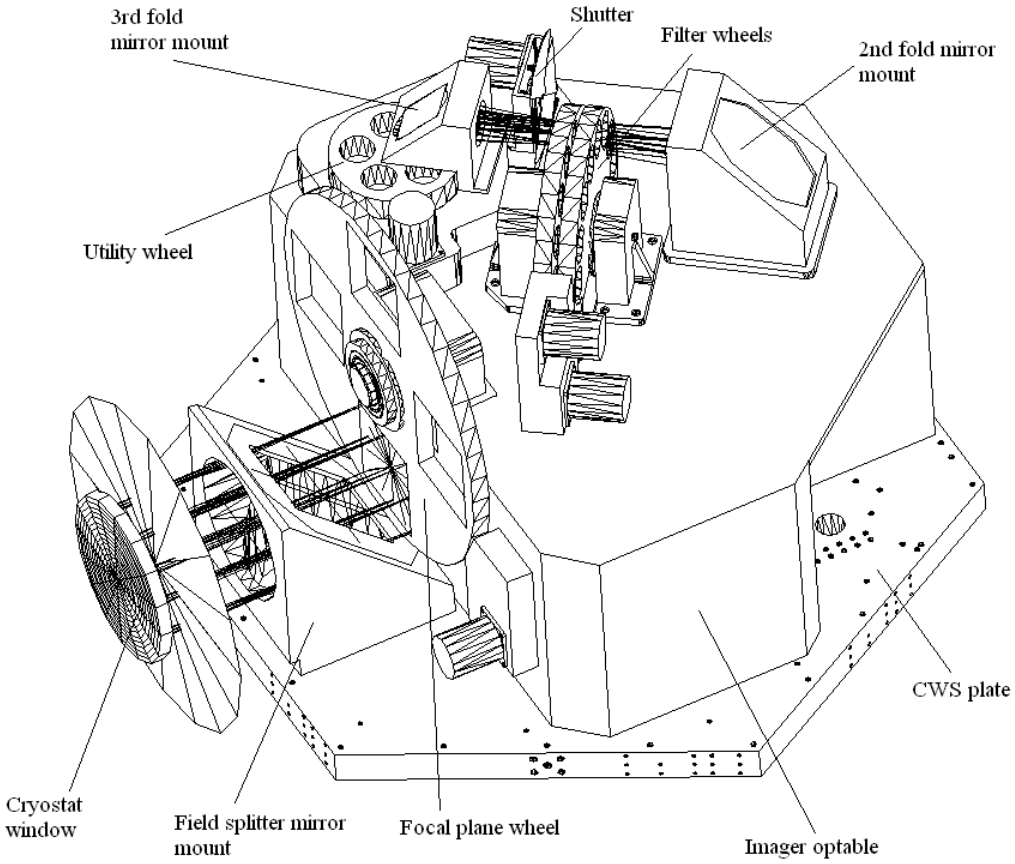

Figure 40: The GSAOI imager positioned in the NIRI/NIFS OIWFS section of the cryostat in order to minimize the number of fold mirrors in the system. The figure depicts the elements mounted on top of the imager optable.

After entering the instrument through the cryostat window, the MCAO beam passes through the field splitter mirror. This element separates the square imager field (107.2×107.2 mm) from the original circular input field, which is 151.6 mm in diameter. The imager beam then comes to focus at the focal plane wheel. This wheel contains the field stop and calibration masks.

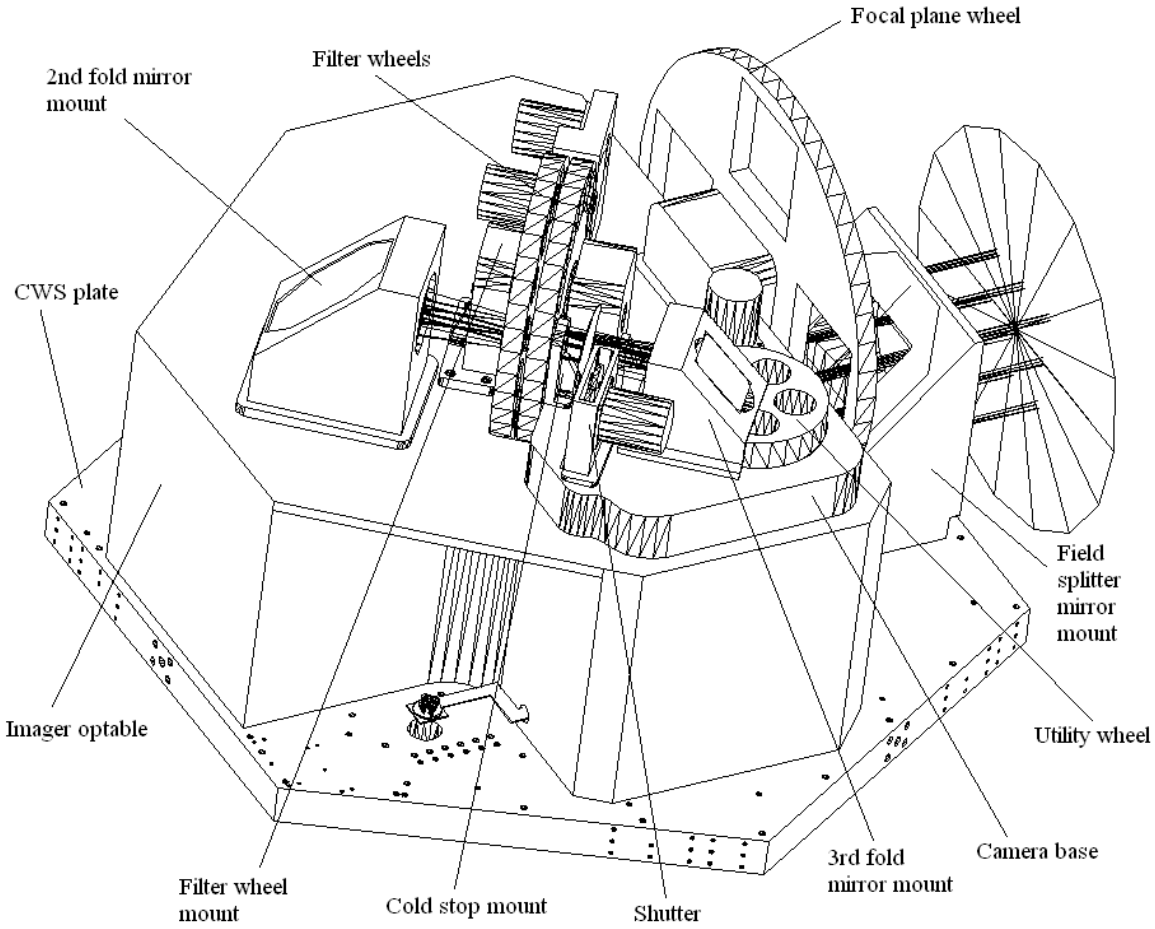

Figure 41: GSAOI imager depicting elements and assemblies on the imager optable.

The beam then enters the imager optable and passes through the field lens. It is then folded up, towards the second optical level, which is 111.75 mm above the top surface of the optable. At this level, the beam is folded for the second time and is rotated 40° towards the front-right cell of the optable, as shown in Figure 41. Along this path, the beam passes through dual filter wheels and the cold stop. It is then folded for the third time towards the CWS plate. After the third fold mirror, the beam passes through the utility wheel and finally comes to focus at the imager detector. The detector is mounted from the CWS plate with the focal plane parallel to the CWS plate.

4.4.1.1 Field Splitter Mirror

The field splitter mirror is a 261×190 mm rectangular glass mirror. A central rectangular region will be cut out in order to pass the central square field to the imager while folding the remaining field to the OIWFS. The size of the central imager field is defined by the size of the imager detector mosaic and the magnification of the imager optics.

The field splitter mirror is mounted in an aluminum mount that is fixed to the CWS plate. The mount will be machined from a solid block of aluminum. This will contribute to its structural stiffness. The mirror will be spring loaded into a kinematic mount to accommodate differential shrinkage due to the cryogenic work conditions.

4.4.1.2 Focal Plane Wheel

A four position 440 mm diameter focal plane wheel will be located at the imager focal plane and attached to the imager optable top face. The contents of this wheel are listed in Table 28. The "Blocked" position will be used for recording bias and dark exposures. The "Clear" position will be used for routine imaging. A focus mask consisting of an array of pinholes will be used for calibration purposes, such as calibrating astrometric distortion within the imager.

Table 28: Focal Plane Wheel Contents

Position	Content
1	Blocked
2	Clear
3	Focus mask
4	Spare

The focal plane wheel mechanism will use a cryogenic stepper motor, Hall-effect-sensor encoder system, and the gear train system adapted from NIFS mechanisms. This is illustrated in Figure 42. The wheel will rotate about a fixed 50 mm diameter shaft on a pair of precision angular contact bearings that are preloaded by Belleville washers and stabilized by a friction brake.

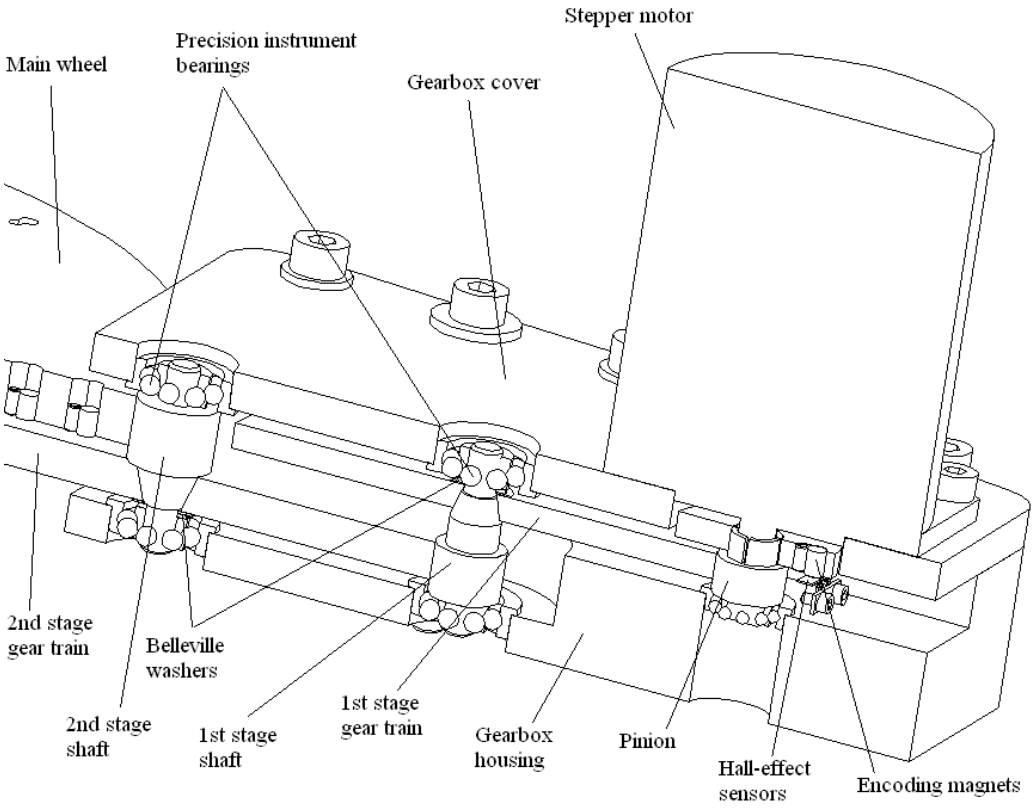

Figure 42: Typical gear train system tested successfully in NIFS

The focal plane wheel has a mass of 5.1 kg and is supported by the two bearings. The distance between the bearings is 20 mm and the remaining free length between the bearings and the mount is 7 mm. The Belleville washers will preload the wheel bearing system by 470 N force, cancelling any clearance that

exists between the balls and the raceways. The friction brake will produce a force of ~ 200 N at the radius of 50 mm, resulting in a constant drag torque of 1000 Nmm. This will be more than sufficient to suppress any backlash in the gear train system and achieve the required stability of the focal plane wheel of < ±0.1 pixels (at the imager detector) and the required tilt stability of < ±0.07 degrees.

The focal plane wheel two-stage gear train system has a gear transmission ratio of 88:1. This provides a positional resolution of 0.051 mm in the f/34 focal plane. This fulfils the requirement of ±0.1 mm positional repeatability. The stepper motors in NIFS have been shown to run reliably at 200 rpm. At this speed, the focal plane wheel will make a full revolution in 26.4 s, which is less than the required 30 s setting time. The gear train will use the same slipping-clutch system that is used in all NIFS mechanisms and has been tested successfully. This protects the fine-pitch gearing (gear teeth module of 0.5) from damage due to possible wheel jam. The slipping-clutch system is illustrated in Figure 42. The gear trains are pushed against tapered-shaft seats by Belleville washers. In the normal operating condition, the friction force generated by this gear-shaft connection is sufficient to transfer the constant drive torque from the stepper motor. In any case of malfunction or wheel jam, the drive torque will increase rapidly, causing slippage between the gears and shafts but without causing any damage in the gear train system.

The gear train system described in this section will be adapted for all imager and OIWFS mechanisms.

4.4.1.3 Imager Optable

The imager optable will be a modified version of the NIRI/NIFS OIFWS optable. Its cell-like structure is depicted in Figure 43. The optable is fixed to the CWS plate, which contributes significantly to the stiffness of the whole instrument.

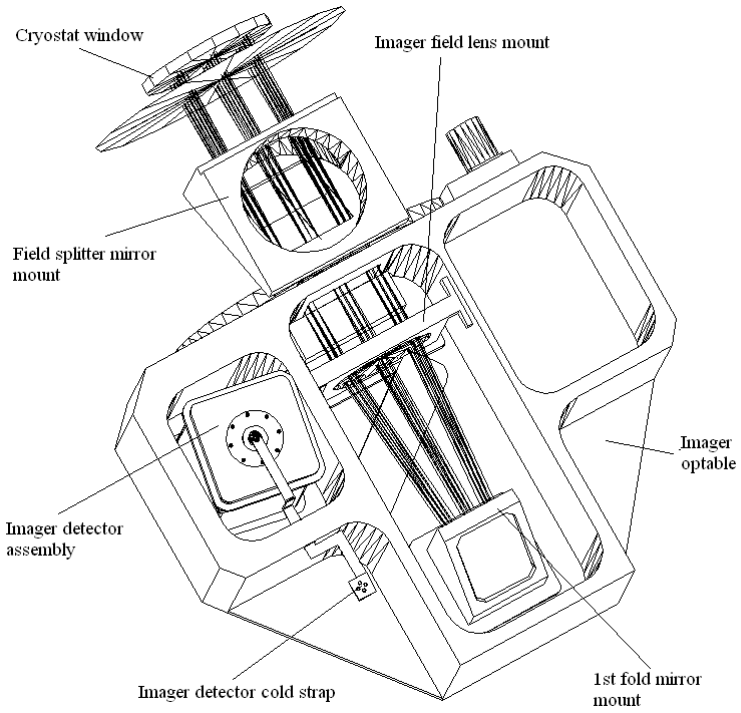

Figure 43: GSAOI imager optable showing elements and assemblies inside the cell-like structure of the optable.

4.4.1.4 Field Lens Mount

The imager field lens mount is positioned in the central section of the optable, as shown in Figure 43. The mount has to retain the CaF_2 field lens, which is 164 mm in diameter and has mass of 1 kg. The mount is fixed from three sides within the central optable section in order to support the lens mass with minimal deflection.

The lens will be fixed by a tangent contact retainer from the front side (§3.7) and spring loaded from the backside to accommodate any axial shrinkage of the lens during cooling. At the same time, the lens will have sufficient radial clearance in the mount at ambient temperature, but zero radial clearance at the 60 K operating temperature. This approach to cryogenic lens mounting is illustrated in Figure 44. The concept has been used successfully with smaller lenses by RSAA in its CASPIR camera. It is being applied in NIFS and will be tested with large lenses during the second NIFS cool down in September 2002.

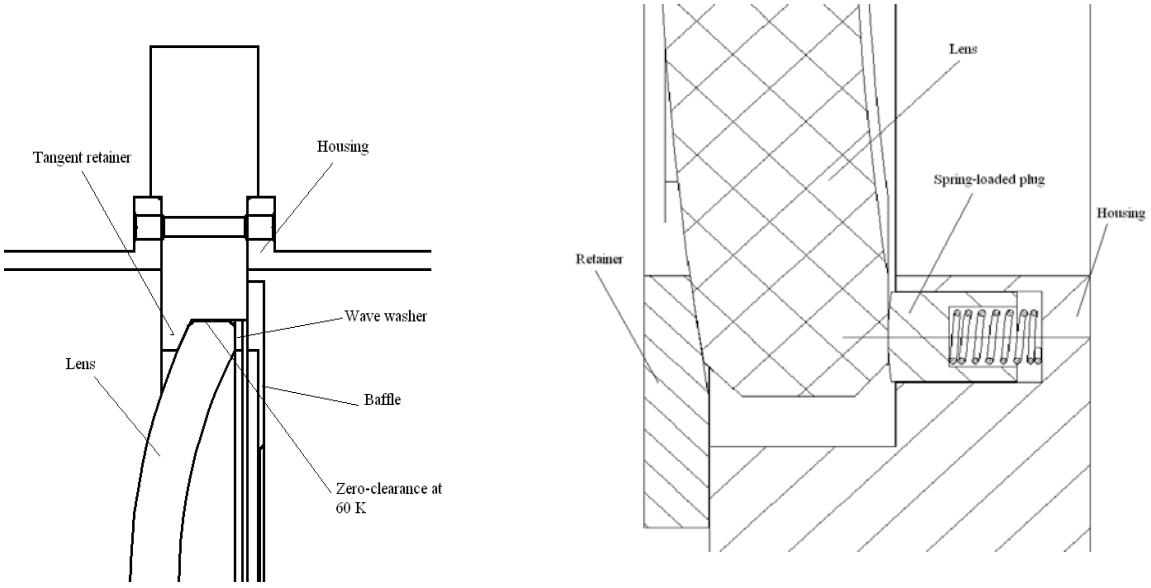

Figure 44: The proposed lens mounting method showing two different approaches to applying axial spring-force and having zero radial clearance between the lens and the housing at the operating temperature.

4.4.1.5 Fold Mirror and Lens Cell Mounts

All imager fold mirrors and lens cells are mounted in a similar fashion using the solid-block aluminum mounts depicted in Figure 45 and Figure 46.

The first fold mirror is mounted against the ceiling of the optable central section while the second and the third fold mirrors are mounted on the optable top surface. The mirrors are mounted on seats provided in the 45° machined surfaces. Lenses are mounted in cylindrical bores ahead of or behind the fold mirrors. Although fixing the fold mirrors would achieve a high level of structural stiffness, it would not permit adequate optical alignment. Therefore, the fold mirrors will be adjustable in tilt while the lenses will be fixed in their housings but the housings will be laterally adjustable relative to their mounts. More details on the adjustment procedures are given §4.6. Both mirrors and lenses will be mounted in a way to accommodate differential shrinkage while cooling to the operational temperature, as explained in the previous section.

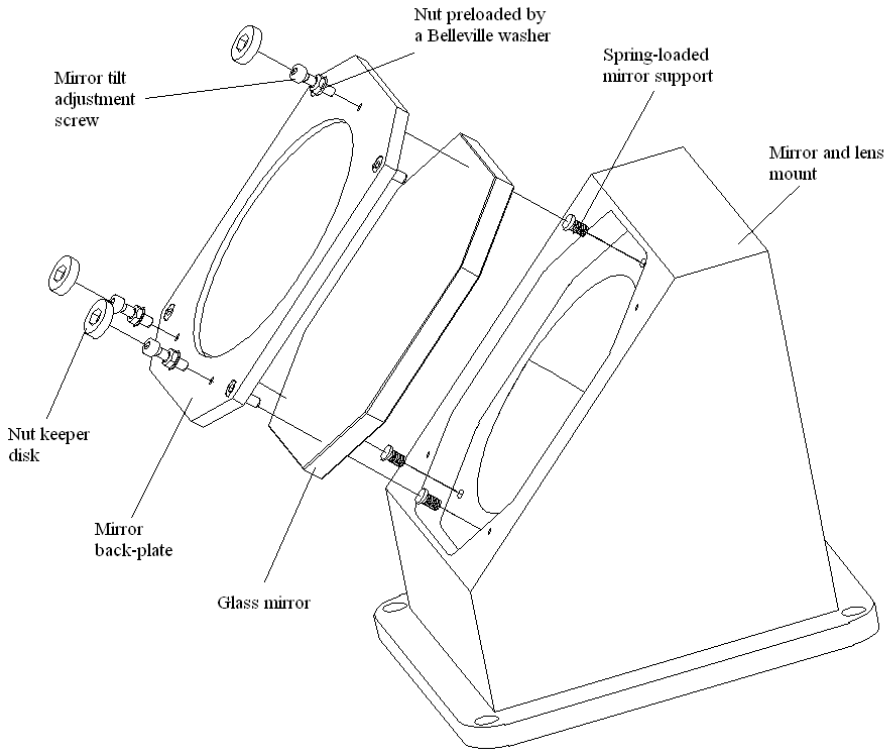

Figure 45: Mirror alignment mechanism.

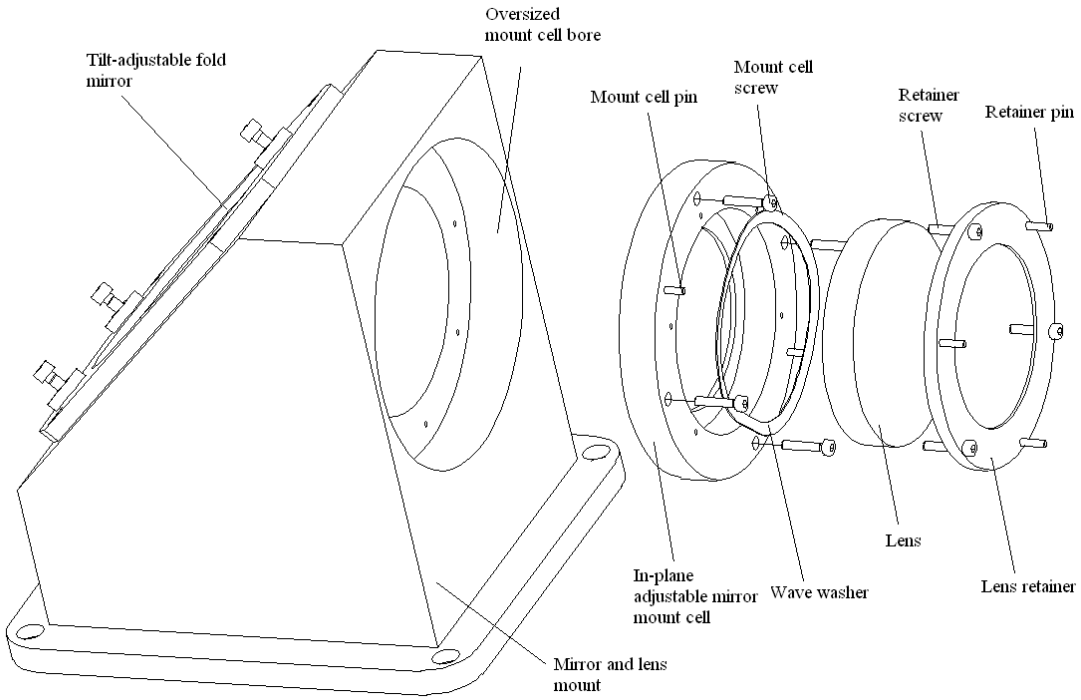

Figure 46: Lens cell alignment mechanism

4.4.1.6 Filter Wheels

The most complex mechanism in the GSAOI imager is the dual filter wheel system. This is illustrated in Figure 47.

Two 15-position filter wheels will be located in the collimated beam ahead of the fixed cold stop. These wheels will contain a range of broad-band and narrow-band imaging filters and a blocked position for measuring bias frames. The complete filter set is listed in Table 29. Each filter is 48 mm in diameter and has a working aperture of 44 mm. The total number of filters can be increased to a maximum of 27. This limit is set by space restrictions within the duplicate NIRI/NIFS cryostat. The software issue of ensuring that two wheels are never simultaneously positioned at their clear positions has been solved already for the NIFS focal plane mask wheel and filter wheel.

Table 29: Upper Filter Wheel Contents

Position	Content	λ_c (μm)	$\Delta\lambda$ (μm)
1	Clear	…	…
2	*Z*	1.010	0.220
3	*J*	1.250	0.180
4	*H*	1.650	0.290
5	*Ks*	2.145	0.310
6	*K*	2.200	0.330
7	*J* continuum	1.207	0.018
8	*H* continuum	1.570	0.024
9	CH_4 (short)	1.580	0.095
10	CH_4 (long)	1.690	0.101
11	*Ks* continuum	2.090	0.031
12	*Kl* continuum	2.270	0.034
13	Spare	…	…
14	Spare	…	…
15	Spare	…	…

Table 30: Lower Filter Wheel Contents

Position	Content	λ_c (μm)	$\Delta\lambda$ (μm)
1	Clear	…	…
2	He I 1.0830 μm	1.083	0.016
3	H I Pγ	1.094	0.016
4	H I Pβ	1.282	0.019
5	[Fe II] 1.644 μm	1.644	0.025
6	H_2O	1.996	0.050
7	H_2 1-0 S(1)	2.122	0.032
8	H I Brγ	2.166	0.032
9	H_2 2-1 S(1)	2.248	0.034
10	CO 2-0 (bh)	2.294	0.034
11	CO 3-1 (bh)	2.323	0.035
12	Blocked	…	…
13	Spare	…	…
14	Spare	…	…
15	Spare	…	…

Both wheels will rotate about the same fixed shaft on two pairs of precision angular contact bearings. The bearings will be preloaded by tandem positioned Belleville washers (Figure 47). The wheels will be position-stabilized using friction disk brakes. Filter positions will be encoded using Hall-effect sensors in the same way as in NIRI/NIFS.

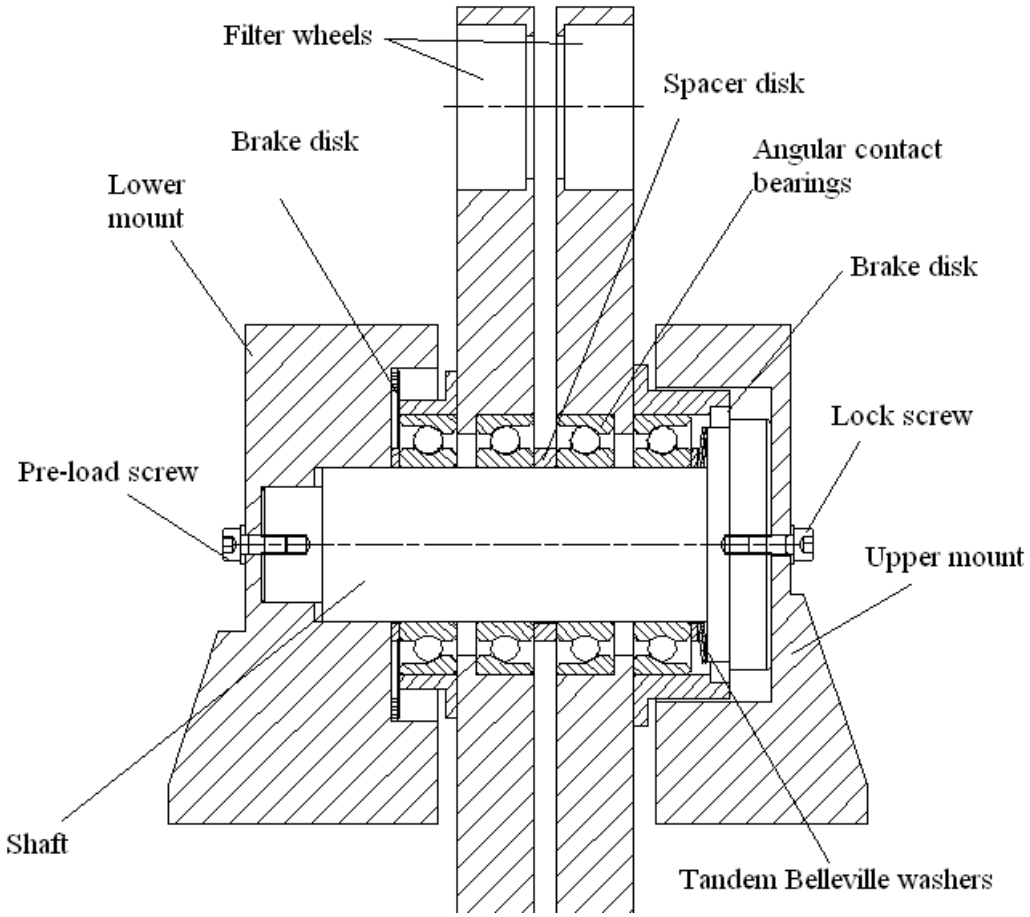

Figure 47: Filter wheel assembly cross section.

The filter wheel drive system is similar to the focal plane wheel mechanism and the NIFS mechanisms. The filter wheels will be driven at their circumferences using spur gears with a two-stage reduction of 70:1. Each filter wheel will be driven independently using separate cryogenic stepper motors. They will complete one revolution in 21 s (at a stepper motor speed of 200 rpm) with a repeatability of 0.05 mm. This performance is within the requirements of 30 s and 0.1 mm, respectively, specified in the FPRD (see Vol. 3). The position repeatability of the filter wheels will meet requirements for flat field reproducibility where it is important that filters return accurately to their set positions.

The whole filter wheel mechanism is tilted by 3° with respect to the optical axis in order to suppress ghost images caused by reflections from the back surfaces of the filters. This was possible since there is no strong requirement on filter tilt.

4.4.1.7 Fast Shutter

A fast cold shutter is needed to intercept the beam in < 1 s if the MCAO system determines that the AO correction is inadequate or the SALSA system initiates a laser shutdown. The mechanism consists of a shutter blade, housing, gear train, and stepper motor (Figure 48). The butterfly-like blade is made of 0.5 mm thick aluminum sheet metal and is normally in the vertical (i.e., open) position. It is driven by a pair of spur gears and a stepper motor. The gear train has a transmission ratio of 1:1 and serves only to offset the stepper motor to a more convenient location. The gear train is a simplified version of the system used in other imager mechanisms. It does not have a slipping clutch or a friction brake since there is no requirement for precise blade positioning. The 12.2 g blade produces an inertial torque of 2.77 Nmm,

which is much smaller that the stepper motor torque capacity of 450 Nmm. The shutter closing/opening time is 75 ms (using a stepper motor speed of 200 rpm). The position of the blade will be tracked by counting the stepper motor micro-steps and by using the Hall-effect-sensor encoding system. The blade can be driven in either direction.

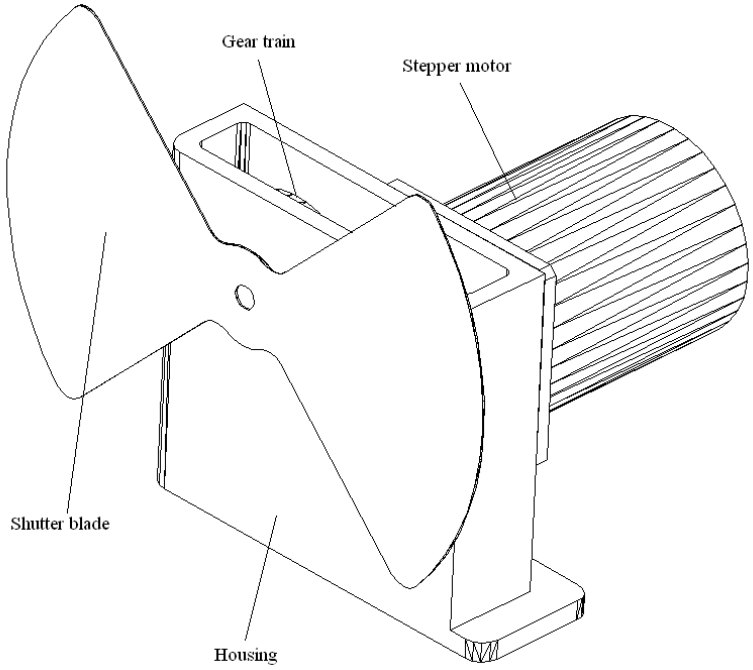

Figure 48: Shutter mechanism in 'closed' position.

4.4.1.8 Utility Wheel

The five-position utility wheel is used primarily to insert the pupil-viewer lenses into the beam. It contains a clear position that is used for normal imaging, a blocked position that can be used for recording bias and dark frames, and convex and concave defocus lenses that are used to record out-of-focus images for wave-front error determination.

The utility wheel mechanism is part of a more complex assembly that consists of the cold stop mount, the fast shutter mechanism, the 3rd fold mirror mount, the utility wheel mechanism, the utility wheel, and the camera base, detector tube, and detector assembly with its mount base. These are illustrated in Figure 49.

The main part of this assembly is the camera base, which connects all the elements of the assembly. It is firmly fixed to the imager optable in the form of a light-tight lid on the optable front-right cell. This completely isolates the detector assembly. The camera base also houses the last lens of the imager optics.

The utility wheel is designed for high positional tolerance and repeatability. It is driven in the same way as the other imager mechanisms by a two-stage gear train that has a gear transmission ratio of 84:1. Consequently, the 150 mm wheel has a positional repeatability of 0.016 mm and makes a full revolution in 25 s. This is within the requirement of 0.05 mm for the pupil-viewer lens centricity.

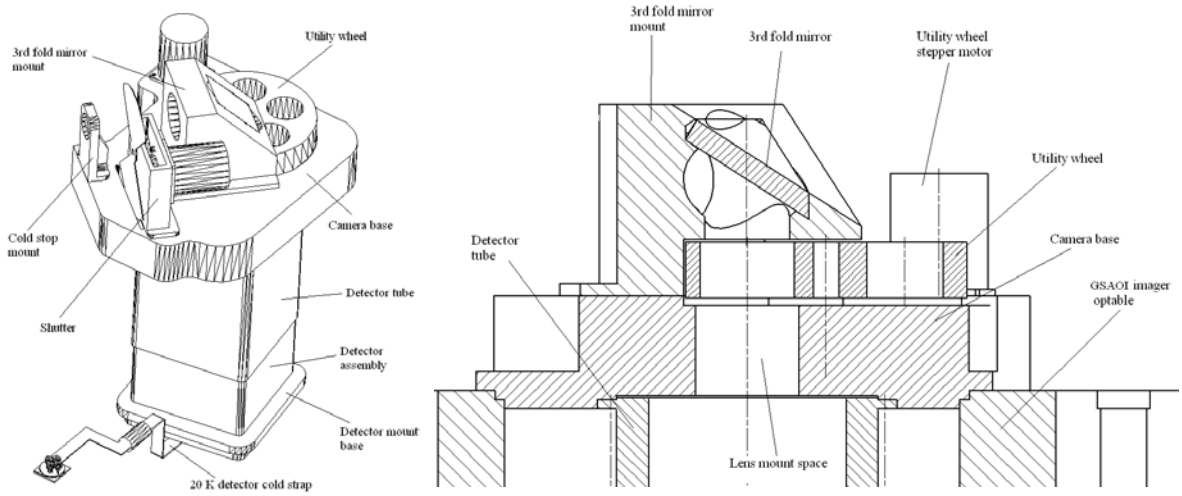

Figure 49: Utility wheel assembly shown in isometric and section view.

4.4.1.9 Imager Detector Mounting and Cooling System

The imager detector assembly is located within the front-right imager optable cell. It is fixed to the CWS plate through the detector mount base as illustrated in Figure 49. This location is dictated by the need to minimize the number of fold mirrors in the optical system. It results in the detector focal plane being parallel to the CWS plate, but the detector assembly is located within the sealed optable compartment. Access to the detector wiring and cold strap connection is restricted on the imager side of the CWS plate. However, a cut-out through the CWS plate will be used to gain access from the OIWFS side. This cut-out exposes the rear of the detector assembly and allows manual connection and disconnection of the detector flex-circuit cables and cold strap. The cut-out will also be used during alignment of the imager optics.

The imager focus will be set by inserting appropriate spacer-washers between the detector assembly and the detector mount base, and so axially repositioning the detector assembly.

4.4.1.10 Imager Detector Assembly

The imager detector assembly will be designed and fabricated through a subcontract to Gerry Luppino (GL Scientific) in consultation with RSAA. This approach has been used successfully in the design and fabrication of the RSAA Wide Field Imager 8k×8k CCD mosaic focal plane assembly.

An exploded view of the imager detector assembly is shown in Figure 50. It consists of a closed aluminum housing that carries the HAWAII-2RG (H2RG) detector mosaic, the detector focal plane mounting plate, the detector cold finger, and the detector motherboard.

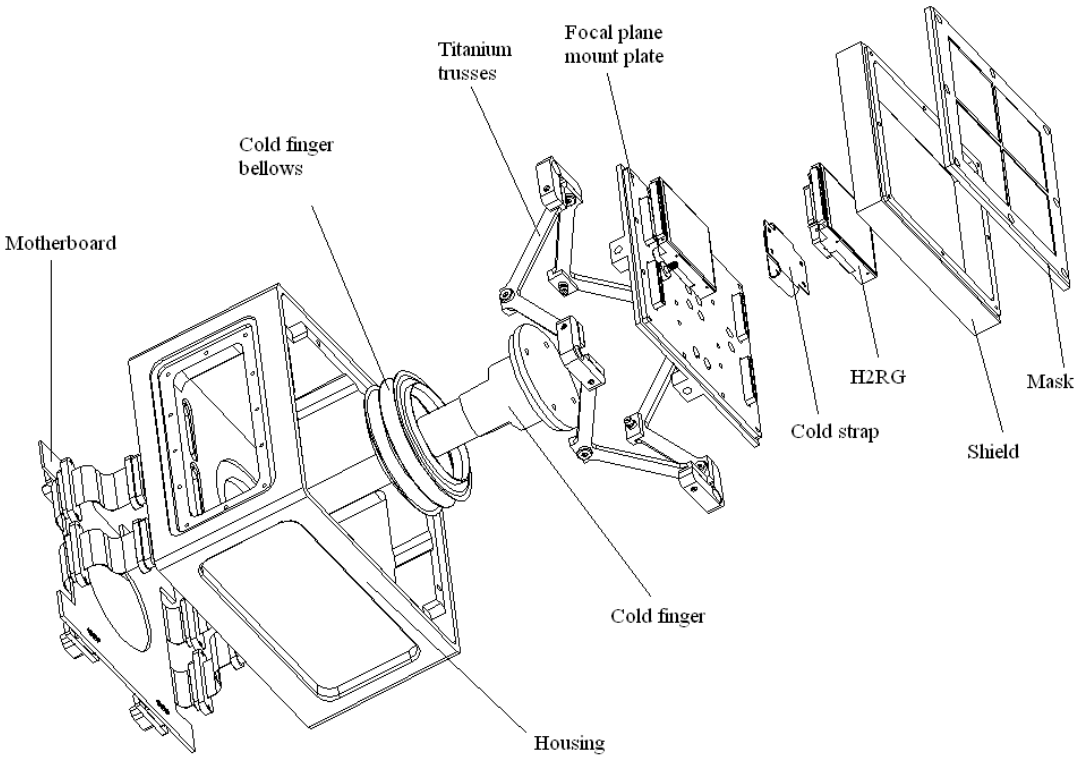

Figure 50: Exploded view of the detector assembly showing the detector and associated components (based on a concept design by Gerry Luppino; GL Scientific).

The array of four H2RG detectors is mounted onto a molybdenum mounting plate. The plate contains the 3-point mount holes (pin/slot/oversize-hole) for each of the detectors and a slot to provide access to each connector. Otherwise, the plate is light tight from the bottom side. Light-tight feed-throughs will be used to connect to the motherboard via flex-circuits. The detectors are then surrounded by a side shield that attaches to the mounting plate and forms a light-tight shield around the edges. The shield also serves as a platform for attaching the focal plane mask. This light baffle attaches to the top of the side shield. It serves to mask out various reflective components in the focal plane (bond-wires, parts of the MUX located beyond the active areas, etc.). Copper cold-straps are clamped to the detector package and to the focal plane mounting plate using molybdenum clamps. These straps are soldered to the clamps to form self-contained, 3-piece, modular units. The bottom piece of each strap unit is tapped and is pulled down onto the focal plane mounting plate from behind by two screws. The detectors are pulled down onto the plate by their invar stud/pins using nuts and Belleville washers. The precision hole/slot/oversize-hole for each detector enables the H2RG devices to be mounted in a pseudo-kinematic fashion.

The focal plane mounting plate is suspended from a titanium truss. This serves to thermally isolate the focal plane from the rest of the housing, allowing precise thermal control of the detectors (~ 10 mK) without having to control the housing temperature very precisely (~ 1 K). The truss attaches to the four corners of the upper portion of the detector housing. The truss structure is extremely stiff. Similar designs have shown sub-micron motion of the focal plane from flexure of the truss.

A cold finger makes thermal contact to the back of the focal plane mounting plate. The detectors are thermally connected to the focal plane mounting plate through the copper strap modules. A heater resistor and temperature sensors are buried in the cold finger. The cryocooler is attached to the cold finger by clamping a cold-strap fixture onto the cylindrical end of the cold finger using a bolted connection.

The cold-finger bellows serves to make the cold-finger assembly light tight where it pierces the low-background section of the focal plane housing. One end of the bellows is epoxied to the cold finger and the other end to the housing. The truss and focal plane are then mounted into the housing. This very compact design will be light tight, thus affording another level of protection against unwanted background illumination.

The detector housing serves as the mechanical reference point for the assembly. There are two regions of the housing: the upper, low-background region where the detectors are mounted and the lower cavity where the electrical motherboard and thermal control circuitry are located.

The motherboard is a rigi-flex board that has flexible portions that pass into the low-background region of the detector housing (using light-tight feed-throughs that are not shown) and mate to the connectors on the HAWAII-2RG devices. Any glow or other background problems from the motherboard and its components are isolated from the low-background region. If implemented, Application Specific Integrated Circuits (ASICs) will be mounted on the motherboard. Four 15-pin micro-D connectors then serve as the input/output attachments. A different motherboard will be used if ASICs are not implemented. Much larger connectors will then be needed, but these can be accommodated.

4.4.1.11 Baffling

A large part of the baffle system consists of conforming apertures cut in thin sheet metal, similar to the baffling system developed for NIFS. This system approaches as closely as possible to an infinite cavity system where scraper baffles surround the beam. Any scatter from the baffles enters the nearby infinite cavity and does not return to the optical system. The main baffle stack consists of U-shaped pieces of sheet metal with turned out bottom edges that attach directly to the imager optable walls and top surface as illustrated in Figure 51. Struts between the tops of the metal sheets stiffen the assembled structure so that it does not vibrate.

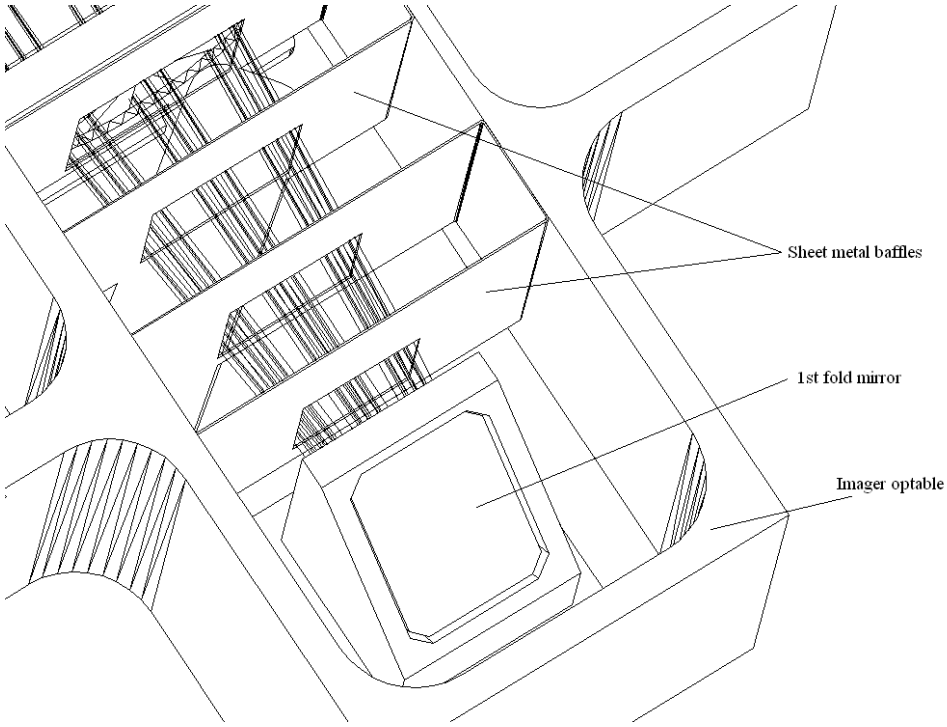

Figure 51: Sheet-metal baffles between the first fold mirror mount and the field lens mount viewed from the CWS plate side.

The cell-like structure of the optable also will serve to separate the detector from the incoming non-filtered light. The photon shield around the elements mounted on the outer face of the optable will further isolate the imager optics from possible scattered light leaks.

4.4.2 Mechanical Design – Telecentric Imager Layout

The non-telecentric output optical design may produce a ghost image from multiple reflections within the detector substrate. An alternative telecentric-output optical design has been considered to avoid this potential problem. In this section, the mechanical implementation of this alternative optical design will be addressed. The baseline mechanical design requires minimal modification to accommodate the alternative optical design (Figure 52).

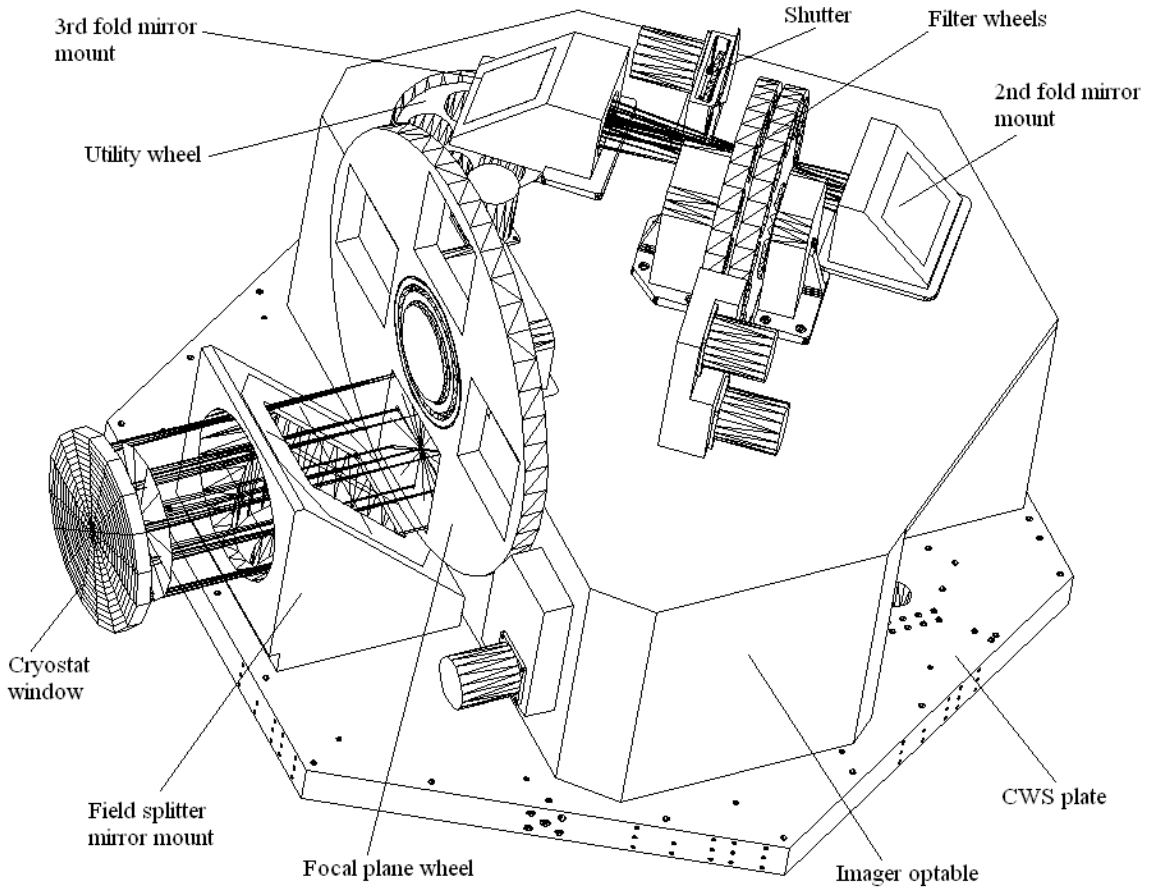

Figure 52: Telecentric imager layout in isometric view showing components on top of the optable.

Three fold mirrors are used in the same arrangement as in the non-telecentric layout. The only difference is the height of the second optical level; instead of being at 111.75 mm, it is at 36.75 mm from the top optable surface. Consequently, the filter wheel assembly and the cold stop are closer to the second fold mirror mount. The major impact of the telecentric layout on the mechanical design is evident after the cold stop. Due to the lower light-path folding, the detector assembly is now positioned within the CWS plate, as shown in Figure 53.

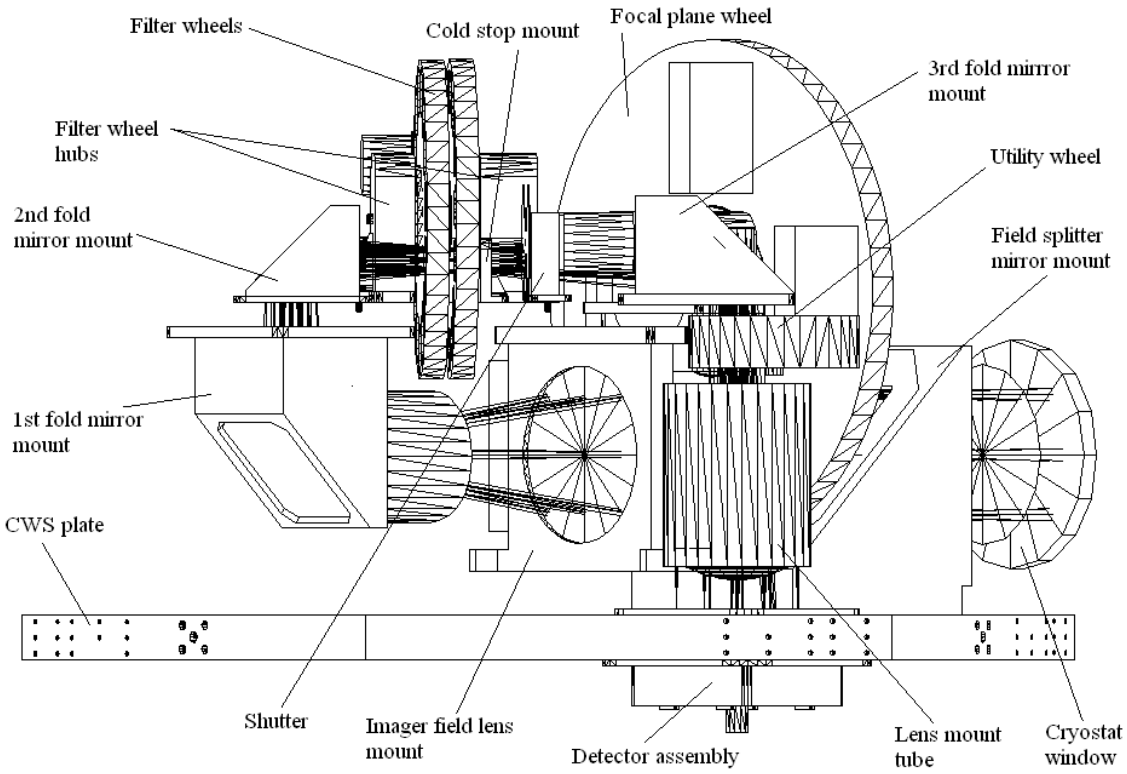

Figure 53: Telecentric imager layout in plane view without the optable being shown.

The utility wheel and its gear train are positioned within the top optable surface, while a lens-mount tube is fixed on the lower side of that surface (within the optable front-right cell). This mount tube carries a small telephoto lens on one end and a large field-flattener lens on the other. As in the non-telecentric layout, the detector is mounted from the CWS plate, so it is independent from the optics. The detector can be easily approached from the OIWFS side of the CWS to establish connection with the controller connectors and the cryocooler cold straps. It is also electrically isolated from its mount by fibreglass spacer washers.

The non-telecentric optical design has been chosen as the baseline design due to its superior optical performance.

4.5 OIWFS Mechanical Design

The GSAOI OIFWS is mounted from the CWS plate on the opposite side from the imager. This is the location of the science instrument in NIRI and NIFS. The field splitter on the imager side of the CWS plate separates the 107.2×107.2 mm square imager field from the circular 151.6 mm diameter input field, and folds the remaining field towards the OIWFS.

The beam path through the OIWFS elements is illustrated in Figure 54. After being folded by the field splitter mirror, the beam continues through an outer section of the field lens of the beam steering system. Cut-outs are provided in the second fold mirror mount disk to pass the beam. At the level of 304.6 mm from the CWS plate, the beam is folded for the second time and sent through outer sections of the beam steering system collimator lenses towards the steerable mirror. The steerable mirror reflects the incoming beam and sends it back through the same optical elements along the optical axis. The returning beam is then folded back towards the error sensing system field lens. It is folded again to be parallel to the CWS at the level of 78.3 mm, just before reaching the beam steering system field lens. The beam then passes

through the aperture wheel, error sensing system field lens, and the filter wheel, before it is reflected at 45° at the 3rd fold mirror towards the prism/detector module.

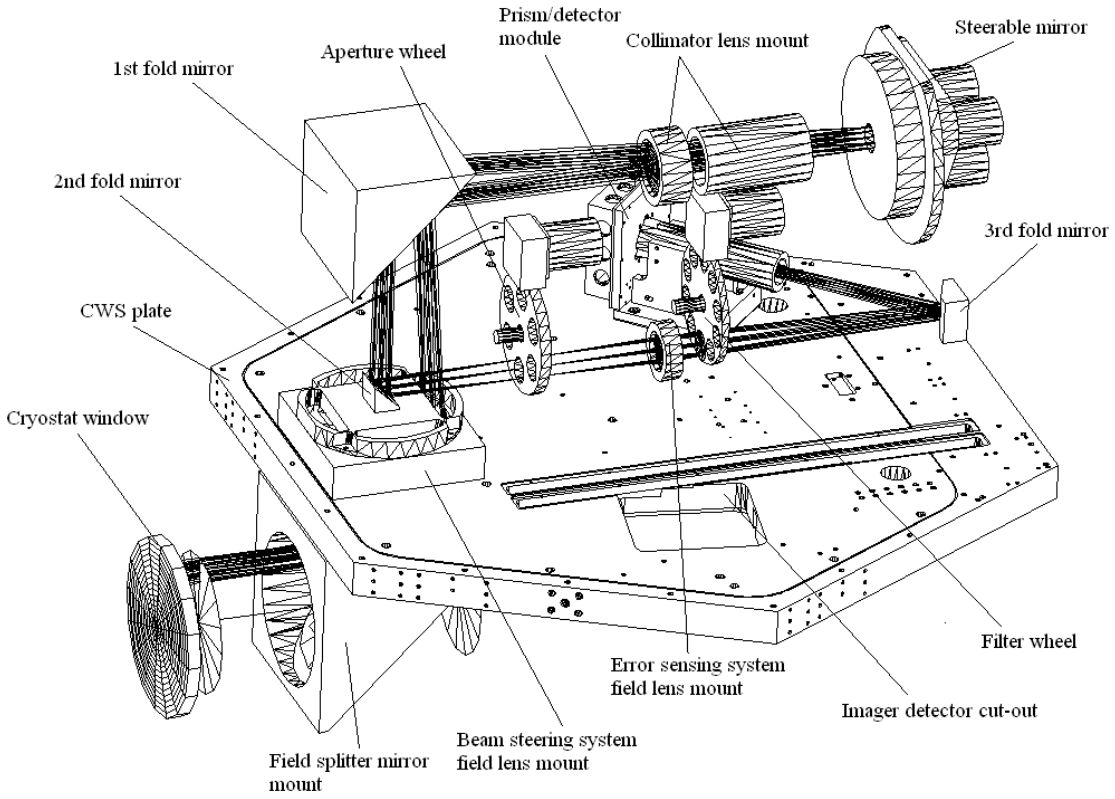

Figure 54: GSAOI OIWFS elements and assemblies within the optable (not shown). All OIWFS elements are mounted against the optable except the beam steering system field and the second fold mirror. This improves the system stability and minimizes its deflections.

4.5.1 OIWFS Optable

The OIWFS optable (Figure 55) will primarily serve to increase the stiffness of the overall instrument. It also acts as a photon shield and a support structure for the elements of the OIFWS. The only element that will be outside the optable is the steerable mirror, all other elements and assemblies are accessible after removing the optable and appropriate light-tight covers on the optable. The cell-like structure of the optable, similar to the structure of the imager optable, will serve to separate various levels of the light path and to provide support for mechanisms, mirrors, and lens mounts (Figure 56).

The OIWFS optable will not cover the whole area of the CWS plate. One side of the CWS plate will be free to allow direct access to the imager detector through an appropriate cut-out. This is necessary to allow proper alignment of the imager optics and for connecting the cold-straps and detector-controller cables to the imager detector.

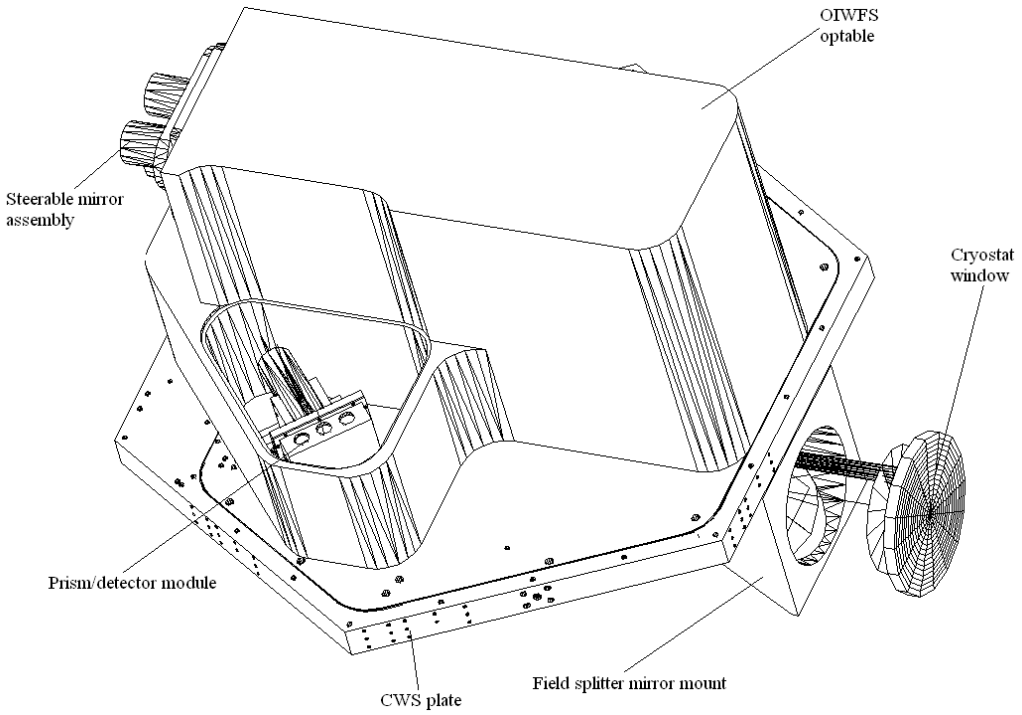

Figure 55: GSAOI OIWFS optable and prism/detector module.

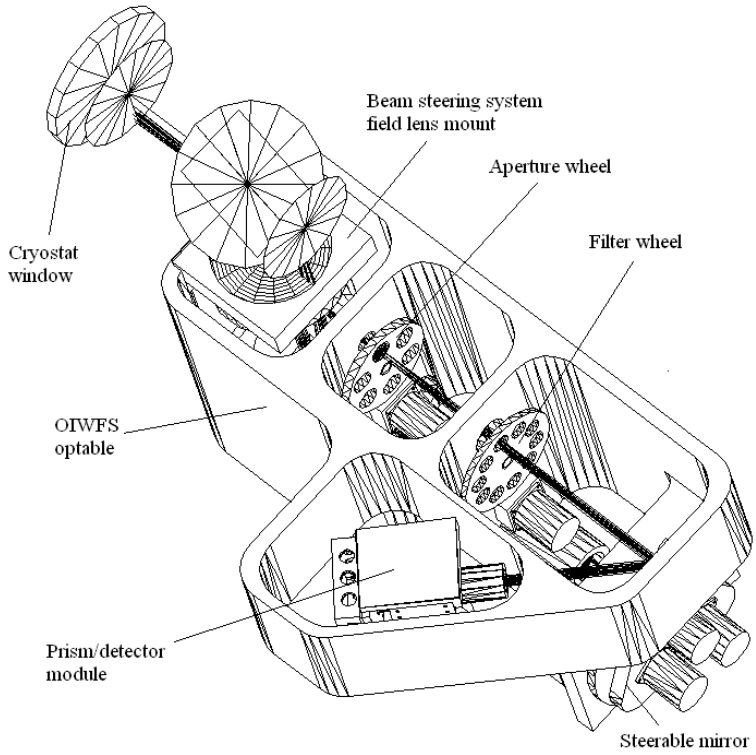

Figure 56: GSAOI OIWFS showing elements and assemblies mounted in the cell-like structure of the optable.

4.5.2 OIWFS Lenses

All OIWFS lenses will be mounted in close-fitting bores and spring loaded in a similar way to the imager lenses in order to accommodate contraction during cool down. All mounts will be supported against the optable walls or the CWS plate.

4.5.3 Fold Mirrors

The OIWFS optical system will be folded by five physical fold mirrors (including the steerable mirror).

The field splitter fold mirror and the first fold mirror (Figure 54) will be glass mirrors elastically mounted in aluminum mounts in a similar way to the imager fold mirrors. The other two fold mirrors, due to their size and position, will be made by diamond turning. This is similar to the fold mirrors in NIFS.

4.5.4 Steerable Mirror Mechanism

Guide stars are selected by driving the steerable mirror in tip and tilt. Once selected, differential movement between this star image on the OIWFS detector and the field image on the imager detector is required to be less than 0.002″ over periods of one hour. The steerable mirror must be extremely stable in its set position to achieve this.

One design option for this device would be to adapt the gimbal mechanism used for the same purpose in NIRI and NIFS. Changes to accommodate the different beam size and scan range are feasible. However, this system has an asymmetric drive system, so flexure in the structure causes mirror tilt as attitude changes. Analysis indicates that stiffening is needed in order to meet the stability requirement.

An alternative mechanism is therefore proposed that features three drive axes arranged in a circularly symmetric pattern. This circular symmetry means that the mirror is intrinsically free from tilt induced by gravitational flexure of the structure.

A conceptual design of this system is shown in Figure 57. The mirror and its mounting plate are suspended from the base plate by means of a thin flexure ring that provides rigid radial location, but is flexible in tip and tilt. The center of gravity of the suspended mass is located in the plane of the ring. This suspension ring also preloads the plate against three equally spaced lead screws. The lead screws are engaged with rigidly mounted nuts at one end, and with preload nuts carried in axially flexible diaphragm cells at the other. A drive gear is mounted to the end of each lead screw by means of a spring-loaded clutch, and this is driven by a pinion on the stepper motor shaft. The lead screw and gear move axially as they rotate, so tilting the mirror plate. Movement of the three lead screws is coordinated so that the center of the mirror does not move axially.

Each lead screw is equipped with a stop that limits travel in the retracting direction. To calibrate the system, all three screws are retracted until the end stops engage and the clutches slip. The motors are then stopped with all three lead screws in a known position, and reversed by a fixed number of steps to establish the datum condition. Hall-effect sensors are used to monitor the process. The end stops are arranged to apply stalling force circumferentially rather than axially, so providing a clearly defined angular stopping position without loading the threads, and allowing drive reversal without risk of jamming.

The collimated beam projected onto the mirror has a diameter of 26 mm. The mirror must be tiltable by ~ 2° to capture guide stars from the edge of the MCAO field. The lead screws have a thread pitch of ~ 1 mm, and are placed on a pitch circle radius of ~ 80 mm. The required lead screw travel is ~ 7 mm. The travel to displace an image on the imager detector by 1 pixel is ~ 1 μm, which corresponds to ~ 1 full step of the drive motor. The stability requirement is ~ $1/10^{th}$ of this. With the motor running at a speed of 200 rpm, the time taken to travel the full field diameter is ~ 13 sec.

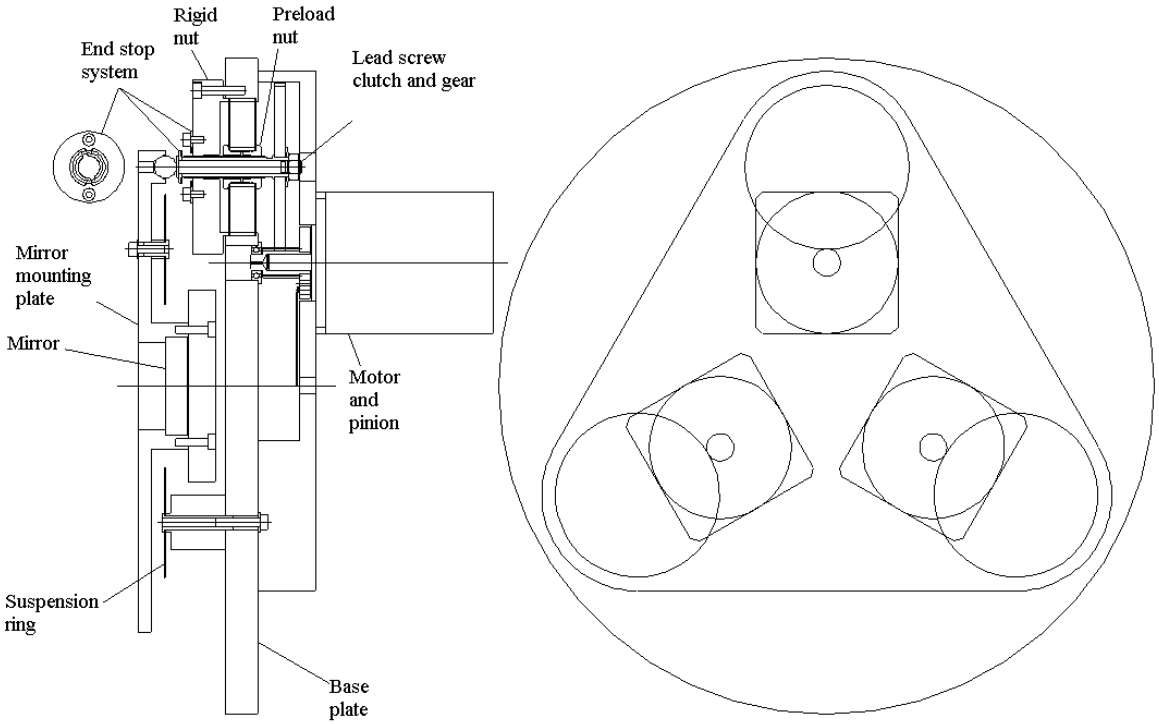

Figure 57: Steerable mirror concept design.

4.5.5 Aperture Wheel

The six position OIWFS aperture wheel will contain a selection of OIWFS field-defining apertures. The contents of the OIWFS aperture wheel are listed in Table 31. These apertures match the centered 8×8 pixel and the offset 40×40 and 80×80 pixel windows read out by the NIRI-duplicate OIWFS Detector Controller software.

Table 31: OIWFS Aperture Wheel Contents

Position	Content
1	Clear
2	0.52″ diameter circular aperture
3	2.6″ offset square aperture
4	5.2″ offset square aperture
5	Spare
6	Blocked

The OIWFS aperture wheel mechanism will be similar to the imager filter wheel mechanism and NIFS mechanisms. It is driven by a two-stage gear train with a gear transmission ratio is 75:1, which makes the 150 mm diameter wheel have a positional repeatability of 0.021 mm (0.002″) and a full revolution time of 22.5 s.

4.5.6 Filter Wheel

The ten position OIWFS filter wheel will contain standard broad-band filters that are 25 mm in diameter. These are listed in Table 32.

Table 32: OIWFS Filter Wheel Contents

Position	Content	λ_c (μm)	$\Delta\lambda$ (μm)
1	Clear	...	...
2	*Z*	1.010	0.220
3	*J*	1.250	0.180
4	*H*	1.650	0.290
5	*Ks*	2.145	0.310
6	*K*	2.200	0.330
7	*ZJ*	1.120	0.440
8	*HK*	1.935	0.860
9	Blocked	...	...
10	Spare	...	...

The OIWFS filter wheel mechanism will be similar to the imager filter wheel mechanism and mechanisms in NIFS. The shaft will be fixed to a boundary wall between the second and third optable cell. The wheel will be driven by a two-stage gear train and a cryogenic stepper motor. The gear transmission ratio is 75:1, which makes the 150 mm diameter wheel have a positional repeatability of 0.021 mm and a full revolution time of 22.5 s. The filter wheel is the entrance to an otherwise light tight cavity containing the detector. For this reason, the region of the OIWFS optable above the filter wheel, which contains the upper layer of beam steering optics, will be completely sealed off by a light-tight separator.

4.5.7 Baffling

Baffling of the OIWFS beam will be achieved using sheet metal baffles, similar to the baffling of the imager. The collimator lenses will be carried in the mount tube, which will also serve to baffle the steerable mirror. Light-tight separators, supported against the optable walls, will seal off the beam steering optics from the error sensing optics. This will be applied to all three optable cells. Baffling of the first optable cell (in the vicinity of the 2nd fold mirror) will be carried out with the greatest attention since it contains both the incoming and returning beam from the steerable mirror.

4.5.8 OIWFS Prism/Detector Module

A HAWAII-1 detector will be used in the OIWFS. This is the same detector used in the NIRI and NIFS OIWFSs. Therefore, the same detector mount will be used. Some minor redesign is necessary to the camera barrel in order to mount new camera lenses and the four-facet Shack-Hartmann prism. The prism/detector module will be located in a separate optable cell from the rest of the OIWFS elements. It will be placed under a light-tight cover and firmly bolted to the CWS. This simplifies the alignment and focus adjustment procedures and ensures a low-background environment for the detector.

4.6 Instrument Alignment

The process of optical aligning is complicated by the fact that the system is folded. Lenses must be aligned to an optical axis that is itself displaced by reflections, and therefore subject to alignment error. The basic principal adopted here is that fold mirrors are fixed in position, but adjustable in orientation, and that lens groups are fixed in orientation and axial position, but adjustable in radial position. In turn, each mirror will be adjusted to square the reflected optical axis to the following lens cell, and each lens cell will be adjusted to center it on the reflected axis.

The two types of adjusting mechanism are shown generically in Figure 45 and Figure 46. Mirrors are supported in three-point kinematic mounts. One of the three points is set to a design position, and the other

two are used for adjustment. Lenses are accurately registered within carrier cells that can be shifted radially on a fixed mounting face.

4.6.1 Imager Fold Mirror and Lens Cell Alignment

Alignment of the GSAOI imager mirrors and lens cells is based around a Taylor-Hobson alignment telescope and associated alignment equipment. This section describes the alignment method; a more detailed step-by-step alignment procedure will be developed as the project matures. Most of the alignment equipment and methods used here are described in "Optical Alignment" by R. H. Dagnall & B. S. Pearn (1967; TS 513.D27). The alignment process is shown schematically in Figure 58. Similar procedures are routinely used at RSAA for the alignment of telescopes and instruments.

Alignment begins by mounting the Taylor-Hobson telescope on the window trunnion support. The window trunnion support is a rigid cover that mounts over the cryostat window to allow flexure testing about the optical axis. It also serves as a reference surface during the alignment process. The telescope is squared to the window trunnion support by auto-collimating it from a reflective target. The telescope must be square to < 50 μrad with respect to the trunnion support mounting face to match the Gemini telescope alignment tolerance. Dagnall & Pearn (1967) note that a good operator can square the telescope to within 10 μrad by auto-collimation. The assembled trunnion support and Taylor-Hobson are then fitted to the GSAOI cryostat.

A Taylor-Hobson mirror target and lamp house is now accurately centered and seated off the conical lens seat of the imager field lens cell. The Taylor-Hobson telescope is then used to measure center error with the Taylor-Hobson coupled micrometers and tilt error via auto-collimation. Errors in center and tilt are corrected by X-Y adjustment and or tilt machining. The first fold mirror is now assembled and the Taylor-Hobson target moved to the second lens cell in the optical train. The first fold mirror and the second lens cell are now squared and centered by iterative X-Y shifts and auto-collimation. This process accurately squares the first fold mirror and aligns the second lens cell in tilt and center. This alignment process is progressively repeated for all subsequent mirrors and lens cells. For longer lens barrels, a semi-transparent Taylor-Hobson target will be placed at either end of the barrel to square the entire barrel (see Dagnall & Pearn 1967). Finally, a Taylor-Hobson target is placed at the center of the detector housing. This is then centered and squared to the optical axis.

The cold stop is also aligned to the optical axis during this process. This ensures that the imager cold stop will be accurately aligned with the MCAO exit pupil. The cold stop must then be rotated 22.8º to accommodate the tilted MCAO pupil. The orientation of this tilt defines a unique orientation in which GSAOI must be mounted relative to MCAO on the ISS.

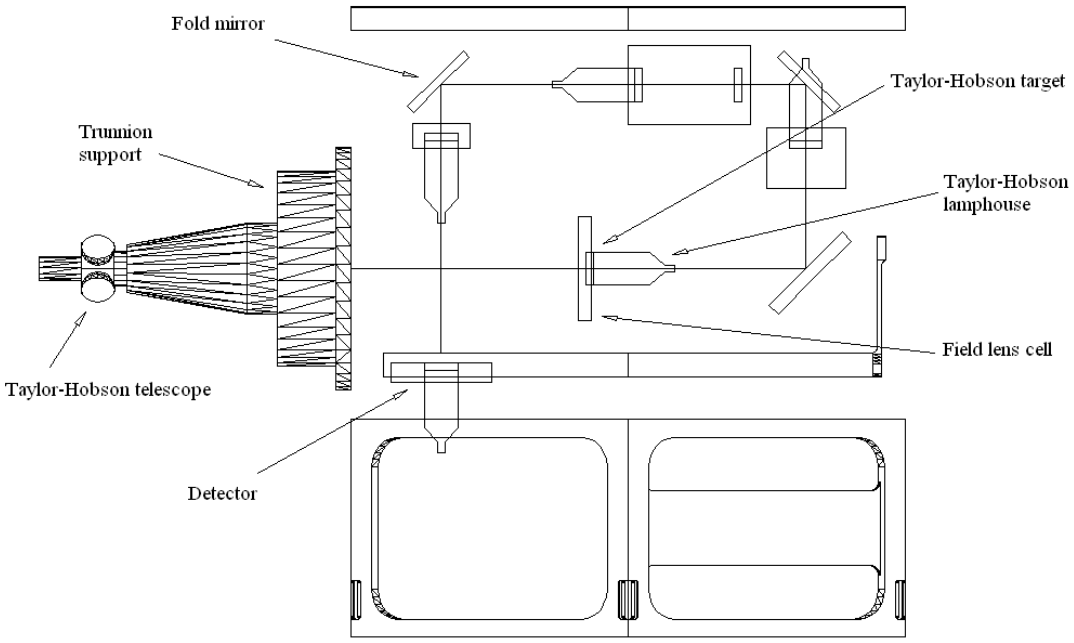

Figure 58: Progressive lens cell and fold mirror alignment.

4.6.2 Imager Lens Alignment

After the imager fold mirrors and lens cells have been aligned, the lenses will be inserted and a polarising alignment interferometer will be used to verify lens alignment for the imager. This alignment instrument mounts outside the cryostat on the trunnion support. The alignment method is based on ideas by Hopkins (1976, Opt. Eng., Vol. 15 No. 5).

The alignment system uses a polarised laser, spatial filter, polarising beam-splitter cube, 50 mm diameter collimation lens, and a tilted quarter-wave plate to pass plane-parallel polarised wave fronts into the optical system. These wave fronts reflect off the curved optical surfaces in the imager optics, pass back into the interferometer, and are reflected out of the optical system by the beam-splitter cube onto a small CCD camera. This camera records circular fringes formed by wave-front interference between each pair of curved surfaces. A black card is placed behind the first lens group in the system and the first lens cell is aligned in X-Y and tilt to return concentric fringes. The black card is then moved progressively further along the optical axis behind the next lens group, and this group is in turn checked for tilt and X-Y center and moved or machined to correct these if necessary. One important feature of this alignment method is that it will work when the imager is both hot and cold. The instrument will be used as GSAOI is cooling to check for temperature-induced misalignment, black painted blanks in the filter wheel and utility wheel will allow three parts of the optical system to be isolated progressively. Many concentric circles will overlap when the complete optical system is tested.

4.6.3 OIWFS Alignment

Alignment of the GSAOI OIWFS is a more complex task than for the imager. It requires both centered and de-centered alignment procedures. The Taylor-Hobson alignment equipment and methods that were described for the imager alignment will also be used for the OIWFS.

Centered alignment of the OIWFS begins by temporarily replacing the pierced fold mirror in the field splitter mount with a full mirror. A Taylor-Hobson reflective target and illuminator is now placed in the

beam steering system field lens cell and the field splitter mount and the field lens cell are centered and squared. The first fold mirror and collimator cell are now inserted with Taylor-Hobson targets mounted at either end. The fold mirror and collimator cell are then squared and centered. The steerable mirror is now inserted and is auto-collimated back to the Taylor-Hobson. This mirror position is recorded (as stepper motor steps from the datum position for the three motors) for later use. When centered alignment is complete, the pierced field splitter mirror, field lens, and collimator lenses are inserted in their cells.

De-centered alignment begins by offsetting the Taylor Hobson mount by 62 mm on the window trunnion support and re-squaring it to the trunnion support face. This allows the Taylor-Hobson to look into the OIWFS off one of the four quadrants on the field splitter mirror. The steerable mirror is now tilted to allow the Taylor-Hobson to see a centered target placed in the aperture wheel. The Taylor-Hobson target is now moved to the error sensing system field lens mount, and this is centered and squared. The Taylor-Hobson target is then moved to the Shack-Hartmann optics, and it and the intervening fold mirror are centered and squared. Lastly, the target is moved to the OIWFS detector mount, and this is centered and squared.

4.6.4 Focus Testing - Focus Coincidence

Both the GSAOI imager and OIWFS will be constructed without focus mechanisms. An external star projector will be used to measure initial defocus and verify that the foci are ultimately coincident. This focussing process will take place over several cool downs. The external star projector is a 1:1 re-imager and attaches outside the cryostat window. A pinhole target is carried on an X, Y, Z stage at the outboard end of the projector and an *H* band LED source illuminates this pinhole. This projector has already been designed by RSAA for aligning NIFS. It is currently being manufactured. The following test is performed cold and adjusted during the ensuing warm-up.

The imager focus is tested by mounting the window trunnion support on the GSAOI cryostat, and then mounting the external star projector on the trunnion support. This assembly is shown in Figure 59. The cryostat window assembly is under the window trunnion support. An *H* filter is now selected in the imager and alternate images are recorded of the projected spot from the external star projector and an illuminated pinhole in the GSAOI focal plane wheel. The star projector is used for the pinhole illumination by simply removing the pinhole carrier slide in the star projector. These images are compared. If the imager focal plane wheel pinhole is out of focus, the star projector pinhole is moved axially until alternate image pairs produce the same spot size (FWHM). Now the star projector pinhole is moved axially until it is in focus. The difference in axial positions of the pinhole gives the refocus direction and distance at the focal plane wheel. To first order, the focus adjustment required at the imager detector is 0.49 times the calculated axial distance. The actual refocus distance will be found by ray tracing and optimising for best focus. Lastly, a Hartmann mask in the star projector will be used to verify focus position when both the imager and OIWFS are near correct focus. This external Hartmann mask can be rotated to any angular position allowing both systems to be checked for astigmatism. This system will be used for a final aberration check of both optical systems.

The GSAOI OIWFS will be focussed by a similar procedure using the external spot projector. However in this case, the spot projector will be decentered by 62 mm on the window trunnion support to place the projected spot over one of the four quadrants of the field splitter mirror. The OIWFS is now focussed to the axial value of the external star projector that gives the best imager focus. This process ensures that both the imager and its OIWFS have co-incident foci when it is placed on the Gemini telescope.

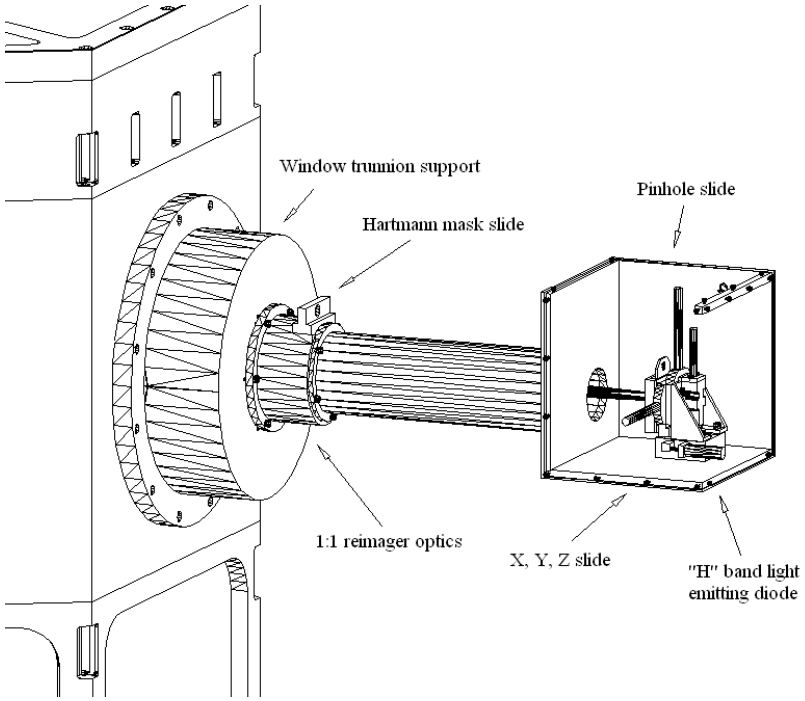

Figure 59: External star projector.

4.7 Flexure Analysis

Flexure is dealt with separately for the bulk structure and local mechanisms because different techniques are used to control it. The modelling of the bulk structure is relatively simple. Even where complex geometry prevents the use of algebraic analysis, numerical (FEA) methods can be applied. By contrast, the stability of mechanisms involves the additional factor of joint behaviour that is difficult to quantify.

4.7.1 Bulk Structure

4.7.1.1 Flexure Model

Differential flexure between the imager and the OIWFS was identified as a key mechanical issue of the GSAOI. A flexure model is developed to assess this differential flexure. This model estimates individual flexures of all mechanical elements and also takes account of their interactions as part of a complete system. The flexed element positions were input into the Zemax ray tracing program to transform the individual flexures to image offsets at the imager and OIWFS detectors for each of the scenarios considered. The absolute values of the two image offsets were then subtracted. This gives the maximum differential flexure between the imager and OIWFS for the adopted scenario.

Flexure is investigated for the preferred non-telecentric imager and OIWFS in two worst-case scenarios. These scenarios are characterized by their different orientations of the imager and OIWFS optables. It is hypothesized that while in compression (gravity vector perpendicular to the CWS plate) movement of the optables can induce only negligible flexure to the elements that are mounted on them. However, when the gravity vector is parallel to the CWS plate, the optables will have maximum sag due to flexure. Consequently, the two worst case scenarios are identified when the gravity vector is parallel to the CWS plate and parallel or perpendicular to the cryostat window optical axis.

4.7.1.2 Flexure Performance

The flexure requirement is that differential image movement between the imager and OIWFS detectors must be < 0.1 pixels at the imager detector (i.e., < 1.8 μm). The first step in assessing differential image movements between the two detectors is to estimate the mechanical flexures of all relevant elements in the system. Standard beam and plate theories and numerical simulations (predominantly FEA) were applied to determine these mechanical flexures.

The results are presented in Table 33 and Table 34. Individual deflections of the elements are listed in local (Zemax) coordinates (i.e., a right-hand coordinate system with the Z-axis always along the optical axis and pointing towards the detector and the Y-axis pointing upwards). The α, β, and γ rotations listed in the tables are rotations about X, Y, and Z axes, respectively. Empty cells have zero values. The values in the first table rows (marked with a asterisk) represent deflection of the imager and OIWFS optables. These deflections are incorporated into the individual deflections of the elements since most of the elements are in contact with optables on both sides of the CWS plate. In the case of the OIWFS optable, deflections of 0.3 and 0.15 μm were calculated for the upper and lower sections of the optable, respectively.

Finally, deflections in the Z direction were not taken into account since they do not contribute to lateral image movements.

It can be concluded that the flexure budget requirement is fulfilled for both of the flexure scenarios investigated.

It is obvious that the flexure of the fixed instrument components can contribute little to the differential image movement. Even if such deformation existed in the system, it could have been easily minimized by improving the stiffness of the problematic component. However, a significant contribution to the image movement can be induced by deformations of an optical element, which is, by its functionality, a kinematic, rather then a static component. It is clear that the steerable mirror is the only element in the instrument that matches this description. Steerable mirror tilt oscillations due to mechanism flexures could have influence on the lateral image movement at the OIWFS detector. In other words, a steerable mirror tilt of ±1 arcsec would move the image on the OIWFS detector by 1.8 μm (i.e., 0.1 pixel). When this is translated to a positional (axial) error of the threaded drive shafts, the resulting shaft displacement is ±0.4 μm. Although, this is an extremely small positional tolerance, it is estimated to be achievable since the new symmetric steerable mirror mechanism design is effectively free of any flexure as long as the sufficient pre-load force is applied to the shafts.

Table 33: Mechanical Flexure - ***Scenario 1 (gravitational vector parallel to the window axis)***

Imager Mechanical Flexure						
Component	**Translation [μm]**			**Rotation [μrad]**		
	X	**Y**	**Z**	**α**	**β**	**γ**
Imager Optable			**0.43***			
Field Lens Mount			0.53	1.19		
1st Fold Mirror			0.45	0.1		
1st Lens		-0.44				
2nd Fold Mirror	0.28		-0.345	0.1		
2nd Lens (Doublet)	0.3		-0.345			
Cold Stop	0.28		-0.33			
3rd Lens (Doublet)	0.28		-0.33			
3rd Fold Mirror	0.28		-0.33		0.67	
Utility wheel lenses	0.28	0.33				
4th Lens	0.28	0.33				
Detector Assembly					0.386	
Detector Image Movement	0.0	0.0	N/A			

OIWFS Mechanical Flexure						
Component	**Translation [μm]**			**Rotation [μrad]**		
	X	**Y**	**Z**	**α**	**β**	**γ**
OIWFS Optable			**0.3&0.15**			
Field Splitter			0.01	0.16		
Pupil Imager Lens						
1st Fold Mirror			0.3			
Collimator Lens 1			0.3			
Collimator Lens 2			0.3			
Steerable Mirror			0.3			
2nd Fold Mirror						
Pupil Relay Lens			0.15			
3rd Fold Mirror			0.15			
Prism/Detector Module	-0.1		-0.1			
Detector Image Movement	-0.1	0.0				

Differential Image Movement	0.1	0.0	N/A			

Table 34: Mechanical Flexure - *Scenario 2 (gravitational vector perpendicular to the window axis)*

Imager Mechanical Flexure						
Component	**Translation [μm]**			**Rotation [μrad]**		
	X	**Y**	**Z**	**α**	**β**	**γ**
Imager Optable	**0.43***					
Field Lens Mount	-0.43					
1st Fold	-0.45					
1st Lens	-0.44					
2nd Fold Mirror	-0.33		-0.3	0.1		
2nd Lens (Doublet)	-0.35		-0.3			
Cold Stop						
3rd Lens (Doublet)	-0.33		-0.28			
3rd Fold Mirror	-0.33		-0.28		0.67	
PV lenses	-0.33	0.28				
4th Lens	-0.33	0.28				
Detector Assembly	-0.6	0.71			0.386	
Detector Image Movement	-0.6	0.71	N/A			

OIFWS Mechanical Flexure						
Component	**Translation [μm]**			**Rotation [μrad]**		
	X	**Y**	**Z**	**α**	**β**	**γ**
OIWFS Optable	**0.3&0.15**					
Field Splitter	-0.01					
Pupil Imager Lens						
1st Fold Mirror	-0.3					
Collimator Lens 1	-0.3					
Collimator Lens 2	-0.3					
Steerable Mirror	-0.3					
2nd Fold Mirror						
Pupil Relay Lens	-0.15					
3rd Fold Mirror	-0.15					
Prism/Detector Module	0.1		-0.1			
Detector Image Movement	0.1	0.0				

Differential Image Movement	0.1	0.0	N/A			

4.7.2 Mechanisms

The bulk structure of the instrument is used to support a number of local mechanisms. These include lens modules, tilt-adjustable mirror modules, and the steerable mirror unit. In general, flexure within the elements of the mechanisms is readily calculated, but uncertainties remain because joint behaviour is difficult to model. Tilt errors resulting from these movements can be serious, but they can also be annulled by making the mechanisms circularly symmetrical. This is the approach proposed for the GSAOI mechanisms.

This is demonstrated in the preliminary design presented for the steerable mirror mechanism (§4.5.4), which is the most demanding mechanism involved. Tilt-adjustable mirror mounts will likewise be arranged to place the center-of-gravity coincident with the center of a kinematic mounting system. Lens mounts will also be circularly symmetrical.

4.8 Instrument Integration

Figure 60 shows GSAOI ready for attachment to one of the side-looking ports of the ISS. The overall dimensions and mass of the assembled instrument are the same as for NIRI; length 2400 mm, width 3300 mm, height 1300 mm, and overall mass 2000 kg. The top part of the integration frame will lie just below the primary mirror cell when the instrument is attached to a side-looking port of the ISS. The instrument will be transported to the ISS on a scissor lift air pallet (ICD 1.5.3/1.9, Dwg 89-GP-1000-6100). One of the four instrument interface pads that locate the instrument on the integration frame trolley can be seen on the lower rail of the integration frame in Figure 60.

The large integration frame is at the center of Figure 60. This frame carries the thermal enclosure support frames, which in turn carry the two thermal enclosures. The ISS interface plate is shown at the lower left of Figure 60. The integration frame attaches to this plate and in turn to the ISS. Ballast weights will be attached to the integration frame to bring the instrument to the Gemini-specified mass of 2000 kg and moment of 20 kNm (ICD 1.5.3/1.9, p. 4). The patch panels from where connections to the cryostat are made are shown on the lower inside faces of the thermal enclosures. These are readily accessible even when the instrument is on the telescope. The hexagonal cryostat is mounted from the ISS interface plate. The cryostat houses the GSAOI imager in its upper part and the OIWFS in its lower part. One of the two helium cryocoolers can be seen protruding from the cryostat. The SDSU-2 controller for the imager detector can be seen just below the helium cryocooler.

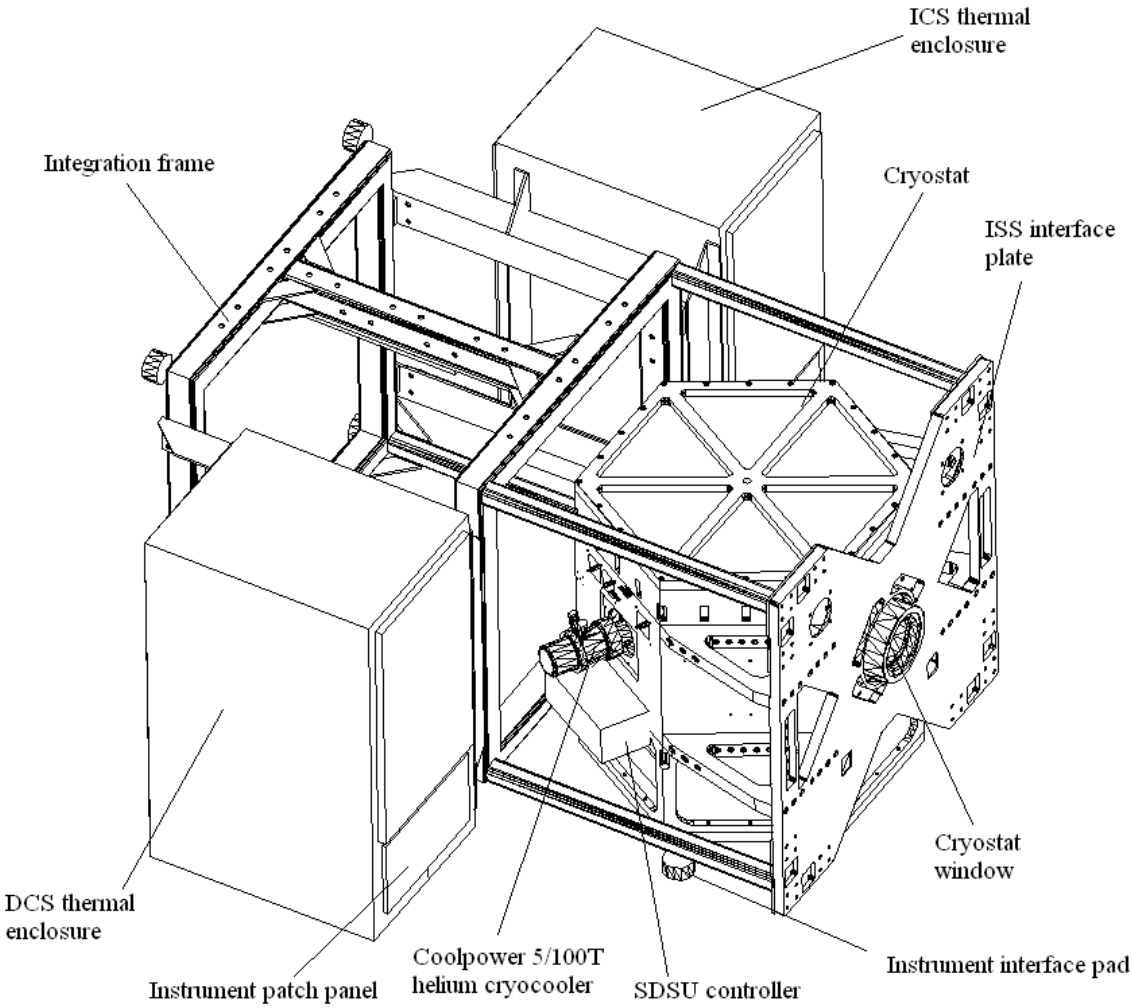

Figure 60: Complete GSAOI assembly ready for attachment to a side-looking port of the ISS.

4.9 Handling Procedures

RSAA will build a wheeled handling trolley for GSAOI. This trolley facilitates the integration of the GSAOI cryostat and integration frame both at the RSAA and in the Gemini South instrument preparation laboratory. The frame is designed to carry the integrated instrument from the instrument preparation laboratory, via the dome elevator, to the dome floor for attachment to the ISS. This trolley measures 1700×1300×300 mm and will be identical to the trolley supplied to Gemini North with NIFS. This trolley is detailed in the NIFS drawing No 89-ANU-4250-0409 and is shown in Figure 61.

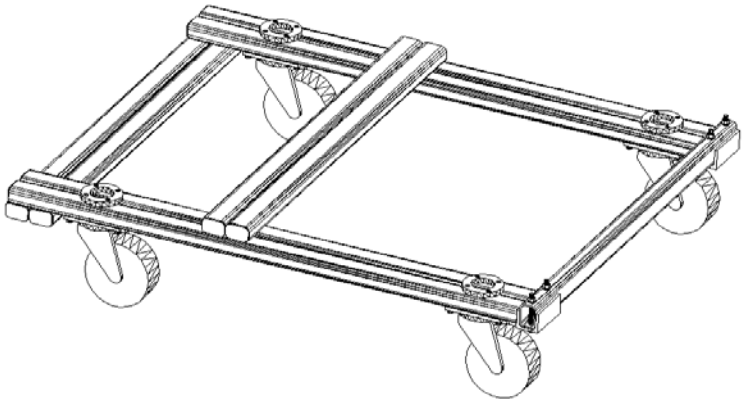

Figure 61: GSAOI integration frame trolley.

RSAA will build a wheeled hydraulic handling trolley to carry the GSAOI cryostat during instrument integration both at the RSAA and in the Gemini South instrument preparation laboratory. This trolley will be identical to that supplied by RSAA with NIFS. This trolley is detailed in the NIFS drawing No. 89-ANU-4250- 444, and shown in Figure 62.

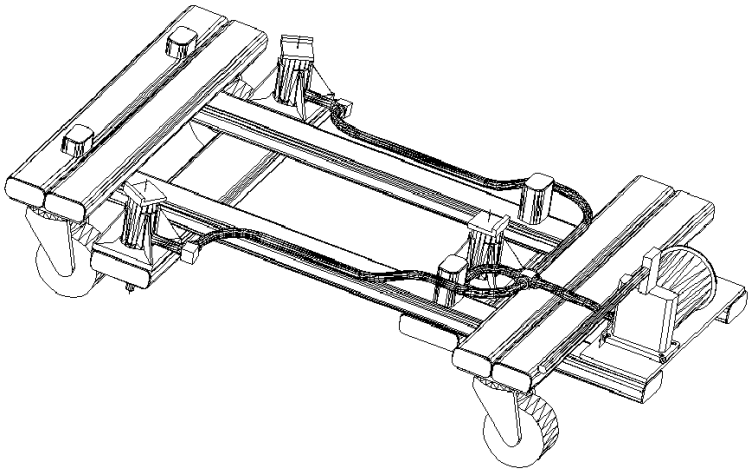

Figure 62: GSAOI cryostat hydraulic handling trolley.

Both of these trolleys will be delivered to Gemini South with the GSAOI instrument. Most of the remaining handling equipment required to integrate and service GSAOI, such as overhead hoists, are already in the Gemini South dome.

Due to the limited overhead space in the RSAA workshop, the instrument will be integrated in the horizontal position. This is also the most convenient way to handle the cryostat during routine servicing at the telescope. Figure 63 shows the assembly method.

The integration frame is carried on the integration frame trolley located under an overhead crane. This trolley has an open center with a removable front cross bar. This leaves the area under the cryostat free to the floor for the cryostat trolley to enter. The hydraulic jack pads on the cryostat trolley will allow the cryostat to be raised or lowered a few millimeters for levelling and alignment. To install the cryostat in the

integration frame, nylon slings are attached to four points on the center section. Next, the 600 kg cryostat is lifted 110 mm from the trolley and is passed through the open end of the integration frame with 20 mm vertical clearance. The cryostat will need to be rotated a little as it passes through the frame, and the frame moved sideways a little to clear the outboard ends of the helium cryocoolers. The cryostat trolley is now passed under the integration frame, with just a few millimeters clearance, and the cryostat is lowered back onto the trolley. This places the cryostat on its trolley inside the integration frame and at the right height for attachment to the ISS interface plate. Finally, the ISS interface plate with attached brackets is lifted into position using the overhead crane. All three heavy components are now brought together and attached. This completes the assembly of the large components.

When assembled, the cryostat window housing protrudes throughout the ISS interface plate. The environmental cover (not shown in Figure 63) is now attached to the protruding housing. The environmental cover cannot pass through the hole in the ISS plate so it must be the last of the large components to be assembled.

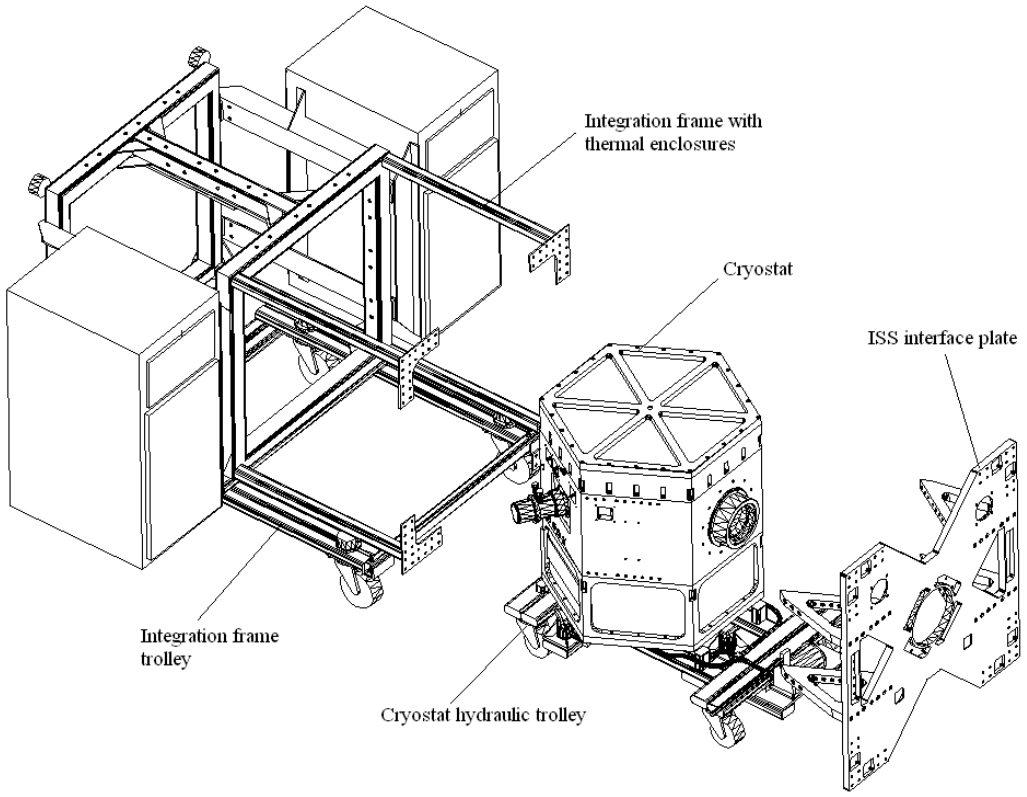

Figure 63: Integrating the complete 2000 kg instrument in the horizontal position.

4.10 Mechanical Design Risks

4.10.1 Lens Mounting Method

The lens mounting method provides accurate lens alignment by confining lenses within close-fitting mount cells, which are positioned in precision housing bores. The fits between lenses and mount cells are arranged to be near zero at the cryogenic operating temperature. The differential thermal strain characteristics of the lens and cell materials ensure that clearance will exist. During cool down, however, it is possible that temperature lag in the lenses will cause an interference condition to develop, resulting in lens damage.

This lens mounting method will be used in NIFS. The first trial will be during the second NIFS cool down in September 2002.

4.10.2 Steerable Mirror Development

Implementing a new mechanism for the OIWFS steerable mirror is a schedule and budget risk. The benefit of a stiffer and more reliable mechanism makes this risk acceptable. The risk will be mitigated by developing the mechanism early in the design phase. This will be tested as soon as the GSAOI cryostat becomes available.

5 Detector Control Systems

5.1 Introduction

GSAOI has two detector control systems (DCSs): one for the imager and one for the OIWFS.

The imager detector hardware provides the low temperature (60-90 K), high stability (±1 mK), low flexure (< 0.1 pixel per 15° change in attitude), and low background environment in which to safely mount and optimally readout the imager 4096×4096 pixel detector consisting of a mosaic of four Rockwell HAWAII-2RG (H2RG) HgCdTe/CdZnTe Molecular Beam Epitaxy (MBE) devices. These detectors will be read out in less than 10 s with exposure times from 5 s to 10,000 s. Fixed-format regions of interest and standard noise reduction techniques of correlated double sampling (CDS) and Fowler sampling will be supported. An On-Detector Guide Window (ODGW) mode will be supported where image translation is sensed directly on the imager detector for tip-tilt and flexure monitoring. The detector will be optimized to have high well depth (~ 100,000 e), good quantum efficiency, and good linearity (~ 1 %), while minimizing read noise (< 14 e), dark current (< 0.1 $e\ s^{-1}\ pix^{-1}$), drift (< 50 e/hr), cross-talk, and cosmetic defects. GL Scientific will perform the mechanical design, construction, and assembly of the focal plane assembly and align the H2RG packages. Two designs for the detector controller are presented. One uses a SDSU-2 detector controller. The other uses Application Specific Integrated Circuits (ASICs), which are under development at Rockwell. These will be connected to a communication interface subrack. Both designs communicate with the Detector Controller (DC) Input/Output Controller (IOC) through a 12.5 Mpixel/s fiber-optic link via a SDSU PMC interface board. The SDSU-2 detector controller design is preferred. It meets the performance requirements, has low risk and cost, and is compatible with the requirement for a fast-track instrument. An upgrade option with shorter imager readout time is suggested to improved observing efficiency for short exposures.

Verbal agreement has been reached between RSAA and Don Hall at the Institute for Astronomy (IfA) of the University of Hawaii to collaborate on the design, optimization, and characterization of the GSAOI imager detector system. IfA are world leaders in developing infrared instruments using HAWAII HgCdTe detectors. They are currently co-developing H2RG technology for NGST. Don Hall will be testing the GL Scientific focal plane assembly design as part of the NGST detector development.

The OIWFS detector hardware provides a similar low temperature (60-90 K), stable (±1 K), low flexure environment in which to read out the OIWFS detector. A Rockwell 1024×1024 pixel HAWAII-1 HgCdTe/Sapphire PACE detector has been chosen because it is adequate for the task and this choice allows all of the NIRI/NIFS OIWFS detector hardware and software to be re-used without modification. Consequently, the OIWFS detector will be controlled via a SDSU-2 detector controller connected to the A&G IOC via a SDSU-2 VME interface board. RSAA will manufacture this system based on the NIFS OIWFS detector system.

5.2 Imager Detector System

5.2.1 HAWAII-2RG Description

The GSAOI imager detector mosaic will use four 2048×2048 pixel Rockwell HAWAII-2RG detectors. Each detector has 18 μm pixels and is mounted in a three-side buttable package. Detailed mechanical dimensions of the H2RG package are given in Appendix B (§9.1). The minimum separation between the active areas is 2.14 mm (Figure 64). Mounting constraints dictate that the actual separation will be < 2.5 mm. The four edge rows and columns of each detector are masked for use as reference pixels, so the light-sensitive area consists of 2040×2040 pixels. Gemini has already entered a contract with Rockwell to supply these detectors. The performance parameters defined in this contract are listed in Table 35. The first HAWAII-2RG devices are expected in July 2002 (Table 36). The multiplexer will be required by January 2004 and the two engineering grade devices by May 2004. Delivery of the GSAOI science grade devices is scheduled for June 2004. They are not required until September 2004.

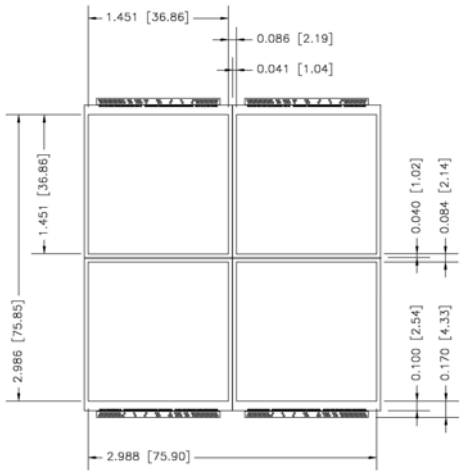

Figure 64: H2RG 4K×4K mosaic construction detail.

Table 35: H2RG Performance Parameters

Parameter	Offer	Goal
Total Pixels	2048×2048	
Pixel Pitch	18.0 μm	
Fill Factor	> 90%	
Outputs	4	
Spectral Range	0.9 μm to 2.5 μm	0.8 μm to 2.5 μm
Cutoff @ 77 K	2.5 μm	
Operating Temperature	77 K	
Quantum Efficiency @ 77 K		
@ 2.3 μm	> 0.65	> 0.80
@ 2.0 μm	> 0.65	> 0.80
@ 1.5 μm	> 0.65	> 0.80
@ 1.0 μm	> 0.65	> 0.80
@ 0.9 μm	Not specified	> 0.50
Charge storage capacity	> 80,000 e	> 100,000 e
Pixel operability	> 95%	> 98%
Dark Current @ 77 K (mean)	< 1 e/pixel/s	< 0.01 e/pixel/s
Read noise @ 77 K & 100 kHz	< 15 e/pixel rms (CDS)	< 10 e/pixel rms (CDS)
Read noise @ 77 K & 5 MHz	< 100 e/pixel rms (CDS)	< 20 e/pixel rms (CDS)
Power Dissipation at 100 kHz	< 4 mW	
Power Dissipation at 5 MHz	< 20 mW	

Table 36: H2RG/ASIC Development Schedule.

Device	Development Schedule
H1RG	H1RG have been manufactured and first device has been tested by Don Hall.
H2RG	H2RG mask fabrication has been completed and first devices are ready for testing.
ASIC	At advanced stage of design. Will be taped out in July 2002 and manufactured September/October 2002.
ASIC Assembler/Simulator	Available end of 2002.

A complete listing of the H2RG signals is given in Appendix B (§9.3).

The HAWAII-2RG is a complex device. It offers many features that are not relevant to ground-based, high-background imaging. Implementation of these features for GSAOI is both unnecessary and incompatible with the fast-tracked development of this instrument. We discuss only those features that will be implemented.

5.2.1.1 Outputs Pads Configuration

The H2RG has 32 output channels (OutputA/B[0-15]), one reference output (RefOutA/B) (§5.2.1.2) and one guide window output (WindowOutA/B) (§5.2.1.4). Each output can be configured according to Figure 65. Each output is brought out on two pads, A and B. Pad A offers three options; 100 kHz unbuffered, 100 kHz buffered, and 5 MHz unbuffered. Pad B offers the same three options plus the additional configuration for 5 MHz buffered. Two pads are needed because the 5 MHz buffer adds significant capacitance (~ 6 pF) to the line even if disabled. The signals to enable and disable the various options are described in the H1RG Technical Document.

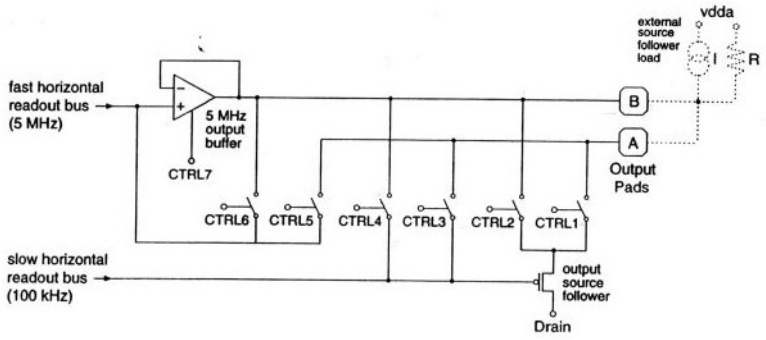

Figure 65: Circuit diagram of various output pad configurations.

5.2.1.2 Reference Output

A modest level of bias stability is required of the imager detector (< 50 e/hr). This is based on an expected minimum background signal of ~ 40 e in 60 s through the lowest background narrow-band filters (Table 9 of Vol. 1). The H2RG has a separate reference output (Figure 66) for tracking bias variations. This reference output can be configured in different ways. REFMODE in the OutputModeReg register selects whether or not the pixel is treated as a normal pixel. When REFMODE = 0, the pixel is reset at the same time as the upper left (0,0) pixel is reset. Between resets, the pixel node floats and will move slightly due to leakage current in the connected transistor. When REFMODE = 1, the pixel stays in the reset state and is permanently connected to either DSUB (when REFVOLT = 1) or Vreset (when REFVOLT = 0). REFVOLT is a bit in the OutputModeReg register.

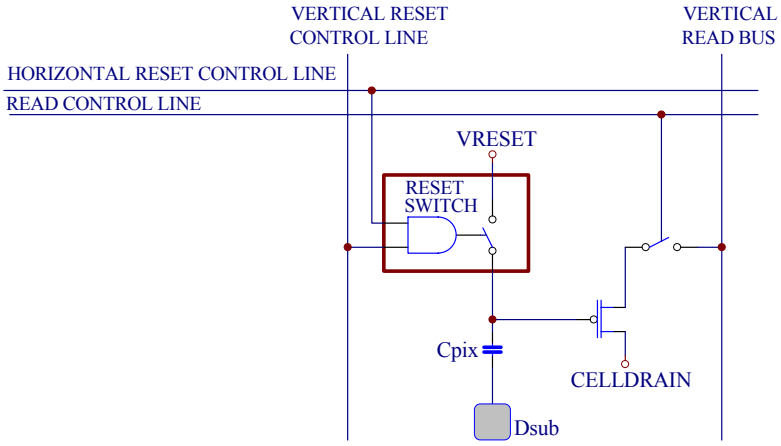

Figure 66: Circuit diagram of the reference pixel.

In 5 MHz fast readout mode, the reference output is connected to a column sample and hold stage plus column buffer similar to normal pixels and no permanent connection between the pixel and the output pad exists. This means that a new reference value is sampled every level change of SAMPLECLK and then held for the remaining readout time of the row.

5.2.1.3 Readout Speed

The H2RG 2RG multiplexer (MUX) supports two readout speed modes; 100 kHz slow readout and 5 MHz fast readout. The slow readout mode has an offer/goal read noise of 15/10 e and the fast readout mode has an offer/goal read noise of 100/20 e (Table 35). The predicted background noise in a 60 s integration through the broad-band imager filters is typically ~ 50 e and for the narrow-band filters is typically ~ 12 e (Table 9 in Vol. 1). Consequently, read noise will not add significantly to background noise in the slow readout mode when using broad-band filters, but it is likely to be comparable to the background noise in narrow-band observations. Longer integration times will be beneficial for these observations. The fast readout mode is unsuitable for broad-band and narrow-band observations, especially if the 5 MHz read noise is as high as 100 e.

In the slow readout mode, a 2-3 times faster readout rate can be achieved by increasing the bias current of the output amplifier to reduce settling times. Read noise increases as the square root of the bandwidth and amplifier glow is increased due to the higher currents. However, the observing duty cycle is improved by reading out the detector faster. The increase in glow is not likely to be serious because the H2RG has been designed to minimize glow. Cable lengths between the detector and the controller will be kept short to further reduce the output amplifier settling time.

The imager detectors will be read out using the 100 kHz slow readout mode. Three readout speed options will be implemented; a fast 300 kHz speed for instrument setup, a medium 200 kHz speed for broad-band observations, and a slow 100 kHz speed for narrow-band observations where low read noise is desirable. The CDS full frame read time using the 200 kHz mode and four amplifiers per H2RG will be ~ 10 s. This is adequate for the foreseeable future because tests with our implementation of the DHS show that imager data frames cannot be transferred from the DC IOC to the DHS in under ~ 20 s (§7.3.4.5.3) and Gemini has stated that it is unlikely that the DHS throughput will be improved. Options for upgrading the imager detector readout speed are discussed in §5.2.7.

The 5 MHz channel has higher read noise and would require untried techniques to implement. This is incompatible with the development of a fast-tracked instrument.

5.2.1.4 Guide Window

The HAWAII-2RG MUX can read out any rectangular region of the pixel array while the remainder of the area is integrating. The sub-region is selected by loading pixel coordinates into MUX registers.

This feature will be used to implement separate On-Detector Guide Windows (ODGWs) on each of the four imager detectors. These will be read out repeatedly during an imager integration to monitor image translation for slow tip-tilt or flexure correction.

It is desirable to continue reading the ODGW while a full imager frame is being read out. This would allow slow tip-tilt and flexure correction to be initiated before an imager integration commenced and would maintain these functions over the full imager integration time. However, interlacing guide window and imager reads is logistically complex and incompatible with the fast-tracked nature of GSAOI. Consequently, this will not be implemented. Instead, the ODGW will be read out only while the imager is integrating or is idle. In practice, the observer will configure and test the ODGW before an integration begins. ODGW read out will stop while the initial imager Fowler samples are recorded. ODGW read outs will then resume for the duration of the integration, but will cease before read out of the final imager Fowler samples begins.

Acquisition of ODGW guide stars will be straightforward because these can be selected directly from a full imager detector frame.

5.2.1.5 Detector Package

The HAWAII-2RG detector has a hybrid construction consisting of a HgCdTe detector layer deposited on a CdZnTe substrate that is bonded to a HAWAII-2RG multiplexer to form a H2RG Sensor Chip Assembly. The H2RG Sensor Chip Assembly is bonded to a molybdenum package base (Figure 67 and Figure 68). Three invar studs screwed into the bottom of this base are used to mount the package in the focal plane on a psuedo-kinematic mount. A fourth stud can be added if desired. Precision-ground molybdenum spacers are used to accurately align the package with the focal plane. A ceramic circuit is attached to one side of the package. This provides wire-bond connections to the Sensor Chip Assembly on its top surface and an external wiring connector and surface-mounted filter components on its bottom surface. There are three variants of the detector packages; a NGST non-ASIC detector package, a ASIC detector package, and a 32-output non-ASIC detector package.

The NGST non-ASIC detector package will be used for the baseline GSAOI design because its development is fully funded as part of the NGST project so this design is most likely to be realized on a short time scale. The NGST non-ASIC detector package uses a 6-layer ceramic circuit attached to the molybdenum package base. External wiring is connected via a 65-pin Nanonics input/output connector. This restricts the number of outputs to four signal, one reference, and one guide window.

The 32-output non-ASIC detector package (Figure 69) is being designed for Gert Finger of ESO and we understand that it is also fully funded (Luppino, priv. comm.). Accessing all 32 signal outputs, one reference output, and one guide window output requires a larger connector than can fit on the normal ceramic circuit. Instead, the package uses a flexirigid wirebond ceramic where one end of a small length of a polymide flex circuit is glued to the wirebond ceramic and the other end has a 92 pin 0.5 mm pitch Hirose connector soldered to it. If available, this package could be used to upgrade the ASIC detector controller design to readout through 32 outputs (§5.2.7).

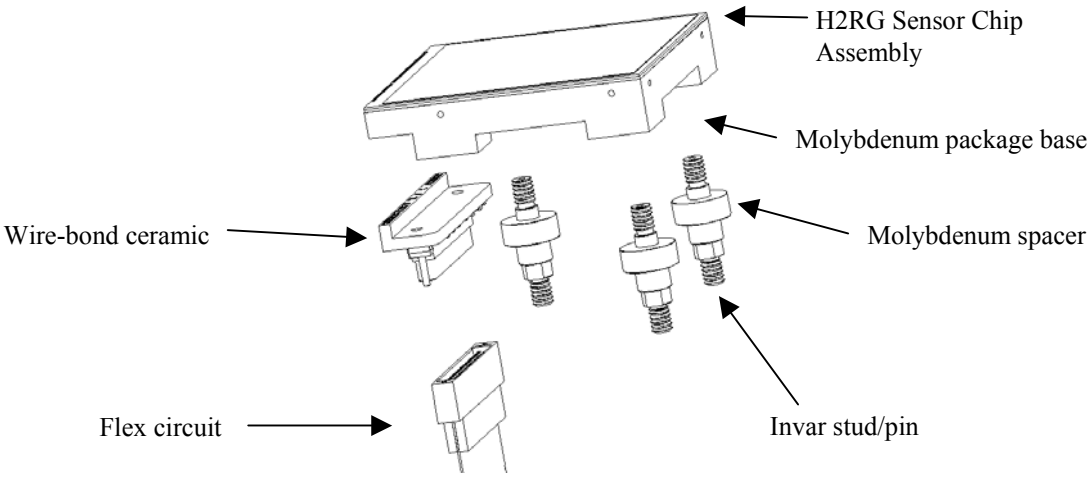

Figure 67: Exploded view of a H2RG NGST non-ASIC detector package.

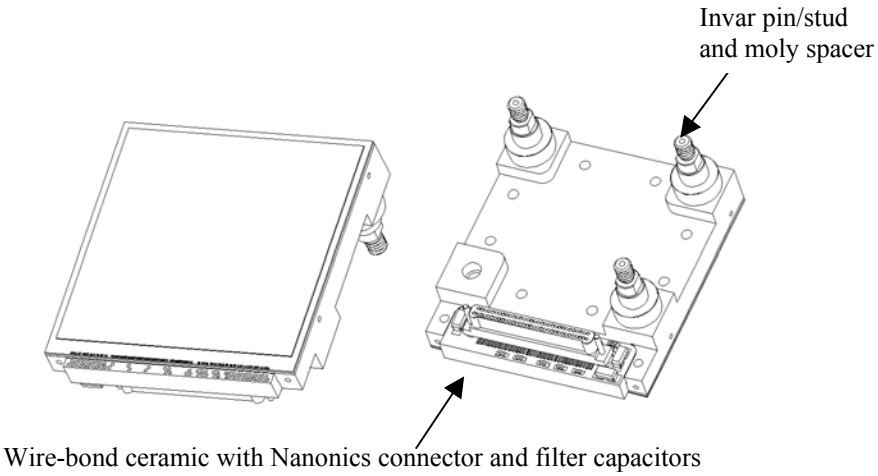

Figure 68: H2RG 3-edge-buttable NGST non-ASIC detector package.

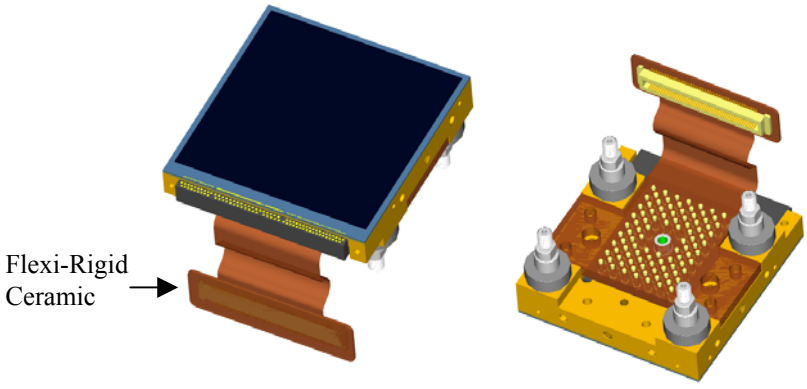

Figure 69: H2RG 32-output non-ASIC detector package.

5.2.2 Focal Plane Assembly

The focal plane assembly is the cryogenic subsystem in which the imager detector mosaic is mounted. It consists of the imager detector, the detector base plate, the detector cold finger, the detector motherboard, the connectors for thermal and electrical control, and the detector housing.

5.2.2.1 GL Scientific/RSAA Collaboration

The design and construction of the focal plane assembly will be subcontracted to Gerry Luppino through GL Scientific. Luppino has been successfully involved in designing and fabricating mosaic focal planes for many years. He was subcontracted by RSAA in 1997 to build the focal plane for its Wide Field Imager (WFI) 8k×8k CCD mosaic camera. This initiated a continuing, fruitful interaction between Luppino and RSAA staff. Luppino is currently contracted by Rockwell to package all HAWAII-1R, HAWAII-1RG, and H2RG focal plane assemblies ordered through Rockwell. Luppino has agreed to amortize the non-recurring engineering design costs over four customers, so his is a cost-effective solution.

5.2.2.2 Requirements

The details of Luppino's focal plane assembly design are still fluid. RSAA will work closely with Luppino to ensure that the final design meets the following requirements:

- Flexure at all orientations of the focal plane with respect to the detector housing shall be < 0.6 μm in the *x* and *y* directions, where the *z* direction is normal to the detectors.
- The spacing between the detectors shall be ≤ 2.5 mm, and the columns of all detectors shall be parallel to < 4 pixel in 2048.
- The focal plane assembly shall shield the detector from, and not generate, background radiation such that the detector dark current requirement of < 0.1e/s/pixel can be met.
- The focal plane assembly shall allow the detector temperature to be thermally controlled to ±1 mK between 60 K and 90 K.
- Heat flow in the vicinity of the detector mosaic shall be symmetric to the greatest extent possible in order to minimize temperature gradients within the detectors.
- Cold strap connections shall be made from the back of the detector housing via a single contact for ease of assembly/disassembly.
- Electrical (both temperature and detector) connections shall be made from the back of the detector housing for ease of assembly/disassembly.
- The focal plane assembly shall be electrically isolating from the rest of the cryostat and connected to detector ground to allow the detector housing to act as a Faraday shield to reduce electrical noise pickup.
- Convenient attachment points shall be provided on the front face of the detector housing for mounting to the camera body.

A design concept that meets these requirements is shown in Figure 70.

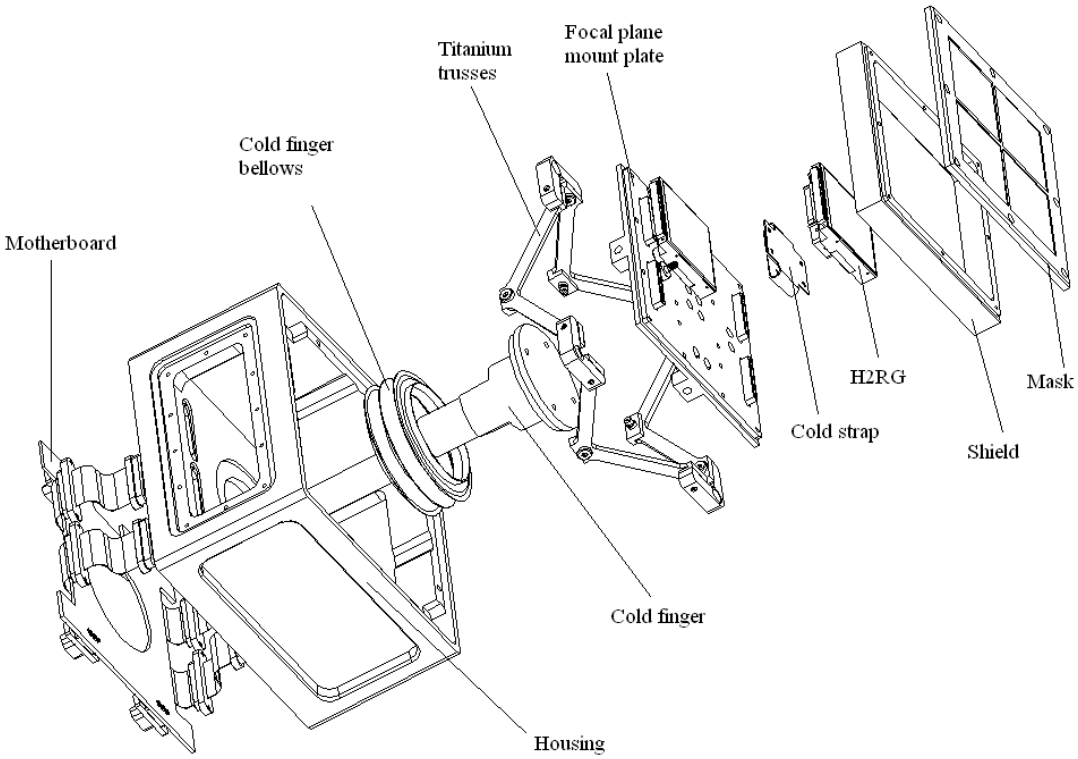

Figure 70: Exploded view of the detector assembly showing the detectors and associated components (GL Scientific).

5.2.2.3 Thermal Design

The temperature of the H2RG mosaic must be controlled to mK accuracy (Don Hall, priv. comm.) to achieve the required level of bias stability (< 50 e/hr). This specification can be relaxed if reference outputs and reference pixels prove to work (§5.2.1.2).

A schematic of the thermal design is shown in Figure 71. A cold strap connects the second stage of one cryocooler to the detector housing. The temperature of the detector housing is servo-controlled to 5 K less than the focal plane to a stability of ±0.1 K using the secondary loop of the Lakeshore Model 340 temperature controller (§5.2.10). The mass of the detector housing thermally decouples the focal plane from temperature fluctuations of the cryocooler. A cold strap connects the detector housing to the focal plane mounting plate. The temperature of the focal plane mounting plate is set to between 60 K and 90 K and is servo-controlled to mK stability using the primary loop of the Lakeshore Model 340 temperature controller.

A similar approach has been implemented successfully for the NIFS spectrograph detector system.

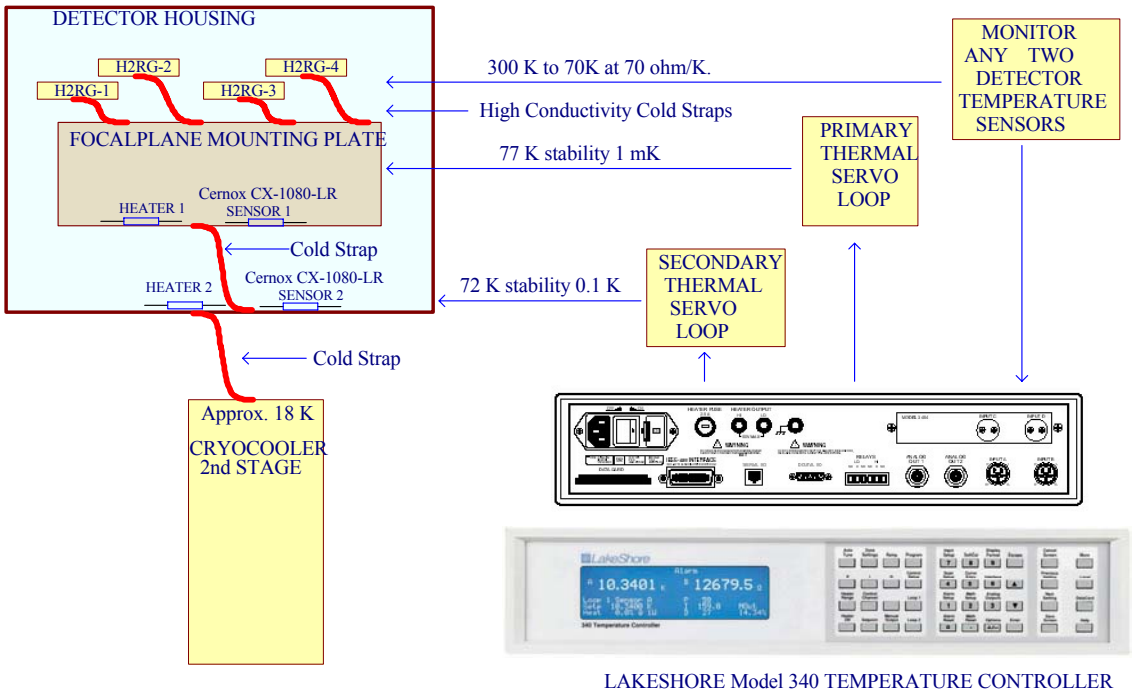

Figure 71: Detector assembly thermal design.

5.2.2.4 Electrical Isolation

The focal plane assembly will be electrically isolated from the cryostat and tied to detector ground. The detector housing then acts as a Faraday shield to reduce electrical noise pickup by the detectors circuitry. This configuration has been used successfully in the NIFS spectrograph detector system and in the CASPIR near-infrared camera built by RSAA.

5.2.3 Detector Wiring

The imager detector wiring consists of the focal plane motherboard in the focal plane assembly, the flex circuits and cables that connect the focal plane motherboard to the cryostat hermetic connectors, and the cryostat hermetic connectors.

5.2.3.1 Focal Plane Motherboard

The focal plane motherboard provides connections to the four H2RG detectors. It is located in the lower section of the detector housing to prevent locally generated heat, glow, and electrical noise affecting detector performance. The focal plane motherboard is a flexi-rigid printed circuit board. The flexible portions pass through light-tight labyrinths into the low background section of the detector housing and mate with the 65-pin Nanonics connectors on the detector packages (Figure 50). The rigid portion of the focal plane motherboard supports surface-mounted filtering components, external connectors, and possibly four ASICs. Four high-density micro-D subminature connectors provide external connections in the SDSU-2 detector controller design. If the ASIC controller design is adopted, the ASICs will be mounted on the focal plane motherboard and one high-density microminature-D connector will be used for all external connections (Figure 72). The ASICs will be thermally heat sunk through their lids to the base plate of the detector housing for better thermal stability.

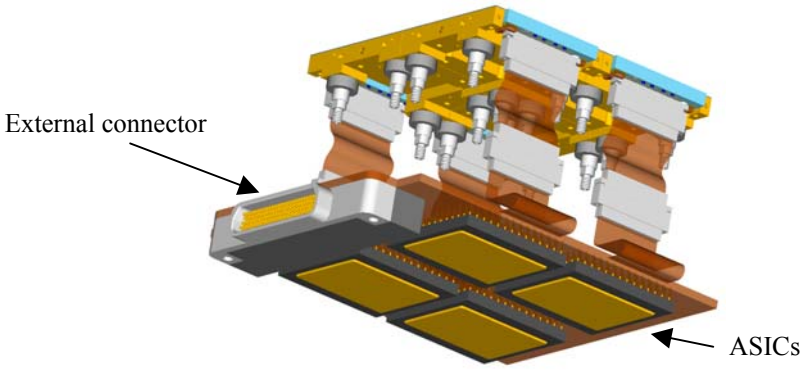

Figure 72: ASICs focal plane motherboard.

5.2.3.2 Cryostat Wiring

The cryostat wiring connects the focal plane motherboard to the cryostat hermetic connectors. The cryostat wiring designs are different in the SDSU-2 and ASIC detector controller design options.

5.2.3.2.1 SDSU-2 Cryostat Wiring

The SDSU-2 detector controller system will use polymide flex circuits to connect the focal plane motherboard to the hermetic connectors. The flex circuits will be clamped to the warm vacuum jacket near the hermetic connectors to stop moisture condensing on the hermetic connectors outside the cryostat. They will be clamped at the imager radiation shield to shunt the main heat load to the cold work surface plate[1]. Then, they will be clamped to the detector housing stabilizing the wiring temperature before connection to the focal plane motherboard. This will eliminate temperature gradients across the detectors due to variable heat flow through their wiring.

The flex circuits will be manufactured using 125 μm (0.005 inch) thick polymide substrate with 40 μm thick copper tracks deposited 100 μm (0.004 inch) wide with a minimum of 100 μm (0.004 inch) spacing. This track width is an acceptable compromise between electrical and thermal performance. Polymide is preferred because of its low capacitance, low dissipation factor, low dielectric constant, flexibility, and low out-gassing rate. A 25 μm (0.001 inch) polymide top and bottom cover layer will insulate the tracks and allow close thermal contact at thermal shunts. The copper tracks will be widened and the density of criss-cross grounds and shields will be increased near thermal shunts to maximize heat transfer. Polymide/fiberglass stiffeners will be added at connectors to improve mechanical strength.

Flex-ability[2] (C.E.C.C. 23000[3], BS 9760[4], and UL 94[5] approval) has been identified as potential manufacturer of the cryostat wiring. They have the required capabilities and have been used successfully in the past for similar applications.

5.2.3.2.2 ASIC Cryostat Wiring

The ASIC detector controller places different requirements on the cryostat wiring. The interface between the ASIC and the ASIC controller consists of several 20 Mb/s Low Voltage Differential Serial (LVDS)

[1] Thermal Anchoring of Wires in Cryogenic Apparatus, J.G. Hust, The Review of Scientific Instruments, Volume 41, Number 5
[2] http://www.flex-ability.co.uk/
[3] .E.C.C. 23000 (incorporating EN ISO 9002) Reg. No. M-0225-CECC-UK
[4] BS 9760 (incorporating BS EN ISO 9002) Reg. No. 1348/M, BS 9764, BS 9765
[5] UL 94 Reg. No. 157114M

comunication links, a LVDS master clock, and power supplies (Figure 73). The transfer of data will be asynchronous with the readout, so electromagnetic radiation should be minimized.

A composite cable of shielded twin-axial cables with low skew between pairs will be used to connect the focal plane motherboard to the radiation shield. The mating connector will be soldered to a flex circuit that connects to the hermetic connector. The flex circuit will be clamped to the imager radiation shield to provide the main thermal shunt, and to the vacuum jacket inner wall to stop moisture condensing on the hermetic connector outside the cryostat. The flex ciruits will be of similar construction to the SDSU-2 cryostat wiring. Care will be exercised to match the electrical lengths of pairs and to match the impedances of all cables, flex circuit tracks, and connectors to achieve good transmission line performance.

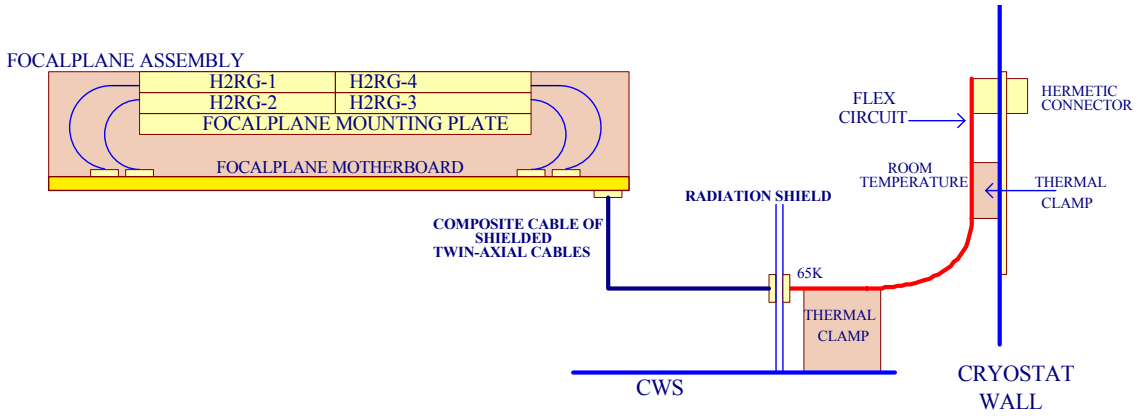

Figure 73: Block diagram of the ASIC cryostat wiring.

5.2.3.3 Hermetic Connectors

GSAOI will use RSAA-standard, 55-pin, circular hermetic connectors with PCB solder pins for ease of soldering to flex circuits. The SDSU-2 detector controller design requires 30-40 pins per H2RG detector and one connector per device for a total of four. The ASIC design requires a lower total pin count of between 30 and 40 and will use a single hermetic connector.

5.2.4 Detector Controller Requirements

The imager detector controller will be implemented using either a SDSU-2 detector controller or ASICs developed by Rockwell. Other controller options that were investigated, but not adopted, are discussed in Appendix B (§9.6). Both designs must communicate via a standard Gemini IOC and meet the following functional requirements:

- Correlated double sampling and Fowler sampling (1 to 64 samples) read out methods shall be supported. Justifications for this are given in Appendix B (§9.10).
- Integration times from 1 s to 10,000 s shall be supported.
- Coaddition of between 1 and 1000 data frames shall be supported before the result is transferred to the DHS and archived.
- Fixed-format regions of interest shall be supported with pre-defined 64×64, 256×256, 512×512, and 1024×1024 pixel windows at the center of the mosaic and at the centers of each H2RG detector.
- The use of the reference output and reference pixels shall be supported to improve bias stability.
- The use of the fast shutter shall be supported to allow MCAO system to pause exposures in period of poor adaptive-optics correction and when the MCAO SALSA system triggers a laser shutdown.
- An idle mode shall be supported whereby the imager detectors are continuously readout or reset to maintain thermal stability and to prevent them saturating.

They must also meet the following performance requirements:

- The full imager detector shall be read out using CDS in < 10 s.
- The controller noise shall be sufficiently low to achieve an effective detector read noise of < 10 e.
- The controller stability shall be sufficient to achieve a detector bias variation of < 50 e/hr.
- The controller gain stability shall be sufficient to achieve a detector gain variation of < 1% per hour.

They must also read out the ODGWs (one per detector) under the control of the DC IOC and transmit the data to the A&G IOC. To do this, both detector controller designs must meet the following ODGW functional requirements:

- Correlated double sampling and Fowler sampling (1 to 64 samples) ODGW read out methods shall be supported.
- ODGW integration times from 10 ms to 1000 s shall be supported.
- Fixed format 8×8, 12×12, 16×16, and 32×32 guide windows shall be supported on any combination of the four H2RG detectors. The guide windows can be at different locations on the four detectors, but each guide window must have the same dimensions.
- The subtraction of an ODGW sky background frame shall be supported.

They must also meet the following performance requirement:

- A 12×12 pixel guide window shall be read out using CDS at a maximum continuous frame rate of ≥ 100 Hz. Guide window reads will stop while the full imager detector is read out.

5.2.5 SDSU-2 Detector Controller

One design for the imager detector controller is based on the San Diego State University SDSU-2. This is an attractive option because both RSAA and Gemini have extensive experience designing and operating detector systems based on this controller. RSAA recently developed the HAWAII-2 spectrograph detector system for NIFS. This is based on a SDSU-2 detector controller in a configuration similar to that proposed for the GSAOI imager detector.

The SDSU-2 detector controller housing will be mounted to the vacuum jacket adjacent to the imager detector hermetic connector. This close proximity to the image detector minimizes wiring capacitance, and so reduces the required drive currents.

The SDSU-2 detector controller design consists of the following components (Figure 74):

1. One SDSU-2 detector controller configured with the following components:

- Two SDSU Octal Channel IR Video Processor Boards (video boards) configured for H2RG devices. Each board has eight video processing channels and seven programmable bias generators. The video processing channels have programmable bandwidth and gain.
- One custom Output Load Board. This board provides 20 loads for the 16 signal and 4 reference outputs of the imager detector mosaic.
- One custom Bias Board. This board provides the 24 ultra low noise, high stability biases and power supplies required for the imager detector mosaic.
- Two modified SDSU IR Clock Driver Boards (clock boards). Each board provides 24 clock/bias generators in two banks of 12 clocks/biases. One bank will drive each H2RG detector. The standard clock boards will be modified to provide faster clock rise and fall times.
- One SDSU 12.5 Mpixel/s Fiber-Optic Timing Board (timing board). This board provides the timing sequencer and the communication hub for the other boards.

- Two core fiber-optic communication cables. A 3 m length runs from the timing board to the DC IOC input/output connection panel, and a 2 m length runs from the DC IOC input/output connection panel to the PMC interface board.
- One SDSU Power Controller, one SDSU 12-slot back plane, and one SDSU enclosed housing.

2. One 12.5 Mpixel/s SDSU PMC interface board. This board plugs into the PMC slot on the DC IOC processor board. It provides the fiber-optic communication interface between the SDSU-2 detector controller and the DC IOC.
3. Two VMIVME-5588-000[6] Reflective Memory boards. One board plugs into the DC IOC and the other into the A&G IOC. They handle the transfer of ODGW data from the DC IOC to the A&G IOC via the Gemini Synchro Bus.
4. An IOC input/output connection panel with two fiber-optic feedthroughs and a power supply feedthrough connector. This panel provides a reliable place to connect and disconnect the fiber-optic cables from the PMC interface board.
5. One air-cooled SDSU-2 large power supply for a 12 slot system with custom cables to connect through the IOC input/output connection panel. The power supply will be mounted inside the DCS thermal enclosure. A 3 m cable runs from the SDSU-2 detector controller to the DC IOC input/output connection panel, and a 2 m runs from the IOC input/output connection panel to the power supply.
6. Custom external wiring manufactured from a composite of cables and wires. This wiring provides the connection from the cryostat hermetic connectors to the SDSU-2 detector controller inputs.
7. A RSAA-standard water jacket and hoses for cooling and temperature stabilizing the SDSU-2 detector controller housing.

Other configurations that were investigated, but not adopted, are discussed in Appendix B (§9.5).

[6] http://www.vmic.com/products/reflectivememory

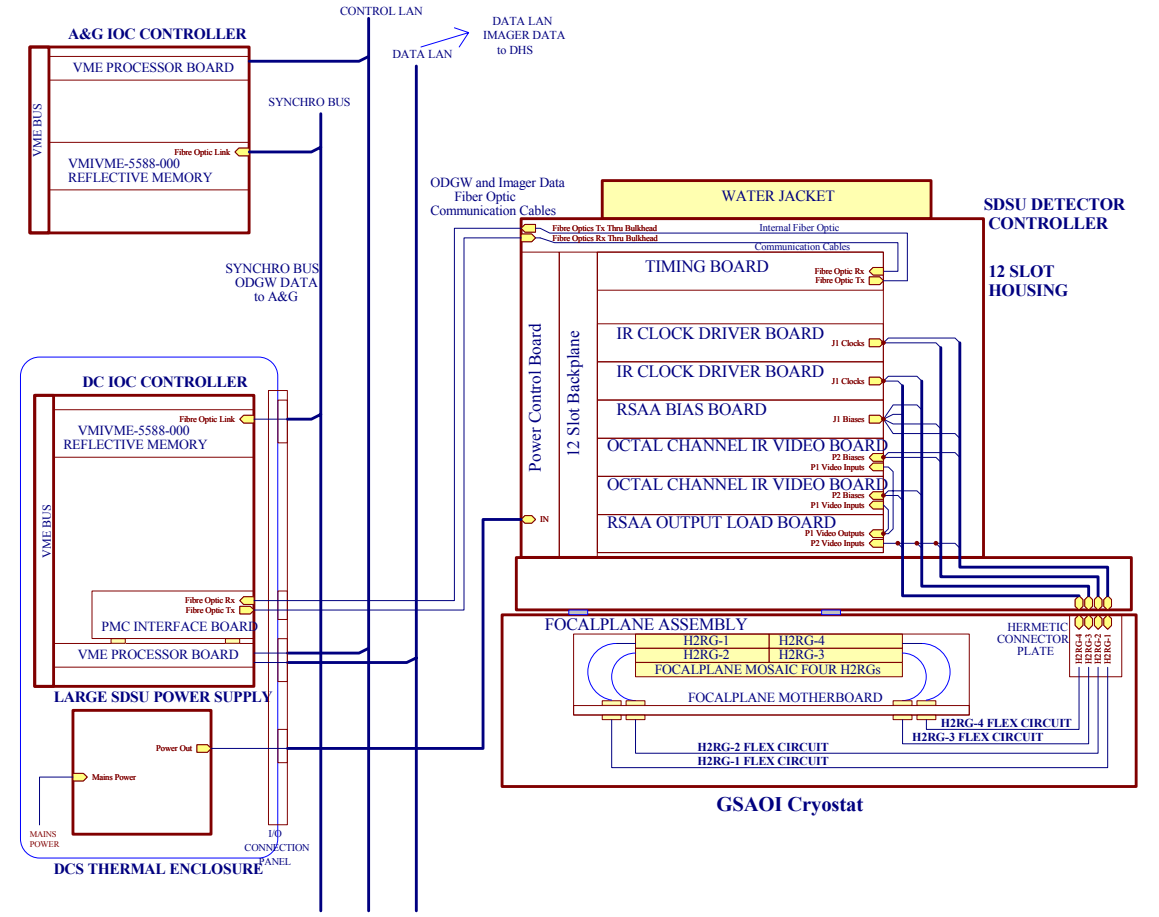

Figure 74: Block diagram of SDSU-2 detector controller design.

5.2.5.1 Functional Description

5.2.5.1.1 Communications Interface

Communication with the SDSU-2 detector controller is via the SDSU 12.5 Mpixel/s PMC interface board mounted on the DC IOC processor board. A fiber-optic link connects the SDSU PMC interface board to the timing board in the SDSU detector controller. The DC IOC sends commands to and receives responses and data from the SDSU-2 timing board. This interface will be implemented by extending the NIFS protocol.

Both imager and ODGW data are returned via the fiber-optic link to the PMC interface board. The imager data are processed by the DC IOC and then transferred to the DHS. The ODGW data are routed to the A&G IOC via the VMIVME-5588-000 reflective memory boards and the Gemini Synchro Bus. The A&G IOC will control the ODGW via the DC IOC using an appropriate EPICS command interface.

5.2.5.1.2 Timing Sequencer

A Motorola DSP560002 Digital Signal Processor (DSP) is at the heart of the timing board. This DSP has a 50 MHz clock and runs at 40 ns per instruction. It controls the setting of clocks, biases, video offsets, and power supply voltages. It controls the sequencing of clocks and analog switches on the video boards while reading out the detector. It controls the use of clocks to provide the serial communication path to set the programmable registers in the H2RG multiplexers. And, it controls the transfer of detector data from the ADCs on the video boards via the fiber-optic link.

5.2.5.1.3 Bias Generators

The mosaic requires a total of 36 biases to support the 100 kHz slow readout mode. Each H2RG requires 9 biases. These are listed in Appendix B (§9.3).

The stability of the SDSU-2 bias generators has been a concern during the NIFS spectrograph detector development (see NIFS CDR Vol. 1, §6.7) and for IfA during their testing of the first HAWAII-1R device (Ev Irwin & Don Hall, priv. comm.).

It is proposed to build a custom low-noise, high-stability bias board for GSAOI with 24 bias generators. This board will plug into a spare slot in the SDSU housing. Without knowing the sensitivity of the detector outputs to variations of its biases, it is not possible, at present, to specify the stability requirements of the biases. The progress of testing at IfA will be monitored to define this specification early. IfA have flagged DSUB, VRESET, and CELLDRAIN as very sensitive biases.

The 14 bias generators on the two video boards will provide the less sensitive biases.

5.2.5.1.4 Clock Drivers

The mosaic requires a total of 40 clocks to support the 100 kHz slow readout mode. Each H2RG requires 10 clocks. These are listed in Appendix B (§9.3). Two SDSU clock driver boards provide the 40 clocks. Each clock driver board has the capability to drive two banks of 12 clocks. Each H2RG will be driven by one dedicated bank to simplify the sequencing code. Further simplification will be achieved by jumpering the two clock boards to have the same switch state address, and by clocking the two clock banks on each board together.

The standard SDSU clock driver boards have rise and fall times of 250 ns. The H2RG requires clock rise and fall times of 80 ns for 100 kHz slow readout. Bob Leach will modify the standard SDSU clock driver board by replacing the clock drivers (normally Analog Devices AD829) with faster rise time devices (Analog Devices AD811). This was successfully done to clocks 0-3 for NIFS to drive CLK1, CLK2, CLKB1, CLKB2 of the HAWAII-2. The AD811 feedback resistors will be adjusted to reduce overshoot to < 200 mV.

5.2.5.1.5 Detector Configuration

Each imager detector will be read out through four amplifiers. The detectors will be configured in the 100 kHz slow readout mode. The full mosaic will normally be clocked at a slightly faster readout rate of 200 kHz (i.e., 5 μs/pixel). The ODGW will be read out at 100 kHz (i.e., 10 μs/pixel) to reduce read noise by ~ $\sqrt{2}$.

The signal and reference outputs will use PAD A configured for 100 kHz buffered operation (§5.2.1.1) because low dark current is not important, output amplifier glow is not a critical issue, and an external preamplifier will not be used between the detector and the video inputs.

5.2.5.1.6 Output Loads

The standard Octal Channel IR Video Processor Boards do not provide loads for the detector output amplifiers. A custom Output Load Board will be designed and built by RSAA for this purpose. The board will provide a total of 20 loads comprising 16 output loads and 4 reference loads, and will plug into a spare slot in the SDSU-2 housing.

The loads are expected to be simple pull-up resistors. However, these may be replaced with current source loads if it proves necessary to improve linearity, increase the gain of the output amplifier, and/or lower their output impedance. This choice will be made when more information is available about the performance of the H2RG output amplifiers.

5.2.5.1.7 Imager Video Chain

Two video boards provide 16 video channels to digitize the 16 output signals from the H2RG mosaic.

It is normal practice to customize the input stages of the IR video boards to suit the way in which they are used. As the baseline design has no pre-amplifier, the full gain of ×24 is provided by the second (×2) and third (×12) stages of the video chains. The video inputs are configured as differential amplifiers to improve bias stability and to eliminate noise pickup in the cabling. The signal outputs are fed to the inverting inputs and reference outputs are fed into the non-inverting inputs. The noise reduction filter time constants on the bias and video offset generators will be increased to 20 row read times (i.e., 20 rows × 512 pixels/row × 5 μs/pixel ~ 50 ms) in order to effectively attenuate $1/f$ noise during a row read.

The video channel contains an integrator with a selectable time constant of either 1 μs or 4 μs. This provides a programmable bandwidth function that allows the noise bandwidth to be minimized for different detector readout speeds. This is integral to the implementation of three readout speeds (§5.2.1.3) and to the implementation of different read out speeds for the full mosaic frame (200 kHz) and the ODGW (100 kHz).

A Linear Technology LTC1608 16-bit straight-binary ADC follows the integrator. The 2 μs conversion time, which includes 400 ns for the internal sample/hold, is safely smaller than the 5 μs/pixel fastest read time. The ADC has programmable gain. This is implemented by changing the ADC upper reference voltage. This voltage is set by a 12-bit DAC in the same way that the bias voltages are set.

5.2.5.1.8 Imager Data Pre-Processing

Addition, subtraction, and division of imager data are required to implement CDS and Fowler sampling and to coadd data frames. This full-frame pre-processing will be performed in the DC IOC before the data are transmitted to the DHS.

5.2.5.1.9 On-Detector Guide Window Video Chain

The H2RG detectors will be configured to readout the ODGW through one of their normal outputs (Output#7). The ODGWs will therefore be processed by the same video channels that process the imager. The ODGW is sampled at 100 kHz (i.e., a pixel rate of 10 μs/pixel) to achieve a read noise that is $\sqrt{2}$ lower than the full frame read noise. It is expected that this read noise advantage will be required to detect faint ODGW guide stars with short integration times. A consequence of reading out the ODGW and the full frame at different speeds through the same video channel is that different video bandwidths are required for the different speeds. The programmable bandwidth feature of the video boards will be used to implement this requirement.

5.2.5.1.10 On-Detector Guide Window Data Pre-Processing

Addition, subtraction, division, and unraveling of ODGW data are required to implement CDS and Fowler sampling and to subtract a sky background frame. These functions will be implemented in the SDSU-2 timing board DSP code. The largest (32×32) guide window requires 4 Kwords of DSP Y: data memory and 4 Kwords of X: data memory (Table 37). This can be accommodated within the available 32K×24bits memory (8K of P: program memory, 8K of X: data memory, and 16K of Y: data memory).

Table 37: DSP Memory Usage For The 32×32 Pixel ODGW

Mode	Array Type	Data Type	DSP X memory	DSP Y memory
Four 32×32 Guide Windows	Subtract frame	16 bit integer	4096	
	Accumulate Frame	24 bit integer		4096
	Total Memory Usage		**4096**	**4096**

The timing board DSP (Motorola DSP560002 with an instruction time of 40 ns) provides sufficient arithmetic processing capability to perform the calculations.

The memory and processing requirements are similar to the NIRI/NIFS OIWFSs, which are also implemented using SDSU-2 detector controllers. The ODGW will have better performance than the NIRI/NIFS OIWFSs because the H2RG MUX has a more efficient window readout technique and the GSAOI SDSU-2 detector controller has a faster fiber-optic communication interface (12.5 Mpixel/s versus 2.5 Mpixel/s).

5.2.5.2 Performance

5.2.5.2.1 Input Noise

The detector controller should have an input noise that is small relative to the detector read noise of ~ 10 e. Using a video chain gain of 24 means that 1 ADU corresponds to 6 μV at the detector. The video chain noise with a 1 kΩ input load is expected from past experience to be < 3 e. Consequently, controller noise should add less than 4% to the detector read noise (~ 10 e).

5.2.5.2.2 Bias and Gain Drifts

Uncorrected bias variations are required to be at a level of < 50 e/hr, and gain variations are required to be < 1%/hr. Temperature variations in the detector controller can cause bias and gain variations. These will be reduced by stabilizing the controller housing temperature to ±2 K using water cooling. The custom bias board will provide ultra low noise, high stability biases to reduce detector output bias and gain drifts due to detector bias variations. Additional filtering will be added to the video offsets on the video boards to reduce $1/f$ noise.

The reference outputs will be used to track and electrically subtract drift (§5.2.5.1.7). The outer four rows and columns of reference pixels will be sampled. These can be subtracted during data reduction to attenuate $1/f$ noise at periods greater than one row read time.

5.2.5.2.3 Dynamic Range

The H2RG has a usable well depth of 1.0×10^5 e (§5.2.1) and a read noise goal of 10 e (§5.2.1) using CDS. This yields a maximum dynamic range of ~ 10^4. The 16-bit ADC on the video board will adequately digitize this analog signal.

5.2.5.2.4 Imager Full Frame Read Time

The imager detector CDS full frame read time is required to be < 10 s. This will be achieved by reading out each H2RG device through four amplifiers using the 100 kHz slow readout mode, but clocked at a slightly faster readout rate of 200 kHz (i.e., a pixel rate of 5 μs/pixel). The 40 ns clock time resolution of the timing sequencer and the 2 μs conversion time of the video board ADC are consistent with a pixel rate of 5

μs/pixel. The 200 kHz readout rate requires a data rate between the SDSU-2 detector controller and the DC IOC of 3.2 Mpixel/s. This is easily met by the 12.5 Mpixel/s speed of the fiber-optic communication link.

5.2.5.2.5 Regions of Interest

Readout times for various regions of interest that are centered on the mosaic and centered on each detector are estimated in Table 38.

Table 38: CDS readout times at 200 kHz readout speed for various regions of interest that are centered on the mosaic and centered on each H2RG.

Region	Region centered on H2RG		Region centered on Mosaic		
	Number of Outputs Used	CDS Read Time at 200 kHz (sec)	Number of H2RGs	Number of Outputs Used per H2RG	CDS Read Time at 200 kHz (sec)
8×8	2	0.00048	4	1	0.00024
16×16	2	0.0016	4	1	0.0008
32×32	2	0.0058	4	1	0.0029
64×64	2	0.022	4	1	0.011
128×128	2	0.084	4	1	0.042
256×256	2	0.33	4	1	0.17
512×512	2	1.32	4	1	0.66
1024×1024	2	5.3	4	1	2.6
2048×2048	4	5.3	4	2	2.6
4096×4096	N/A	N/A	4	4	10.5

5.2.5.2.6 On-Detector Guide Window Frame Rate

The detector controller is required to read out a 12×12 pixel guide window using CDS at a maximum continuous frame rate of ≥ 100 Hz. The ODGW is read out at 100 kHz (i.e., a pixel rate of 10μs/pixel) through one video channel. Consequently, the CDS read time for a 12×12 guide window is 3.4 ms, which achieves an 83% ODGW integration duty cycle relative to the total frame time (10 ms). The 144 pixels will be transmitted via the 12.5 Mpixel/s fiber-optic communication link in less than 12 μs.

5.2.5.3 DSP Code

Code is required for the DSP on the timing board. Much of the DSP code developed for the NIFS HAWAII-2 detector will be reused for GSAOI. The code will support CDS and Fowler sampling of the full imager detector in its standard clocking mode with only minor changes to the program and timing waveforms. The code supports an idle mode whereby the imager detectors are continuously readout or reset in order to stop them from saturating or for thermal stabilization.

Some additional DSP code will be required. This is described in the following sections.

5.2.5.3.1 Regions of Interest

Regions of interest support has already been developed for the SDSU-2 at RSAA. This code can be added easily by incorporating sections of the RSAA CCD DSP code. The RSAA CCD DSP code uses a flexible and efficient way of defining a region of interest. Definition parameters are written into a 48 words reserved area of the timing board DSP Y: data memory starting at address Y:3F0. The memory is allocated as follows:

- The first location contains number of parallel region descriptors, NPREGION.
- This is followed by NPREGION parallel region descriptors, where each parallel region description contains:
  - The number of parallel rows to skip;
  - The number of parallel rows to read;
  - The number of serial region descriptors, NSREGION;
    - This is followed by NSREGION serial region descriptors, where each serial region description contains:
      - The number of pixels to skip;
      - The number of pixels to read;
      - The number of pixels to skip to clean up the serial register.

This description can be used to describe very complicated regions. The only limitation is the amount of memory it uses. GSAOI will be restricted to 20 pre-defined regions of interest (§5.2.4).

For each of the regions of interest, a matching predefined region of reference pixel rows and columns will be implemented. A parameter defining the number of reference samples to take of each reference pixel will also be required.

5.2.5.3.2 Read Out Speeds

Code will be required to support different imager detector read out speeds. Support for different read out speeds has already been developed for RSAA CCD instruments. This code can be easily added by incorporating sections of the RSAA CCD DSP code.

5.2.5.3.3 H2RG Internal Registers

Code will be required to write to the H2RG internal registers to set various operating modes of the multiplexer (e.g., guide window definition, horizontal and vertical readout direction, output mode, output amplifier configuration, clocking mode, and power down control). IfA has developed code to write to the H2RG registers. This code will be available for GSAOI as part of the collaboration with IfA.

5.2.5.3.4 Fast Shutter

New code will be written to support the operation of the fast shutter. Pause and resume commands will be added to extend the integration period when the shutter is closed.

5.2.5.3.5 ODGW Support

New code will be written to support ODGW. Parts of the NIRI/NIFS OIWFS SDSU-2 DSP code will be used as a basis for this code.

5.2.5.3.6 Imager/ODGW Interaction

New code will be written to coordinate interaction between the imager readout and the ODGW readout.

5.2.6 ASIC Detector Controller

Rockwell is currently developing Application Specific Integrated Circuits (ASICs; Appendix B, §9.2) that will perform the function of a conventional detector controller. This development may be completed on a timescale compatible with the GSAOI development. Consequently, we have developed an alternative conceptual design for the imager detector controller based on these ASICs. RSAA and Gemini will decide between these alternatives at an appropriate time during the GSAOI preliminary design phase. This decision should be made at or before the Preliminary Design Review to avoid impacting the GSAOI schedule.

ASICs are mounted in the cryostat near the detector, so they offer potential improvements in noise, cross-talk, readout speed, and power consumption over conventional detector controllers. They provide all clock and bias voltages necessary to operate the H2RG detector and contain ADCs to digitize the outputs. One ASIC drives one H2RG detector.

The ASIC detector controller design consists of the following components (Figure 75):

1. Four ASICs mounted on the focal plane motherboard driving the four H2RG detectors.
2. One ASIC communication sub-rack. The ASIC communication sub-rack provides the drive signals for the ASIC and the communication interface between the ASICs and the fiber-optic link to the DC IOC. It is mounted externally on the cryostat adjacent to the detector hermetic connector. The ASIC communication sub-rack consists of the following components:

- One custom ASIC communication board. This board provides the power supplies and master clock to drive the ASICs and the communication interface between the 20 MBaud LVDS serial links that connect to the four ASICs and the 12.5 Mpixel/s fiber-optic link that connects to the PMC interface board in the DC IOC.
- Two core fiber-optic communication cables. A 3 m length runs from the ASIC communication board to the DC IOC input/output connection panel, and a 2 m length runs from the DC IOC input/output connection panel to the PMC interface board.
- One SDSU Power Controller, one SDSU 6 slot back plane, and one SDSU enclosed housing.

3. One 12.5 Mpixel/s SDSU PMC interface board. This board plugs into the PMC slot of the DC IOC processor board. It provides the fiber-optic communication interface between the ASIC communication board and the DC IOC.
4. Two VMIVME-5588-000 Reflective Memory boards. One board plugs into the DC IOC and the other into the A&G IOC. They handle the transfer of ODGW data from the DC IOC to the A&G IOC via the Gemini Synchro Bus in the same way as for the SDSU-2 detector controller design.
5. An IOC input/output connection panel with two fiber-optic feedthroughs and a power supply feedthrough connector. This panel provides a reliable place to connect and disconnect the fiber-optic cables from the PMC interface board.
6. One air-cooled SDSU-2 small power supply for a 6 slot system with custom cables to connect through the IOC input/output connection panel. The power supply will be mounted inside the DCS thermal enclosure. A 3 m cable runs from the ASIC communication sub-rack to the DC IOC input/output connection panel, and a 2 m cable runs from the IOC input/output connection panel to the power supply.
7. Custom external wiring manufactured as a composite cable of shielded twin-axial cables with low skew between pairs. This cable transmits the ASIC LVDS signals and power supplies between the detector hermetic connector and the ASIC communication board. The electrical length of pairs will be matched and the cable impedance will be matched to that of the ASIC cryostat wiring.
8. A RSAA standard water jacket and hoses for cooling the ASIC communication sub-rack.

Alternatives to the custom ASIC communications board that were investigated, by not adopted, are described in Appendix B (§9.7).

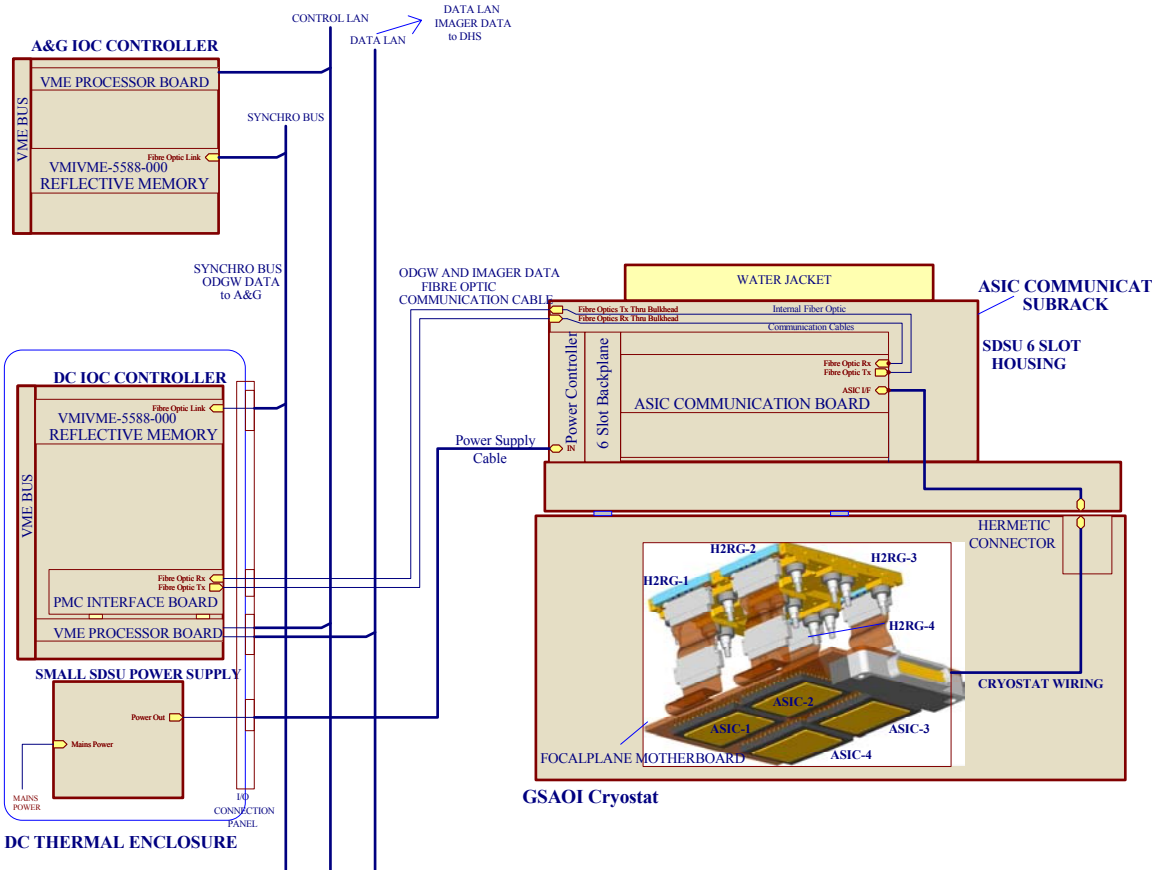

Figure 75: Block diagram of ASIC detector controller.

The ASIC detector controller design uses several SDSU-2 detector controller components to reduce development time and spares requirement. The ASIC communication board fiber-optic section will also reuse the design for the fiber-optic communication section of the SDSU-2 timing board. Joint development with the MCAO project of the device driver for the SDSU PMC interface board is also possible.

5.2.6.1 Functional Description

5.2.6.1.1 ASIC Location

The ASIC are mounted on the focal plane motherboard. This has the advantage that heat generated by the ASIC remains outside the low-background region of the detector housing away from the H2RG detectors and provides complete freedom in how the ASICs are wired to the H2RG detectors. The ASIC are thermally heat sunk to the base plate of the detector housing for better thermal stability.

The focal plane motherboard in this design must be more complex than in the SDSU-2 detector controller design. It will be implemented using a multi-layer PCB.

This solution is preferred over the possibility of mounting the ASICs closer to the detectors because of concerns about thermal stability near the detectors. Other options also require the use of H2RG packages that are still at the conceptual level.

5.2.6.1.2 ASIC Synchronization

The four ASICs must be synchronized to reduce cross-talk and beating effects. This is done by configuring the ASICs in a master/slave arrangement with one master and three slaves. One digital output signal from the master is connected to one of its own interrupt lines and to the same interrupt line of the slaves. *Read* commands are sent to the slaves. These commands do not initiate the readout, but set up the slaves ready for the readout and place them in a loop waiting for an interrupt. A *Read* command is then sent to the master. It prepares for the readout and then outputs an interrupt signal to itself and to the slaves. The four ASICs then execute identical interrupt code that performs the readout. This synchronizes the ASICs to the instruction level. The four ASICs are driven from the same master clock generator to synchronize them to the clock level. This synchronization technique has been used successfully to synchronize the two SDSU-2 detector controllers in RSAA's WFI CCD camera.

5.2.6.1.3 Communications Interface

Communication with the ASIC is via the SDSU 12.5 Mpixel/s PMC interface board mounted on the DC IOC processor board, as for the SDSU-2 detector controller design. A fiber-optic link connects the SDSU PMC interface board to the ASIC communication board in the ASIC communication sub-rack on the cryostat. Communication between the ASIC communication board and the four ASICs is via separate LVDS serial links to each ASIC (Figure 76). Two 20 Mbaud LVDS serial links connect to each ASIC; a command link and a response/data link. The ASIC communication board also generates the master clock and the power supplies required by the ASICs.

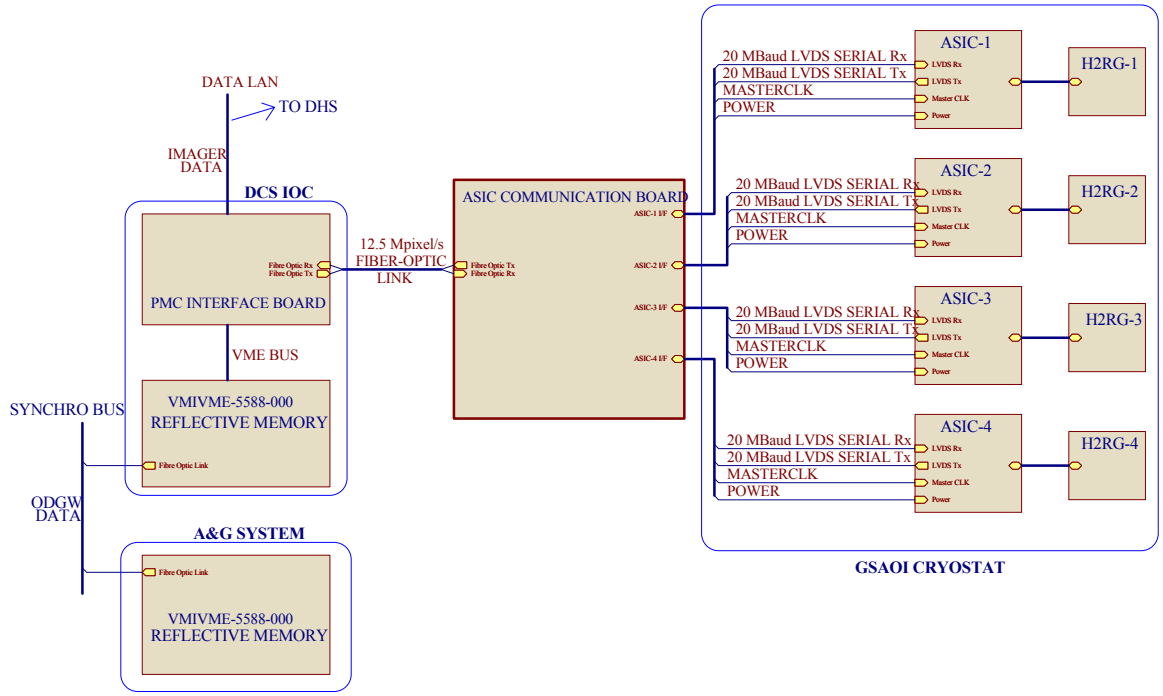

Figure 76: Communication block diagram for the ASIC detector controller.

The communication protocol between the DC IOC and the ASICs will be implemented by adapting the NIFS protocol to the greatest extent possible.

The data flow in the DC IOC is the same as for the SDSU-2 detector controller design. Both imager and ODGW data are returned via the LVDS serial/fiber-optic link to the PMC interface board. The imager data

are processed by the DC IOC and then transferred to the DHS. The ODGW data are routed to the A&G IOC via the VMIVME-5588-000 reflective memory boards and the Gemini Synchro Bus in the same way as for the SDSU-2 detector controller design. The A&G IOC controls the ODGW via the DC IOC using the same EPICS command interface proposed for the SDSU-2 detector controller design.

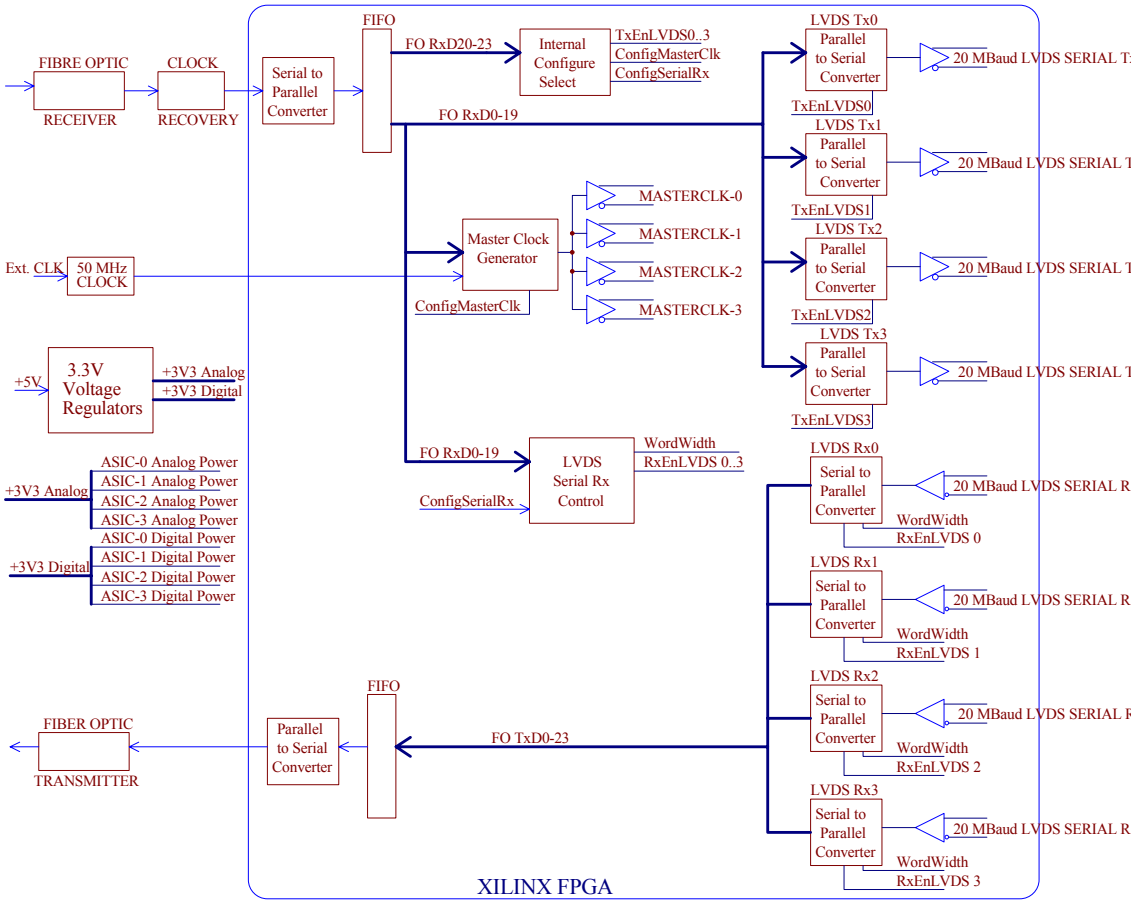

Figure 77: Block diagram of a preliminary design for the ASIC communication board.

5.2.6.1.4 ASIC Communication Board

The design of the ASIC communication board (Figure 77) is based around either Virtex or Spartan Xilinx[7] Field Programmable Gate Array (FPGA). The Virtex or Spartan FPGA drive the LVDS signals directly. They have internal RAM to implement FIFOs, and they have phase lock loops to implement clock generators. The design of the fiber-optic transmitter/receiver will be adapted from the 12.5 Mpixel/s SDSU timing board. However, the logic will be implemented in the Xilinx FPGA. The design will support the following features:

- Standard SDSU line protocol for the fiber-optic link to the SDSU PMC interface board.
- The ability to drive up to four ASICs.
- 20 Mbaud command and 20 Mbaud response/data LVDS serial communication links to four ASICs.
- Programmable clock generator to provide master clocks for four ASICs. All ASICs must be clocked at same rate.

[7] http://www.xilinx.com/xlnx/xil_prodcat_landingpage.jsp?title=Devices

- Separate analog and digital low noise +3.3 V voltages to provide the power supplies for four ASICs.
- Low latency and deterministic communication between the DC IOC and the ASICs.

5.2.6.1.5 Timing Sequencer

The ASIC uses a programmable 50 MHz 16-bit microcontroller for configuring the H2RG multiplexer, clocking it, controlling the ASIC video chains and ADCs, programming and setting the bias and clock voltages and currents, and for communicating with the DC IOC. The microcontroller has a 40 ns instruction time, so is comparable in speed to the SDSU-2 DSP. A boot program will be loaded into the microcontroller on power up via the LVDS serial/fiber-optic link. The boot program will have enough capability to communicate with the DC IOC and to download the control program. Code for the microcontroller will be adapted from code that is expected to be available from Rockwell and from IfA.

The microcontroller has the following features:

- Maximum clock rate of 50 MHz (probably faster, especially when cooled below room temperature).
- 8 kwords, 16 bits/word, of program memory (possibly 16 kwords). Memory is single event upset hardened and error code protected.
- 8 kwords, 16 bits/word, of data memory. Memory is single event upset hardened and error code protected.
- 32 kwords, 24 bits/word, of data SRAM memory. Memory can be used by the microcontroller and by special functions that provide simple arithmetic operations (e.g., adding, subtracting, and shifting) on all 36 channels in parallel.
- Two types of internal registers; standard 16 bits wide registers and extended 24 bits wide. Most instructions operate on the 16 bit registers, but all Arithmetic Logic Unit (ALU) instructions operate on both 16 bit and 24 bit registers.
- ALU instructions include the following:
  - add, sub
  - add with carry, sub with carry
  - average (add plus right shift in single cycle)
  - multiply (16 × 16 integer and 24 × 16 pseudo-floating point)
  - divide (16 × 16 integer and 24 × 16 pseudo-floating point)
  - AND, OR, XOR, NOT, NEG
  - shift left or right (arithmetic and logical)
  - rotate left or right (with and without carry)
  - set/reset/complement/test individual bits
- All instructions are single cycle, except the divide instruction which may take up to 4 cycles depending on the clock speed and program control instructions (jmp, call, ret) that can be 1, 2, or 3 cycles depending on the jump condition and the exact coding (i.e., due to the pipeline architecture).

5.2.6.1.6 Bias Generators

The power supplies, references, and analog biases required by the H2RG will be provided by 9 of the 20 programmable voltage/current generators configured as voltage generators. The voltages of the bias generators are set by 10 bit DACs over two selectable ranges of 0-2 V and 1.3–3.3 V for a resolution of 2 mV. The current sources/sinks are set by 7-bit switchable current mirrors over three selectable ranges of 100 nA–10 μA, 1μA–100 μA, 10 μA–1 mA. The bias configuration and voltage values are programmed from the microcontroller by writing to control registers.

5.2.6.1.7 Clock Drivers

The ASIC will have 32 I/O channels to provide the clocks for the H2RG. Each I/O channel can be configured in the following ways:

- As input, output, or high impedance.
- When set as an output, have the output driver strength set from 20 μA to 20 mA.
- Be permanently set to high, low, or off.
- Be set as negative or positive logic.
- Be set as clock generators by programmably dividing down the master clock.

The clocks are configured from the microcontroller by writing to control registers.

The 10 clocks required by the H2RG will be provided by 10 of these I/O channels configured as simple positive logic outputs.

5.2.6.1.8 Detector Configuration

The detector will be configured as for the SDSU-2 detector controller design. Each imager detector will be read out through four amplifiers. The detectors will be configured in the 100 kHz slow readout mode. The full mosaic will normally be clocked at a slightly faster readout rate of 200 kHz (i.e., 5 μs/pixel). The ODGW will be read out at 100 kHz (i.e., 10 μs/pixel) to reduce read noise by ~ $\sqrt{2}$.

The signal and reference outputs will be configured as for the SDSU-2 detector controller design; PAD A configured for 100 kHz buffered operation (§5.2.1.1).

5.2.6.1.9 Output Loads

The ASIC front-ends will be configured to provide current source loads for the H2RG output amplifiers. Current sources provide best linearity and shortest settling time for the output signals.

5.2.6.1.10 Imager Video Chain

One ASIC will be assigned to each H2RG detector.

Each ASIC supports 36 video channels to process up to 32 signal outputs, one guide window output, one reference output of a H2RG, and to read the two on-detector temperature sensors. Each video channel input provides an optional internal pull-up resistor, pull-down resistor, or current source, and a differential preamplifier. This is followed by a programmable gain stage of 0-24 dB in 3 dB steps and programmable bandwidth consisting of a tunable low-pass filter. The video channel then provides either of two ADC options; a 100 kHz /16 bit (expected to be up to 1 MHz) ADC or a 5 MHz/12bit (probably up to 10 MHz) ADC.

The ASIC detector controller design reads out each H2RG detector through four signal outputs. The ASIC video chain inputs are configured by the microcontroller as differential amplifiers. The H2RG signal outputs are fed to the inverting inputs and the reference outputs are fed to the non-inverting inputs in order to reduce bias drift. The programmable gain stage will be set for a system gain of ~ 2 e/ADU.

The programmable bandwidth option as for the SDSU-2 design allows the noise bandwidth to be minimized for different detector readout speeds. This is integral to the implementation of the three readout speeds (§5.2.1.3).

The 100 kHz/16-bit ADCs will digitize all outputs. The ~ 1 μs conversion time is well suited to the 5 μs/pixel read out rate.

The proximity of the ASIC video chain to the H2RG detectors offers the potential for improved noise impunity. However, adequate suppression of interference from the ASIC microcontroller is yet to be demonstrated.

5.2.6.1.11 Imager Data Pre-Processing

As with the SDSU-2 detector controller design, addition, subtraction, and division of imager data are required to implement CDS and Fowler sampling and to coadd data frames. This full frame pre-processing will be performed in the DC IOC before the data are transmitted to the DHS, in the same way as for the SDSU-2 detector controller design.

5.2.6.1.12 On-Detector Guide Window Video Chain

The ODGW is read out through the H2RG dedicated guide window output, WindowOut, and processed by its own ASIC video chain optimized for low read noise 100 kHz read out speed (Appendix B §9.4).

5.2.6.1.13 On-Detector Guide Window Data Pre-Processing

As with the SDSU-2 detector controller design, addition, subtraction, division, and unraveling of ODGW data are required to implement CDS and Fowler sampling and to subtract a sky background frame. These functions will be implemented in the ASIC microcontroller. The largest (32×32) guide window requires 2 Kwords of data memory (Table 39). This is available within the 8 Kword of program memory and 32 Kword (24 bit/word) of data memory. The 50 MHz 16 bit microcontroller with 40 ns instruction time provides sufficient arithmetic processing capability to perform the calculations. Consequently, the ODGW should have similar performance in both detector controller designs.

Table 39: ASIC Microcontroller Memory Usage For The 32×32 Pixel ODGW.

Mode	Array Type	Data Type	Microcontroller memory
Four 32×32 Guide Windows	Subtract frame	16 bit integer	1024
	Accumulate Frame	24 bit integer	1024
	Total Memory Usage		**2048**

5.2.6.2 Performance

5.2.6.2.1 Input Noise

The adequacy of ASICs to meet the noise performance requirement of the video chain is unknown at present. This is the area of most concern with this design.

5.2.6.2.2 Bias and Gain Drifts

The adequacy of ASICs to meet the bias variation and gain stability requirements is also unknown at present. Given their stable thermal environment, it is expected that their performance in these areas will be superior to the SDSU-2 detector controller design.

The reference outputs will be used to track and electrically subtract drift (§5.2.6.1.10). The outer four rows and columns of reference pixels will be sampled, and can be subtracted during data reduction as in the SDSU-2 detector controller design.

5.2.6.2.3 Dynamic Range

ASICs use 16-bit ADCs that provide adequate digitization.

5.2.6.2.4 Imager Full Frame Read Time

The imager detector should again be read out using CDS in < 10 s. The configuration used to achieve this is identical to that used for the SDSU-2 detector controller design. Namely, the detector will be read out through four amplifiers in the 100 kHz slow read out mode, but clocked at 200 kHz. The 40 ns instruction time of the microcontroller is the same as for the SDSU-2 and is sufficient to clock the device at this speed. The ASIC ADCs have a conversion time of > 1 μs, which is also adequate.

The 200 kHz readout rate requires a data rate between each of the four ASICs and the ASIC communication board of 16 Mbaud, and a data rate of 3.2 Mpixel/sec between the ASIC communication board and the DC IOC. This is met by the 20 MBaud speed of the LVDS serial data links to each ASIC, and the 12.5 Mpixel/s speed of the fiber-optic link between the ASIC communication board and the DC IOC.

The data reliability performance of the 20 Mbaud LVDS serial links is adequate as the wiring distance is 400 mm inside and 200 mm outside the cryostat. Proper precautions will be followed in the design of the cabling (see Appendix B, §9.8).

5.2.6.2.5 On-Detector Guide Window Frame Rate

The ODGW should again be read out at a maximum continuous frame rate of ≥ 100 Hz. As with the SDSU-2 detector controller design, the ODGW is read out at 100 kHz (i.e., a pixel rate of 10 μs/pixel). However, it differs from the SDSU-2 design in that the guide window is readout through a dedicated video channel. The CDS read time for a 12×12 guide window is the same as for the SDSU-2 design at 3.4 ms, which achieves the same 83% ODGW duty cycle.

The ODGW data are processed locally by the ASIC microcontroller. Processing to perform the CDS, bias subtraction, and amplifier unraveling takes ~ 10 instruction clock cycles per pixel including memory access and looping. Consequently, ~ 1440 clock cycles are required to process a 12×12 pixel frame. This takes the ASIC microcontroller ~ 60 μs.

The 144 pixels will be transmitted via the 20 MBaud LVDS serial link and the 12.5 Mpixel/s fiber-optic link in ~ 150 μs.

5.2.6.3 ASIC Microcontroller Code

The ASIC detector controller requires new code for the ASIC microcontroller. Rockwell will provide an assembler and simulator to develop this code. It will be available towards the end of 2002. Boot code is required to provide basic communication with the IOC DC on startup. Program code is required to support the following functions:

- Read out the imager detector using CDS and Fowler sampling at slow, medium, and fast read out speeds while synchronizing the read outs of the four ASICs.
- Read out 8×8, 12×12, 16×16, and 32×32 ODGW windows on all or on any combination of the four H2RG devices. The code must perform addition, subtraction, division, and unraveling on the ODGW data for CDS and Fowler sampling, and subtract a sky background frame.
- Set the imager data region of interest to one of a pre-defined set of 64×64, 256×256, 512×512, and 1024×1024 pixel windows at the center of the mosaic and at the centers of each H2RG device.
- Write to the H2RG internal registers for setting various operating modes of the multiplexer such as guide window definition, horizontal and vertical readout direction, output mode, output amplifier configuration, clocking mode, and power down control.
- Write to the ASIC control registers for configuring the video chain and for setting the bias and clock voltage levels.
- Support the operation of the fast shutter. The code will support pause and resume commands to extend the integration period when the shutter is closed.

- Support an idle mode whereby the imager detectors are continuously readout or reset to maintain thermal stability and prevent them saturating.

An Interface Control Document will be written to define the command/response/data interface between the microcontroller and the DC IOC.

Template code for the microcontroller is expected to be available from Rockwell or through our collaboration with IfA. As much as possible of the existing NIFS, CCD, and OIWFS SDSU code and ideas will be ported to the ASIC platform.

5.2.7 Readout Speed Upgrade

The SDSU-2 and ASIC detector controller designs read out the imager detector in 10 s using four amplifiers per H2RG at 200 kHz using the 100 kHz slow readout mode. These designs are conservative in order to comply with the requirement for a fast-track instrument. They follow the NGST approach in using the same style of detector package and read out the detector using the same number of outputs and the same slow readout mode.

Short exposures of order 1 min may be required when bright MCAO guide stars are within the imager field, or to achieve accurate sky subtraction using dithered telescope offsets. An integration duty cycle of 84% will be achieved for a 10 s readout time and a 60 s integration time using the baseline designs. This increases to 92% for a 120 s integration time. A faster readout option is considered here to increase the duty cycle and improve telescope utilization for short integration times. Other options investigated, but not adopted, are described in Appendix B (§9.9).

The ASIC detector controller design can be upgraded to read out the imager detector in ~ 2.7 s (CDS) using 32 amplifiers per H2RG at 100 kHz using the 100 kHz slow readout mode. This improves the duty cycle to 96% for a 60 s integration time and to 98% for a 120 s integration time. It is our understanding that development of a 32 channel HAWAII-2RG detector package (§5.2.1.5) has now been funded (Luppino, priv. comm.). Gemini should consider seeking a contract modification to specify this packaging if the ASIC upgrade option is to be pursued. The number of ASIC LVDS serial data links between the ASIC and ASIC communication board must be increased from one to four in order to limit the maximum serial link data rate to < 20 Mbaud. Data rates faster than 20 Mbaud are difficult to implement and have high risk (NGST will use a maximum data rate of 10 Mbaud per link). The upgrade costs are as follows:

1. The design of the ASIC communication board will be 2-3 times more complex.
2. More and/or higher pin count connectors will be required between the ASIC communication board and the ASIC motherboard.
3. The design and fabrication of the external and cryostat wiring will be more complex.
4. The design of the ASIC motherboard to handle the extra serial links and the additional 28 amplifier signals between the H2RG and ASIC will be more complex and additional time will be required for its design and layout.
5. Testing of the detectors will take longer to characterization their read out using 32 amplifiers per H2RG. Early detector characterization by the NGST group will focus on 4 amplifiers per H2RG.

Reading out through 32 outputs using the 100 kHz slow readout mode has risks. The larger number of outputs increases the number of potential glow centers as well as increasing the power dissipation and the likelihood of instability problems in both the H2RG and the ASIC. It also relies on the successful development and availability of the 32-output non-ASIC detector package.

Transferring the data from the DC IOC to the Gemini DHS is still a bottleneck. This cannot be addressed without either modification of the DHS, which we understand will not happen in the short term, or the addition of an expensive local disk to the DC IOC, which we see as unwarranted and incompatible with a fast-tracked instrument.

5.2.8 Grounding Plan

Figure 78 shows the preliminary imager detector grounding system. Close attention will be paid to the detector grounding and shielding to achieve the required low noise performance of the detector. The GSAOI cryostat forms the primary shield around the detector. It is not practical to completely electrically isolate the cryostat from the telescope and mains grounds, and ground the cryostat only through the detector controller. This is because of the physical size and weight of GSAOI and its low flexure requirement. Instead, the cryostat will be grounded to the telescope. The telescope ground is reported to be a noisy ground so is not ideal for detector grounding purposes. Consequently, GSAOI will also use an internal detector shield that is insulated from the cryostat. Ideally, this internal shield would completely enclose the detectors, focal plane, and the cryostat wiring and be connected to the detector controller ground. An approximation to this ideal will be achieved.

The detector focal plane assembly will be electrically isolated from its surroundings and will be connected electrically to detector ground. The cryostat wiring will be shielded by running ground tracks between each signal line, by placing ground planes on the bottom of flex circuits, and by shielding all cables. The detector controller grounding scheme (Figure 78) is based on making the video boards the star point, and radiating short ground wires from it to the clock boards, bias boards, output load board, the detector controller chassis, and detector ground. The star point is ultimately attached to Gemini's quiet instrument ground (Mark Hunten, priv. comm.).

Figure 79 shows the proposed Instrument Control System (ICS) ground system. Care will be taken so that motors, encoders, cryocooler lines, cryocooler drives, cables, and mechanical couplings do not ground the cryostat. This would cause multiple ground loops through the instrument.

The cryocooler radiates a strong magnetic field. The intensity and extent of this magnetic field are known. The detector controller, focal plane assembly, and cryostat wiring will be kept out of this field as much as possible. Otherwise, magnetic shielding of these components will be required. The radiation from the cryocooler is directional so care will be exercised when orienting the cryocooler head with respect to the detector controller. The detector controller is housed in a sealed aluminum box and therefore has good electrical (but not necessary good magnetic) shielding. Noisy cables (e.g., ICS cables) will be routed so that they are as far as practical away from the detector controller. Local motors will be powered down when not driving. Motor leads will be shielded and the shields broken at the cryostat wall.

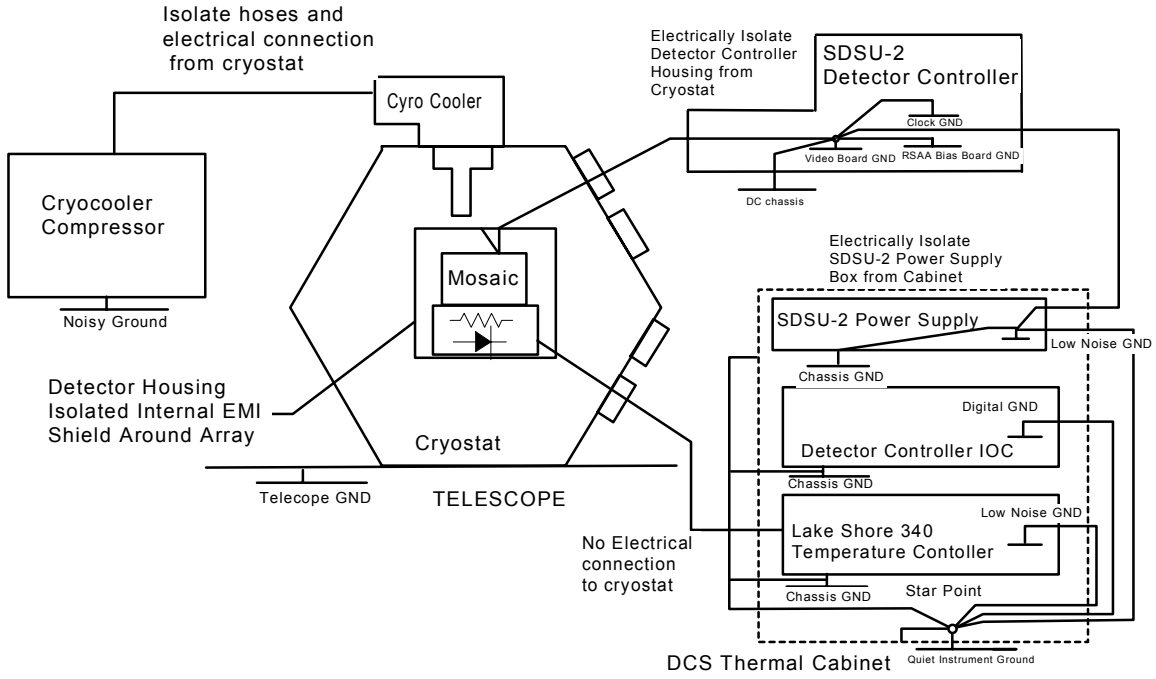

Figure 78: Detector grounding system.

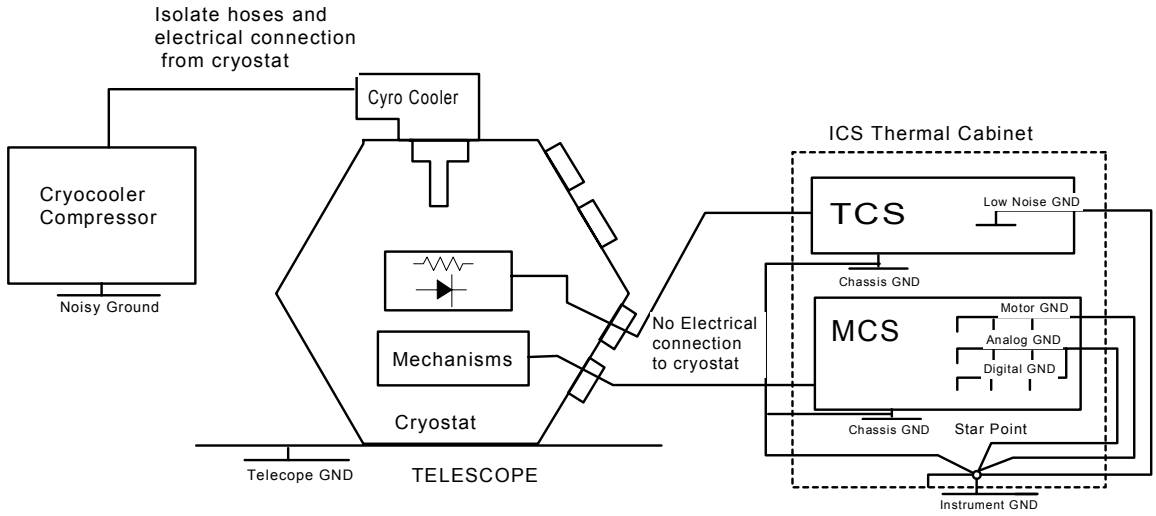

Figure 79: Instrument Control System grounding system.

5.2.9 Shielding Philosophy

It is very important to properly design the grounding and shielding to obtain reliable operation and the best noise performance. As far as possible the following rules will be adhered to:

1. Shielded coax or twisted pair cable will be used to interconnect components. The shields of these cables will only be connected at one end to avoid ground loops.

2. Electrically noisy components and signals will be kept away from low level sensitive ones, and ground shields will be placed in between. The detector controller will be mounted on the cryostat, and kept away from the noisy DC IOC, which will be mounted in one thermal enclosure, and the ICS electronics and IOC, which will be mounted in the other thermal enclosure.
3. Noisy grounds will be kept separate from low-level electronics grounds. Several grounds will be used, and these will be connected at one star point. The first ground will be a hardware ground used for mechanical enclosures, chassis, racks, and so on. The second will be a noisy ground used for relays, and motors. The third will be a digital ground, and the last will be a quiet analog ground. The AC power ground will be connected to the hardware ground.

5.2.10 Thermal Control

The imager detector thermal control system must regulate the temperature of the imager detector to milliKelvin stability in the range of 60-90 K to meet the low drift requirement (§5.2.2.3). A Lake Shore[8] Model 340 temperature controller coupled with a Cernox CX-1080-LR temperature sensor will be used to achieve this requirement. The specification, and performance of this combination are described in Table 40. The same combination has been successfully used to control the temperature of the NIFS HAWAII-2 detector to mK accuracy. The Lake Shore controller will be mounted in the DCS thermal enclosure.

Table 40: Lake Shore Model 340 Temperature Controller and Cernox Performance Data.

Sensor Type	Cernox
Temperature Coefficient	Negative
Sensor Units	Ohms
Input Range	10 ranges 10 ohm to 300 kohm
Sensor Excitation (constant current)	10 mV max (10 current settings from 30 nA-1 mA)
Temperature Range	1.4-325 K
Standard Curve	Requires Sensor Calibration
Typical Sensor Sensitivity	-5 ohm/K at 77 K
Measurement Resolution:	0.5 mK at 77 K
Electronic accuracy: Sensor Units Temperature Equivalence	 ±0.02%RNG±0.1%RDG ±80 mK at 77 K
Control Stability	±1 mK at 77 K

5.2.10.1 Lake Shore Model 340 Temperature Controller

The Lake Shore Model 340 temperature controller is a 32-bit microprocessor-based controller. It has four independent sensor inputs when purchased with the 3462 option. Two PID loop controllers are supplied; the primary is a full-featured loop powered to 100 W, and the secondary control loop has reduced features and lower power (1 W). In GSAOI, the primary loop will be used to control the temperature of the focal plane while the secondary loop will be used to control the detector housing temperature. The two spare sensor inputs will be used to monitor the temperature sensors on the H2RG. Useful features of the Model 340 include:

1. Heater Output Protection: The controller has set point temperature limit, heater current range limit, internal heater diagnostics, and a fuse in the heater output wiring.
2. Set point ramping, and zones: The set point ramp feature allows smooth, continuous changes in set point at a prescribed rate. The zones feature allows different PID constants to be set for different detector temperature ranges.

Full specifications of the Model 340 temperature controller are described in Appendix B (§9.11, and §9.12).

[8] http://www.Lakeshore.com

5.2.10.2 Cernox Temperature Sensor

The detector temperature stability requirement dictates that a CX-1080-LR Cernox temperature sensor be used on the focal plane cold finger. For simplicity, the same type of sensor will also be used for the detector housing. The CX-1080 sensor is a Lake Shore Cernox™ ceramic oxynitride thin film over sapphire negative temperature coefficient resistance temperature detector. A CX-1080-LR-20L sensor will be used. This sensor is calibrated over the temperature range 20 K to 325 K. The chosen package (SD package soldered in a LR mount) is described in Figure 80, Figure 81, Table 41, and Table 42. The LR package was chosen for ease of mounting, low thermal mass, and small size. The LR package has an SD packaged sensor mounted on a slightly more than half-rounded cylinder. This package inserts into a 3.2 mm (1/8 inch) diameter hole. Note that the solder used in this package limits the maximum upper useful temperature to 325 K. The same sensor has been used successfully in NIFS with a Lake Shore Model 340 temperature controller.

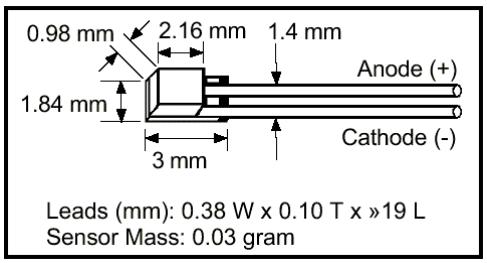

Figure 80: Lake Shore SD temperature sensor package.

Table 41: Lake Shore SD Temperature Sensor Package

Material of Package	Sapphire base with alumina body, and lid. Molybdenum/manganese metallization on base, and lid top with nickel, and gold plating. Gold tin solder as hermetic lid seal.
Leads	Qty: (2) Size: 0.38 mm × 0.1 mm thick × 12.7 mm long.
Lead Material	Nickel, and gold plated Kovar, uninsulated.

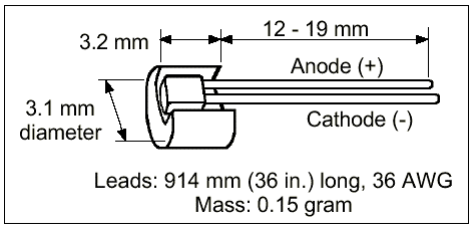

Figure 81: Lake Shore LR temperature sensor package.

Table 42: Lake Shore LR Temperature Sensor Package

Material of Adaptor	Flat cylindrical copper disk, gold plated (SD soldered to adaptor).

5.2.10.3 Heater Resistor

The heater resistor should be located so that heat flow between the cooling power and the heater is minimized. This requires that it be in close thermal contact with the cooling power, and if possible that it be mounted by the same screw that holds the cooling strap. The heater resistor should also have low thermal resistance and thermal time lag to allow the temperature control to react quickly to temperature disturbances. The imager detector temperature control system will use the Vishay RTO series TO-220 package heater resistors shown in Figure 82 to meet these requirements. This series has a low thermal resistance of 2.6 K/W. These types of resistors have been successfully used in the NIFS cryostat, and is the same package type used by ESO.

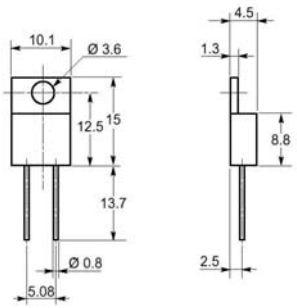

Figure 82: Vishay RTO series TO-220 package dimensions.

5.2.11 Test Facilities

The four HAWAII-2RG imager detectors will require extensive testing and characterization before they are installed into the GSAOI cryostat. The GSAOI cryostat will not be available for detector installation until late in the project and the cryostat would be inefficient for detector testing because of its long thermal cycle time (8-10 days). A separate detector test system will be required. This will consist of a test cryostat of sufficient size to accommodate the GSAOI focal plane assembly, a duplicate temperature control system, a test focal plane assembly include the motherboard, flex circuits, and mounting brackets, a suitably equipped detector controller and cabling, and sufficient test software to perform detailed detector characterization.

5.2.11.1 Test Cryostat and Temperature Controller

A large, and very low background test cryostat will be required to perform characterization tests on the imager detector. We plan to construct a new facility for this purpose. This test cryostat will have a cool down/warm up time of < 24 hours. It should cool the focal plane to 60 K and allow it to be heated to 90 K while maintaining the focal plane temperature to within 1 mK over a 600 s exposure time. It must be capable of accommodating the final GSAOI focal plane assembly and cryostat wiring so that these items can be pre-tested before transfer to the GSAOI cryostat. The test cryostat must also be able to completely blank off the detectors for dark current measurements and to illuminate the detectors fully or partially in each of the *J*, *H*, and *K* photometric bands for measurements of flat fields, persistence, cross-talk, and quantum efficiency. The baseline design of the test cryostat is described in Appendix B (§9.13).

A second Lake Shore Model 340 temperature controller and Cernox sensors will be required for use with the test cryostat.

5.2.11.2 Test Focal Plane

A duplicate imager focal plane assembly will be required. This is because we expect that the science grade imager detectors will be delivered late in the project when the engineering grade detectors are already installed in the GSAOI cryostat. A duplicate imager focal plane assembly will be required to characterize

the science-graded detectors in the test cryostat while a separate engineering system is being used in the GSAOI cryostat for alignment tests and instrument characterization. The second focal plane assembly will be manufactured and assembled by GL Scientific.

5.2.11.3 Test Detector Controller

A duplicate detector controller will be required initially for software development, and eventually to allow the four GSAOI science-grade detectors to be characterized at the same time as the two engineering-grade detectors are being used to align and test the GSAOI instrument. The test detector controller will require a 12.5 Mpixel/sec PCI interface board to communicate with CICADA test software, which runs on a Sparcstation. An additional 12.5 Mpixel/sec PCI interface board will be required to use with the final detector controller for CICADA development work, and for alignment and GSAOI instrument testing while the final DC IOC software is developed.

5.2.11.4 Test Software

The in-house CICADA software for operating SDSU-2 detector controllers has been modified to communicate with the NIFS SDSU-2 detector controller through an SBUS interface board. This software controls a 2048×2048 HAWAII-2 detector. Some modification to this software is expected in order to interface through a 12.5 Mpixel/sec PCI interface board, to handle the larger data flow of 4096×4096 pixels, to support the additional features of the HAWAII-2RG detector, to support the definition and readout of the ODGW, and to meet the additional requirements of the GSAOI detector system. For the ASIC detector controller option, further modifications will be required to support its different interface requirements. These modifications are discussed further in §7.3.4.3.2.7.

5.2.12 Detector Characterization

The detector will be characterized by varying detector temperature and bias voltages to obtain the best quantum efficiency, well depth (~ 100,000 e), linearity (~ 1%), and cosmetic quality while minimizing read noise (< 20 e), dark current (0.1 $e\ s^{-1}\ pix^{-1}$), and cross-talk. Tests will be performed to characterize persistence, stability, the effect of power down of the output amplifier, linearity, and the effect on the imager frame of reading out the ODGW.

5.2.12.1 Persistence

There are conflicting reports on whether or not persistence is a problem with MBE detectors. Preliminary tests by Don Hall with a 5.0 μm HAWAII-1R show no persistence, while tests by Augustyn Waczynski (GSFC/GST) with a 1.7 μm HAWAII-1R show persistence. Tests will be required to characterize the persistence of the GSAOI H2RG 2.5 μm detectors.

5.2.12.2 Stability

The stability requirement for the imager is more relaxed than for NIFS, which uses a HAWAII-2 (50 e/hr versus 2e/hr). By the time the characterization of the imager detector begins, the techniques for obtaining good stability from HAWAII type detectors driven by SDSU detector controllers will be known. These techniques were discussed in the NIFS Critical Design Review. The imager SDSU detector controller will be temperature stabilized by water-cooling (§5.2.5) and high stability biases will be provided. Further tests will be required to characterize the use of the ODGW while exposing the imager (§5.2.12.5.2).

Less is known about the stability of the ASIC detector controller. The ASIC is less temperature sensitive than the H2RG MUX. Temperature variations in the H2RG directly affect the threshold voltages of the internal FETs that translate into direct voltage shifts at the output. However, the ASIC is affected by changes in the current sources through the threshold voltage shifts. Rockwell intends to mount the ASIC in a custom Pin Grid Array (PGA) package. The ASIC will sit inside a cavity surrounded by the pins of the PGA. The backside will be "capped" (Cu?) with a thermal heat sink to extract heat and maintain a uniform temperature. A temperature controlled copper block can be attached to the “cap” to obtain good

temperature stability. Rockwell currently does not have stability performance data for the ASIC. The data will not be available until tests are performed on the finished devices. Consequently, the GSAOI ASIC detector controller design provides temperature stabilization of the ASICs by thermally connecting them to the detector housing. The thermal stability of the detector housing is specified at tens of mK. This is not as good as the detector focal plane, but is expected to be sufficient.

Tests will be performed to determine how best to use the H2RG reference pixels and embedded reference outputs.

5.2.12.3 Output Amplifier Power Down

Tests will be performed to characterize the effect on detector stability and glow of powering down the signal and reference output amplifier during integrations. Glow is eliminated when the output amplifier is powered down. On the other hand, power down and power up of the output amplifier changes the power dissipation and heating of the detector. Temperature changes from this heating could cause instability. The output amplifier used in slow 100 KHz readout mode is powered down by either resetting or overclocking the horizontal register or lowering the READEN signal. The power down and power up of the reference output is more complicated. Bits in the configuration register select between two options. One option uses the end of line status signal, LINECHK, to power down the reference. The other uses the line synchronization clock, LSYNCB.

5.2.12.4 Linearity

There are two main causes of non-linearity in infrared detectors:

1. Non-linearity due to charge storage at the pixel. The detector capacitance changes with the detector reverse bias voltage. The detector reverse bias voltage changes as charge is accumulated on the detector.
2. Non-linearity due to the detector output amplifier.

The HAWAII-2 detectors are linear to the 1-2% level (Klaus Hodapp priv. comm.). It is likely that the H2RG will have similar linearity. Tests will be carried out to measure both low and high level non-linearity, and to identify the major causes of non-linearity. Varying the type (resistor or current source) and value of the output amplifier load will be investigated. If linearity correction is necessary then the standard technique of using α to parameterize the non-linearity will be used, where

$$N_m = N_t \times \left[1 + \alpha \times N_t\right],$$

N_m is the measured (i.e., non-linear) counts in ADU above the bias level, and N_t is the true (i.e., linear) counts in ADU above the bias level.

5.2.12.5 ODGW

For ODGW tip-tilt and flexure monitoring, the H2RG guide window will be read out at up to 100 Hz throughout the exposure of the imager detector. The ODGW readout may cause additional read noise, instability, and glow problems.

5.2.12.5.1 Read Noise

Tests will be performed to characterize the effect on the read noise of the imager detector of reading out the ODGW at a readout speed of 100 kHz and at an ODGW frame rate of 100 Hz. The agreed H2RG read noise specification for 100 kHz slow readout mode is 15/10 e (offer/goal). At the baseline readout speed of 200 kHz, the read noise should increase by the √BW to 14/21 e (offer/goal). As the 100 kHz slow readout design is similar to HAWAII detector predecessors, the goal read noise of 14 e is expected to be achieved. Gemini has recognized the potential problem of the ODGW readout causing additional imager read noise and in the contract with Rockwell for the H2RGs has negotiated specific read noise requirements when reading out the guide window. These are that the Root Mean Squared (RMS) read noise of pixels (up to

ten-pixel distance) surrounding the guide window should not exceed 10 e above the mean and pixels outside this region should not exceed 5 e above the mean. These requirements are specified for a guide window readout rate of 5 MHz and no mention is made of how many reads of the guide window are performed to meet these requirements.

5.2.12.5.2 Stability

Tests will be performed to characterize the effect on the stability of the imager detector of reading out the ODGW at a readout speed of 100 kHz and at an ODGW frame rate of 100 Hz. The read out of the ODGW during the imager detector exposure will dissipate power and cause heat flow in the detector. This heat flow may introduce instability problems. This can be reduced by lowering the drive current to the guide window output amplifier and/or using external amplifiers. Its impact can be reduced by reading the ODGW before the imager exposure so that the history of power dissipation of the start reads and end reads of the CDS are similar.

5.2.12.5.3 Glow

Tests will be performed to characterize the extent of glow generated by reading out the ODGW. Output or multiplexer glow should not be a problem with the H2RG during the readout of the imager detector because the H2RG has special design features to minimize glow. However, glow may be an issue when the ODGW is used. A small amount of glow from each read of the guide window will add during the imager exposure. As only one output amplifier is used to read out the ODGW this glow should be restricted to a small subregion around that output. If glow is a problem, techniques such as lowering the drive current to the output amplifier and the use of external amplifiers will be employed.

5.3 OIWFS Detector System

5.3.1 OIWFS Requirements

The OIWFS detector controller provides the biases and the correct sequence of clocks to drive and read out the OIWFS HAWAII-1 detector. The OIWFS detector controller communicates with the Gemini A&G IOC. The A&G IOC sends commands through a 2.5 Mpixel/s SDSU fiber-optic link to the detector controller to set operational parameters and initiate readouts. The detector controller transmits replies and acquisition and guide window data in responses to these commands. The detector controller must support the following OIWFS functional requirements:

- Correlated double sampling and Fowler sampling (binary values from 1 to 64 samples) readout methods on a guide window and acquisition windows;
- Coaddition of between 1 and 128 (binary values) guide window and acquisition window data frames before the result is transferred to A&G IOC;
- Integration times from 10 ms to 1000 s on guide window and acquisition windows;
- Fixed guide window of four 8×8 pixel subimages;
- Fixed acquisition windows of 40×40 and 80×80 pixel subimages;
- Acquisition and subtraction of a sky background frame on the guide window;

and meet the following performance requirements:

- Readout the guide window using CDS at a maximum continuous frame rate of ≥ 100 Hz;
- Have low enough read noise to achieve the effective detector read noise requirement of < 20 e;
- Have bias variations over 30 s of less than the read noise.

5.3.2 Design Overview

RSAA will duplicate the NIRI/NIFS HAWAII-1/SDSU-2 OIWFS detector system for GSAOI. No modifications to the NIRI/NIFS OIWFS detector system are foreseen.

Other detectors have been investigated. However, none offer sufficient performance improvement to warrant the additional design and development costs that their implementation would entail.

A single quadrant science quality HAWAII-1 (1Q HAWAII-1) detector (Figure 83).will be purchased from Rockwell. Its should have low noise and have a good cosmetic subregion of 80×80 pixels adjacent to the output amplifier. Rockwell has quoted a delivery time of 12 months.

5.3.3 Detector Selection

HAWAII-1R and HAWAII-1RG devices were evaluated as alternative OIWFS detectors. The HAWAII-1RG was considered for compatibility with the imager detector and to take advantage of the guide window mode of the multiplexer. The guide window mode allows fast readout of a guide window located any where on the array. In contrast, fast readout of a HAWAII-1 detector restricts the guide window location to the corner of one quadrant near the output amplifier. The 40×40 and 80×80 pixel acquisition windows must then be offset from the guide window, so it is necessary to offset the OIWFS steerable mirror to center the target in the acquisition window.

HAWAII-1R and HAWAII-1RG detectors also have lower dark current, no persistence, and reference pixels. However, for the fast-readout application of the OIWFS, the higher dark current, persistence, and reduced stability of the HAWAII-1 detector are not limiting factors.

The performance of the existing system meets the requirements of the OIWFS and the steerable mirror can be repositioned accurately with minor impact on observing efficiency, so the extra costs of developing and implementing a different OIWFS detector system are deemed not to be warranted.

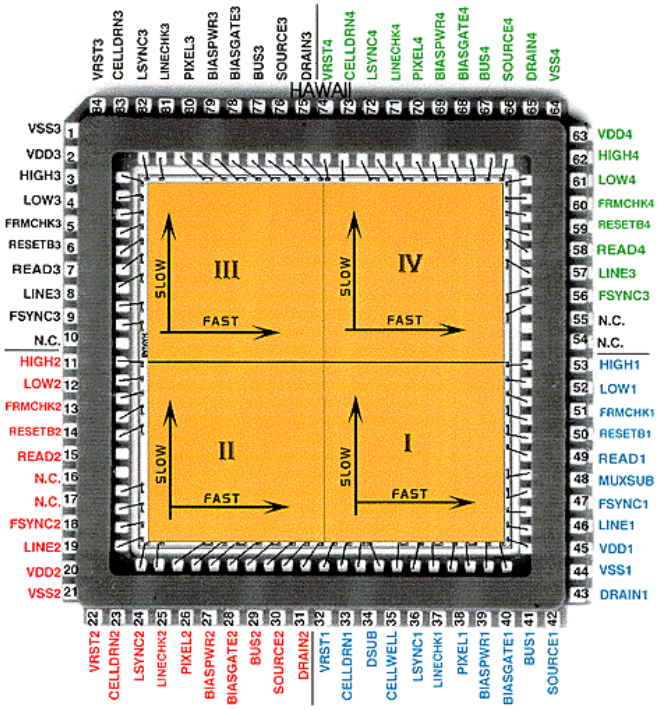

Figure 83: HAWAII 84 pin Leadless Chip Carrier pad layout.

5.3.4 Possible DSP Code Upgrade Option

The baseline OIWFS design will use existing DSP code without change. Corinne Boyer (Gemini) has expressed concern over the readout performance of the current NIRI/NIFS OIWFS DSP code. The OIWFS DSP code has been inspected and areas have been identified where doing operations in parallel can speed up the readout. The expected duty cycle improvement is of the order of 35% at 150 Hz frame rate, 19% at 100 Hz, and 8% at 50 Hz. It is our understanding that Tim Hardy (National Research Council Canada) has been approached about upgrading the current DSP code (Doug Simons, priv. comm.). If this does not eventuate, an option of RSAA upgrading this DSP code is offered.

Table 43: Expected Duty Cycle Improvement at Different Frame Rates From Faster DSP Code.

	Guide Window Size	Single Read Time (ms)	CDS Read Time (ms)	Total Pixels	Processing time at 10 instructions per pixel at 40 ns per instruction (ms)	Transfer Time up 2.5 Mpixel/s link (ms)	Total Cycle Time (ms)	Duty Cycle At 150 Hz Frame Rate (%)	Duty Cycle At 100 Hz Frame Rate (%)	Duty Cycle At 50 Hz Frame Rate (%)
Current	**four 8×8**	2.6	5.1	256	0.10	0.256	5.5	56%	71%	85%
Upgrade	**four 8×8**	1.6	3.2	256	0.10	0.256	3.6	76%	84%	92%
Improvement		38%	38%	0%	0%	0%	35%	35%	19%	8%

5.3.5 Test Facilities

The HAWAII-1 detector will not go through a characterization phase in a test cryostat, but additional time will be allocated during the OIWFS detector system integration phase for its characterization. This will save on development costs. It is justified because the HAWAII-1 for this application does not require extensive characterization (priv. communication Klaus Hodapp, IfA) and no optimization of the wiring, mounting, or grounding system is required because the design is proven.

5.4 Detector Systems Risks

5.4.1 Detector Delivery

Late delivery of the imager detectors and the OIWFS detector is a schedule risk.

The imager detector MUX is required by January 2004, the engineering detectors are required by May 2004, and the science grade detectors are required by September 2004. This risk will be mitigated by remaining in close contact with Rockwell, by monitoring H2RG detector progress at IfA, and by implementing approaches used by the IfA group in advance of the GSAOI detector delivery.

Rockwell have quoted a delivery time of 12 months for the OIWFS detector. This should not be problematic.

5.4.2 Detector Damage

The imager detector is the most critical components of the system. It is also one of the most fragile. Extreme precautions will be taken in handling and storing the device.

5.4.3 On-Detector Guide Window Performance

The potentially detrimental effect of the ODGW readout on the performance of the imager detector is a concern. This may result in the ODGW being unusable. In this case, the OIWFS will be used for all tip-tilt and flexure monitoring. The GSAOI instrument will be designed for low flexure to ensure that it can be used in this way, even though this will be unnecessary if the ODGW is used.

5.4.4 Focal Plane Assembly Delivery

Late delivery of the focal plane assembly from GL Scientific is a schedule risk. This risk will be mitigated by defining the delivery schedule in the subcontract to GL Scientific, and by remaining in close communication with Gerry Luppino. The RSAA workshops will be available to assist in the manufacture of the focal plane assembly should this prove necessary.

5.4.5 SDSU-2 Induced Bias Drift

The imager detector output has to meet the low bias drift requirement. To achieve this specification, drifts induced by the SDSU-2 detector controller video processors, clock voltages, and bias voltages must be controlled.

Bias drift induced by the SDSU-2 detector controller has been investigated in developing the NIFS detector system. Sources of bias drift have been eliminated to the greatest extent possible by replacement with more stable components. It has been necessary to temperature control the SDSU-2 controller to reach the high levels of stability that are required. The same procedures will be implemented for GSAOI.

A custom high stability, low noise bias generator board will be designed to supply the more sensitive biases needed for the H2RG detectors.

5.4.6 ASICs Induced Bias Drift

The same low bias drift requirement applies to the ASIC detector controller. The stability of the ASICs is a potential limiting factor in the imager detector performance. To mitigate this risk, we will monitor ASIC performance during testing at IfA and elsewhere. The focal plane assembly will have a facility for heat sinking the ASICs to the base plate of the detector housing to improve their thermal stability.

5.4.7 ASICs Performance

The development of the ASICs is currently at the design phase and there are no data available to determine whether they will meet GSAOI performance requirements. To mitigate this risk, the development of the ASIC will be monitored and through collaboration with IfA early test data will be sought to determine the adequacy of ASICs to meet GSAOI requirements.

5.4.8 SDSU Detector Controller Delivery

5.4.8.1 PMC Interface Board

The SDSU PMC interface board has not been fully developed yet. The circuit design of the PMC board is identical to the PCI interface board that is already available, but the board dimensions and connectors are different. Bob Leach does not intend to complete this design until he receives his first order. He estimates that it will take four months to repackage the PCI board. Placing the order for the PMC interface board as soon as possible will mitigate the risk of late delivery. The PCI interface board will be used for development of test software and initial detector testing.

5.4.8.2 Octal Channel IR Video Processor Boards

The Octal Channel IR Video Processor Boards are still being developed. They are at the stage of first prototype testing. They should be available within the next couple of months. Placing the order for the Octal Channel IR Video Processor Boards as soon as possible will mitigate the risk of late delivery. The progress of testing the Octal Channel IR Video Processor Boards will be monitored. Quad Channel Coadder IR Video Processor Boards or Dual Channel IR Video Processor Board will be used if the Octal Channel boards are not available in time.

5.4.9 ASIC Microcontroller Code Development

Development of ASIC microcontroller code is a schedule risk because little is known about the sophistication of the development system that Rockwell will provide. This risk will be mitigated by obtaining template microcontroller code from Rockwell and from IfA.

5.4.10 Test Cryostat Development

The need to develop a separate cryostat for testing the imager detector focal plane assembly is a schedule and cost risk because the design of this test cryostat is yet to be finalised. Negotiations have begun to possibly duplicate the test cryostat developed by Don Hall at IfA.

6 Instrument Control System

6.1 Introduction

The GSAOI instrument is a complex arrangement of optical elements, wheels, and sensors that need to be thermally controlled as well as configured with high precision in order to assure maximum scientific potential and versatility. It is the function of the Instrument Control System (ICS) to control these operations. Broadly speaking, the ICS can be thought of as two separate control systems operating under the same VME single-board processor: the Mechanisms Control System (MCS) and the Temperature Control System (TCS).

The MCS is a closed-loop stepper-motor control system responsible for all movable elements within the cryostat. Although there is a motion feedback loop within the MCS, it is primarily used for "datum" detection. Most motion control within the cryostat relies upon dead reckoning stepper motor counts from a datum position through a reduction gearbox to ensure sufficient resolution.

The TCS is responsible for temperature regulation and control of the imager detector, the OIWFS detector; and the Cold Work Surface (CWS) plate during cool down and warm up. This is achieved using two temperature controllers and a temperature monitor in the ICS thermal enclosure, and a separate temperature controller in the DCS thermal enclosure.

GSAOI will use the same motors, encoding philosophy, and thermal control as NIRI and NIFS. This allows the GSAOI ICS to be nearly a direct copy of the NIRI/NIFS ICS, and as such will be the second refinement of a successful existing design. A major benefit of this design strategy is in the reuse of design documents, schematics, and artwork, effectively bootstrapping the design to an advanced stage.

This section describes the operation of the GSAOI ICS, and highlights areas where the GSAOI ICS will differ from that used in NIFS.

6.2 Mechanisms Control System

The Mechanisms Control System is responsible for moving and positioning all of the optical elements associated with the GSAOI instrument. There are two major assemblies within the cryostat; the imager and the OIWFS. Externally there is also an environmental cover.

All movable elements within the GSAOI cryostat can be categorized as:

1. Rotary positioned,
2. Linearly positioned, or
3. Open/closed (or in/out).

The GSAOI MCS will control and position ten active elements. Table 44 lists the GSAOI mechanisms with their corresponding NIFS mechanisms and the mode of actuation.

Table 44: GSAOI and NIFS Motor-Controlled Mechanisms and their Mode of Actuation.

GSAOI Mechanism	NIFS Mechanism	Actuation
OIWFS Steerable Mirror Axis-A	OIWFS X-Axis Gimbal	Linear
OIWFS Steerable Mirror Axis-B	OIWFS Y-Axis Gimbal	Linear
OIWFS Steerable Mirror Axis-C	N/A	Linear
OIWFS Filter Wheel	OIWFS Filter Wheel	Rotary
OIWFS Aperture Wheel	N/A	Rotary
Imager Focal Plane Wheel	Spectrograph Focal Plane Mask Wheel	Rotary
N/A	Spectrograph Flip Mirror	In/out
Imager Utility Wheel	Spectrograph Grating Drive	Rotary
Imager Upper Filter Wheel	Spectrograph Order Blocking Filter Wheel	Rotary
Imager Lower Filter Wheel	N/A	Rotary
Imager Fast Shutter	N/A	Rotary
Environmental Cover	Environmental Cover	Open/closed

6.2.1 Control Strategy

An open loop scheme using stepper motors and dead reckoning is employed using Hall-effect sensors to provide "datum" positions. Once a zero-point is established, the number of steps taken by the stepper motor determines position.

Hall-effect sensors consist of a small block of semi-conductor material, such as indium, sandwiched between two electrodes. They produce a weak direct current voltage, typically 10 millivolts per kilogauss across the electrodes, in the presence of a magnetic field. The polarity of the potential difference is a function of the "pole orientation" of the magnet field (north-seeking or south-seeking), as well as the polarity of the Hall-effect sensor excitation voltage.

The position monitoring and calibration system will use stationary Hall-effect sensors and small position-indicating magnets mounted on specific moving parts of all stepper motor driven optical component mechanisms. Additional (redundant) Hall-effect sensors, which are software selectable, will be incorporated to improve reliability.

6.2.1.1 Rotary Positioned Elements

The output from the Hall-effect sensor, as the magnet passes under it, rises to a peak as more magnetic flux passes through the area of the Hall-effect sensor and then declines again as the magnet moves away (Figure 84).

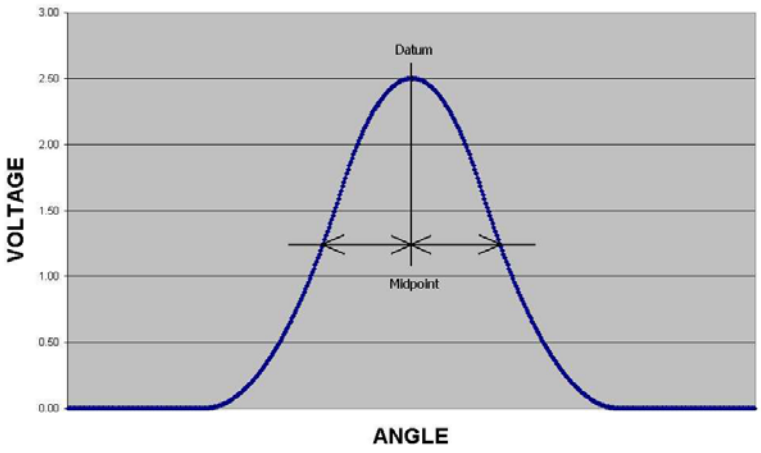

Figure 84: Hall-effect sensor output voltage versus magnet angle.

The "datum" sensor is comprised of a stationary Hall-effect sensor aligned with a magnet mounted in the drive gear on the stepper motor shaft. The datum position is found by finding the midpoint between two points of identical flux (output voltage from the Hall-effect sensor). This provides a high level of repeatability and is tolerant to sensor sensitivity and voltage drifts or offsets introduced by the Hall-effect sensor amplifiers.

Mechanism positions are monitored using a second set of magnets mounted in the final rotating element of the mechanism (e.g., the filter wheel) and a stationary Hall-effect sensor. Placing another Hall-effect sensor in parallel with the first provides redundancy. Rather than mounting it on top of the primary, it is placed to the side on a slightly different radius. By then adding additional magnets of variable field strengths, a two or three track positioning system can be incorporated with little additional effort. At each mechanism position, the output voltages of the Hall-effect sensors are measured and compared with those stored in a calibration table. If these values are out of tolerance, an error is signalled.

The position indicating magnets are samarium cobalt rod-shaped magnets, which produce a magnetic field intensity of approximately one kilogauss. Adjusting the depth of the mounting hole controls the field intensity at the Hall-effect sensor.

Being a rotary system, there is no need for limit switches or hard stops to prevent excess travel.

6.2.1.2 Linear Positioned Elements

The OIWFS steerable mirror A, B, and C-axis positioners are linearly positioned elements. These linear elements move back and forth on threaded screws over a finite travel distance. Position is determined by setting a datum and counting steps from that datum.

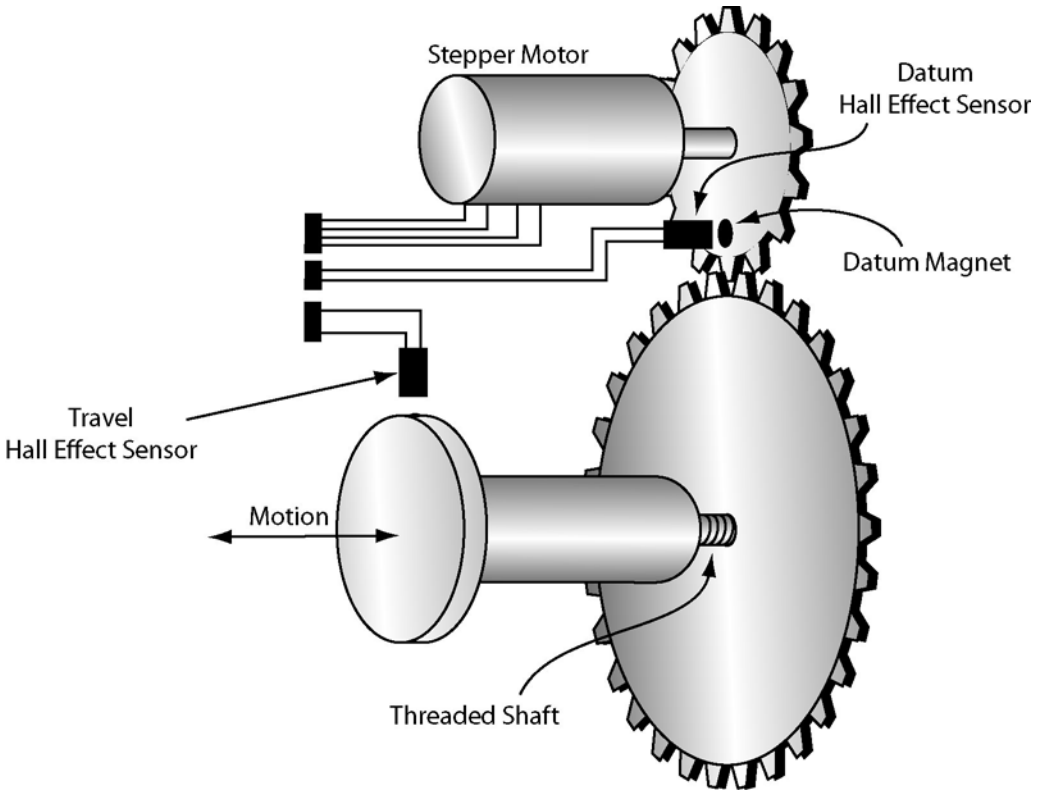

Figure 85: Encoding scheme for linear positioned elements.

Accurate datuming of the steerable mirror is accomplished using a mechanical stop at the end of travel of the threaded shaft and a clutched drive from the stepper motor. To datum, the threaded shaft is simply reversed into this stop until the clutch slips. The motor can then be stopped at a selected step count and forward motion from this point will be in absolute step counts from the datum position.

Hall-effect sensors are located on the motor shaft drive gear to indicate motor revolutions as well as on the threaded shaft to indicate linear travel. These sensors are not required for datuming or position indication during operation. They are provided primarily as a diagnostic tool.

For redundancy, all Hall-effect sensors operate in pairs, mounted in parallel with a software switch choosing between primary or backup sensor. Should one Hall-effect sensor fail, the computer will switch to the backup sensor.

6.2.1.3 Open/Closed Elements

The environmental cover is an open/closed element. The cover is a two vane sliding cover, driven by a DC servo motor with limit switches signalling the end of travel (Figure 86). In the "Closed" position, the cover should be light tight and protect the cryostat window from dirt, dust, and moisture likely to be encountered during storage or shipping. In the "Open" position during operation, the cover should be retracted and provide an unobstructed path for light to enter the cryostat.

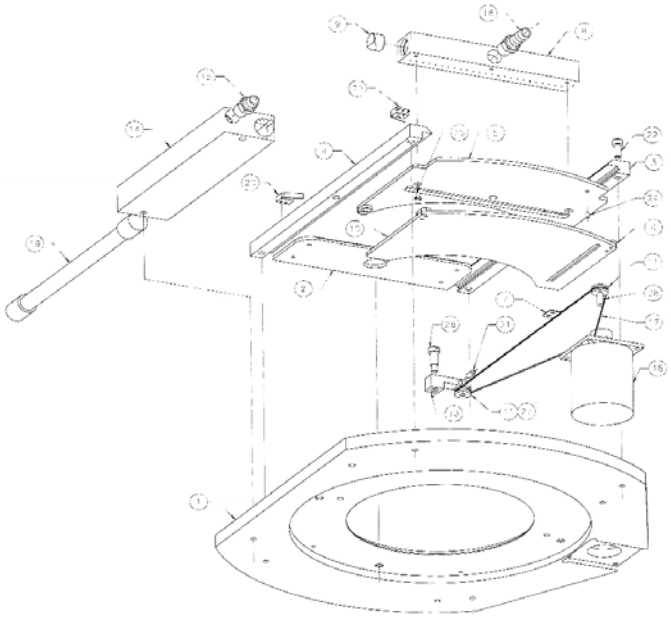

Figure 86: Environmental cover assembly drawing.

The environmental cover will be a duplicate of the NIRI/NIFS cover, but will be modified by replacing the NIRI/NIFS stepper motor with a DC motor and gearbox. This is required for two reasons. First, GSAOI will use all of the stepper motor drivers in the MCS for cryogenic stepper motors. Second, the stepper motor used with the NIRI/NIFS environmental cover does not hold the cover against gravity so the cover can slide closed during observing. The use of a DC motor will overcome this problem. Solid state relays operated by digital I/O from the VME crate will be used to control the DC motors.

An ioniser/sprayer head (item 14 in Figure 86) is separate to the mechanism for opening and closing the environmental cover but part of the same sub-assembly. This head is responsible for venting de-ionized,

dry, non-turbulent air over the cryostat window in order to prevent moisture condensing during astronomical observations.

A cleaning spray bar (item 8 in Figure 86) is also part of the environmental cover sub-assembly. It uses a high-pressure jet of dry air to clean the lower vane and cryostat window of large detritus.

The control system provides power to the ioniser/sprayer head and controls the operation of the cleaning spray bar.

6.3 Temperature Control System

The Temperature Control System is responsible for temperature control and monitoring during operation, cool down, and warm up of the GSAOI instrument. The GSAOI instrument consists of three main thermal sub-assemblies; the imager detector, the OIWFS detector; and the CWS plate.

6.3.1 Temperature Control

Two Omega CYC321-01 temperature controllers will regulate the CWS plate and the OIWFS detector sub-assemblies. The imager detector temperature must be regulated to milliKelvin level (§5.2.10). GSAOI will use a Lake Shore Model 340 temperature controller to control the imager detector temperature. This is a dual PID controller. The primary control loop will control the focal plane assembly cold finger temperature. The secondary control loop will control the detector housing temperature. The temperature set-point, heater On/Off, curve data, and output data for each temperature controller will be controlled over separate RS232 links via an XVME 490 Serial I/O board located in the ICS VME crate.

Heaters will be used to control heat flow such that the imager and OIWFS detectors are always maintained at a slightly positive temperature differential with respect to their surrounding environments in order to minimize condensation of any residual matter onto the detector surfaces.

6.3.2 Temperature Monitoring

Additional temperature sensors will be mounted at various locations within the cryostat for use during accelerated warm up and for thermal diagnosis. An Omega CYD-208 8 channel digital thermometer located in the stepper motor driver and heater control crate in the ICS thermal enclosure will monitor these sensors. The digital thermometer relays temperature readings via an RS-232 link to the Serial I/O board located in the ICS VME crate.

6.3.3 Cryocooler Control

The two closed-cycle helium cryocoolers are used to cool GSAOI. The first stage of the cryocooler head has the greater refrigeration capacity. These are both attached via cold straps to the CWS plate. The second stage of one cryocooler head, which achieves a lower temperature, is attached via a cold strap to the imager detector. A cold strap from the first stage of the other cryocooler head cools the OIWFS detector. The second stage of this cryocooler is attached to the vacuum getter.

CoolPower 5/100T cryocoolers will replace the CoolPower 130 cryocoolers used in NIRI/NIFS. The CoolPower 5/100T cryocoolers use pneumatically driven cold heads in which a stepper motor controls valve action. Varying the motor speed regulates the cooling rate, as it does in the mechanically driven CoolPower 130 cold heads. During normal cool down operation, the speed of the cryocooler will be set to high speed. Once a nominal cryostat operating temperature has been achieved, the speed of the cryocooler will be reduced to a value consistent with normal operation heat-load requirements. The high and low speed values will be set initially based on empirical data from NIFS and fine tuned during GSAOI commissioning.

The cryocooler stepper motor control signals are monitored by the cryocooler Motor Backup Module. This is a custom-designed board that monitors the integrity of the cryocooler stepper motor signals. In its basic mode of operation, the Motor Backup Module will take over the generation of the cryocooler stepper motor signals should they fall out of specification. This protects the cryostat from unexpected warm up in the case of control system malfunction.

6.3.4 Controlled Warm Up

Controlled warming of the GSAOI cryostat is achieved by turning off the cryocoolers and raising the set point of the thermal regulation systems.

The TCS controls the temperatures of the imager and OIWFS detectors during controlled warm up so that the detectors are always slightly warmer than the CWS plate. This helps prevent detector contamination.

6.3.5 Accelerated Warm Up

Accelerated warm up is possible by diverting power normally dedicated to the stepper motors to additional heater resistors located on the CWS plate. An additional 800 W will become available in this way.

Initiation of the accelerated warm-up operation requires active human intervention. To start an accelerated warm-up operation, the following must be accomplished:

1. A panel circuit breaker must be set.
2. A panel timer must be set.
3. All cryostat thermostat switches must be below 40 °C (100 °F).
4. A panel spring-loaded normally-off key-switch must be momentarily switched on.
5. UPS and telescope mains power must be present.

The TCS utilizes the computer-independent Auto-Shutdown and Interlock Safety System to prevent overheating of critical cryostat parts should any of the accelerated warm up systems fail. The safety interlock system will:

1. Prevent accidental turn-on of the high power heater system.
2. Require periodic "human verification" that cryostat temperatures are within normal limits.
3. Automatically shutdown the high power heater system if an UPS power failure should occur that could affect the accelerated warm up operation.
4. Automatically shutdown the high power heater system if cryostat temperatures exceed 40 C (100 F).
5. Provide a computer-independent temperature display of cryostat temperatures so that an operator can verify nominal warm up operation.

During accelerated warm up, the Auto-Shutdown System has the ability to disconnect the mains voltage to the power supply powering the cryostat heaters. Thermal switches, located inside the GSAOI cryostat, will trigger the shutdown. The Auto-Shutdown System will also be equipped with a timer that must be periodically reset in order to continue the accelerated warm up operation. This part of the Auto-Shutdown System will terminate the warm up operation and prevent overheating should weather conditions prevent observatory access. Additionally, the digital thermometer will allow crew personnel to visually check the cryostat temperatures.

6.4 Thermal Enclosures

GSAOI will use two Gemini-supplied thermal enclosures; the ICS thermal enclosure and the Detector Control System (DCS) thermal enclosure.

The ICS and DCS thermal enclosure layout diagrams are presented in Figure 3 and Figure 4. Their power requirements are listed in Table 3 and Table 4.

Figure 87 and Figure 88 show overviews of the ICS and its wiring to the cryostat. Figure 89 shows an overview of the DCS and its wiring to the cryostat. Figure 90 shows the cabling between the GSAOI ICS and the Cassegrain Connector Panel.

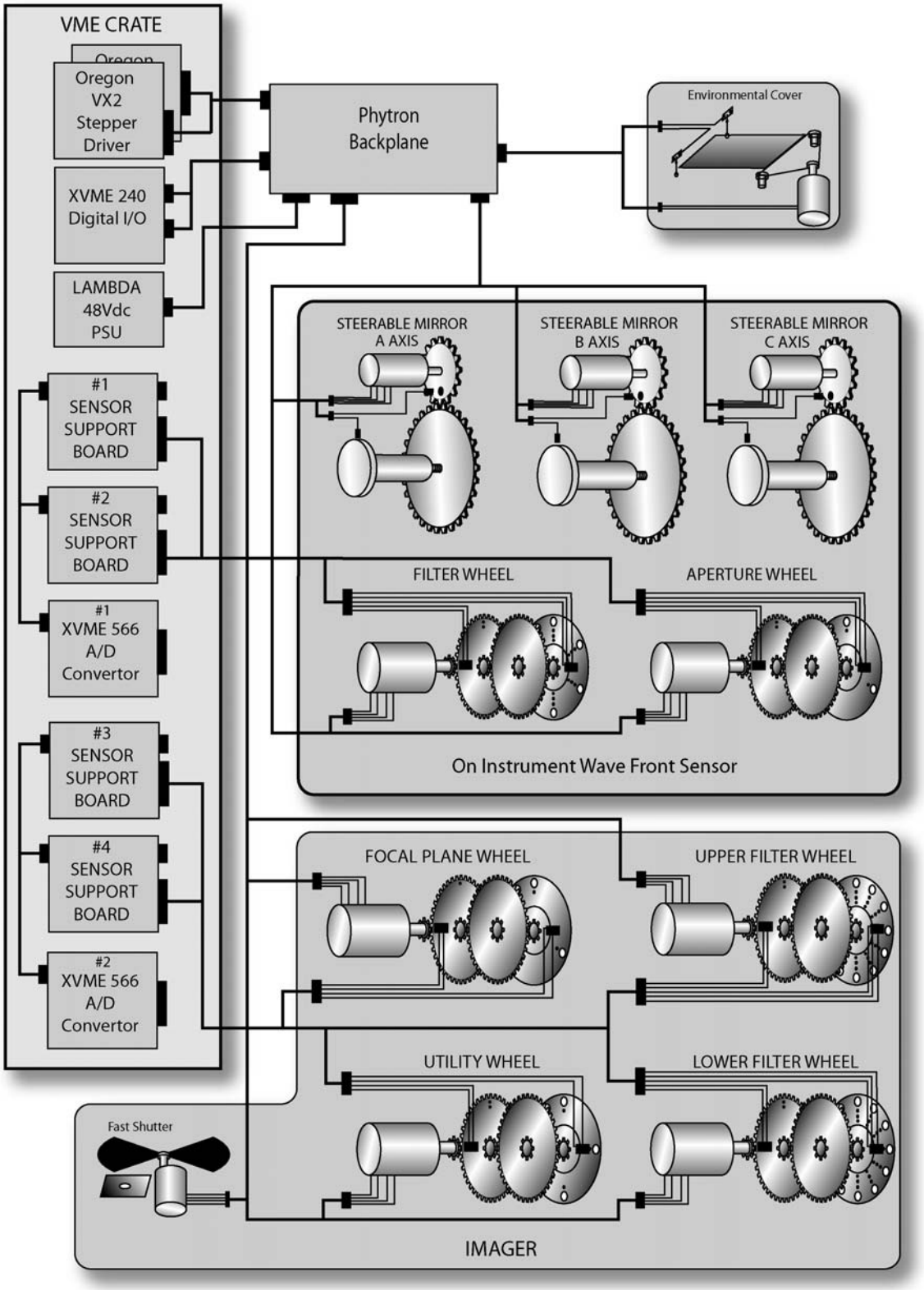

Figure 87: Mechanisms Control System wiring.

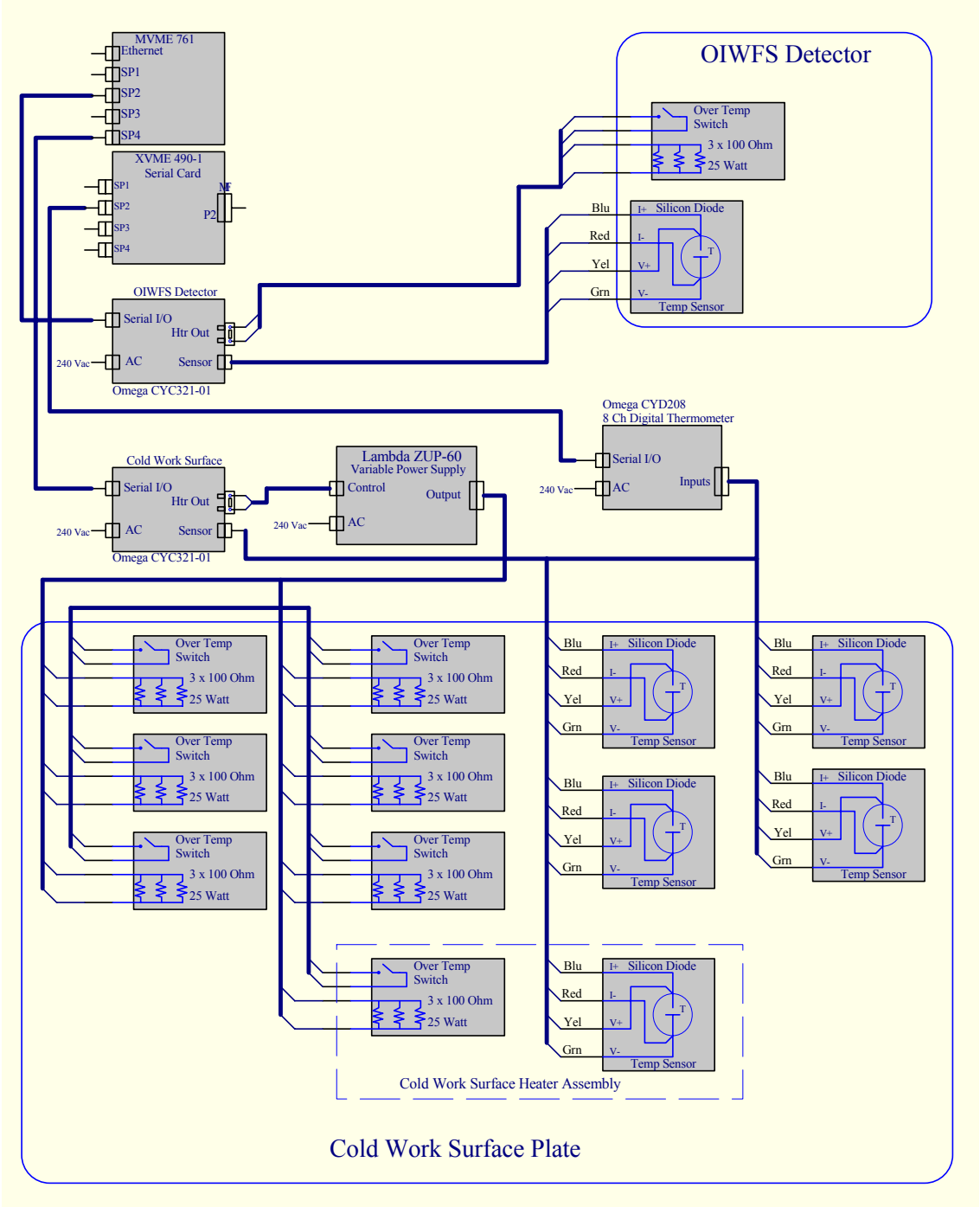

Figure 88: Temperature Control System wiring.

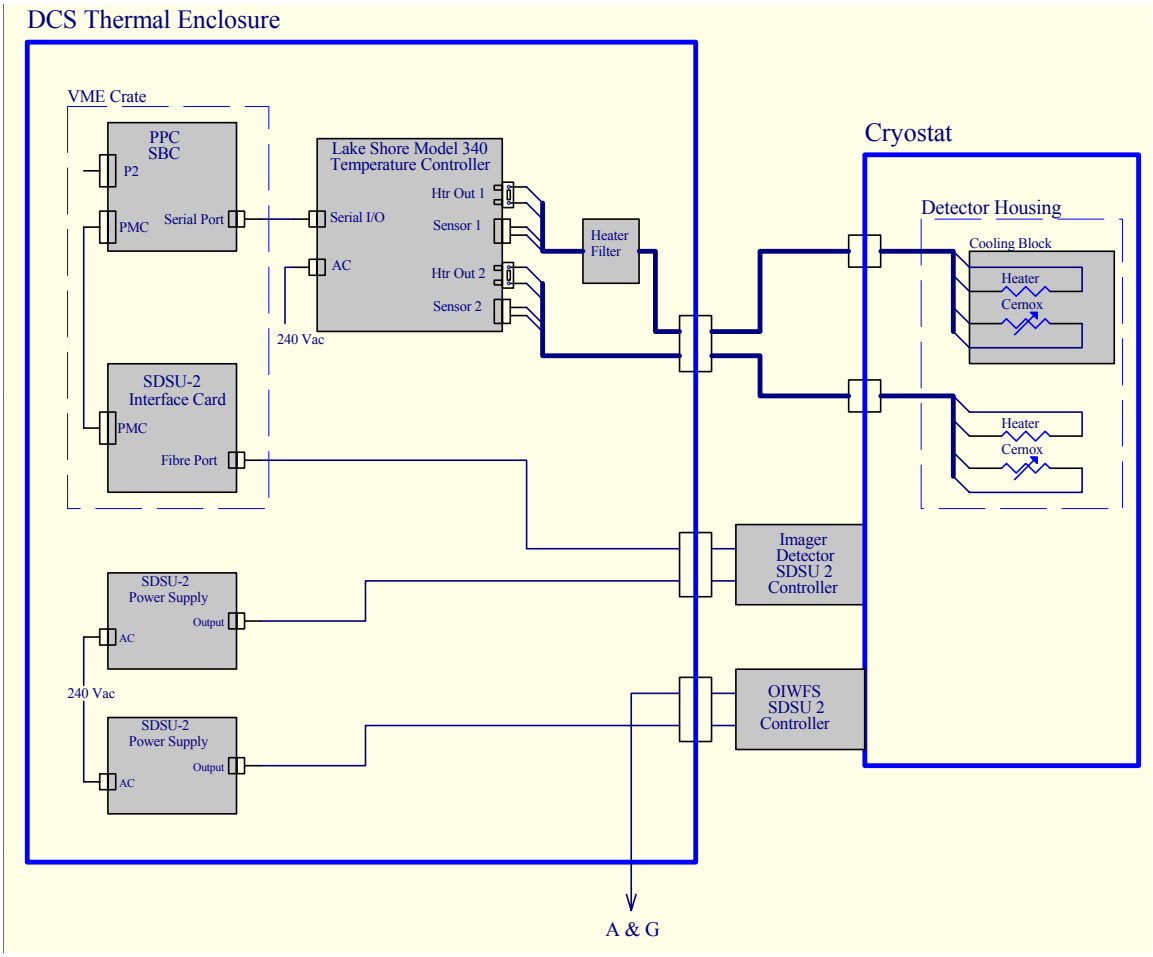

Figure 89: Detector Control System wiring.

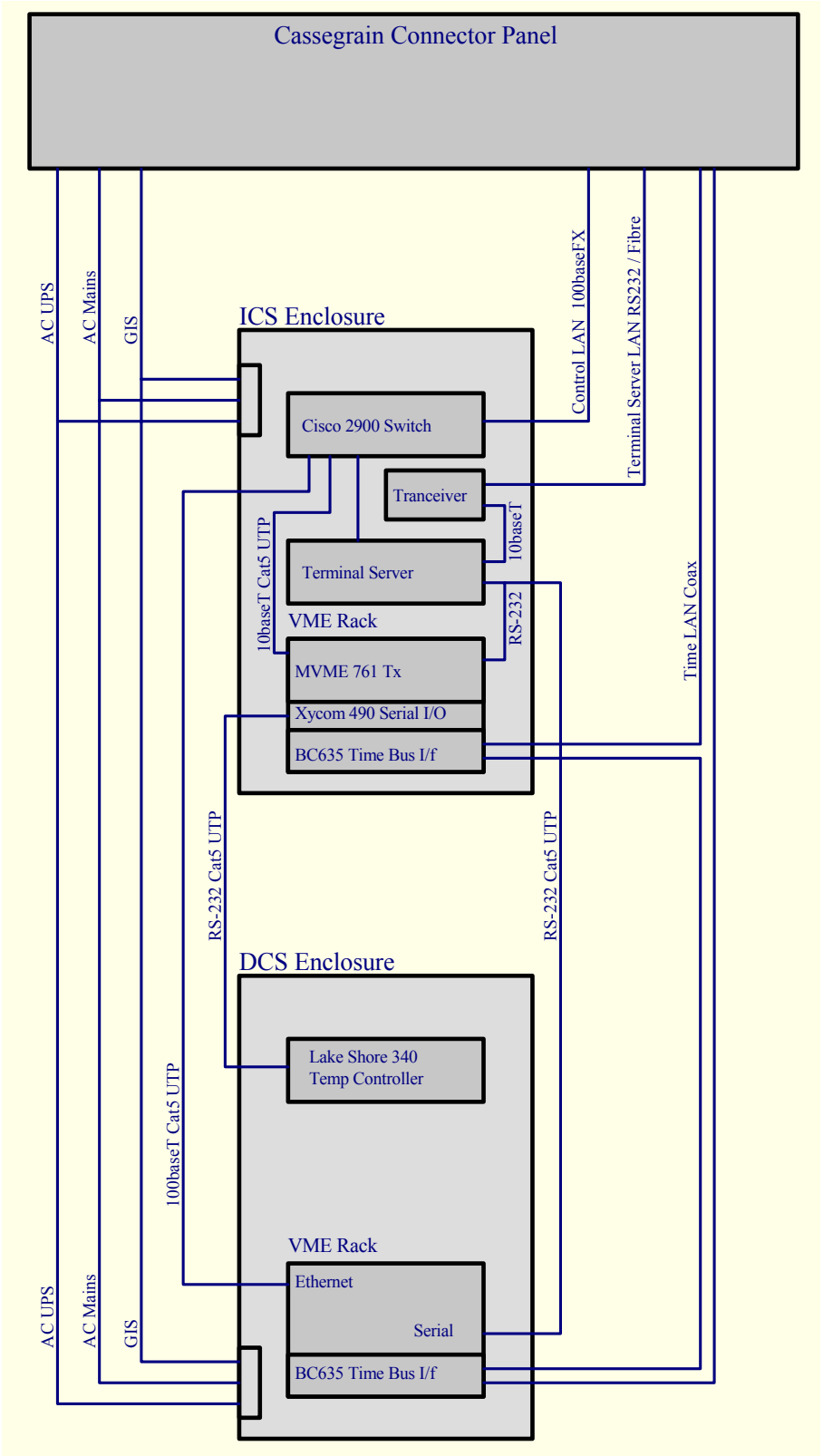

Figure 90: Interconnections between the thermal enclosures and the Cassegrain connector panel.

6.5 Manufacture

6.5.1 Printed Circuit Boards

The printed circuit boards (PCBs) necessary for the GSAOI ICS are listed in Table 45.

Table 45: GSAOI ICS Printed Circuit Boards.

Circuit Board Assembly	Number Required
Sensor Support Board	4
IDC64 – KPTO-55 Convertor	4
Phytron Backplane	1
Motor Backup Module	1
Thermal Isolation Board	8

The Sensor Support Boards (SSBs) are based on the boards used in the NIFS design.

The IDC64 – KPTO-55 Convertor is used to adapt the 64 pin IDC connector from the SSB VME backplane connector to a military-style circular connector on the ICS thermal enclosure back panel.

The Phytron Backplane PCB serves several purposes in the ICS. It provides the VME mounting connectors for the stepper motor driver modules. The stepper motor control signals from the stepper controller modules and datum signals derived from the Sensor Support Boards are grouped and routed through DB-37 connectors to the various parts of the cryostat. Separate circuitry supports the routing of the OIWFS steerable mirror limit switch signals and the safety interlock system.

The cryocooler Motor Backup Module PCB provides a safety backup for the cryocooler stepper motor controller should it fail in operation.

Thermal isolation boards are thermal shunt boards within the cryostat.

6.5.2 Electronics Hardware

6.5.2.1 ICS Thermal Enclosure

The contents of the ICS thermal enclosure are listed in Table 46.

Table 46: ICS Thermal Enclosure Contents.

Crate	Description	Size
1	ICS VME Electronics	8U
2	Stepper Motor Drive and Heater Control	9U
3	Cryocooler Drive Electronics	2U
4	Network Communications	4U

A diagram of the ICS thermal enclosure front panel is shown in Figure 3 in §2.11. Most components will have their own front panel hardware and any open spaces will be covered by blank panels to ensure positive ventilation of the enclosure. The contents of each crate are described in the following sections.

6.5.2.1.1 ICS VME Electronics Crate

The ICS VME electronics crate is an 8U, 21 slot ELMA 12V-0920-RV21J21-P750-D VME frame. 13 of the 21 slots will be occupied by the components shown in Table 47, with the remaining slots covered by blanking panels.

Table 47: ICS VME Electronics Crate Contents.

Component	No.
Motorola MVME 2700 Single Board Computer	1
Datum Inc. BC635VME Time and Frequency Processor Board	1
Xycom XVME-240 TTL Digital I/O Card	1
Oregon Microsystems VX2 Stepper Motor Controllers	2
Sensor Support Board	4
Xycom XVME-566 Analog I/O Card	2
Motorola MVME 761-001 Transition Module	1
Xycom XVME-490-1 Serial Port Card	1

6.5.2.1.2 Stepper Motor Drive and Heater Control Crate

The contents of the 9U Stepper Motor Drive and Heater Control crate are listed in Table 48.

Table 48: Stepper Motor Drive and Heater Control Crate Contents.

Component	No.
Phytron ZSO 42-40 Mini Stepper Motor Driver Modules	10
Lambda FE-2000-48-RA 48Vdc 42A Power Supply	1
Phytron Backplane	1
Omega CYC321-01 Temperature Controller	2
Lambda ZUP60-3.5/U 60Vdc 3.5A remote Power Supply	1

6.5.2.1.3 Cryocooler Drive Electronics Crate

The contents of the 2U Cryocooler Drive Electronics crate are listed in Table 49.

Table 49: Cryocooler Drive Electronics Crate Contents.

Component	No.
Pacific Scientific 6410-001-N-H-K Microstepping Drive	2
Lambda FE0500-48 48Vdc 11A Power Supply	2
Omega CYD208 Digital Thermometer	1

6.5.2.1.4 Network Communications Crate.

The 4U network communications crate contains a Cisco 2900 network switch and a Xylogics Annex 2000 terminal server.

6.5.2.2 Detector Control System Thermal Enclosure

The contents of the DCS thermal enclosure are listed in Table 50.

Table 50: DCS Enclosure Contents.

Crate	Description	Size
1	DCS VME Electronics	8U
2	Lake Shore 340 Temperature Controller	2U
3	SDSU Power Supplies	6U

A diagram of the DCS thermal enclosure front panel is shown in Figure 4 in §2.11. Most components will have their own front panel hardware and any open spaces will be covered by blank panels to ensure positive ventilation of the enclosure. The contents of the DCS VME electronics crate are described in the following section.

6.5.2.2.1 DCS VME Electronics Crate

The DCS VME electronics crate is an 8U, 21 slot ELMA 12V-0920-RV21J21-P750-D VME frame. Three of the 21 slots will be occupied by the components shown in Table 51, with the remaining slots covered by blanking panels.

Table 51: DCS VME Electronics Crate Contents.

Component	No.
PPC Single Board Computer	1
Datum Inc. BC635VME Time and Frequency Processor Board	1
SDSU-2 PMC Interface Card	1
VMIC Reflective Memory Card	1

6.6 Instrument Control System Risks

There are no significant technical, schedule, or budgetary risks associated with manufacturing the GSAOI ICS.

7 Control Software

7.1 Introduction

The GSAOI software will be based on the recently-developed NIFS software. As such, the Engineering Interface, the Instrument Sequencer (IS), the imager Components Controller (CC), the OIWFS Components Controller (OIWFS CC), and the OIWFS Detector Controller (OIWFS DC) will be close copies of the corresponding NIFS software. The bulk of the software effort will be in developing support for the new imager detector mosaic. Consequently, most of this chapter is concerned with the imager Detector Controller (DC) software.

The imager DC software will draw on a strong heritage from the NIFS spectrograph DC and the Wide Field Imager CCD mosaic software developed at RSAA. The NIFS DC software is nearing completion at RSAA. It controls a 2048×2048 pixel HAWAII-2 detector through a SDSU-2 controller in the Gemini environment. This heritage makes the SDSU-2 controller option (§5.2.5) highly cost-effective. The Wide Field Imager is a 8k×8k CCD mosaic that is controlled by dual SDSU-2 controllers. Much of the regions of interest and data handling software developed for this instrument is directly applicable to the GSAOI imager. Much of this heritage will also be applicable if the ASIC controller option (§5.2.6) is adopted.

7.2 Software Requirements

7.2.1 General Requirements

There are two general software requirements:

- The software must comply with the requirements described in ICDs 1-16 and SPE-C-G009/05.
- GSAOI is required to be a fast-track instrument.

7.2.2 Functional Requirements

The proposed GSAOI software is based on the Gemini Core Instrument Control (CICS) model (Beard 1997, "Core Instrument Control System - Introduction and Specification", cics_smb_002/20). In the CICS model, the software is broken into five main sub-systems: the Instrument Sequencer, the imager Components Controller, the imager Detector Controller, the OIWFS Components Controller, and the OIWFS Detector Controller. Each of these subsystems has its own requirements.

7.2.2.1 Instrument Sequencer

This subsystem accepts commands from the Observatory Control System (OCS) and coordinates the actions of the imager CC and the DC. Its requirements are:

- To respond appropriately to the sequence commands described in ICD1a and ICD1b.
- To prevent an observation starting when the instrument is configuring.
- To prevent the instrument from reconfiguring during an observation.

7.2.2.2 Imager Components Controller

This subsystem is responsible for the mechanisms that define the science optical path through the instrument and for controlling the instrument's environment.

The CC will control and position six active elements:

- Focal plane wheel.
- Upper filter wheel.

- Lower filter wheel.
- Fast shutter.
- Utility wheel.
- Environmental cover.

All components will be controlled from an Engineering Interface that does not rely on the presence of the OCS.

7.2.2.3 Imager Detector Controller

This subsystem is responsible for controlling the imager detector, and obtaining and processing data from it. The DC will be set up using standard Gemini Command Action Directive (CAD) and APPLY Experimental Physics and Industrial Control System (EPICS) records. It will use Gemini Command Action Response (CAR) records to indicate status of applied CADs and Gemini Status Information Records (SIR) to show system status.

7.2.2.3.1 Imager Detector

The GSAOI science detector will be a 2×2 mosaic of Rockwell HAWAII-2RG (H2RG) devices (§5.2.1). Each of these detectors will be read out simultaneously using four readouts per device forming a stream of interleaved pixel data. The DC software will preprocess the data into a correct sequence before it is sent to the Data Handling System (DHS) and quick-look display (QLD).

7.2.2.3.2 Imager Detector Controller

The imager detector controller electronics will either be the SDSU-2 (§5.2.5) or the ASIC detector controller (§5.2.6). The DC software will support the direct configuration of the chosen controller and handle all communications via the SDSU-2 PCI Mezzanine Card (PMC) interface card installed in the DC Input-Output Controller (IOC).

The DC software must support the following functional requirements:

- Correlated double sampling (CDS) and Fowler sampling (1 to 64 samples) readout methods.
- Integration times from 1s to 10,000s.
- Co-addition of between 1 and 1000 data frames before the result is transferred to the DHS and archived.
- Fixed-format regions of interest with pre-defined 64×64, 256×256, 512×512, and 1024×1024 pixel windows at the center of the mosaic and at the centers of each H2RG device.
- The use of the reference output and reference pixels to improve bias stability.
- Three readout speeds; a fast 300 kHz speed for instrument setup, a medium 200 kHz speed for broad band observations, and a slow 100 kHz speed for narrow band observations where low read noise is desirable. CDS readout times for these three speeds will be ~ 5 s, 10 s and 15 s, respectively.
- The use of a fast shutter to allow for the pausing and continuing of exposures.

7.2.2.3.3 Support for On-Detector Guide Windows

Each of the imager detectors has a continuously accessible, fast-readout, programmable guide window that is used to implement On-Detector Guide Windows (ODGWs). These ODGW will be read out repeatedly during an observation to monitor image translation for slow tip-tilt and flexure corrections. Extra support will be required to configure and process data from these guide windows and then for transfer of the data to the Acquisition and Guidance (A&G) IOC.

The DC software must support the following ODGW functional requirements:

- CDS and Fowler sampling (1 to 64 samples) read out methods.
- Integration times from 10ms to 1000s.
- The fixed definition of 8×8, 12×12, 16×16, and 32×32 pixel guide windows on all or on any combination of the four H2RG devices of the mosaic. The guide window can be at different locations on the four devices, but each guide window must have the same dimensions.
- The acquisition and subtraction of a sky background frame on the guide window.

7.2.2.4 OIWFS Components Controller

This subsystem is a separate Components Controller responsible for the OIWFS mechanisms.

The OIWFS CC will control and position five active elements:

- Steerable Mirror Axis-A.
- Steerable Mirror Axis-B.
- Steerable Mirror Axis-C.
- Aperture Wheel.
- Filter Wheel.

All components will be controlled from an Engineering Interface that does not rely on the presence of the OCS.

7.2.2.5 OIWFS Detector Controller

GSAOI will use the same OIWFS DC software as is used for NIRI/NIFS.

7.2.3 Performance Requirements

7.2.3.1 Imager Components Controller

Individual imager mechanisms are required to set in < 30 s and a complete reconfiguration of the instrument should be achieved in < 1 min. The imager CC software overhead on the mechanism configuration time must allow this requirement to be met.

7.2.3.2 Imager Detector Controller

The maximum continuous frame rate is achieved when the data are processed and transferred to the DHS during the minimum CDS readout time. This prevents delays in subsequent observations. Data caching can ameliorate short-term delays to some extent. However, the best continuous readout rate will be limited ultimately by the time it takes to process and deliver data to the DHS. The minimum CDS readout time is expected to be 10 s (i.e., two frame reads of 5 s each with a read interval of 0 s).

The DC software, in co-operation with the A&G system, must be able to readout a 12×12 pixel ODGW using CDS at a maximum continuous frame rate of ≥ 100 Hz. Guide window reads will stop during a full imager detector read.

7.2.4 Software Development Environment

GSAOI software will be developed according to Gemini software development standards that are described in document SPE-C-G009/05[9]. These standards comprise the following elements:

[9] Wright, J., Goodrich, B., & Wampler, S. 1997, "Software Programming Standards. Internal Gemini Report, 1994-1997", SPE-C-G009/05.

- Software Programming Standards

  The Gemini standards require that all code developed adheres to rules governing language selection, coding practices and style, module layout and formatting, and other related issues. For instance:

  - Language Selection
    GNU C and C++ compilers are required for both Unix and VxWorks cross-development. The Tcl/Tk scripting tool is to be used for all interpreted applications.

  - Coding Practices
    Rules for modular techniques, function and data declarations, include files, error handling, style and comments are defined.

  - GNU make
    Code will be maintained and built using the GNU make utility.

- EPICS

  Gemini require that all VME-based applications be developed using EPICS. Specific requirements are:

  - The EPICS database creation tool required to be used is Capfast.
  - EPICS records must conform to the Gemini-specified naming convention for the instrument. For GSAOI this mean that all records should have the prefix "gsaoi:".
  - EPICS engineering screens will be created using dm (an EPICS extension tool).
  - EPICS programming should be done in either:
    - EPICS database code – for ease of reuse, to take advantage of existing client side tools and to utilize the documentation and structural aspects of Capfast.
    - C code encapsulated in record, device, or driver support routines – for support of complex code and new hardware interfaces.
    - State-Notation-Language (SNL) – for ease of expressing database state transitions.

- VxWorks with a PPC Board Support Package (BSP)

  VxWorks from WindRiver Systems is the IOC real-time operating system environment chosen by Gemini. All new Gemini IOCs should use the Motorola PPC single board computer, so the GSAOI ICS will be developed for the PPC. The latest development environment is Tornado V2.2/VxWorks 5.5.

- Solaris (Unix Sys V Rel 4, POSIX)

  Sun Solaris is the Gemini operating system of choice for the user operating and software developer environment. The Tornado development environment will be run on Solaris for cross-development for the PPC.

- The UAE Environment

  All EPICS development will be within the Universal Application Environment UAE – see the Keck EPICS Programming manual. UAE provides a means for developing and releasing code in a fashion similar to the way EPICS code is developed.

- External Software Libraries

  Gemini uses the external software libraries SLALIB, ASTLIB, CFITSIO, and TIMELIB.

- Source Code Control

  Developers are encouraged to use the GNU CVS source code control environment.

7.2.5 Testing and Simulation

During the GSAOI development phase, software will be developed in parallel to the GSAOI hardware. This makes it necessary to build hardware emulators that can be used to fully test software in the absence of real hardware. These emulators are required for all of the software external interfaces, that is:

- The OCS – provided by the Engineering Interface. The Engineering Interface will emulate the OCS by using the same EPICS channel access that the OCS will use and by providing all the commands expected from the OCS.
- The DHS – Gemini provides a test DHS for local installation that can be used by instrument developers.
- The imager detector – it is important to build a dummy software imager detector that emulates the behavior of the real infrared mosaic, so that full detector controller software testing can be carried out in the absence of the detector.
- Optical mechanisms – the NIRI developers built emulators for the NIRI mechanisms. GSAOI will make use of these, just as has been done for NIFS.

7.3 Software Solution

GSAOI will use as much of the NIFS software as is possible. This helps ensure that the two general requirements, Gemini compliance and a fast-track development, are met. Since NIFS complies with the Gemini software requirements, GSAOI software should also comply. Only minor modifications are expected to the IS, CC, and OIWFS CC to make them suitable for GSAOI.

7.3.1 Software Architecture – CICS Model

GSAOI will employs CICS, the Gemini Core Instrument Control System (Figure 91), which was developed to provide a template for instrument developers to use. It handles common operations of the Gemini telescope as well as providing standard schematics for handling instrument control. CICS consists of a suite of Capfast schematics implementing Command Action Directive (CAD), Command Action Response (CAR), Status Information Record (SIR), and APPLY records as well as State Notation Language (SNL) code, C-code, and user interfaces.

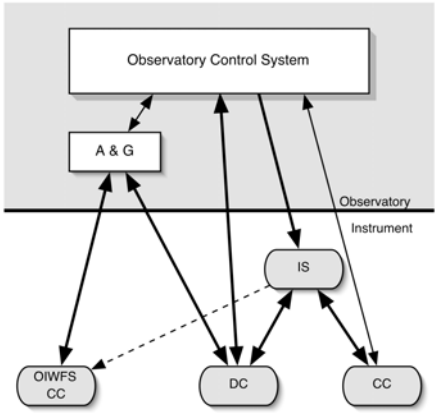

Figure 91: CICS software architecture.

7.3.2 Network Architecture

GSAOI will employ two IOCs running under VxWorks on a Power PC system and the Operator Interface running on a Sun workstation. One IOC will be dedicated to the Detector Control System and the other IOC will be dedicated to the Instrument Control System.

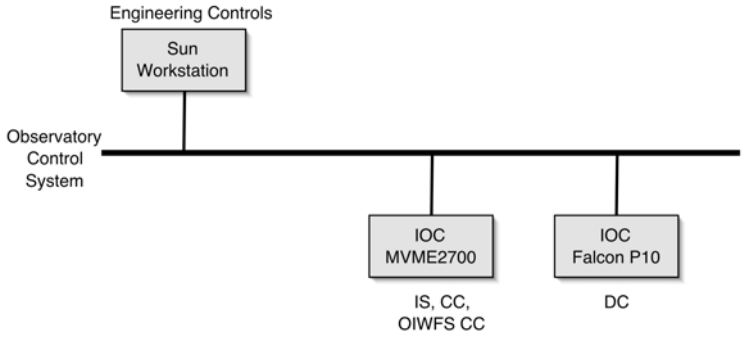

Figure 92: Computer systems used for GSAOI.

7.3.3 Instrument Sequencer, Imager Components Controller, and On-Instrument Wavefront Sensor Components Controller Software Design

7.3.3.1 Software Reuse – Taking Advantage of NIFS

The GSAOI IS, CC, and OIWFS CC will be copies of the NIFS software. Figure 93 illustrates the NIFS software for these databases. In each of the databases, commands are issued through CADs in the normal way. The IS supports the standard Gemini sequences:

TEST, *INIT*, *DATUM*, *PARK*, *VERIFY*, *ENDVERIFY*, *GUIDE*, *ENDGUIDE*, *STOP*, *OBSERVE*, *ABORT*, *PAUSE*, *CONTINUE*, *ENDOBSERVE*, *REBOOT*, and *DEBUG*.

When one of these commands is issued, the appropriate CADs in the CC and OIWFS CC databases are activated through channel access. The CADs in the CC and OIWFS CC databases trigger sequence code that then coordinates the hardware databases, controlling mechanism movement, system temperature, and interlocks. The sequence code also updates the status and health records of the CC and OIWFS CC. In turn, these records communicate with the IS Status and Alarm Database (SAD) using channel access.

The only difference between the GSAOI and NIFS instruments from the perspective of the software is the number and type of components. The changes required to the NIFS software to accommodate the GSAOI components are small. The only exception to this is the three-axis OIWFS steerable mirror.

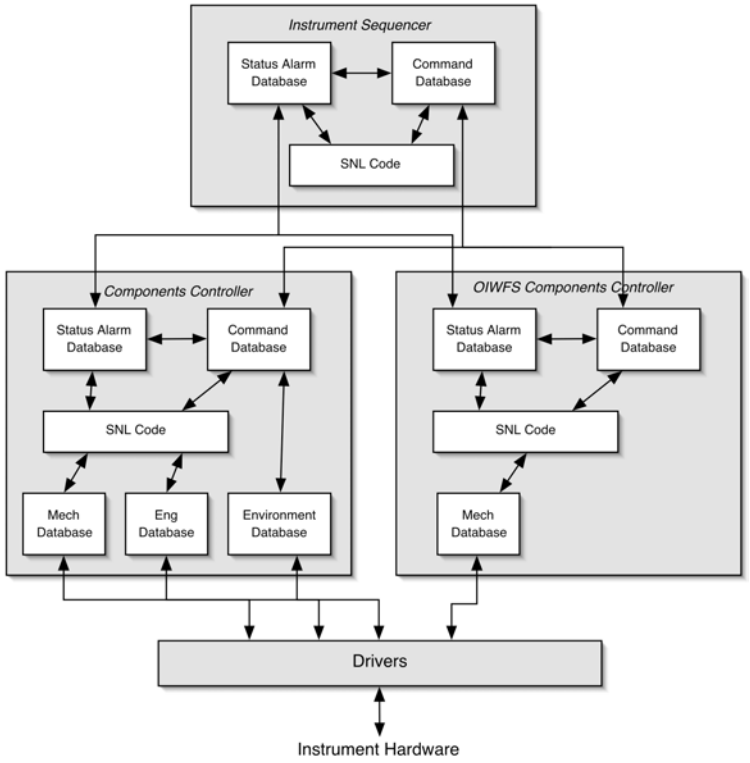

Figure 93: NIFS databases that will be replicated for GSAOI.

7.3.3.2 New Mechanism Type - OIWFS Steerable Mirror

The OIWFS steerable mirror (§4.5.4) uses a new scheme for obtaining the datum position for each axis. Rather than use Hall-effect sensors, a mechanical stop is used to locate the datum. Hall-effect sensors are positioned on each of the motor axes to indicate motor action, and a pair of Hall-effect sensors are positioned on the mirror adjacent to each lead screw to indicate mirror motion. These Hall-effect sensors are used only as a diagnostic tool. A new device handler will be written to accommodate this new design. The existing record support and driver code will be used, thus minimizing the effort required.

7.3.3.3 OIWFS Detector Controller

GSAOI will use the HAWAII-1 detector for the OIWFS. This is the same as used in NIRI/NIFS, so the software that was used previously will be reused for GSAOI.

7.3.4 Imager Detector Controller Software Design

GSAOI will read out four times as much data as NIFS in the same time. Thus, the DC software solution will need to accommodate this quadruple data rate. Specifically, we need to address the data throughput of the detector controller interface, the data processing engine, and the throughput to the DHS and QLD.

The data processing aspect of this problem is handled by an appropriate software architecture described in the following sections.

7.3.4.1 Software Reuse – Taking Advantage of NIFS and WFI

The design for the DC has been driven by the need to fast-track the construction of the GSAOI instrument, and therefore reuses as much software as possible from multiple sources. To meet Gemini interface

requirements and to make the design as simple as possible, it was decided to copy the "thin EPICS layer" approach adopted for NIFS. This is coupled with a suitably modified copy of RSAA's existing IR camera C++ interface software to take advantage of code reuse.

Procedures for handling the large data rate have already been developed by the RSAA software team during their development of the Wide Field Imager (WFI). WFI is a 8k×8k CCD mosaic driven by two SDSU-2 detector controllers. These data handling procedures include using processor vector units where possible and by using a parallelized data processing pipeline. This pipeline handles concurrent processing and transfer of received data while new detector data are being read out.

7.3.4.2 DC Software Architecture

The DC software consists of a multiple task architecture designed to optimally support the requirements of the GSAOI imager detector.

The DC architecture (Figure 94) uses tasks written as EPICS SNL code to interface to Gemini using CAD, CAR, APPLY, and SIR records. We refer to these as the *Control* tasks. They are responsible for interfacing to the Gemini system using EPICS channel access. The *Control* tasks pass commands to the *Slave* task for taking exposures and setting up the detector controller. The *Slave* task monitors the progress of the *Readout* task during a detector readout and signals readout progress to the *Data* task. Progress is monitored by the tuned polling of a readout progress register maintained by the readout device driver code. When signaled, the *Data* task will transfer image data to the Gemini DHS for storage and quick look display.

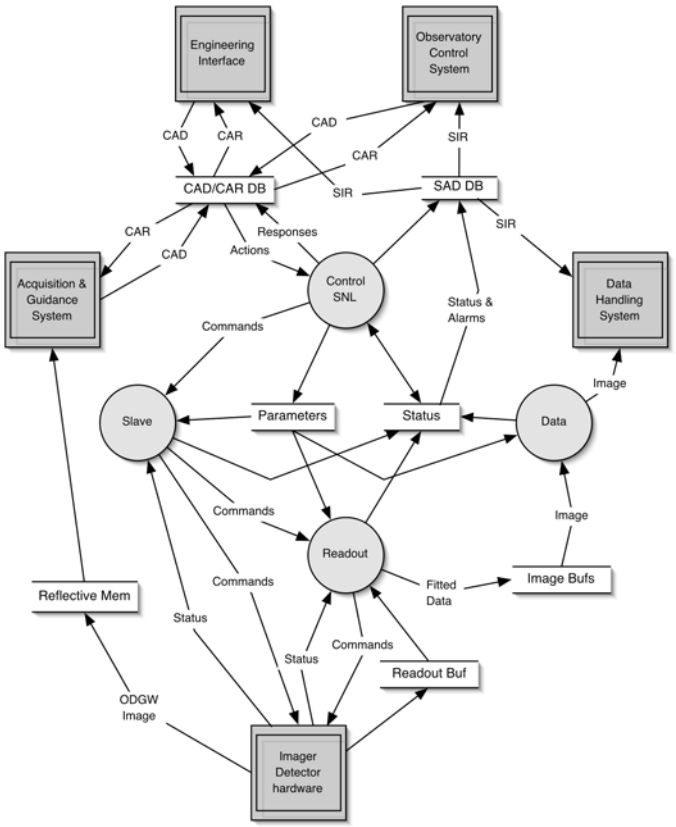

Figure 94: GSAOI DC software architecture.

The architecture has five external systems and seven internal data stores. Two of the data stores are EPICS databases for storing configuration (CAD) and status information (SAD). There are also common memory

areas for storing operational parameters, copied from the EPICS CAD database, and status information before being moved to the EPICS SAD database. A common memory area is again used for storing the detector image data at various stages of processing. There is a memory area for the detector controller interface card's device driver to deposit image and progress data. And lastly, there is a Synchro Bus reflective memory area for holding the ODGW data.

In general, the DC architecture supports setting up and executing observations. During an exposure the ODGW sub-system will send data to the A&G system for slow tip-tilt and flexure corrections. Image data will be read out from the detectors, processed, and possibly co-added, before being sent to the DHS and QLD.

7.3.4.2.1 Control Tasks

As mentioned above, the *Control* tasks are written in SNL. There are three of these:

1. An SNL task is used to start up the *Slave* and *Data* tasks when an *INIT* directive is received. It then monitors the *INIT* and *REBOOT* CADs while the system is running so that it can be ready to perform a reset operation. A heartbeat counter is also updated when in the *Running* state (see Figure 95).

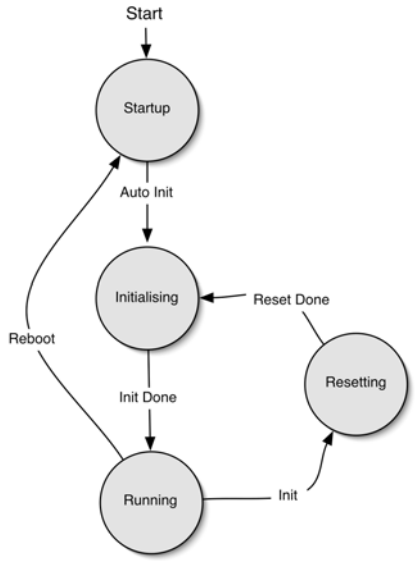

Figure 95: Main *Control* SNL State Diagram.

2. A second SNL task is used to monitor the *START* directive of the *OBSERVE* CAD and then responds as necessary, usually by depositing a command message in the *Slave* task's message queue. During an observation it monitors the *PAUSE*, *CONTINUE*, *STOP*, and *ABORT* CADs while in *ACQ* state. The *ABORT* CAD is also monitored in the *RDOUT* state (see Figure 96). While not *OBSERVING* the system can, optionally, go into *VIEW* mode where the detector is continually read out and data is sent to a QLD.

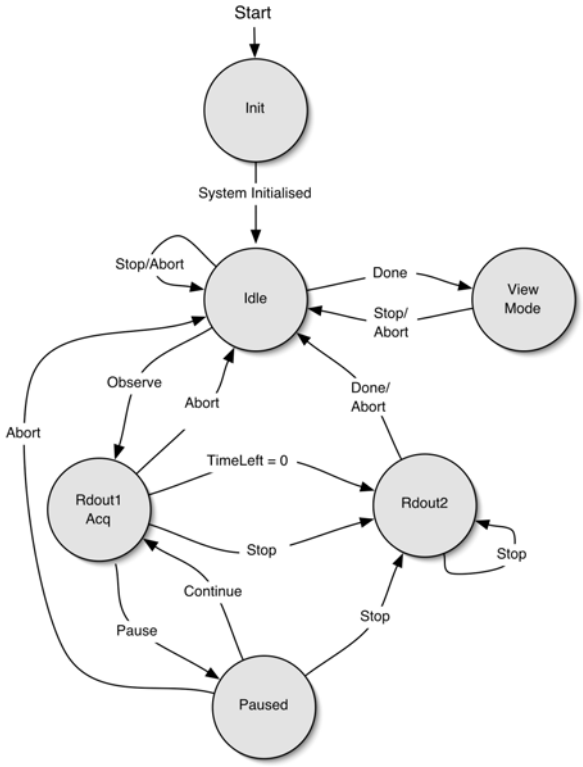

Figure 96: SNL State Diagram for the *Observe* sequence.

3. The last SNL task in the *Control* set is for handling the CADs that control the detector controller. These are the *TEST*, *PARK*, and *SETUP* CADs. Again the *START* directive of the CADs are monitored by the SNL and when triggered a message is deposited in the *Slave* task's message queue for execution (see Figure 97).

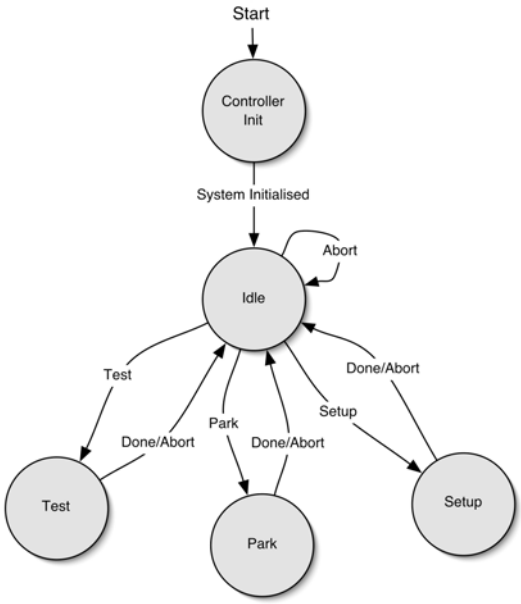

Figure 97: State Diagram for SNL Task to handle Detector Controller CADs.

The SNL *Control* tasks ensure that each CAD record's associated CAR record is handled correctly and is solely responsible for passing back error states to the EPICS database as required in the Gemini model. Other tasks in the DC architecture do not need to worry about handling the Gemini-prescribed EPICS interface – they simply read configuration parameters (CAR attribute values) and write status information (SIRs).

A key requirement of the *Control* tasks is that they have to be responsive. The SNL code monitors the *START* and *STOP* links of the CAD records, enabling fast reactions to commands.

7.3.4.2.2 Slave Task

As explained above, the main *Control* task (Figure 95) starts the *Slave* task when it processes an *INIT* command (and automatically when the system is started). When *Slave* starts it will instantiate an *SDSU2_IR* (or *ASIC_IR*) camera object with constructor parameters set according to initial CAD parameter settings. Once created, the *Controller_init* method is invoked to perform necessary controller initialization. Depending upon initialization configuration options, the *Controller_init* method will initialize the PMC controller interface, load the detector controller code (e.g., SDSU-2 DSP code), set controller voltages, set the idle mode, and turn the power on.

The task then connects to a message queue for receiving further commands from the *Control* tasks. It then sits in its *READY* state. The POSIX message queue facility is used and a signal handler is set up with the *mq_notify* call for notifying *Slave* when a message is delivered by the SNL *Control* tasks. As commands are received they are interpreted and the requested actions are performed. The *OBSERVE* command will put the task into its observing *MONITORING* state where the observation sequence is monitored. Firstly, the exposure is prepared using specified parameters, integration then proceeds along with required readouts (depending on readout mode). Readout processing is performed by the *Readout* task that is started in the preparation phase. The following state diagram (Figure 98) illustrates this process.

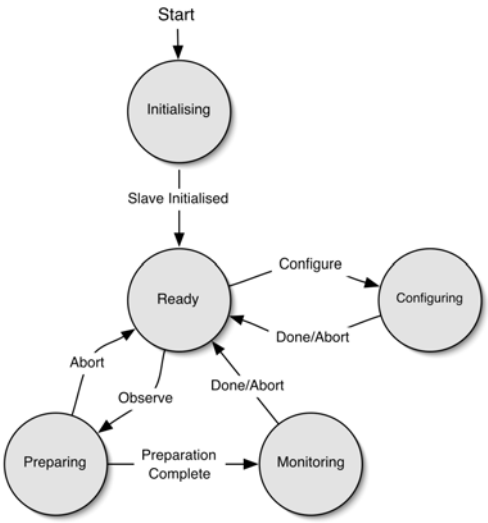

Figure 98: *Slave* task state diagram.

Commands to the detector controller are passed directly into the PMC device driver by either the *Slave* or *Readout* task. The task then awaits a reply from the driver to indicate that the command has completed.

Monitoring is done by polling the exposure progress flags. Status is updated with the exposure counter maintained using the VxWorks clock, which is sufficiently accurate for this purpose. Highly accurate actual exposure timing is performed by the controller electronics.

During this *MONITORING* state, *Slave* needs to remain responsive to *Control* commands so that interrupts such as *PAUSE*, *CONTINUE*, *ABORT, STOP*, and *REBOOT* sequences can be attended to.

7.3.4.2.3 Readout Task

Readout is the task that sends the *start exposure* command to the SDSU-2 (or ASIC) controller interface and waits while it proceeds. It is started by *Slave* and, depending on the readout method, prepares itself to run the exposure. It sets up an interrupt handler to be called in the case of either an *ABORT*, *STOP*, or *REBOOT* command that will cause the task to exit after appropriate cleanup.

As a readout proceeds and data is accumulated in image buffers prepared in the initialization phase, the *Data* task is signaled when data is ready for transfer. This will happen when the readout progress counter maintained by the device driver indicates there is enough data available for processing - i.e., a predetermined fraction of the full readout. *Readout* polls the progress counter, updates the status buffer, and processes and unravels the data in the raw pixel buffer placing the results in the fitted pixel buffer. It then gives a semaphore to *Data* to indicate that data are ready for transfer. The following state diagram (Figure 99) illustrates this process.

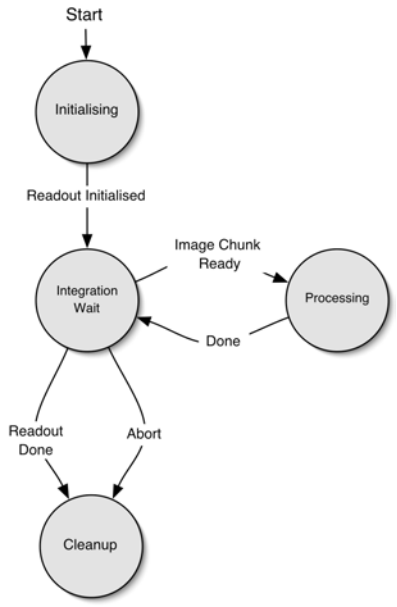

Figure 99: *Readout* task state diagram.

Timing aspects of importance in this design are:

- Frequency of polling the readout progress counter.
- Speed of calculating and unraveling processed data.
- Handshaking with the *Data* task.

7.3.4.2.4 Data Task

Data is solely responsible for getting image data transferred out of the system. It handshakes with the *Readout* task on one side and either the DHS or a FITS server on the other. It prepares data for transfer by shifting it from fitted pixel memory to the DHS data structures. It also performs all necessary DHS data structure set up. *Data* also handles interaction with any quick look displays that are in use.

Data is started by *Control* and waits for a semaphore to be handed it by *Readout* when a data buffer is ready for transfer. It interprets the contents of the data buffer and performs the transfer. Data to be transferred will include:

- Raw data and, optionally, quality data at the end of an exposure for permanent storage and display (up to 80 MB).
- Optionally, raw data after the first readout in a CDS or Fowler sample, for possible permanent storage and/or transient display (64 MB).

Figure 100 illustrates the *Data* task's states.

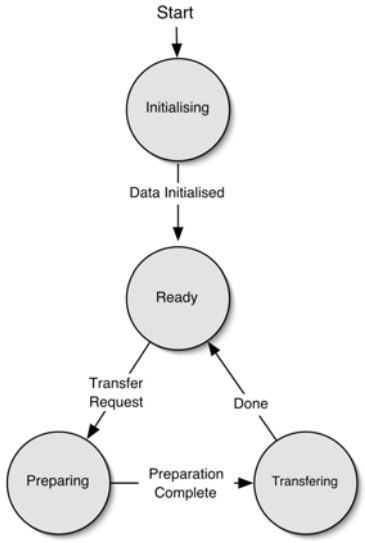

Figure 100: *Data* task state diagram.

There are potential bottleneck problems with this process that need to be considered. These bottlenecks can occur in two places:

1. *Readout* can be blocked while *Data* holds the image semaphore.

This is unlikely as *Data* merely transfers the data from the fitted pixel buffer, which is already unscrambled by *Readout*, to the DHS transfer buffer.

2. *Data* can be blocked by the DHS.

This, in turn, would cause a block further along the processing chain in the *Readout* task. *Readout* will just have to wait until the block clears, thus delaying the next exposures start time.

7.3.4.2.5 Summary - Taking an Observation

The sections above explain how the GSAOI DC software design will work. For the Gemini *OBSERVE* command, the following sequence of actions will occur:

1. The OCS sets up all the observing parameters using the DC CAD records.
2. The OCS then marks the *OBSERVE CAD* and issues the *START* directive to the DC via the IS.
3. Parameters are verified and the command is accepted.
4. SNL code detects the *START* counter update and then sets the *OBSERVE CAR* to *BUSY*.
5. The *Observe* command is passed to the *Slave* task.
6. The *Slave* task starts the *Readout* task, which initiates an exposure with the detector controller.
7. The detector controller device driver updates the readout counter as each NDR sample progresses and moves readout data to the readout ring buffer using direct-memory access (DMA).
8. During the NDR read interval, the detector controller device driver moves ODGW data to the reflective memory buffer for transfer to the A&G.
9. During an NDR, the *Readout* task monitors the NDR progress counter to check that data are ready.
10. The *Readout* task processes and unravels pixels in the chunk of data that is ready.
11. A transfer semaphore is raised by *Readout* when data are ready for transfer.
12. The *Data* task takes the semaphore and moves data into the DHS data structures.
13. The *Data* task releases the semaphore and sends data to the DHS and quick look displays.
14. Steps 7, 9-13 are repeated once the exposure completes for the second set of NDR samples.
15. Finally, full data are sent to DHS for permanent storage.

7.3.4.3 DC Software Interfaces

The proposed software architecture for GSAOI has four external interfaces:

- Observatory Control System and Engineering interface
- Detector Controller interface
- A&G System interface
- Data Handling System

7.3.4.3.1 Observatory Control System and Engineering Interface

As mentioned above, the thin-layer EPICS approach adopted for NIFS will be reused here. By thin-layer, we mean that the DC EPICS database only provides CAD, CAR, and SIR records and no additional functionality, such as hardware interfaces. The CAD, CAR, and SIR records trigger C++ code directly or through SNL code. Each of the VxWorks tasks *Slave*, *Data*, and *Readout* will read and write EPICS database parameters using the RSAA-developed parameter class. This C++ class provides a mapping between VxWorks parameter space and the EPICS database in a simple and convenient way.

7.3.4.3.1.1 Parameter Class Detail

Figure 101 shows how the thin-layer EPICS approach is implemented.

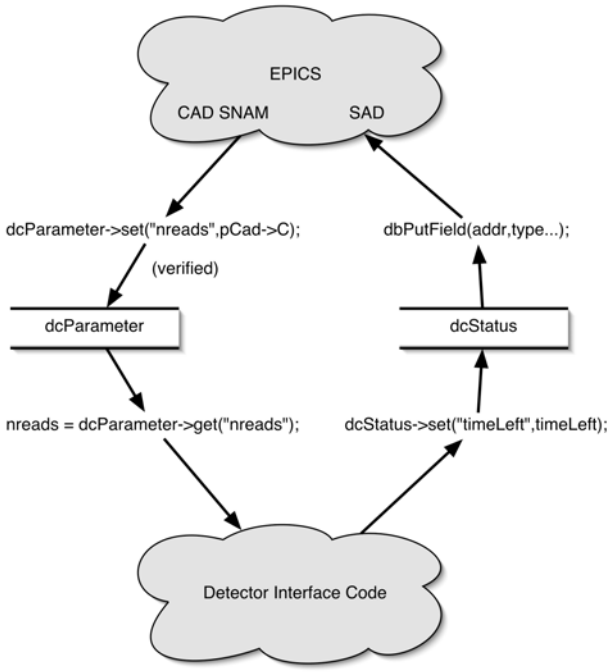

Figure 101: Thin-layer EPICS overview.

A parameter class object includes a STL[10] hash map keyed by parameter name. These maps contain attributes including current parameter value, EPICS process variable name, and validity checking information. Methods are used to set up and maintain the maps. When these objects are instantiated, the maps will be populated with all the GSAOI parameters and their attributes. The following code sample shows how this is done:

```
gsaoiParameter->add("nreads", "gsaoi:dc:seqObserve.C", 0, min, max);
gsaoiParameter->add("qlStream", "gsaoi:dc:setDhsInfo.A", "gsaoiRunQL");
gsaoiParameter->add("readMode", "gsaoi:dc:seqObserve.A", CDS, readModeSet);
.
gsaoiStatus->add("timeLeft", "gsaoiSad:dc:timeLeft", 0);
```

The arguments to the *add* method include parameter name, EPICS variable name, default value, and validity values.

Note that the *add* method is overloaded to handle different data types. The data type for each parameter is remembered and used for any data conversion required from the CAD input string values. Upper and lower value bounds can be specified for numeric values, maximum string length for strings, and set membership for sets. During operation, these maps can be updated or queried using *put* and *get* methods.

The use of these anonymous maps in these classes adds much flexibility: The classes are context free, and each object can be readily extended with new parameters as they are required without code modification. Indeed, they could be easily used in other instruments requiring an interface between VxWorks code and the Gemini EPICS environment.

[10] VxWorks supports the C++ Standard Template Library (STL) which has a hash map implementation.

In the case of the operational parameters, the CAD *SNAM* routines will use the *put* method of the *gsaoiParameter* class to store and verify a CAD input parameter. An example of this use is as follows for the *nreads* parameter:

```
gsaoiParameter->put("nreads", pcad->C);
```

If the parameter setting is valid, the class stores *nreads* in an STL hash map and then its value will be copied to the CAD record's *OUT* field. Otherwise the value remains unchanged and an exception is thrown.

For status parameters, we take another example. The *Slave* task will maintain an exposure counter named *timeLeft*. This will be set with the following method call:

```
timeLeft = exposureRequested – (currentTimestamp – startTimeStamp);
gsaoiStatus->put("timeLeft", timeLeft);
```

Each parameter in *gsaoiStatus* is stored in another STL hash map that is keyed by name, has a value and a SIR record name as attributes. The *put* method looks up the map and deposits the new value in both the map and the SAD database. The *get* method looks up the value in the SAD database and returns the current value.

7.3.4.3.2 Detector Controller Interface

The GSAOI DC software interfaces to the detector controller through the RSAA hardware and controller C++ classes. There are variants of these classes that understand the interface specification for the controller and detector in use. The full RSAA hardware class is depicted in Figure 102.

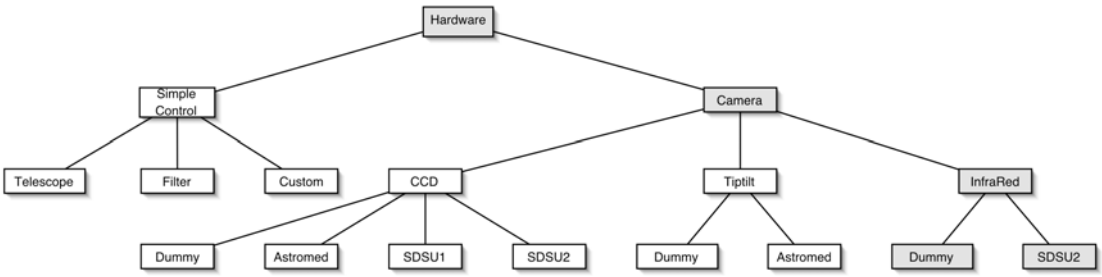

Figure 102: The RSAA *Hardware* class.

The shaded boxes show elements of the hierarchy that will be used for GSAOI. A derived *Camera* object in the hierarchy owns a particular *Controller* object (depicted in Figure 103) for controlling a detector – see the fragment of the C++ class definition following:

```
class Camera: public Hardware {
        ...
        Controller *controller; // Detector controller attached to this camera
        ...
};

class Sdsu_IR: public IR_Camera {
        ...
        Sdsu_Controller *sdsu_controller; // Pointer to sdsu controller used by this IR camera
        ...
        Sdsu_IR () { controller = sdsu_controller = new Sdsu_Controller(); };
        ...
};
```

The code fragment also shows how C++ polymorphism is used to allow generic use of a *Controller* object within the *Camera* class, enabling generic camera functions to be written that do not have to know anything specific about the controller in use.

In this way, these classes model the typical setup of an astronomical instrument and are used extensively to support RSAA's instrumentation at its own telescopes and instruments at other observatories.

The base *Hardware* class contains methods for instantiating parameter databases and other general software infrastructure pieces. The base *Camera* class again instantiates camera specific parameter databases, handles unraveling and verification of pixels, handles transferring data to the associated *Data* process, and provides other general camera specific functions. The *Infrared* class contains methods for handling infrared specific functions such as readout methods and infrared data processing.

The lower level classes *Dummy* and *SDSU2* simply instantiate a particular type of controller that has been configured with the camera.

This hierarchical design lets us use the camera in a generic way in the software design. Thus it is simple to switch between a simulation camera (*Dummy*) and the real *SDSU2* camera without changing the program logic in the *Slave*, *Readout*, and *Data* tasks.

7.3.4.3.2.1 Using the RSAA *Camera* Class to Support the H2RG

The RSAA *Camera* class has been designed to support detectors of arbitrary configuration and size. It supports both single detectors with single readouts and detector mosaics with potentially more than one readout per detector. The software also supports mosaic configurations, possibly controlled by multiple controllers with synchronized readouts. Arbitrary readout orientation and layouts are also supported. The software configures itself based on a hierarchical set of setup tables for the camera.

Due to this software support for arbitrary detectors, no software changes to the RSAA *Camera* class will be required to support the GSAOI mosaic layout. It will be simply a matter of changing the configuration tables to reflect the GSAOI mosaic layout and number and position of readouts.

7.3.4.3.2.2 Modifying the RSAA *Infrared* Class to Support the Fast Shutter

Currently the RSAA *Infrared* class does not support pausing and continuing an exposure. Because GSAOI will include a fast shutter, this support will have to be added to the class. It is intended to use the Gemini sequences *PAUSE* and *CONTINUE* to trigger operation of the shutter. The DC software will act on these commands, when in *ACQ* mode, by sending a *PEX* SDSU instruction to the controller when pausing and then a subsequent *REX* instruction to continue. The SDSU DSP code will be responsible for recording accurate exposure times that will be reconciled with times kept in the CC which will perform the actual shutter open/close operations.

7.3.4.3.2.3 Detector Interface Baseline Solution - SDSU-2 IR Controller

The lower layers of code running in the *Slave*, *Readout*, and *Data* tasks are triggered by commands from the *Control* task. These codes interface directly with the SDSU-2 electronics. RSAA has experience using this controller and intends to take advantage of code already in use for NIFS. However, because of the throughput needs described earlier, support for the new SDSU PMC interface card will need to be added for GSAOI. For a full description of the baseline SDSU hardware configuration proposed for GSAOI see §5.2.5.

7.3.4.3.2.4 Modifying the RSAA SDSU *Controller* Class to Support the H2RG

The RSAA *Controller* class is used to interface with a detector controller. This is another hierarchical arrangement of C++ classes that is designed to support multiple controller types and therefore contains much common code at the higher layers in the hierarchy (see Figure 103). The shaded boxes represent parts

of the current RSAA class hierarchy that will be used in GSAOI. The *Camera* class described above instantiates at least one of these *Controller* objects, depending on the camera configuration, for each camera. For GSAOI, our baseline solution includes one SDSU-2 controller.

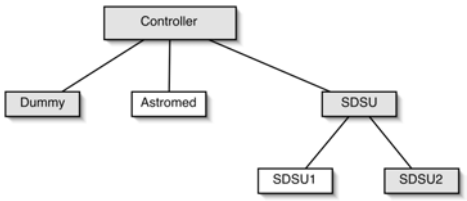

Figure 103: The RSAA *Controller* class.

The base *Controller* class contains common methods used in all derived objects including instantiating parameter databases, setting up the image buffers, setting up and generating simulation data for readout verification, setting up for a readout, and defining place-holders for methods (pure-virtual methods) that require derivation in sub-classes.

The *Dummy* definition is used for simulating data from an arbitrarily defined detector configuration. This class is heavily used in testing the data flows in the system and it attempts to provide as realistic a simulation as possible. Data can be either generated or, alternatively, read from an existing FITS file and are output as a stream of interleaved pixels from the configured detector readout, just as would be expected from a real controller.

The *SDSU* class understands how to interface with the SDSU family of controllers. It can interface to these controllers through SBUS, VME bus, and (soon) PCI interface cards. The class is tightly coupled with the DSP code developed to run on the SDSU timing, utility, co-adder, and VME DSP chips. Depending on the interface card in use, it also is tuned to work with the appropriate device driver; either the RSAA SBUS *astro* driver or the planned RSAA-modified SDSU VxWorks PCI/PMC *astro* driver.

The *SDSU2* variant of this class is currently used to control the NIFS detector. For GSAOI, this class will need extensions to support the following:

- Interfacing to the new PMC device driver (§7.3.4.3.2.5).
- Guide window definition and setup (§7.3.4.3.2.6).

Otherwise the code will be as used for NIFS. It is worth noting that infrastructure support for different interface cards is already built into the class as both the SDSU SBUS and VME bus cards are being used in the development of NIFS.

7.3.4.3.2.5 SDSU PMC Interface Card – VxWorks PMC Device Driver

GSAOI will require an interface card to the detector controller that has a much higher throughput than the NIFS VME interface card. SDSU are developing a PMC format version of their PCI interface card for the MCAO project. This card runs at 12.5 Mpixels/s. RSAA would like to use this card to achieve our performance goal in preference to the older slower VME interface card that will not be developed further by SDSU. Consequently, the NIFS DC software will be extended to handle the new PMC interface card and the higher data rate.

Gemini plan to subcontract the task of writing a VxWorks driver for this PMC card so that it will be available for MCAO. The timing of this work might not coincide with GSAOI development, so, as a contingency, we plan to develop a driver for this card ourselves. By making use of the driver already supplied by SDSU for the Solaris and Linux platforms and, possibly, by using tools such as *WinDriver* and *DriverBuilder* from Jungo Ltd. (htpp://www.jungo.com) this task should be efficiently achievable.

The RSAA controller class requires that the driver provide the following facilities:

- Handling of a full CDS or Fowler readout with data placed in a DMA ring buffer.
- Handling of the read interval in a CDS or Fowler readout.
- Updating of read progress registers, including frame count, byte count, and frame read time.
- Timeout handling.
- Handling of ODGW readout mode.

Except for the ODGW mode, these facilities are currently available in RSAA's SDSU Solaris SBUS *astro* driver and the RSAA VME DSP code for performing readout handling for NIFS.

Figure 104 shows the state diagram planned for the GSAOI device driver.

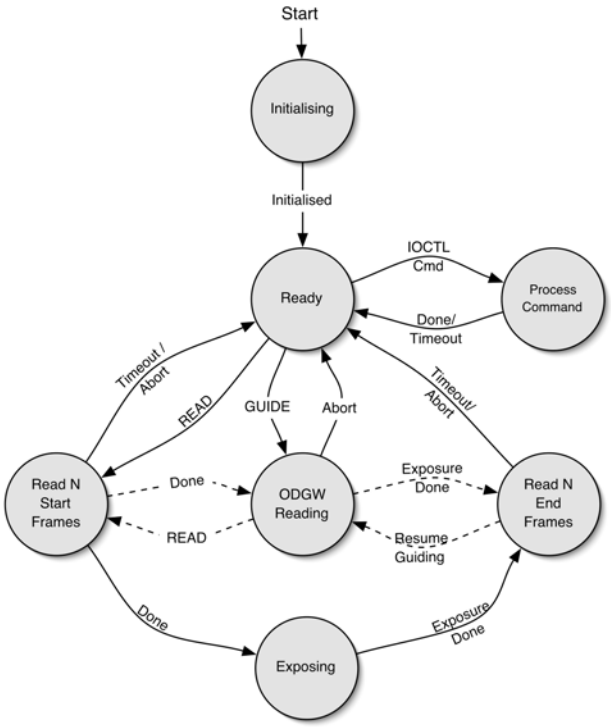

Figure 104: Detector Controller device driver state diagram.

The dotted lines represent possible state transitions depending on whether continuous guide mode has been enabled or not. As described in §5.2.1.4, it will be normal to guide just before an exposure is started then continue guiding during the exposure interval and, perhaps, resume guiding after the readout has finished.

7.3.4.3.2.6 Setting up the ODGW

CADs will be provided for specifying details of the detector guide windows. These parameters will include the size and position of the guide windows for the four detectors and the CDS exposure time. The number of ODGW CDS readouts performed during the observation will be calculated from the observation read interval. The SDSU timing board DSP processor will handle all of the ODGW preprocessing required – including CDS/Fowler sampling, pixel unraveling, and bias frame subtraction. ODGW bias frames will be acquired and retained by the DSP code when instructed by the A&G System.

The *Controller* class will be extended to include support for the setting up of these ODGW parameters and commands.

7.3.4.3.2.7 Detector Interface Alternative Solution - Application Specific Integrated Circuits

As described in §5.2.6, the Rockwell-developed ASICs might be available to control the detector readouts as an alternative to the SDSU-2. A new C++ *Controller* class in place of the *SDSU* class will be developed to interface to these electronics if the decision is made to deploy ASICs in preference to the SDSU controllers. The new class will slot into place instead of the SDSU controller class in RSAA's camera/controller class hierarchy (see darker shaded boxes in Figure 105 and Figure 106).

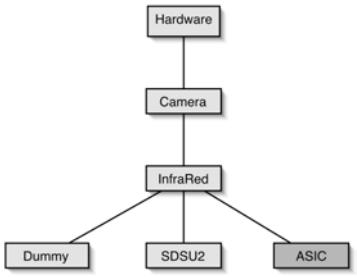

Figure 105: The GSAOI version of the RSAA *Hardware* class with ASIC support.

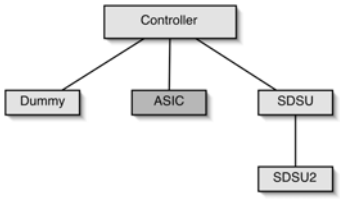

Figure 106: The GSAOI version of the RSAA *Controller* class with ASIC support.

7.3.4.3.2.8 ASIC Communication Card – VxWorks PMC Device Driver

As described in §5.2.6.1.3, the baseline design for communicating with the ASIC controller will be through the same SDSU PMC interface card specified for the SDSU-2 controller alternative. This has the advantage that there will be essentially no difference in the device driver for the two options. Figure 107 is a block diagram of the two alternative software architectures related to interfacing with the detector controller. Note that the design shows a *Camera* object that owns a *Controller* object but is not concerned with what type of *Controller* object it is. This is achieved by using C++ polymorphism. The interface to the device driver will be designed so that it can carry either SDSU-2 or ASIC protocol messages. All of the ASIC-specific command knowledge will be contained in the *ASIC Controller* class.

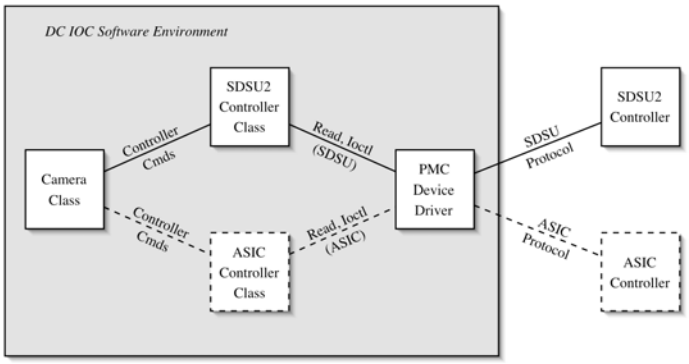

Figure 107: ASIC software interfaces.

7.3.4.3.3 A&G System Interface - ODGW

The technique to be used for moving ODGW data to the A&G System is described in §5.2.5.1.1. A reflective memory board attached to the Gemini Synchro Bus will be installed in the DC IOC. Already unraveled ODGW data will be written to the Gemini assigned reflective memory area by the PMC device driver during guiding mode. The SDSU timing board DSP code will process and unravel data from each of the guide windows before sending it up the fiber optic link to the PMC card. The data will be written directly into the reflective memory board for deterministic transfer to the A&G System reflective memory. When complete, an interrupt will be raised on the A&G System to indicate that a new ODGW frame is ready.

7.3.4.3.4 Data Handling System Interface

GSAOI will interface to the DHS using the Gemini-prescribed method described in ICDs 1c and 3. For a configuration with 4 readouts per detector, FITS files written by GSAOI will have 16 image extensions, 16 pixel reference sections, and 16 quality data extensions. The quality data will indicate which pixels are bad.

One QLD stream will be used for GSAOI observing and another will be used for GSAOI *view* mode. *View* mode will be used to continually readout the detector using the same readout methods employed for an observation but with a set of readout parameters that can be set independently. This mode is sometimes thought of as *movie* mode and it will enable the observer to monitor the detector view during observation preparation.

7.3.4.4 DC Data Processing

The DC system will need to perform the following processing during each observation:

- Device driver DMA handling.
- Readout method calculations.
- Pixel data unraveling.
- Region of interest and reference pixel handling.
- World Coordinate System (WCS) calculations.
- DHS data transfer.

7.3.4.4.1 Device Driver DMA Handling

The PMC device driver will need CPU time for the setting up of its DMA registers prior to a readout. It will also need CPU time for handling any device interrupts and handling requests for progress information from the DC *Readout* task. Progress requests require a query to the PMC DSP code to return the value of its current DMA pointer. All of these tasks will have minimal impact on the CPU.

7.3.4.4.2 Readout Method Calculations

Two readout methods will be supported; correlated double sampling and Fowler sampling. The processing required for these methods can be expressed by

$$I = \left[\sum_{j=1}^{m} \left(\left(\sum_{i=1}^{n} I2_i - \sum_{i=1}^{n} I1_i \right) / n \right)_j \right] / m$$

where:

I1	detector sampled at the beginning of an exposure.
I2	detector sampled at the end of an exposure.
I	final output image sent to the DHS.
n	number of samples (1 for CDS method).
m	number of co-adds.

This significantly reduced the processing requirements of the DC IOC compared to the linear-fitting method used by NIFS.

7.3.4.4.3 Pixel Data Unraveling

Each of the four imager detectors is organized into four strips with one readout per strip. This is illustrated in Figure 108. Pixel data will arrive in an interleaved order from the sixteen output amplifiers. It will be necessary to unscramble these pixel data before they are sent to the DHS.

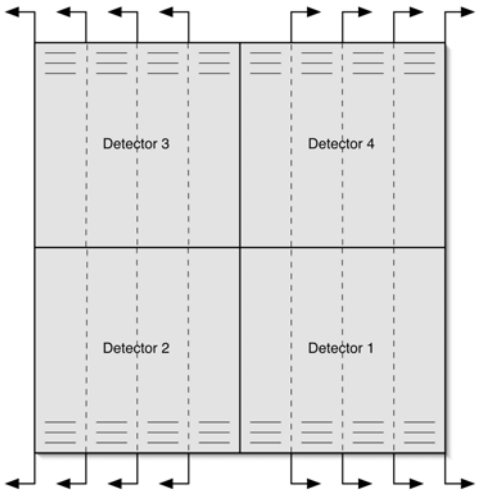

Figure 108: GSAOI detector readout arrangement.

Pixels will arrive from the detector in the order:

$d1s4_{x,1}$, $d2s1_{1,1}$, $d3s1_{1,y}$, $d4s4_{x,y}$, $d1s3_{x,1}$, $d2s2_{1,1}$, $d3s2_{1,x}$, $d4s3_{x,y}$, ... $d1s2_{1,y}$, $d2s3_{x,y}$, $d3s3_{x,1}$, $d4s2_{1,1}$, $d1s1_{1,y}$, $d2s4_{x,y}$, $d3s4_{x,1}$, $d4s1_{1,1}$

where a pixel is addressed by $dNsM_{i,j}$ with

dN detector number *N* (*N*= 1,4),
sM strip number *M* (*M*=1,4),
i,j x and y location from the bottom-left corner of each strip.

The *Camera* class needs to know how the detector is laid out to enable the unraveling of data to proceed. Specifying the number, location, size, orientation, and readout direction of each readout strip origin does this. This information is contained in a structure with the parameters in Table 52 specified for each detector readout.

Table 52: Detector Layout Parameters

Parameter	Data type	Description
xo	U16	x offset of first pixel
yo	U16	y offset of first pixel
width	U16	number of columns
height	U16	number of rows
xdir	S16	direction of readout – columns
ydir	S16	direction of readout – rows
orientation	Boolean	orientation of readout – either row or column

In addition, each detector will be positioned in the mosaic according to x and y offsets from the bottom left corner of the mosaic (Table 53).

Table 53: Detector Position Parameters

Parameter	Data type	Description
xo	U16	x offset of first pixel in mosaic co-ordinate system
yo	U16	y offset of first pixel in mosaic co-ordinate system
width	U16	number of detector columns
height	U16	number of detector rows

The unscrambling algorithm used by the *Readout* task will work as described in the following pseudo-code:

```
For each readout amplifier
    For each detector
        Set index into input array to start of row/column
        For each row/column on detector strip
            Compute output row/column based on readout direction/orientation
            For each pixel in row/column
                Compute output column/row position based on readout direction/orientation
                Copy pixel from input location to output location
                Increment input pixel pointer by number of interleaved readouts
            End loop over pixels
        End loop over rows/columns
    End loop over detectors
End loop over amplifier
```

The RSAA *Camera* class implements this algorithm as a C++ template method so that different input and output data types are easily handled. Note that performance of this unraveling algorithm depends heavily on maintaining memory locality of reference. Performance is maximized by ensuring that each detector strip is filled in order.

7.3.4.4.4 Regions of Interest

GSAOI will support a number of predefined regions of interest (ROI) on the detector mosaic. These ROI will enable shorter readout times and consequently shorter exposure periods required for certain applications (§3.1.3.1 of Vol. 1).

An important component of the configurability of RSAA's software package CICADA is its ability to handle the geometry of detector mosaic layouts in a generalised way. The above set of ROI may be a simple rectangular region in mosaic coordinates but may actually span multiple detectors and readouts of the mosaic at the readout level. The RSAA *Regions* class is a general solution to the problem of converting the specified rectangular readout sub-region (in mosaic coordinates) into the actual pixels clocked out by the controller(s) (in detector/amplifier coordinates). We plan to use this software for GSAOI ROI handling.

The *Regions* class is capable of dealing with almost any practical mosaic geometry. It handles any (reasonable) number of detectors of any size, with arbitrary multiple readout positions and directions, including support for reference pixels in rows and columns for each readout (it also supports independent pixel binning in either axis). The only assumption made is that the size of the full readout of each amplifier must be the same for all amplifiers. This constraint is likely to be true for all conventional detector mosaic systems. In general, a single mosaic ROI spanning multiple amplifiers is converted to multiple smaller readout regions, one region per readout amplifier.

The information returned from the *Regions* class will be used by GSAOI to:

1. Setup the detector controller with ROI parameters in units the controller understands.
2. Construct the output pixels for the DHS from the interleaved stream of pixels coming from the detector controller.

7.3.4.4.5 Reference Pixels

For each of the ROI described above a matching predefined number of reference pixels in rows and columns will be available. These reference pixels will be able to be sampled multiple times (see §5.2.5.3.1).

7.3.4.4.6 WCS Issues

The World Coordinate System (WCS) calibration will be obtained in the manner described in Gemini ICD 18, *viz.* a star with accurately known coordinates will be positioned on one detector of the array at position (x,y). The pixel coordinate (i,j) of the star is measured. This is then repeated for several positions on the same detector, and a transformation matrix is obtained for that detector. Each detector in the array is calibrated independently. During an observation, telescope context information is obtained from the TCS, and this information is used with the four transformation matrices to write the world coordinate information into the FITS header.

7.3.4.4.7 DHS DataTtransfer

During transfer to the DHS, CPU will be required by the data transfer tasks for moving data from memory to the fast-Ethernet interface. Because of the data volumes involved, these tasks are expected to be busy and their performance is important in the overall throughput of the instrument. These performance issues are explored further in §7.3.4.5.3.

7.3.4.5 DC Performance Issues

Five areas of performance are important in the GSAOI DC software design:

1. Throughput from the detector controller to the IOC.
2. Data processing time – summing, subtracting, averaging, and co-adding samples from an exposure.
3. Throughput to the DHS and QLD.
4. Data transfer throughput – ODGW to A&G System.
5. Data transfer throughput – OIWFS to A&G System.

7.3.4.5.1 Throughput from the Detector Controller to the IOC

The controller will read out the array in 5 s. This is a rate of 3.2 Mpixels/s. The SDSU PMC interface board can handle 12.5 Mpixels/s, thus providing ample headroom. The 33 MHz PCI bus on a single-board computer will allow transfer of data to RAM at a maximum of 66 Mpixels/s. The memory bus speed on typical single-board computers runs at 100 MHz. So, it is clear that the data rate can be easily handled by the proposed SDSU PMC card installed on a typical VME single-board computer with a PMC slot.

7.3.4.5.2 Data Processing Time

Testing was performed to gauge the CPU capacity required to handle the data processing described in §7.3.4.4 on a Synergy VGM5 single-board computer running at 400 MHz with 512 MB of RAM (i.e., the NIFS DC IOC processor). Table 54 shows the results obtained for an example Fowler sample readout with 4 samples repeated 4 times (i.e., 4 co-adds).

Table 54: GSAOI Data Processing Times

Operation (n=4, nc=4)	Time (s)	Time with Altivec (s)	Time with Altivec and shift division (s)
Sum samples - $\sum_{i=1}^{n} I_i$	3.6	3.6[11]	3.6
Difference and average - $(SI2 - SI1)/n$	3.1	1.9	1.5
Average co-added pixels - SCI/nc	1.2	0.7	0.7
Unravel pixels	3.7	3.7[12]	3.7
Total	**11.6**	**9.9**	**9.5**

It is proposed that the G4 Altivec instruction set be used to handle the subtraction/division operations as the vector unit is well suited to the processing required. That is, because pixels will need identical operations performed on them, they can be sequenced four at a time with the 128 bit Altivec vector unit. One can also restrict both *n* and *nc* to values that are a power of two so that shift division can be used.

The numbers indicate that the test processor is adequate for the goal of processing the data in 10 s. But it will not be able to handle both the data processing and DHS transfer in this time. This is discussed further in §7.3.4.5.3. Time will also be required for the PMC device driver readout and ODGW handling.

7.3.4.5.2.1 Pipeline Processing

Data processing is done in a parallel processing pipeline where possible. As soon as enough pixels are read out by the detector electronics, the *Readout* task will start working on them. During the first readout, pixels will be accumulated in a summing buffer, then once the second readout starts pixels will be processed to their final values before unraveling and handing to the *Data* process for transfer to the DHS. Figure 109 illustrates this process.

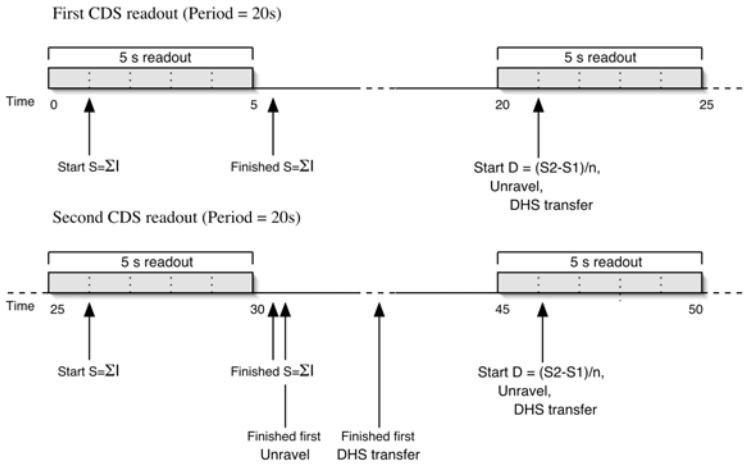

Figure 109: Processing pipeline during readout.

This pipeline design ensures that the next exposure can be started as soon as possible. It will also determine the minimum readout period that will allow continuous exposures.

[11] The Altivec instruction set cannot be used for this operation as it involves the promotion of unsigned 16 bit numbers to unsigned 32 bit numbers.
[12] The Altivec instruction set cannot be used for this operation as it involves the movement of data from locations 16 pixels apart, i.e., each detector strip in the output array is filled in turn from the pixel stream.

7.3.4.5.2.2 Memory Required

Fowler sampling requires that the detector be read a number of times continuously - either enough buffer space has to be available to contain up to 64 reads of the detector, or, more sensibly, data will have to be processed and moved out of the input buffer during readout so that input buffer space can be reused.

Table 55 shows the memory required for the large data arrays needed. The size of the circular buffer is set to two in this example. This would allow ~ 10 s (i.e., 2 × 5 s readouts) for moving pixels out of the first frame before it is refilled with the next sample. This should be sufficient.

Table 55: Data Storage Arrays – Correlated Double Sampling and Fowler Sampling

Array Name	Data Type	Size (MB)	Description
Pix × *N*	U16	64.0	Raw pixels (*I*)
SumPix1	U32	64.0	Summed pixels from first set of samples ($\sum I_1$)
SumPix2	U32	64.0	Summed pixels from second set of samples ($\sum I_2$)
CoaddPix	R32	64.0	Cumulative sum for co-added exposures ($\sum I_D$))
Intensity	R32	64.0	Final unraveled pixels for DHS (*F*)
Total		**320.0**	***N*=2**

The *Intensity* array is allocated by the DHS implementation for use during data transfer. Pixels are copied into this space from the *CoaddPix* array and unraveled in the process.

A single-board computer with 512 MB of RAM is a minimum requirement.

7.3.4.5.3 Data Transfer Throughput – DHS and QLD

Data transfer speed tests were performed with a locally-installed version of the DHS (V0.19/no DB). The tests were varied to see what parameters in the transfer process were important in gaining the best performance. In particular, we were interested in seeing the effect of increasing the power of the DHS server machine on transfer times. In all cases, a Synergy VGM5 with 400 MHz PPC 7400 and 512 MB was used as the IOC processor.

Table 56 shows times taken for tests where server processor and server file storage location were varied. Note that increasing the server from a dual processor Ultra 2 to a SunBlade 1000 improved transfer times somewhat, i.e., between 11 and 22%. (It is necessary to make sure that the server has enough RAM for the DHS. For a 64 MB transfer this needs to be greater than 512 MB to prevent the system from page-faulting severely. The DHS server processes use ~ 5× the image size for run-time memory). One might have expected more of an improvement based on processor power, i.e., a factor of 2-3. This was a surprise and led us to perform another set of tests in an attempt to identify the bottleneck. These tests use a simple FITS server in place of the DHS. The results are detailed in Table 57.

Table 56: DHS Performance Tests (average from 5 tests)

DHS Server Host	File Size	Disk Location	Time Taken (s)
Ultra III 2×900 MHz, 1 GB	64 MB	Local FCAL disk	21.8
Ultra III 2×900 MHz, 1 GB	64 MB	Virtual RAM disk	15.4
Ultra II 2×300 MHz, 768 MB	64 MB	Local USCSI disk	28.1
Ultra II 2×300 MHz, 768 MB	64 MB	Virtual RAM disk	17.3

Table 57: FITS Server Performance Tests (average from 5 tests)

FITS Server Host	File Size	Disk Location	Time Taken (s)
Ultra III 2×900 MHz, 1 GB	64 MB	Local FCAL disk	14.9
Ultra III 2×900 MHz, 1 GB	64 MB	Virtual RAM disk	12.3
Ultra II 2×300 MHz, 768 MB	64 MB	Local USCSI disk	21.1
Ultra II 2×300 MHz, 768 MB	64 MB	Virtual RAM disk	16.3

Again the difference between machines here is small (~ 25%). Note that here the optimal time achieved on the fast SunBlade 1000 for a 64 MB file (required for GSAOI) is more than 20% faster than the optimal time achieved with the DHS. Because the DHS first stages the data to disk in */staging/temp* before rewriting the file in FITS format, extra time should be allowed. This should typically be ~ 2 s on the SunBlade 1000 (i.e., a simple Unix *cp* operation on a 64 MB file takes ~ 2 s). A potential bottleneck may lie with how the DHS handshakes with the Interprocess Message Passing (IMP) system server on the IOC or, perhaps, the DHS data dictionary lookups may take significant time. As the FITS server is still running under the fast Ethernet ceiling, i.e., ~ 5 MB/s compared to at least 10 MB/s when running tests between two Solaris machines, the IOC must also limit the speed at which transfers can ultimately be made to go.

Are there any ways that these DHS times can be improved?

Some investigation was made into tuning the VxWorks TCP/IP stack. In particular, the VxWorks TCP socket send buffer size ("tcp_sendspace") was increased from its default value of 8192. Improvements in transfer times were maximized when the value of this variable was set to 32768 or thereabouts. These improvements were more significant with the FITS server tests. The DHS tests remained essentially the same, indicating that some other bottleneck in the DHS communications system needs addressing. See http://www.xs4all.nl/~borkhuis/vxworks/netPerformance.txt for a more detailed discussion of how to configure VxWorks for optimal TCP/IP performance. Table 58 shows new timings with the value of this parameter increased to 32768.

Table 58: DHS Performance Tests with tcp_sendspace=32768

DHS Server Host	File Size	Disk Location	Time Taken (s)
Ultra III 2×900 MHz, 1 GB	64 MB	Local FCAL disk	20.5
Ultra III 2×900 MHz, 1 GB	64 MB	Virtual RAM disk	15.0
Ultra II 2×300 MHz, 768 MB	64 MB	Local USCSI disk	28.0
Ultra II 2×300 MHz, 768 MB	64 MB	Virtual RAM disk	17.2

Similarly, Table 59 shows the significantly improved numbers for the FITS transfer tests with the increased value of "tcp_sendspace". Here the maximum throughput has been increased close to wire speed, i.e., 9.3 MB/s.

Table 59: FITS Server Performance Tests with tcp_sendspace=32768

FITS Server Host	File Size	Disk Location	Time Taken (s)
Ultra III 2×900 MHz, 1 GB	64 MB	Local FCAL disk	9.2
Ultra III 2×900 MHz, 1 GB	64 MB	Virtual RAM disk	6.9
Ultra II 2×300 MHz, 768 MB	64 MB	Local USCSI disk	13.1
Ultra II 2×300 MHz, 768 MB	64 MB	Virtual RAM disk	8.1

Interestingly, it is also worth noting that during the running of these tests our Synergy VGM5 BSP was upgraded to its latest version (V1.21k1 from V1.21h+) and we saw significant improvements in transfer times (e.g., from 30.1s to 21.8s for the DHS test to local disk on an Ultra III with default TCP buffer size).

The significance of increasing "tcp_sendspace" also declined after this upgrade. Perhaps there will be further improvements as the BSP is improved.

To assess the effect IMP might be having on our transfer performance, Keith Shortridge of the Anglo Australian Observatory (the author of IMP) was asked for his opinion. Kindly, Keith ran some tests that showed that IMP was able to run close to the maximum speed possible on a fast-Ethernet link between two Sun machines, i.e., 10 MB/s when the TCP socket buffer sizes were set to large values (262 KB). These tests were repeated for a VxWorks to Sun transfer using the same machines indicated above, and it was found that IMP again can perform close to wire speed, achieving 8.6 MB/s using a "tcp_sendspace" setting of 32768. This is the same sort of performance seen with the FITS transfer tests above when writing to the "/tmp" file system (IMP writes its received data to memory mapped file space). We conclude that the way IMP uses TCP/IP should not impact DHS performance.

To summarize, optimal DHS throughput (without any software redesign) will be achieved if the following are addressed:

- Availability of a fast DHS processor with very fast disk for permanent store and preferably memory-based temporary store.
- Optimal configuration of TCP/IP transfer buffer sizes on both DHS client and server systems.
- Fastest possible network infrastructure.

As shown in our tests, speeds down to ~ 20 s are possible, with our local conditions, to transfer 64 MB images to the DHS.

7.3.4.5.4 Data Transfer Throughput – ODGW to A&G System

The maximum data transfer performance required for the ODGW will be 112.5 KB/s (i.e., readouts of four 12×12 pixel windows at 100 Hz). Data will be moved from the controller over the fiber optic link to the SDSU PMC card hosted by the VME single-board computer. This link can run at 25 MB/s, so the ODGW data are comfortably handled. It will then be moved over the VME bus to the reflective memory board (VMIC VMIVME-5588). The maximum VME bus throughput is stated as 40 MB/s, so the ODGW data can easily be accommodated. Once data are written to the reflective memory board it will appear on the A&G System's reflective memory board at a rate of at least 15 MB/s. For each frame the A&G System will be sent an interrupt to idicate that a new frame is ready for processing.

It is clear that the proposed design will easily handle the planned ODGW data rate.

7.3.4.5.5 Data Transfer Throughput – OIWFS to A&G System

Because GSAOI will use the same OIWFS detector as is used in NIRI/NIFS, the data transfer throughput will be the same as for NIRI/NIFS.

7.3.4.6 Proposed DC Hardware

To implement our software solution, we propose that the following hardware components are required:

7.3.4.6.1 DHS Host Hardware

The DHS system will need to run on the fastest Sun processor available to enable the GSAOI design to approach its goal of being able to deliver a new image every 10 s. Our testing on a SunBlade 1000 system with dual 900 MHz Ultra III CPUs and 1 GB of memory (and without any SyBase access) did not allow us to meet the 10 s goal. Best speeds were gained when fastest permanent storage was used (in our case the Solaris *tmpfs* file system), so fast disk storage is essential.

We have been able to show that the IMP is able to transfer data at close to fast-Ethernet wire speed, so it is reasonably clear that something else within the DHS is taking most of the time.

Note that no QLD testing was performed in this analysis, so allowance will have to be made for any extra time a QLD would take.

7.3.4.6.2 Network Speed – Gigabit?

Would a Gigabit Ethernet Gemini Data LAN make any difference to the DHS turnaround? As indicated in the previous section, most of the time for a DHS transfer is spent within the DHS itself – and not in the actual transfer of data. If we assume data were transferred at close to fast-Ethernet wire speed (a reasonable assumption, given our IMP tests), then the best improvement one could expect would be of order 5 s (i.e., assume a best case of 80% of Gigabit Ethernet wire speed). This would still mean a DHS transfer (no QLD or Sybase) to a fast local disk would take ~ 15 s with systems like those used in our tests.

Our baseline solution does not include a Gigabit Ethernet interface, but we have included a Gigabit Ethernet network-interface card (NIC) in our costings as an option.

7.3.4.6.3 Dual G4 PowerPC

In conclusion, to best approach the fast throughput goals of GSAOI and to retain an IOC configuration that is close to what is recommended by Gemini, we recommend a VME single-board computer that has dual Motorola G4 PPCs. One PPC will be kept busy with DHS transfers while the other will be handling the data processing needs of the next detector readout. As shown in the test results of §7.3.4.5.2, a single 400 MHz PPC is able to just manage the load of processing the readout data, so a dual CPU system is specified.

Table 60 lists three of fast dual-processor VME single-board computers currently on the market with PMC slots. Either of these systems would be satisfactory, but as a baseline solution we recommend the Synergy Falcon VYMD (512 MB version) because of our experience using Synergy with NIFS and it has the later version of the G4 PPC which offers performance improvement. This board also has 128 MB of user flash memory and 2 PMC sites (which would allow for a Gigabit Ethernet upgrade option).

Table 60 Alternative GSAOI DC Dual Processor Single Board Computers

Company	Product	Processors	Speed	Memory	Cost ($US)
Synergy	Falcon VYMD	2×PPC 7410	466 MHz	1 GB SDRAM	$18500
Synergy	Falcon VYMD	2×PPC 7410	466 MHz	512 MB SDRAM	$12900
Synergy	VGM5	2×PPC 7400	466 MHz	512 MB SDRAM	$13700
Radstone	PPCM1	2×PPC 7410	500 MHz	2×512MB SDRAM	N/A[13]

Figure 110 illustrates the proposed DC IOC hardware configuration for GSAOI. It comprises a standard VME crate, the Synergy Falcon VYMD dual G4 PPC processor board with SDSU-2 PMC daughter board, the VMIC VMIVME5588 reflective memory board and the Bancomm BC635VME time board. The Synergy fast-Ethernet interface will be connected to a Cisco fast-Ethernet switch (not shown) that will have fiber-optic connections to both the Gemini Data and Control LANs. The reflective memory board will be attached to the Gemini Synchro bus for communication with the A&G System. Lastly, the time card will be attached to the Gemini time bus for accurate time synchronization.

[13] At time of writing, a quotation for this board had not arrived but the price is expected to be similar to the Synergy boards.

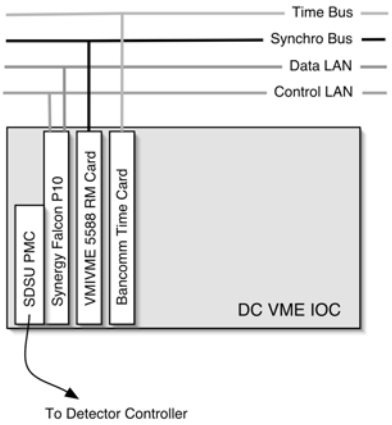

Figure 110: Proposed configuration of the GSAOI DC IOC.

7.3.4.7 DC Upgrade Options

A 32 readout per detector upgrade option is described in §5.2.7 that may be considered if the ASIC controller option is implemented. This option will allow the controller to be read out in ~ 2.7 s. Without changing the processing engine and DHS, data processing and transfer times will remain the same as for the slower readout configuration. Therefore, this option will reduce the minimum continuous frame time only slightly. However, it will improve observing efficiency when short exposures (of order 1 min) are used because the pipelined data processing and transfer will occur largely during the next exposure. To reduce the minimum continuous frame time, significant improvements will be needed in the DHS throughput and the processing engine speed. More processors may need to be deployed in the processing engine, or the DC IOC may need to migrate to a faster Intel-based PC system. This direction would involve significant extra development effort and cost that is not compatible with a fast-tracked instrument.

7.3.4.8 DC Testing and Simulation

It is planned to develop RSAA's CICADA software package[14] to support the H2RG infrared array at the beginning of the project so that software will be available for detector characterization as early as possible. This will be done in the context of the *Camera* class discussed above, so software developed will be directly available for GSAOI.

7.3.4.8.1 PCI Interface Board

Currently CICADA software communicates with the SDSU-2 controller via an SBUS interface board. Some modification of the code will be required to interface through the proposed SDSU PCI board. SDSU provide device drivers for Sun Solaris for this board already, so it is expected that this device driver will be used with some customization to support the CICADA protocol.

7.3.4.8.2 CICADA Simulation Camera

The CICADA package also supports simulation cameras that are used in the absence of real hardware. A simulation camera is directly derived from the *Camera* C++ class, so will be used for testing the GSAOI software design during early development. The aim will be to have data processing and transfer code well developed, independent of the hardware. This code will form the basis of support for Gemini's required simulation modes.

[14] http://www.mso.anu.edu.au/computing/cicada

7.4 Software Risks

7.4.1 Staff Loss

EPICS is a large, complex system which is difficult to learn, in part, owing to poor documentation. Knowledge of this system at RSAA has been hard won, and resides with a few people. Loss of these people could prejudice the software development schedule. To defend against this risk, we are involving other RSAA programmers in this development work, so that the knowledge is shared.

7.4.2 PMC Device Driver Development

The SDSU-2 PMC interface board is currently being developed by Bob Leach for the Gemini MCAO project. Consequently, a VxWorks device driver is unlikely to be ready from the MCAO group in time for RSAA to use it. RSAA will develop their own driver if the MCAO driver is not available (or is not suitable). As RSAA staff do not have any experience developing VxWorks device drivers, this is a relatively risky undertaking. However, we have had experience in the development of a new version of the SDSU SBUS *astro* driver for Solaris. This driver is in use at all our telescopes and also those of the Anglo-Australian Observatory. We will also consider purchasing driver development tools such as the one offered by Jungo Ltd. (htpp://www.jungo.com) to assist with this approach.

8 Appendix A: Optical Design Detail

8.1 Nomenclature

Symbols used in the optical analysis are defined as follows. Some additional symbols are defined locally.

σ	Wave-front error
ε	Surface irregularity
n	Refractive index
d_{beam}	Point-source beam footprint diameter on an optical surface
d_{face}	Face diameter of an optical surface
$\delta\gamma_{sky}$	Angular aberration referred to sky
d_{tel}	Diameter of telescope aperture
r	Radial distance from the center of an optical face
δr	Radial displacement of an interference fringe
R	Radius of curvature of an optical surface
δR	Difference in radius of curvature between two optical surfaces
h	Gap width between two optical faces
δh	Deviation in gap width between two optical faces
λ	Wavelength
i, j	Sequence numbers for interference fringes
θ	Angle position about the center of an optical face
r_1, r_2	Curvature radii of two lens surfaces
d	Diameter of lens housing
e	Eccentricity of lens in housing
ϕ	Wedge angle of lens in housing

8.2 Surface Irregularity and Optical Aberration

Angular aberration caused by surface irregularity is proportional to the slope error of the surface. In principle, this is dependent on both the form and magnitude of the irregularity. For small surfaces, however, polishing methods ensure that the irregularities are smooth and of low spatial frequency. The form of such irregularities is therefore independent of face size, and their effects can be determined by their magnitude alone. To characterize this, surface irregularity is here assumed to take its smoothest possible form, namely, astigmatism. For this, the surface height error is a second-order function of radial position on the surface. The curvature error varies with azimuth on the surface, but is independent of position on the surface.

The adoption of this astigmatism model allows determination of the relationship between surface irregularity and angular aberration. Importantly, the diameter of a point-source beam footprint on a surface can be smaller than the diameter of the surface, and the resulting attenuation of the angular aberration can also be determined.

Likewise, the relationship between surface irregularity and wave-front error can also be determined for any level of under-filling of the surface by the beam footprint.

Useful relationships derived from this model are

$$\sigma = \frac{n-1}{n}\left(\frac{d_{beam}}{d_{face}}\right)^2 \varepsilon$$

$$\delta\gamma_{sky} = 8\frac{n-1}{n}\left(\frac{d_{beam}}{d_{face}}\right)^2\frac{1}{d_{tel}}\varepsilon$$

$$= 8\frac{\sigma}{d_{tel}}$$

Where the surface is a mirror, n = -1.

The second of the foregoing equations relates angular aberration to wave-front error. Oschmann (SPE-S-G0041) has defined a corresponding relationship for the Gemini telescope. According to this, 50 nm RMS wave-front error corresponds approximately to a 0.01″ degradation in 50% encircled energy diameter at 2.2 μm. Assuming that 50% encircled energy is equivalent to the RMS angular diameter, these two relationships agree. This suggests that the astigmatism model is reasonable.

8.2.1 Systematic Effects in Crystal Materials

When a spherical optical surface is produced on a crystal material, systematic surface irregularities tend to develop. Of the materials proposed for GSAOI, experience in the Optical Workshop at RSAA indicates that this effect is most pronounced for magnesium oxide. A test has therefore been done to quantify the irregularity for this material. The results are presented here.

Magnesium oxide has a cubic crystal structure. Assuming that this structure is square to the lens axis, the polished surface has a "quadfoil" irregularity centered on the axis, as shown in Figure 111.

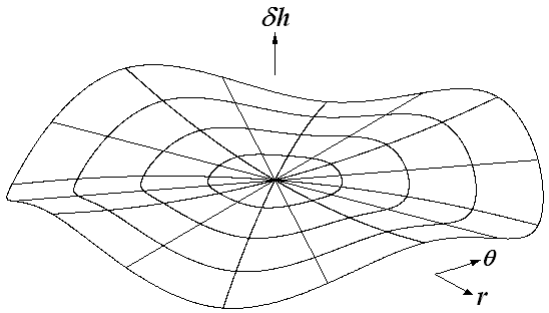

Figure 111: Systematic irregularity for a cubic crystal lens surface.

Where the surface of the material is sloped with respect to the crystal structure, the rate of material removal during the grinding process varies with the direction of the slope. At any given radius (r) from the vertex of the spherical surface, the slope is constant in magnitude but changing in direction, and so the surface depth oscillates with angular position (θ). For any given polishing technique, it is assumed that the amplitude of this oscillation is a function of the surface slope alone.

To quantify this relationship for the polishing technique used at RSAA, a spherical test surface was ground and polished on a magnesium oxide blank, and an interferogram of the surface error was recorded (Figure 112). A flat surface was also produced to confirm that the error pattern did not occur in that case.

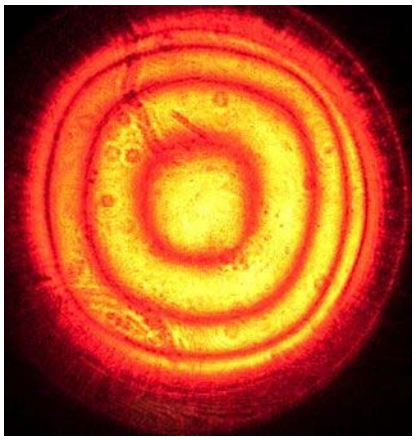

Figure 112: Interferogram for magnesium oxide test surface.

In the interferogram, the quadfoil surface error is indicated by the square distortion of the rings. The theory for interpreting this is developed as follows with reference to Figure 111 and Figure 113.

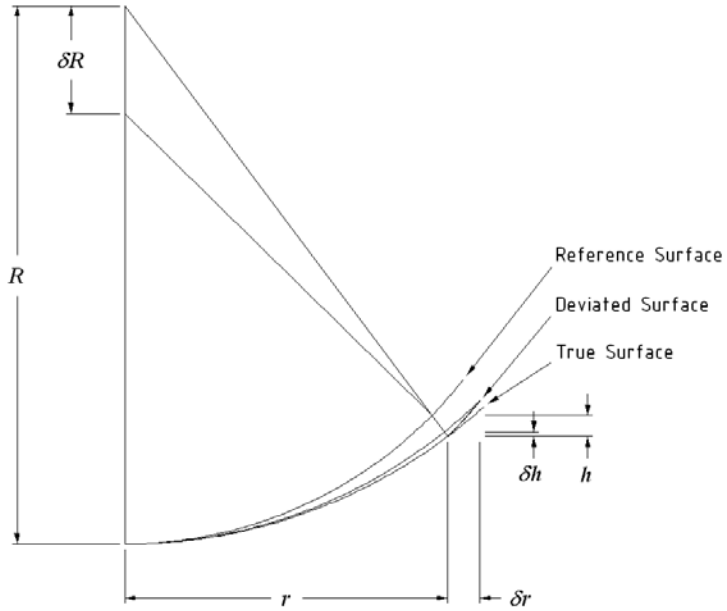

Figure 113: Interference fringe geometry.

Assuming that $r << R$, the separation between the true spherical surface and the reference surface is

$$h = \frac{1}{2}\frac{\delta R}{R^2} r^2 .$$

Using the measured radii on any two fringes, r_i and r_j, this formula can be rearranged to determine the difference in surface radii as

$$\delta R = \frac{(j-i)\lambda R^2}{\left(r_j^2 - r_i^2\right)}$$

If θ is set to zero at a radial ridgeline of the deviated surface, then the surface error can be modeled as

$$\begin{aligned}\delta h &= \frac{dh}{dr}\delta r\cos(4\theta)\\ &= \frac{(j-i)\lambda}{(r_j^2 - r_i^2)} r\delta r\cos(4\theta)\end{aligned}$$

Measuring the fringes (Figure 112) confirms the appearance that they all have the same shape. A constant fringe distortion factor can therefore be defined as

$$\begin{aligned}k &= \frac{\delta r}{r}\\ &= 0.025\end{aligned}$$

Assuming that the amplitude of the surface error at any given radius r is dependent only on the surface slope at that radius (as discussed earlier), a further constant can be defined as

$$K = \frac{(j-i)\lambda R^2}{(r_j^2 - r_i^2)}$$

For this test, λ = 633 nm, and R = 47.6 mm. Using the first and third fringes, i = 1, j = 3, r_i = 5.9 mm, and r_j = 15.9 mm. Substituting gives

$$K = 13200 \text{ nm}.$$

Subtituting these two constants in the previous equation gives

$$\begin{aligned}\delta h &= kK\left(\frac{r}{R}\right)^2\cos(4\theta)\\ &= 330\left(\frac{r}{R}\right)^2\cos(4\theta)\text{ nm}\end{aligned}$$

The term r/R is the surface slope at radius r.

The peak-to-valley irregularity for the whole surface is

$$\begin{aligned}\varepsilon_{p-v} &= 2\delta h_{\max}\\ &= 165\left(\frac{d_{face}}{R}\right)^2\text{ nm}\end{aligned}$$

The corresponding RMS irregularity is

$$\varepsilon_{RMS} = \frac{1}{2\sqrt{6}}\varepsilon_{p-v}$$
$$= 34\left(\frac{d_{face}}{R}\right)^2 \text{ nm}$$

For the test piece, r_{max} = 17.2 mm, R = 47.6 mm, $\varepsilon_{p\text{-}v}$ = 86 nm, and ε_{RMS} = 18 nm.

This surface irregularity has the same form as astigmatism, except that it is quadfoil rather than bifoil. The relationship between surface irregularity and wave front error is therefore the same as that for the astigmatism model investigated in §8.2. That is

$$\sigma = \frac{n-1}{n}\left(\frac{d_{beam}}{d_{face}}\right)^2 \varepsilon$$

Combining the two foregoing equations, and setting n = 1.71 for magnesium oxide, the wave-front error is

$$\sigma_{RMS} = 14\left(\frac{d_{beam}}{R}\right)^2 \text{ nm}$$

For a single lens, the surface irregularity on the two faces has the same orientation, and so the resulting wave-front errors add arithmetically, not in quadrature.

8.3 Lens Eccentricity Wedge

It is proposed that the lenses in GSAOI be mounted as shown in Figure 114. The housing and lens diameter tolerances are arranged so that the minimum clearance is zero. The maximum clearance is then the quadrature sum of the tolerances. Lateral displacement of the lens within its clearance zone then causes the unsupported lens surface to tilt, and so the lens develops a wedge error.

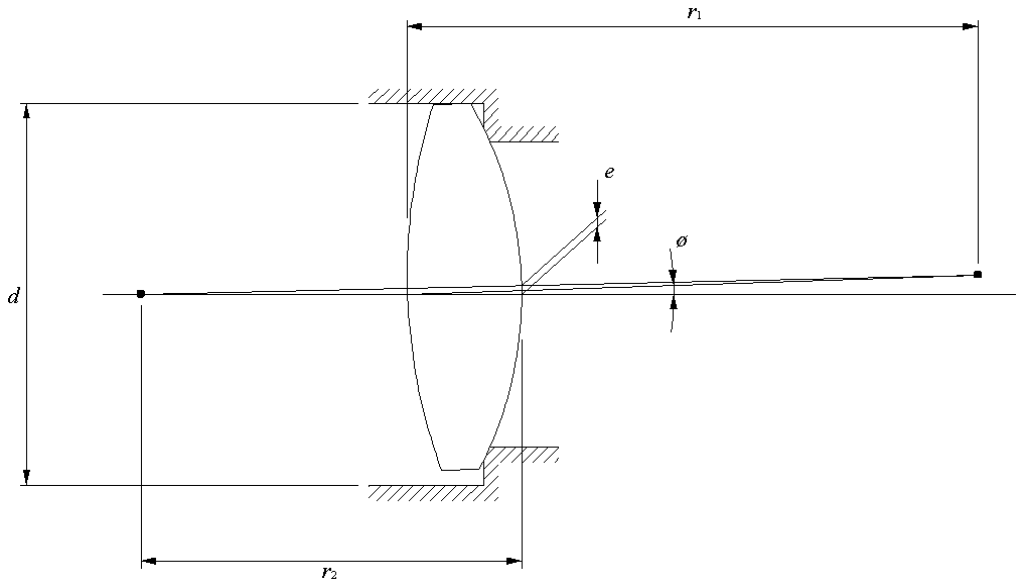

Figure 114: Lens mounting geometry.

Applying conventional precision engineering tolerances (IT7 for the housing and IT6 for the lens, using mm units), the maximum eccentricity of the lens is

$$e = 0.0042 d^{\frac{1}{3}}$$

The corresponding wedge angle is

$$\begin{aligned}\phi &= e\left(\frac{1}{r_1}+\frac{1}{r_2}\right)\\ &= 0.0042 d^{\frac{1}{3}}\left(\frac{1}{r_1}+\frac{1}{r_2}\right)\end{aligned}$$

This is independent of which face is supported, and proportional to the lens power.

8.4 TMA Concepts

A third-order procedure for designing axial, centered mirror systems has been described by Korsch (1991, Reflective Optics, Academic Press: San Diego)). Briefly, the angular ray coordinates at each surface are expressed as

$$\Phi_{xi} = A_i \tau_i^{-4} \tilde{h}_i^2 \tilde{x}_i - B_i \tau_i^2 [\tilde{h}_i^2 \phi_{xi} + 2(\tilde{x}_i \phi_{xi} + \tilde{y}_i \phi_{yi})\tilde{x}_i] + C_i (\tilde{x}_i \phi_{xi} + \tilde{y}_i \phi_{yi})\phi_{xi} + D_i \tilde{x}_i \phi_i^2 - E_i \tau_i^2 \phi_i^2 \phi_{xi}$$
$$+ F_i \Delta s_i' \tilde{x}_i + (1 + \mu_i f_i^{*-1} \Delta s_i')\phi_{xi}$$
$$\Phi_{yi} = A_i \tau_i^{-4} \tilde{h}_i^2 \tilde{y}_i - B_i \tau_i^2 [\tilde{h}_i^2 \phi_{yi} + 2(\tilde{x}_i \phi_{xi} + \tilde{y}_i \phi_{yi})\tilde{y}_i] + C_i (\tilde{x}_i \phi_{xi} + \tilde{y}_i \phi_{yi})\phi_{yi} + D_i \tilde{y}_i \phi_i^2 - E_i \tau_i^2 \phi_i^2 \phi_{yi}$$
$$+ F_i \Delta s_i' \tilde{y}_i + (1 + \mu_i f_i^{*-1} \Delta s_i')\phi_{yi}$$

where the index, *i*, refers to the surface number, $\tilde{x}_i$ and $\tilde{y}_i$ are linear pupil coordinates, $\tilde{h}_i^2 = \tilde{x}_i^2 + \tilde{y}_i^2$, τ_i are the image scale coefficients, ϕ_{xi} and ϕ_{yi} are the angular object coordinates, $\phi_i^2 = \phi_{xi}^2 + \phi_{yi}^2$, $\Delta s_i'$ is the axial defocus, μ_i is the angular magnification, and f_i^* is the system image scale factor. The Seidel coefficients are expressed in terms of the surface conic constants as

$$A_i = c_i^3 \Delta\delta_i$$
$$B_i = t_i \tau_i^{-1} c_i^3 \Delta\delta_i - \varepsilon_i c_i^2$$
$$C_i = 2(t_i^2 \tau_i^{-2} c_i^3 \Delta\delta_i - 2 t_i \tau_i^{-1} \varepsilon_i c_i^2 + c_i)$$
$$D_i = t_i^2 \tau_i^{-2} c_i^3 \Delta\delta_i - 2 t_i \tau_i^{-1} \varepsilon_i c_i^2$$
$$E_i = t_i^3 \tau_i^{-3} c_i^3 \Delta\delta_i - 3 t_i^2 \tau_i^{-2} \varepsilon_i c_i^2 + 2 t_i \tau_i^{-1} c_i$$
$$F_i = f_i^{*-2}$$

where the conic constant $\delta_i = \Delta\delta_i - \varepsilon_i^2$, c_i are the surface curvatures, t_i are the entrance pupil distances, and ε_i are the surface eccentricities. The angular ray coordinates in the final image can then be expressed as

$$\Phi_x = A\tilde{h}^2\tilde{x} - B[\tilde{h}^2\phi_x + 2(\tilde{x}\phi_x + \tilde{y}\phi_y)\tilde{x}] + C(\tilde{x}\phi_x + \tilde{y}\phi_y)\phi_x + D\tilde{x}\phi^2 - E\phi^2\phi_x + F\Delta s'\tilde{x}$$
$$+ (1 + \mu_s f_s^{*-1}\Delta s')\phi_x$$

$$\Phi_y = A\tilde{h}^2\tilde{y} - B[\tilde{h}^2\phi_y + 2(\tilde{x}\phi_x + \tilde{y}\phi_y)\tilde{y}] + C(\tilde{x}\phi_x + \tilde{y}\phi_y)\phi_y + D\tilde{y}\phi^2 - E\phi^2\phi_y + F\Delta s'\tilde{y} + (1+\mu_s f_s^{*-1}\Delta s')\phi_y$$

where the third-order system Seidel coefficients are given by

$$A = -\tau_1^{-4}\sum_{i=1}^{3}(-1)^i\Omega_{si-1}^4 A_i$$

$$B = +\tau_1^{-2}\sum_{i=1}^{3}\Omega_{si-1}^2 B_i$$

$$C = -\sum_{i=1}^{3}(-1)^i C_i$$

$$D = -\sum_{i=1}^{3}(-1)^i D_i$$

$$E = +\tau_1^{2}\sum_{i=1}^{3}\Omega_{si-1}^{-2} E_i$$

$$F = f_s^{*-2}$$

with A measuring spherical aberration, B measuring coma, C measuring astigmatism, D measuring field curvature, E measuring distortion, F measuring defocus, and $\Omega_{si} = \prod_{j=1}^{i}\Omega_j$ are the partial system ray-height ratios and f_s^* is the system image scale factor. The reference image coordinates are defined by

$$\Phi_{rx} = (1+\mu_s f_s^{*-1}\Delta s')\phi_x$$
$$\Phi_{ry} = (1+\mu_s f_s^{*-1}\Delta s')\phi_y$$

so the image aberrations for a centered, axial system at focus ($\Delta s' = 0$) become

$$\Delta\Phi_x = \Phi_x - \Phi_{rx} = A\tilde{h}^2\tilde{x} - B[\tilde{h}^2\phi_x + 2(\tilde{x}\phi_x + \tilde{y}\phi_y)\tilde{x}] + C(\tilde{x}\phi_x + \tilde{y}\phi_y)\phi_x + D\tilde{x}\phi^2 - E\phi^2\phi_x$$
$$\Delta\Phi_y = \Phi_y - \Phi_{ry} = A\tilde{h}^2\tilde{y} - B[\tilde{h}^2\phi_y + 2(\tilde{x}\phi_x + \tilde{y}\phi_y)\tilde{y}] + C(\tilde{x}\phi_x + \tilde{y}\phi_y)\phi_y + D\tilde{y}\phi^2 - E\phi^2\phi_y$$

The three conic constants for the TMA surfaces can be chosen to eliminate three of the third-order aberrations (e.g., third-order spherical aberration, coma, and astigmatism). The geometry can be chosen to also eliminate field curvature using the Petzval condition.

This leaves distortion uncorrected. In principle, distortion can also be eliminated in a centered axial system by suitable choice of geometry. However, the options for doing so in the GSAOI imager optics are limited by the constraint of fitting the design within the NIRI/NIFS cryostat.

In practice, it is necessary to tilt and decenter a TMA system in order to allow the beam to enter and exit without vignetting. That this leads to additional, asymmetric distortion terms can be seen from the following analysis. If the pupil is decentered along the *x* axis such that

$$\tilde{x} = \tilde{r}\cos\theta + \tilde{x}_0$$
$$\tilde{y} = \tilde{r}\sin\theta$$

then the aberrations of the chief ray relative to the reference ray, which measure distortion, are given by

$$\Delta\Phi_{px} = \Phi_{px} - \Phi_{rx} = A\tilde{x}_0^3 - 3B\tilde{x}_0^2 + C\tilde{x}_0\phi_x^2 + D\tilde{x}_0\phi^2 - E\phi^2\phi_x$$
$$\Delta\Phi_{py} = \Phi_{py} - \Phi_{ry} = -Bx_0^2\phi_y + C\tilde{x}_0\phi_x\phi_y - E\phi^2\phi_y$$

Consequently, an axial TMA with a decentered pupil can only be free of third-order distortion when it is corrected for all five third-order Seidel aberrations. The *E* terms in the above equations are the normal pin-cushion or barrel distortion term. The other aberrations produce asymmetric distortions such as are seen in the MCAO system itself (§3.3).

We might aim to cancel the asymmetric MCAO distortion in the GSAOI imager optics. However, the orientation of the MCAO system with respect to a duplicate NIRI/NIFS cryostat is such that this requires a GSAOI TMA to be decentered perpendicular to the cryostat cold work surface plate. This is not a convenient geometry to implement. The result is a system combining two perpendicular asymmetric distortions that would be difficult to model and correct in practice.

8.5 Refractive Index of Detector Substrate

The GSAOI imager detector will be a mosaic of Rockwell HAWAII-2RG devices. These detectors use a 0.82 mm thick CdZnTe substrate (Cabelli, priv. comm.) in front of the HgCdTe detector material. Ghost images produced by internal reflections in this CdZnTe layer are a concern where the incident beam is non-telecentric, and there is therefore a need to know the refractive index of the substrate. This is uncertain, and so is estimated here as follows.

Stiavelli[15] (2000) estimated this index in relation to the tilted focal plane of the Hubble Space Telescope WFC3 IR channel. We follow that procedure. The refractive index of CdTe at 300 K and a wavelength of 1 μm is known to be 2.839 ("Handbook of Infrared Optical Materials" by P. Klocek). Herzberger and Sellmeier 2 formulae are also listed for CdTe in the Handbook, based on refractive index data obtained in the wavelength range 6-22 μm (DeBell et al. 1979, App. Opt., 18, 3114). At 80 K, these formulae extrapolate to values at 1 μm of 2.97 and 2.79, respectively. We adopt a mean of 2.88. We estimate the refractive index of CdZnTe by scaling between this pure CdTe value (with a Cd fraction $X = 1$) and a value of $n = 3.41$ reported for HgCdTe with $X = 0.29$ by Hall (priv. comm. to Stiavelli) under the assumption that CdZnTe and HgCdTe have the same refractive index. This assumption is plausible, but has not been verified. We use the inverse of the relation by Hansen et al. (1982, J. Appl. Phys., 53, 7099) for the energy gap in eV, E, as a function of temperature, T, and Cd fraction, X,

$$E(X,T) = -0.302 + 1.93X + 5.35\times10^{-4}T(1-2X) - 0.810X^2 + 0.832X^3$$

to infer X for the GSAOI imager detectors. They have a detector cut-off wavelength of 2.6 μm at 80 K so the band gap E = 0.477 eV. This leads to a Cd fraction of $X \sim 0.45$, and by scaling we estimate the refractive index of CdZnTe to be ~ 3.29 at 1 μm and 80 K, clearly with considerable uncertainty.

8.6 Pick-off Probe Concept

An alternative means of accessing the maximum possible OIWFS guide field is to use a pick-off probe that is able to patrol the entire science field. The probe should be made as small as possible and placed as close as possible to the MCAO focal plane to minimize the area of the science field that it vignettes. We show below that the required stability of such a pick-off probe places tight constraints on the setting mechanism. This makes this approach unattractive.

8.6.1 Design Concept

A two-axis, cryogenic, robotic, pick-off probe could access guide stars over the full 2′ diameter MCAO field (Figure 115). The pick-off probe consists of a 227 mm long Main Arm and a 180 mm long Probe Arm. The Probe Arm would be located close to the f/34 MCAO focal plane, immediately above the GSAOI focal plane wheel. The Main Arm could be mounted from the science instrument side of the NIRI/NIFS cold work surface plate (Figure 116), which is the OIWFS side in GSAOI. The section of the cold work

[15] http://www.stsci.edu/instruments/wfc3/ISRs/WFC3-2000-01.pdf

surface plate above the titanium tines would be removed to allow the guide arm to swing over the MCAO focal plane.

Guide probe orientations needed to set to field positions over the whole MCAO field are shown in Figure 117.

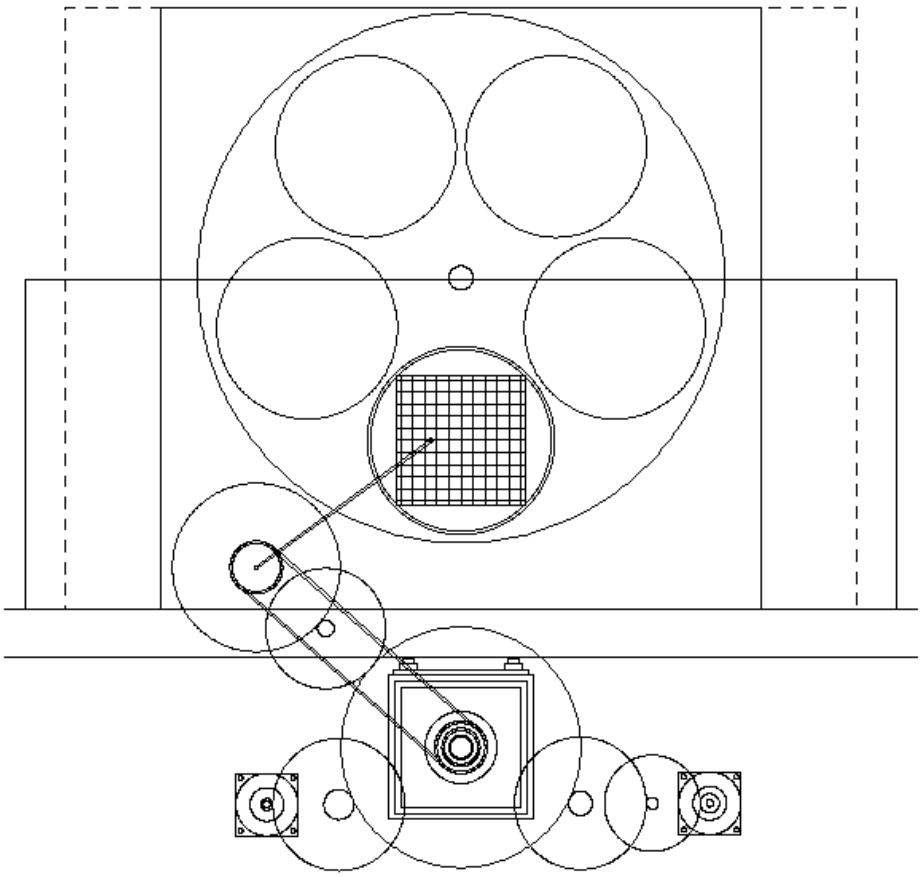

Figure 115: Configuration of the OIWFS pick-off probe showing the MCAO focal plane (*square grid*) and focal plane wheel at top and the pick-off probe mechanism at bottom. The pick-off probe consists of a thin Probe Arm extending over the MCAO focal plane and a thicker Main Arm mounted from the cold work surface plate. Cryogenic stepper motors at lower left and right drive the Probe Arm and the Main Arm, respectively. Duplicates of the NIRI/NIFS prism optics and OIWFS detector housing are mounted from the cold work surface plate below the Main Arm output.

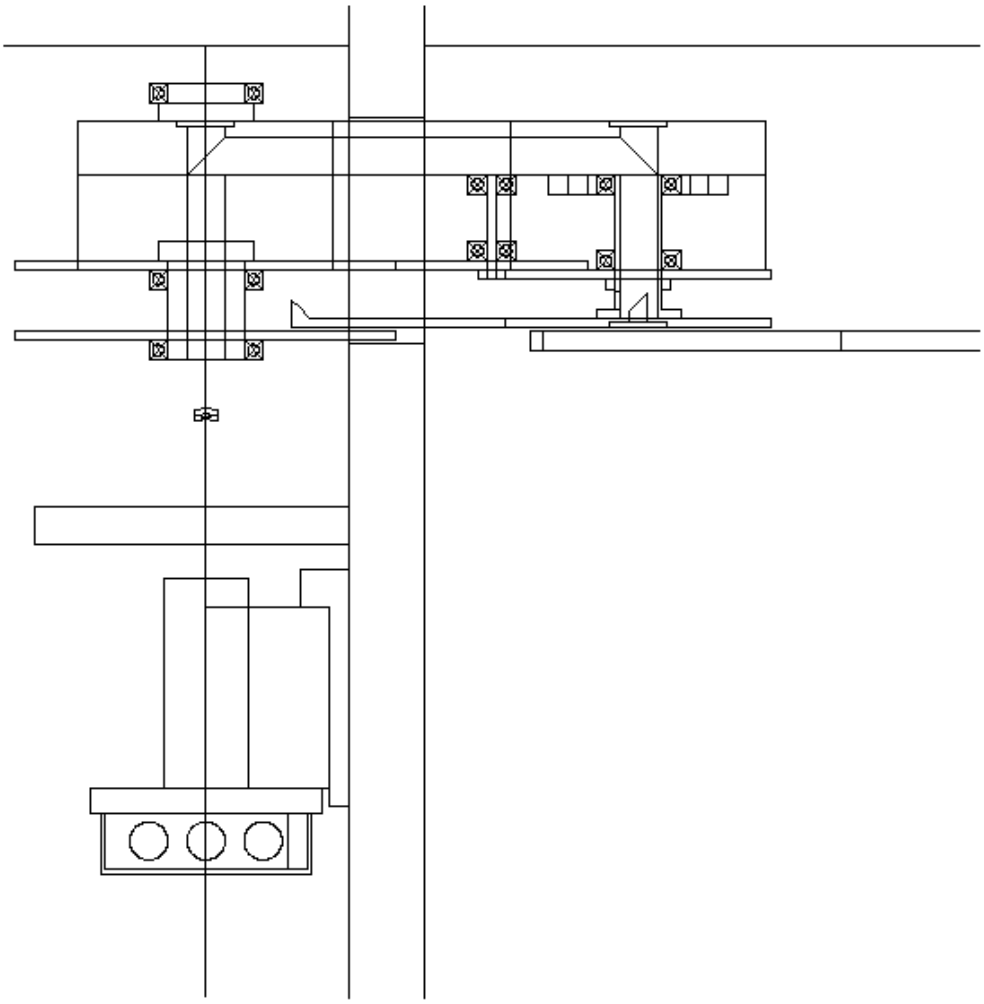

Figure 116: Side view of the OIWFS pick-off probe mechanism showing the Probe Arm rotated under the Main Arm. The NIRI/NIFS OIWFS filter wheel, prism optics, and detector housing are at lower left. The GSAOI imager focal plane wheel is seen at upper right and the vertical cold work surface plate is at center.

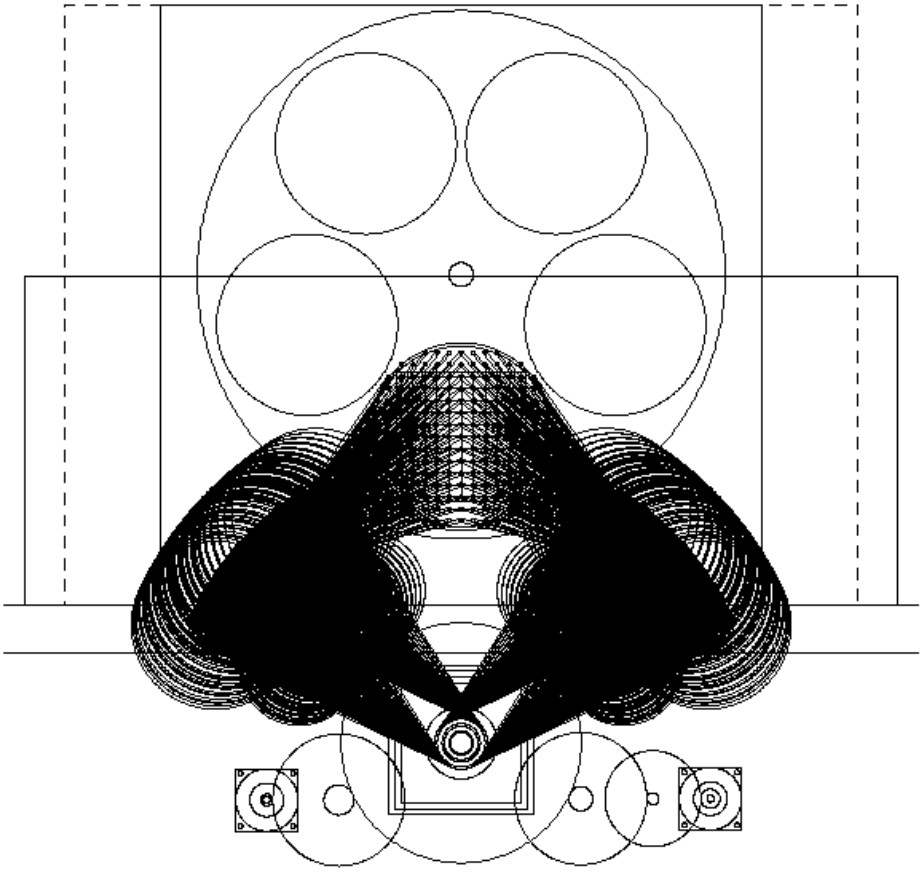

Figure 117: Guide probe orientations to completely patrol the MCAO focal plane.

The 4 mm diameter 45º mirror is diamond machined into the end of the Probe Arm. A 45º mirror at the axis of the Probe Arm reflects the 3.07″ field up the hollow Probe Arm axis. A 45º mirror mounted from the Main Arm at the Probe Arm axis then reflects the beam into the hollow Main Arm, irrespective of the Probe Arm orientation. A fourth 45º mirror on the Main Arm axis finally reflects the beam down the hollow Main Arm axis to the stationary OIWFS prism optics and detector.

A doublet lens in the Main Arm collimates the beam and reimages the MCAO exit pupil at the output of the Main Arm axis (Figure 118). Unlike NIRI/NIFS, the cryostat window would be powered so that it acts as a field lens to make the MCAO focal plane telecentric. The position of the pupil image is then independent of the location of the guide probe within the MCAO field.

A four-element camera lens focuses the probe field onto a field mask after it passes through a filter. The camera lens is a scaled version of the NIRI/NIFS lens used to image the gimbal mirror pupil onto the filter wheel. The re-optimization of this lens was trivial and its performance is excellent (Figure 119). The filter wheel would be an exact duplicate of the NIRI/NIFS OIWFS filter wheel.

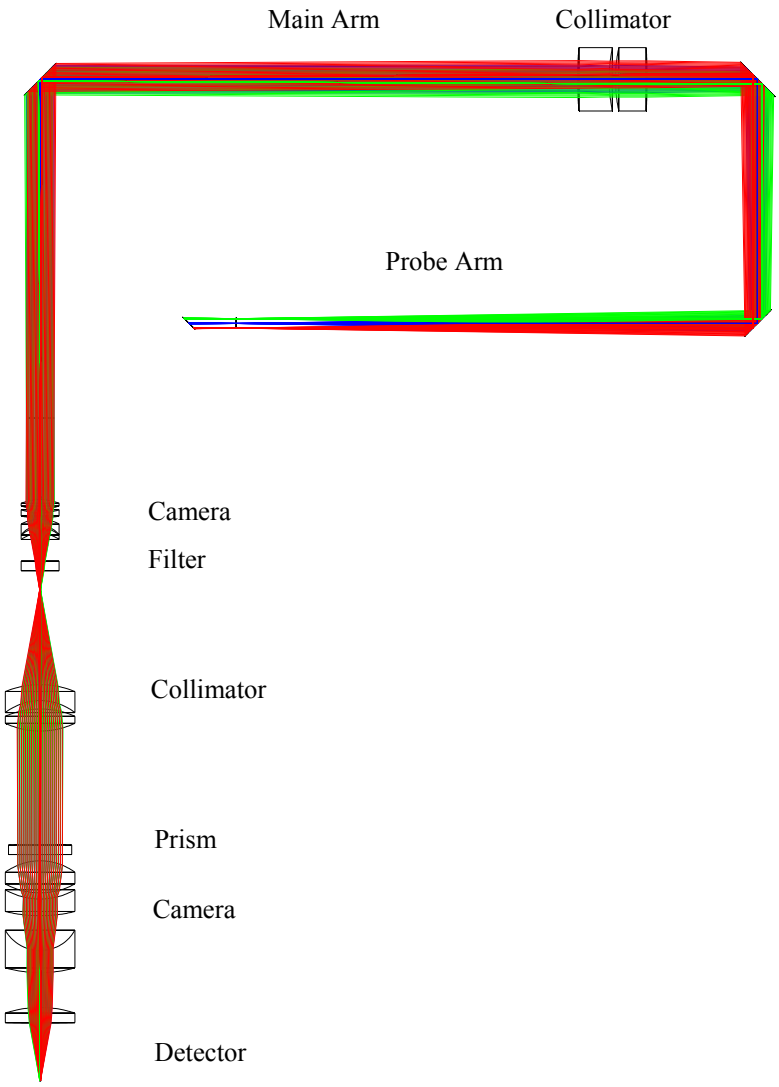

Figure 118: Ray trace of the OIWFS pick-off probe and prism optics. The pick-off mirror is positioned 15 mm above the focal plane. An achromatic doublet collimator reimages the telescope pupil at the output of the probe arm. A scaled version of the NIRI/NIFS OIWFS camera lens then reimages the focal plane at a field mask in a duplicate of the NIRI/NIFS OIWFS filter wheel. Tip-tilt and focus are sampled using duplicates of the NIRI/NIFS prism optics, four-facet prism, and OIWFS detector housing.

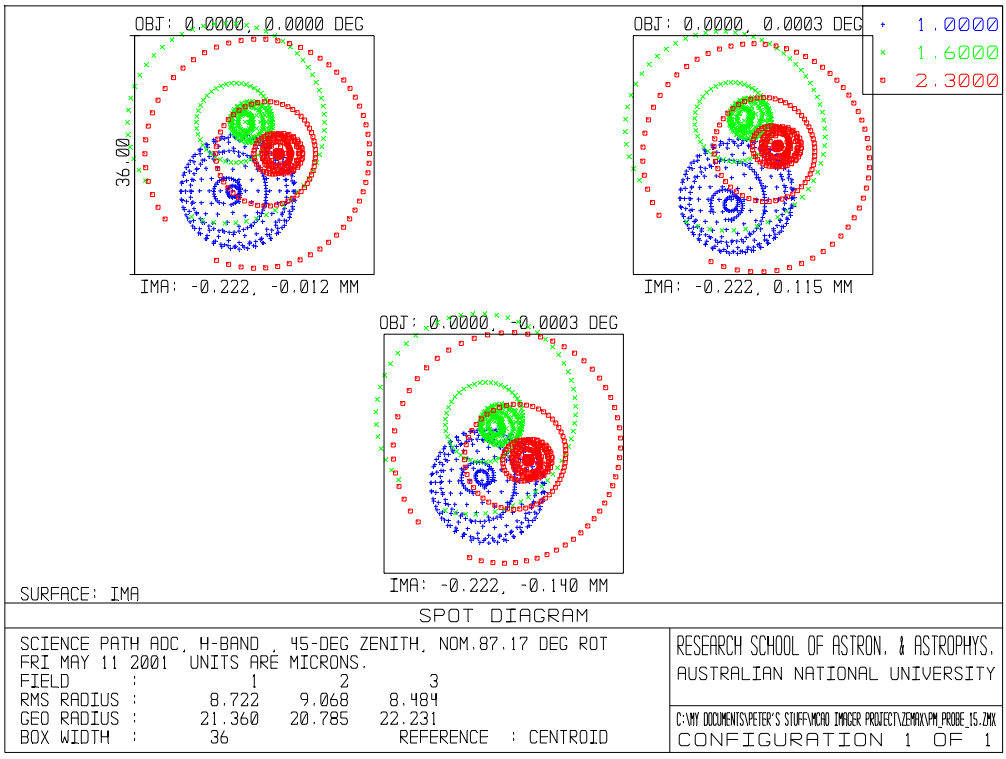

Figure 119: On-axis spot diagrams for OIWFS pick-off probe. The square boxes correspond to 2×2 detector pixels.

A duplicate of the NIRI/NIFS prism optics, OIWFS detector, and OIWFS detector housing would then be used to sense tip-tilt and focus data. The prism optics would be rigidly mounted from the cold work surface plate without focus adjustment using the modification implemented for NIFS. The prism optics are an exact copy of the NIRI/NIFS lenses. These could be readily manufactured by Janos who made the NIRI and NIFS optics.

8.6.2 Setting Accuracy

The pick-off probe drive system is designed to allow a setting resolution of 0.01″ (13.0 μm at the MCAO focal plane). The probe arms would be driven by three stage spur gears using the same Phytron cryogenic stepper motors used in NIRI and NIFS. A slipping clutch and friction brake would be implemented as in the NIFS grating turret drive and focal plane mask wheel and filter wheel drives. The gear ratios for the Probe Arm and Main Arm are listed in Table 61 and Table 62, respectively. The different total ratios for the two arms result from the different arm lengths. The motors operate at 200 rpm when cold so the Main Arm and Probe Arm could in principle be driven through a full revolution in 2.75 min and 2.2 min, respectively. In practice, neither arm is required to move through this large an angle. The drive motors for both arms would be stationary and mounted from the cold work surface plate. The Probe Arm drive is coupled through a second 200 mm diameter spur gear that is free to rotate about the Main Arm axis. This means that the guide probe would have to be repositioned in both axes whenever it is necessary to adjust the Main Arm orientation.

Table 61: Probe Arm Gear Ratios

Gear	Pinion Diameter (mm)	Wheel Diameter (mm)	Gear Ratio
Primary	14	140	10
Secondary	25	100	4
Tertiary	10	110	11
TOTAL	-	-	**440**

Table 62: Main Arm Gear Ratios

Gear	Pinion Diameter (mm)	Wheel Diameter (mm)	Gear Ratio
Primary	20	200	10
Secondary	10	110	11
Tertiary	16	80	5
TOTAL			**550**

Magnets would be mounted in the Probe Arm and Main Arm so that a datum can be obtained for each arm by sweeping it past a stationary Hall-effect sensor as is used in NIRI and NIFS. The control software for these mechanisms would require only small modifications to the existing NIRI/NIFS code.

8.6.3 Stability Requirement

Stability of the OIWFS pick-off probe is crucial. The 0.02″ pixels map to 26 μm at the MCAO focal plane, so 0.1 pixel image stability demands a pick-off probe stability of 2.6 μm. Translations and tilts of the pick-off probe mirror need to be considered. The 180 mm long Probe Arm will be driven by a 70 mm radius spur gear so that a motion of 2.6 μm at the probe mirror corresponds to a motion of only 1.0 μm at the drive gear. Similarly, the 227 mm long Main Arm will be driven by a 100 mm radius spur gear so that a motion of 2.6 μm at the Probe Arm axis corresponds to a motion of only 1.1 μm at the drive gear. These are challenging requirements that make this approach unattractive.

Tilts in the Main Arm and Probe Arm bearings induce opposite tilts in both arm mirrors with no image offset; these mirrors act as corner cubes. Bending of either arm induces differential tilts in the two arm mirrors that would cause image offset; these would need to be considered if this concept proceeded to a detailed design.

8.7 Thermal Strain Models

Thermal strain models have been constructed for the cooled structural and optical materials proposed for the baseline GSAOI by fitting polynomials to published data. For a temperature T (K), the thermal strain is

$$\varepsilon = k_0 + k_1 T + k_2 T^2 + \ldots$$

The number of terms used and the resolution of the coefficients are chosen to provide a fitting accuracy of five decimal places over the temperature range specified. The resulting coefficients are listed in Table 63. The data sources and applicable temperature ranges are listed in Table 64.

Numerical values of thermal strain are listed in §3.8.2 for the operating temperature of 70 K.

Table 63: Thermal Strain Polynomial Coefficients.

Material	Polynomial Coefficient						
	k_0	k_1	k_2	k_3	k_4	k_5	k_6
Grade 6061 Aluminum Alloy	-0.004197	-1.64e-07	-1.477e-09	9.6465e-10	-5.6149e-12	1.3533e-14	-1.2222e-17
Calcium Fluoride	-0.003082	8.95e-07	-5.4373e-08	1.1580e-09	-5.7739e-12	1.2987e-14	-1.1275e-17
Magnesium Oxide	-0.001386	-1.15e-06	8.93e-09	7.51e-11	-1.259e-13	-	-

Table 64: Thermal Strain Data Sources.

Material	Temperature Range (K)	Data Source
Grade 6061 Aluminum Alloy	6 - 350	Infrared & Electro-Optical Systems Handbook, Vol 3, Table 6.15
Calciun Fluoride	6.4 - 321.93	Journal of Chemical Physics, Vol 41, No 8, 2324
Magnesium Oxide	23.15 - 373.15	American Institute of Physics Handbook, Table 4f-3

8.8 Lens Mount Safety

All of the lenses used in GSAOI are radially located by mounting them in close fitting housing bores. In all cases the thermal contraction of the aluminum alloy housing is greater than that of the lens at operating temperature. The housing and lens tolerances are arranged so that the minimum clearance is zero under these conditions.

During the cooling process the lens temperature will lag the housing temperature, and it is therefore possible that a transient interference condition can develop. This phenomenon has the potential to fracture lenses, and so it is investigated here to ensure that the problem is avoided. If need be, the lens clearance can be increased at the cost of some increase in misalignment and consequent aberration.

The analysis used is conservative. With the cooling rate of the cryostat known, the temperature lag of the lenses is determined using the assumption that they are cooled by radiation alone. The clearances between lenses and housings is then determined from these temperatures using the thermal strain relationships presented in §8.7.

The cryostat used for GSAOI is a replica of that produced for NIRI. Data obtained from the NIRI web site has been used to model the cooling rate of the cryostat. If the time (sec) since the start of cooling is t, then the temperature (K) of the cryostat cold work surface plate (and lens housings) is

$$T_1 = 293 - 6.5237\times10^{-4}t + 2.7429\times10^{-10}t^2 + 2.8993\times10^{-16}t^3$$

This relationship is plotted in Figure 120.

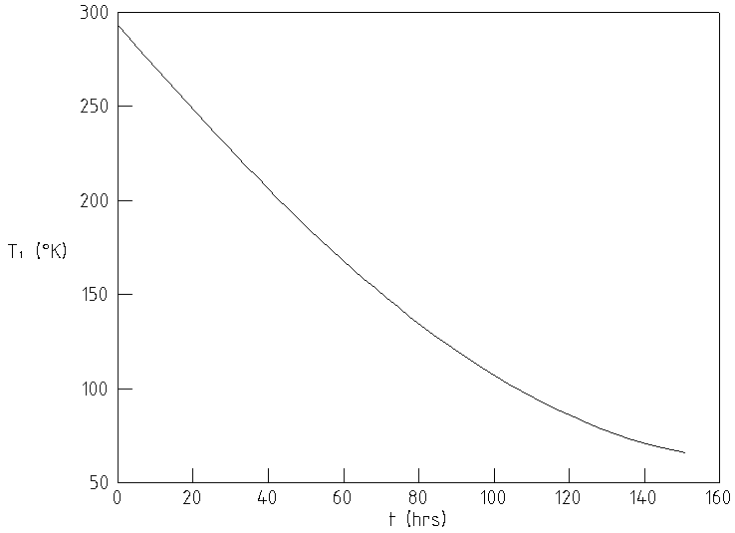

Figure 120: Cryostat cooling curve.

The corresponding cryostat cooling rate is

$$\frac{dT_1}{dt} = -6.5237\times10^{-4} + 5.4858\times10^{-10}t + 8.6979\times10^{-16}t^2$$

The lag in the lens temperature is dependent on the spatial character of the cavity containing it. If this volume is large compared to the lens, it behaves as a black body and the rate of heat transfer is independent of its emissivity (but not that of the lens). If the cavity is closely conforming to the lens, then both emissivities are involved, but if they are equal (as they will tend to be), the rate of heat transfer will be twice that applicable for a large cavity. The cavity is here assumed to be large because this is both roughly realistic and conservative.

The emissivity of the lenses is assumed to be unity because they transmit only over relatively narrow wavelength pass bands. Over the wide range of thermal wavelengths they will be largely absorptive.

Where lenses are mounted as pairs, cooling will be slowed because they shelter each other and the adjacent surfaces are effectively disabled as radiators.

The temperature lag is also dependent on the specific heat capacity of the lens materials. In general it is known that this decreases considerably as temperature is reduces, but the ambient-temperature values are used here because low-temperature data are not readily available. This assumption also makes the analysis conservative.

If the lens mass is m_2, the lens specific heat capacity is C_2, the lens radiating surface area is A_2, the lens emissivity is ξ_2, and the Stefan-Boltzmann constant is σ (5.67051×10^{-14} W mm^{-2} K^{-4}), then the lens temperature is

$$T_2 = \left(T_1^4 - \frac{C_2 m_2}{\sigma A_2 \xi_2}\frac{dT_1}{dt} \right)^{\frac{1}{4}}$$

More correctly, the term dT_1/dt in this relationship should be dT_2/dt, but this simplifying assumption is justified because the difference is small.

The results of this analysis are presented for the worst lagging lenses of the two materials used. The lens properties are shown in Table 65.

Table 65: Properties of the Worst Lagging Lenses

Identification	Material	C_2 (J kg^{-1}K^{-1})	m_2 (kg)	A_2 (mm^2)	ξ_2
Imager Collimator Lens 2	Calcium Fluoride	854	0.10	3400	1
Imager Collimator Lens 3	Magnesium Oxide	879	0.11	3200	1

The calculated temperature lag is plotted in Figure 121.

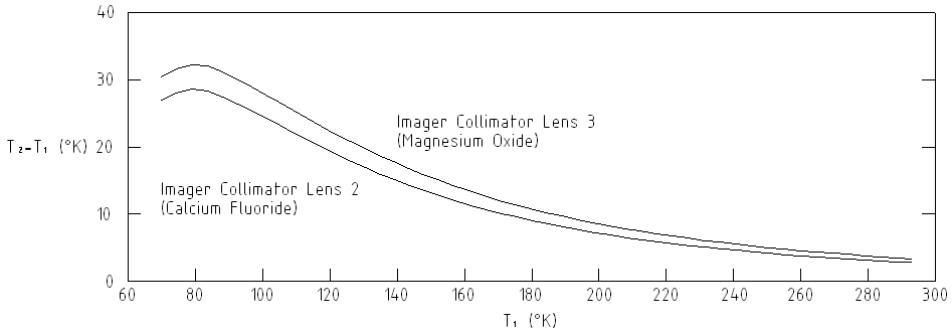

Figure 121: Lens temperature lag during cryostat cooling.

The resulting ratio of lens diametral clearance to lens diameter is shown in Figure 122.

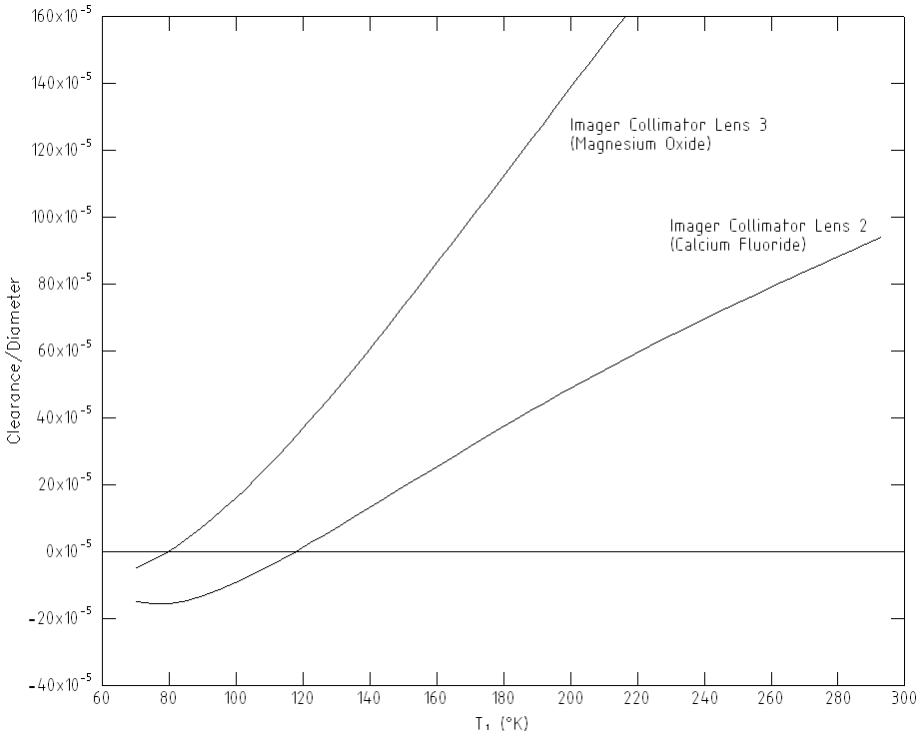

Figure 122: Lens clearance to diameter ratio during cryostat cooling.

Slight interference develops at low temperature for both lenses, and so a compensating increase in clearance is required. The diameter of both lenses is 64 mm. The required clearance increase is 10 μm for the calcium fluoride lens, and 3 μm for the magnesium oxide lens. These are small relative to the 50 μm width of the tolerance zone, and so have no significant effect on optical performance.

8.9 Optical Prescription

The baseline optics for both the imager and OIWFS are presented in Table 66 and Table 67, respectively. They have been designed for ambient conditions, and neither has been cryogenically compensated for refractive index changes or thermal strain (§8.7).

The same global coordinate system has been used for both tables. The origin is the point where the optical axis intersects the ISS interface plane. The optical axis is coincident with the Z-axis until it is deviated by the first applicable mirror. The location of each surface is specified by the X-Y-Z coordinates of its vertex. The orientation of each surface is specified by the Alt-Az coordinates. The Az-axis is parallel to the X-axis, and when Alt and Az are both zero, the surface is perpendicular to the Z-axis at its vertex. Surface radii are positive if the surface is convex when viewed in the +Z direction with Alt and Az both zero.

8.9.1 Imager

The optical prescription of the imager is listed in Table 66. The pupil viewer, focus retractor, and focus extender are included, although they are only deployed in special circumstances, and then only one at a time.

Table 66: Optical Prescription of Imager (including pupil viewer, focus retractor, and focus extender).

Surface Identification	Leading Media	Surface Radius (mm)	X (mm)	Y (mm)	Z (mm)	Az (deg)	Alt (deg)	Size (mm)
MCAO Focal Plane	-	∞	0	0	300	0	0	Ø153
ISS Interface Plane	-	∞	0	0	0	0	0	-
Window A	Air	4761.9	0	0	-47.5	0	0	Ø200
Window B	Calcium Fluoride	∞	0	0	-31.5	0	0	Ø200
Field Mask	Vacuum	∞	0	0	293.95	0	0	108 x 108
Field Lens A	Vacuum	281.44	0	0	426	0	0	Ø164
Field Lens B	Calcium Fluoride	∞	0	0	448	0	0	Ø164
Fold Mirror 1	Vacuum	∞	0	0	761.514	0	-45	Ø110
Collimator Lens 1A	Vacuum	-141.545	62.087	0	761.514	0	90	Ø80
Collimator Lens 1B	Calcium Fluoride	-309.747	71.087	0	761.514	0	90	Ø80
Fold Mirror 2	Vacuum	∞	245	0	761.514	-40	45	Ø86
Collimator Lens 2A	Vacuum	192.251	245	-37.219	717.158	-40	0	Ø66
Collimator Lens 2B	Calcium Fluoride	-115.722	245	-45.576	707.199	-40	0	Ø66
Collimator Lens 3A	Vacuum	-124.467	245	-46.861	705.667	-40	0	Ø58
Collimator Lens 3B	Magnesium Oxide	-428.470	245	-52.003	699.539	-40	0	Ø64
Cold Stop	Vacuum	∞	245	-135.566	599.953	-40	0	~ Ø28
Camera Lens 1A	Vacuum	68.599	245	-199.845	523.349	-40	0	Ø55
Camera Lens 1B	Magnesium Oxide	49.152	245	-204.987	517.220	-40	0	Ø46
Camera Lens 2A	Vacuum	50.335	245	-206.272	515.688	-40	0	Ø54
Camera Lens 2B	Calcium Fluoride	1596.9	245	-213.986	506.496	-40	0	Ø54
Fold Mirror 3	Vacuum	∞	245	-236.483	479.684	-40	-45	Ø64
Pupil Viewer Lens 1A	Vacuum	98.456	212	-236.483	479.684	0	-90	Ø50
Pupil Viewer Lens 1B	Calcium Fluoride	-111.520	203	-236.483	479.684	0	-90	Ø50
Pupil Viewer Lens 2A	Vacuum	40.645	202	-236.483	479.684	0	-90	Ø45
Pupil Viewer Lens 2B	Calcium Fluoride	∞	191	-236.483	479.684	0	-90	Ø45
Pupil Viewer Lens 3A	Vacuum	237.950	189.5	-236.483	479.684	0	-90	Ø40
Pupil Viewer Lens 3B	Fused Silica	-63.627	186.5	-236.483	479.684	0	-90	Ø40
Focus Retractor Lens 1A	Vacuum	86.5	213.855	-236.483	479.684	0	-90	Ø50
Focus Retractor Lens 1B	Calcium Fluoride	69.9	203.855	-236.483	479.684	0	-90	Ø50
Focus Retractor Lens 2A	Vacuum	109.4	198.855	-236.483	479.684	0	-90	Ø50
Focus Retractor Lens 2B	Fused Silica	147.4	188.855	-236.483	479.684	0	-90	Ø50
Focus Extender Lens 1A	Vacuum	516.7	213.855	-236.483	479.684	0	-90	Ø50
Focus Extender Lens 1B	Calcium Fluoride	307.1	203.855	-236.483	479.684	0	-90	Ø50
Focus Extender Lens 2A	Vacuum	307.1	198.855	-236.483	479.684	0	-90	Ø50
Focus Extender Lens 2B	Fused Silica	377.1	188.855	-236.483	479.684	0	-90	Ø50
Camera Lens 3A	Vacuum	-64.535	163.855	-236.483	479.684	0	-90	Ø46
Camera Lens 3B	Calcium Fluoride	1612.7	153.855	-236.483	479.684	0	-90	Ø54
Detector	Vacuum	∞	-74.574	-236.483	479.864	0	-90	76 x 76

8.9.2 OIWFS

The optical prescription of the OIWFS is listed in Table 67.

Table 67: Optical Prescription of the OIWFS

Surface Identification		Leading Media	Surface Radius (mm)	X (mm)	Y (mm)	Z (mm)	Az (deg)	Alt (deg)	Size (mm)
MCAO Focal Plane		-	∞	0	0	300	0	0	Ø153
ISS Plane		-	∞	0	0	0	0	0	-
Window A		Air	4761.9	0	0	-47.5	0	0	Ø200
Window B		Calcium Fluoride	∞	0	0	-31.5	0	0	Ø200
Beam Splitter		Vacuum	∞	0	0	202.646	0	45	76 x 108
Beam Steering System	Field Mask	Vacuum	∞	-91.304	0	202.646	0	-90	Ø153
	Field Lens A	Vacuum	368.947	-188.354	0	202.646	0	-90	Ø164
	Field Lens B	Calcium Fluoride	∞	-210.354	0	202.646	0	-90	Ø164
	Fold Mirror 1	Vacuum	∞	-484.354	0	202.646	0	45	Ø122
	Collimator Lens 1A	Vacuum	60.293	-484.354	0	502.035	0	0	Ø68
	Collimator Lens 1B	Calcium Fluoride	49.564	-484.354	0	517.035	0	0	Ø62
	Collimator Lens 2A	Vacuum	-150.260	-484.354	0	642.272	0	0	Ø56
	Collimator Lens 2B	Calcium Fluoride	-56.269	-484.354	0	655.272	0	0	Ø56
	Collimator Lens 3A	Vacuum	-56.608	-484.354	0	660.272	0	0	Ø56
	Collimator Lens 3B	Magnesium Oxide	-77.715	-484.354	0	668.272	0	0	Ø56
	Tip Tilt Mirror	Vacuum	∞	-484.354	0	768.272	~ 0	~ 0	Ø26
	Collimator Lens 3B	Vacuum	-77.715	-484.354	0	668.272	0	0	Ø56
	Collimator Lens 3A	Magnesium Oxide	-56.608	-484.354	0	660.272	0	0	Ø56
	Collimator Lens 2B	Vacuum	-56.269	-484.354	0	655.272	0	0	Ø56
	Collimator Lens 2A	Calcium Fluoride	-150.260	-484.354	0	642.272	0	0	Ø56
	Collimator Lens 1B	Vacuum	49.564	-484.354	0	517.035	0	0	Ø62
	Collimator Lens 1A	Calcium Fluoride	60.293	-484.354	0	502.035	0	0	Ø68
	Fold Mirror 1	Vacuum	∞	-484.354	0	202.646	0	0	Ø122
	Fold Mirror 2	Vacuum	∞	-256.747	0	202.646	0	0	20 x 20
Error Sensing System	Field Mask	Vacuum	∞	-256.747	0	373.770	0	0	≤ Ø20
	Field Lens A	Vacuum	158.955	-256.747	0	523.770	0	0	Ø50
	Field Lens B	Calcium Fluoride	∞	-256.747	0	530.770	0	0	Ø50
	Filter A	Vacuum	∞	-256.747	0	570.770	0	0	Ø25
	Filter B	Fused Silica	∞	-256.747	0	573.770	0	0	Ø25
	Fold Mirror 3	Vacuum	∞	-256.747	0	847.693	22.5	0	Ø20
	Collimator Lens 1A	Vacuum	45.854	-256.747	142.474	705.219	45	0	Ø16
	Collimator Lens 1B	Magnesium Oxide	63.121	-256.747	146.009	701.684	45	0	Ø22
	Collimator Lens 2A	Vacuum	124.697	-256.747	147.423	700.269	45	0	Ø22
	Collimator Lens 2B	Calcium Fluoride	53.860	-256.747	150.959	696.734	45	0	Ø22
	Shack-Hartmann Prism A	Vacuum	∞	-256.747	175.708	671.985	~ 45	~ 0	Ø28
	Shack-Hartmann Prism B	Fused Silica	∞	-256.747	177.829	669.864	45	0	Ø28
	Camera Lens 1A	Vacuum	-1836	-256.747	179.243	668.450	45	0	Ø20
	Camera Lens 1B	Calcium Fluoride	22.777	-256.747	184.193	663.500	45	0	Ø20
	Camera Lens 2A	Vacuum	22.419	-256.747	184.759	662.934	45	0	Ø20
	Camera Lens 2B	Magnesium Oxide	50.942	-256.747	186.880	660.813	45	0	Ø20
	Camera Lens 3A	Vacuum	319.150	-256.747	199.680	648.013	45	0	Ø32
	Camera Lens 3B	Calcium Fluoride	42.199	-256.747	205.337	642.356	45	0	Ø32
	Camera Lens 4A	Vacuum	29.184	-256.747	251.087	596.605	45	0	Ø22
	Camera Lens 4B	Magnesium Oxide	113.914	-256.747	253.916	593.777	45	0	Ø30
Detector		Vacuum	∞	-256.747	262.401	585.292	45	0	18 x 18

9 Appendix B: Detector Systems Design Detail

9.1 Mechanical Dimensions of the H2RG Package

Mechanical dimensions of the H2RG detector package are shown in Figure 123.

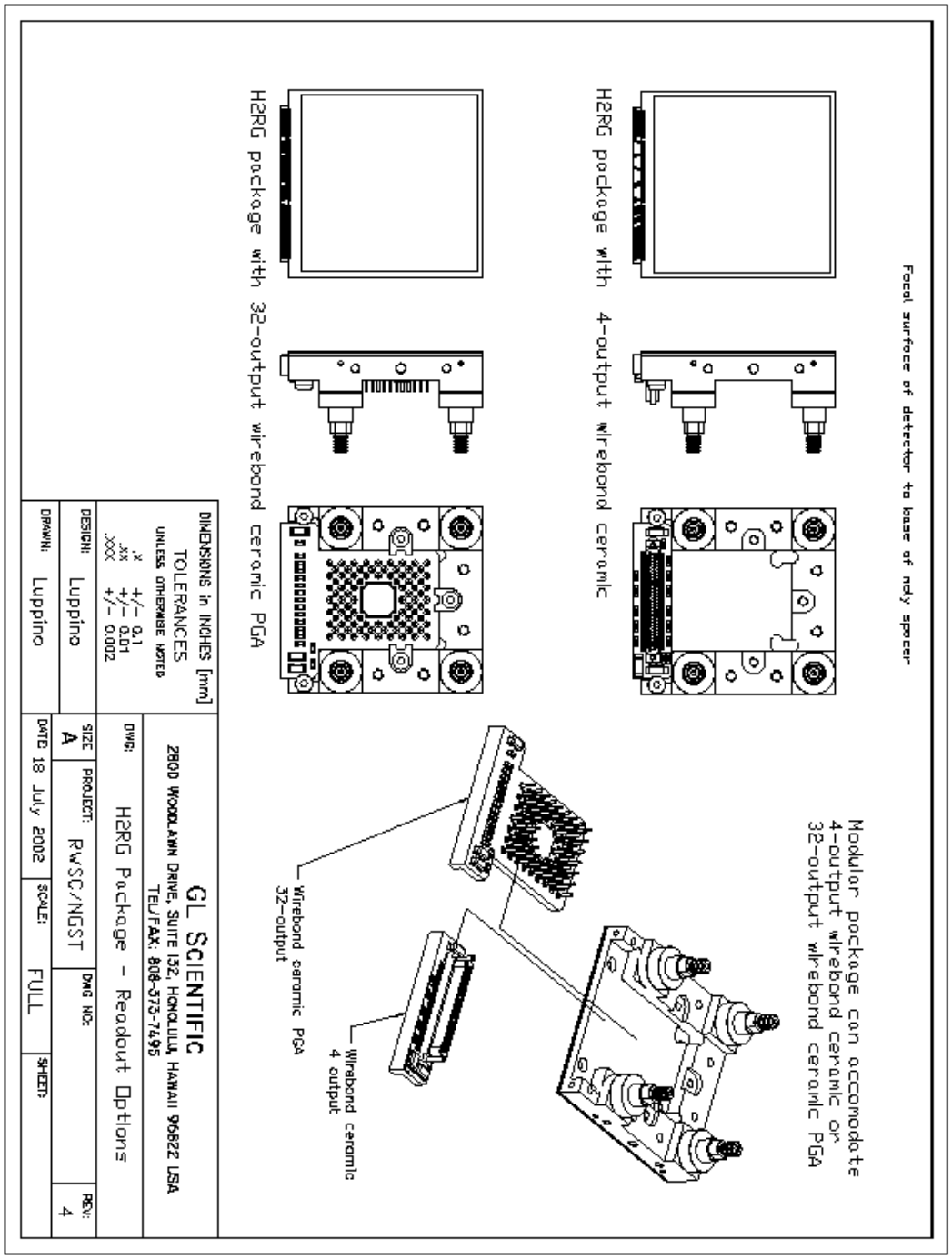

Figure 123: Mechanical dimensions of the H2RG package.

9.2 Mechanical Dimensions of the ASIC Package

Mechanical dimensions of the ASIC package are shown in Figure 124.

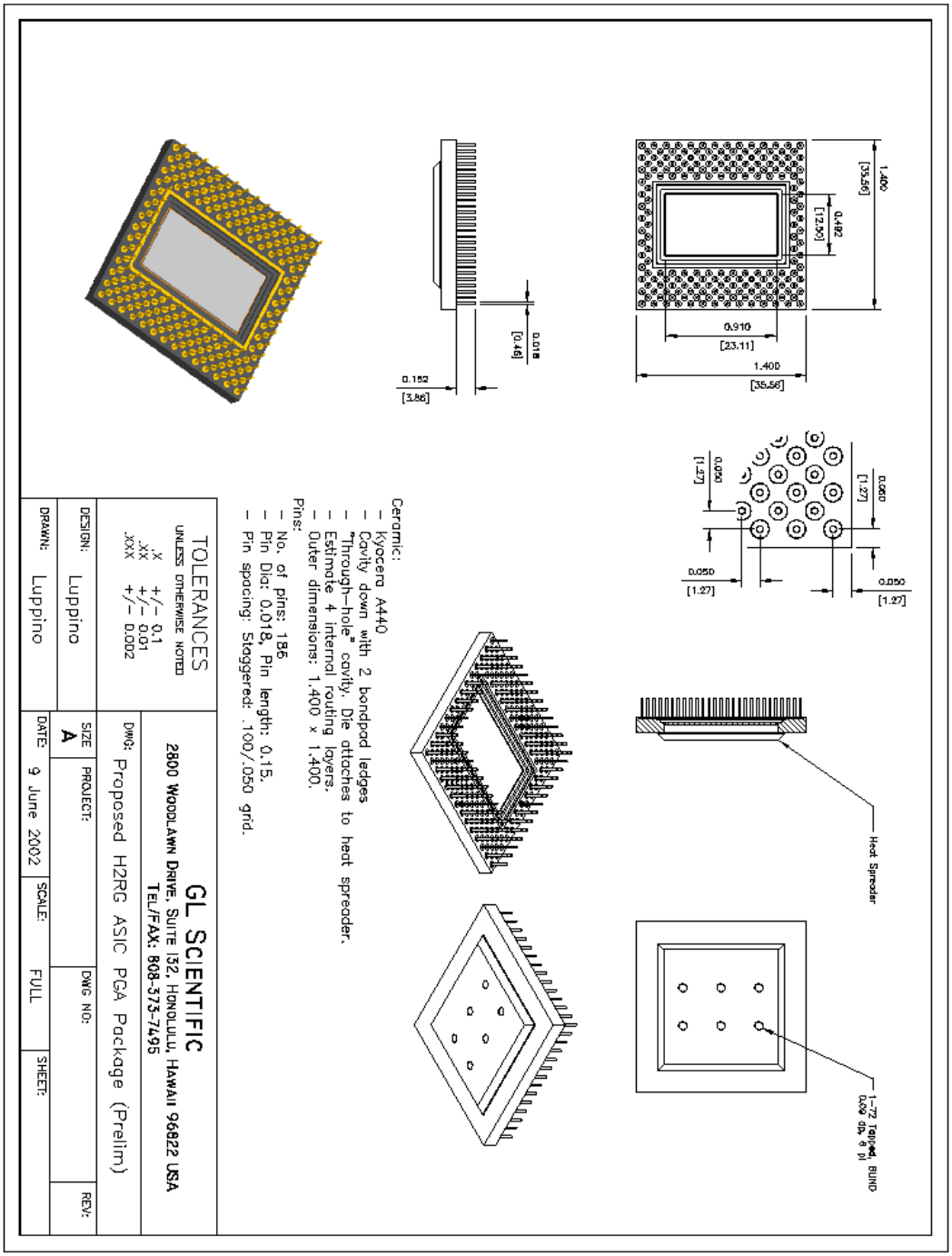

Figure 124: Mechanical dimensions of the ASIC package.

9.3 Definition of H2RG Signals

Table 68 defines the H2RG signals and the number of clocks and biases required for the 100 kHz slow readout mode and the 5 MHz fast readout mode.

Table 68: Definitions of H2RG Signals

Signal Name	Description	Type	Level	Pad Count	Number of Clocks Required for Slow 100 kHz Readout	Number of Biases Required for Slow 100 kHz Readout	Additional Clocks Required for Fast 5 MHz Readout	Additional Biases Required for Fast 5 MHz Readout
GND	Digital low	Power	0.0 V	1				
GNDA	Analog low	Power	0.0 V	1				
VDD	Digital high	Power	3.3 V	1		1		
VDDA	Analog high	Power	3.3 V	1		1		
SUB	Multiplexer substrate	Power	0.0 V	1		1		
DSUB	Detector substrate	Bias	0.0 V	1		1		
VRESET	Detector reset voltage	Bias	0.5-1.0 V	1		1		
CELLDRAIN	Drain of pixel source follower	Power	0.0 V	1		1		
DRAIN	Drain of output source follower	Power	0.0 V	1		1		
BIASPWR	Current source for pixel source follower.	Bias	3.3 V	1		1		
BIASGATE	Gate of current source for pixel source follower.	Bias	2.4 V	1		1		
RefColbuf, Refsample	Reference voltages for column	Ref	0.5-2.0 V	2				2
Vnbias	Bias for 5 MHz column buffer	Bias	0.85 V	1				1
Vncase	Bias for 5 MHz column buffer	Bias	1.2 V	1				1
Vpbias	Bias for 5 MHz column buffer	Bias	2.35 V	1				1
Vpcase	Bias for 5 MHz column buffer	Bias	2 V	1				1
Vbiasoutbuf	Bias for 5 MHz output buffers	bias	0.85 V	1				1
OutputA, OutputB	Outputs	analog	0-3.3 V	64				
RefoutA/B	Reference	analog	0-3.3 V	2				
WindowOutA/B	Window mode output (guide)	analog	0-3.3 V	2				
FSYNCB	Frame sync / Data in (serial interface)	digital	0/3.3 V	1	1			
VCLK	Slow shift register clock/Data clk(serial reg)	digital	0/3.3 V	1	1			
VRESETB	Reset slow shift register	digital	0/3.3 V	1				
LSYNCB	Line syn (start fast shift register)	digital	0/3.3 V	1	1			
HCLK	Fast shift register clock	digital	0/3.3 V	1	1			
HRESETB	Reset fast shift register	digital	0/3.3 V	1				
READEN	Enable row selection for read	digital	0/3.3 V	1	1			
RESETEN	Enable row selection for reset	digital	0/3.3 V	1	1			
VERTWMWM, HORWMEM	Enable vertical/horizontal window mode	digital	0/3.3 V	2	1			
VREADEDGE	Select which edge of FSYNCB is used for read	digital	0/3.3 V	1	1			
HREADEDGE	Select which edge of LSYNCB is used for read	digital	0/3.3 V	1	1			
SAMPLCLK	Column buffer sample clock for 5 MHz operation	digital	0/3.3 V	1			1	
CSB	Chip select (serial register)	digital	0/3.3 V	1				

Signal Name	Description	Type	Level	Pad Count	Number of Clocks Required for Slow 100 kHz Readout	Number of Biases Required for Slow 100 kHz Readout	Additional Clocks Required for Fast 5 MHz Readout	Additional Biases Required for Fast 5 MHz Readout
DATACLK	Data clock (serial register)	digital	0/3.3 V	1				
DATAIN	Data input (serial register)	digital	0/3.3 V	1				
DATAOUT	Data output (serial register)	digital	0/3.3 V	1				
MAINRESETB	Reset serial interface and on-chip registers	digital	0/3.3 V	1	1			
MODECTRL1, MODECTRL2	Select output mode	digital	0/3.3 V	2				
BUFFERDISABLE	Disable on-chip buffers	digital	0/3.3 V	1				
FASTENPAD	Enable fast mode (5 MHz)	digital	0/3.3 V	1			1	
Tenperature	Temperature sensors	analog	0-3.3 V	4				
Test	Test pads	digital	0/3.3 V	12				
Total				**124**	**10**	**9**	**2**	**7**

9.4 On-Detector Guide Window Implementation

The H2RG has a guide window mode capability where a sub-image is readout through a single output at the same time as a long integration time science exposure on the full array. Bit WMOOUTEN of the OutputModeReg register sets whether this output is one of the normal imager outputs, Output#7 (WMOOUTEN=0), or the dedicated guide window output, WindowOut (WMOOUTEN=1).

Table 69 shows CDS read times, processing times to perform CDS, transfer time to the A&G IOC, total cycle time, and duty cycle at different frame rates and frame sizes of the ODGW for a ODGW readout speed of 100 kHz. Duty cycle is defined as the percentage of the effective exposure time of the ODGW compared to the total cycle time to read, process, and transfer the data to the A&G IOC. Table 70 shows the same information for a 200 kHz readout speed.

At an ODGW frame rate of 100 Hz with 100 kHz readout speed, the duty cycle is 92% for an 8×8 subframe and 83% for a 12×12 subframe. At an ODGW frame rate of 100 Hz with 200 kHz readout speed, the duty cycle increases to 96% for an 8×8 subframe and 92% for a 12×12 subframe. However, read noise is expected to scale as the square root of the bandwidth so it increases by ~ 40% in going to 200 kHz. Consequently, the maximum S/N is achieved by reading out the ODGW at 100 kHz with slightly lower duty cycle but much lower read noise than at the faster speed of 200 kHz.

At an ODGW frame rate of 200 Hz and a readout speed of 100 kHz, the duty cycle is still at an acceptable 84% for an 8×8 subframe and 66% for a 12×12 subframe. However, at an ODGW frame rate of 300 Hz and a readout speed of 100 kHz, only an 8x8 subframe can be read out with an acceptable duty cycle of 76%. At the faster speed of 200 kHz, both 8×8 and 12×12 subframes can be read out with duty cycles of 88% and 75%, respectively.

Table 69: Read, Processing, and Transfer Times, and Duty Cycle at Different Frame Sample Rates and Frame Sizes of the ODGW for Readout Speed of 100 kHz.

ODGW Frame Size	Num. of H2RGs	Total Pixels	CDS Read Time at 100 kHz (ms)	Processing time at 10 instructions per pixel at 40ns per instruction (ms)	Transfer Time up 12.5 Mpixel/s Link (ms)	Total Cycle Time (ms)	Duty cycle At 300 Hz Frame Rate (%)	Duty cycle At 200 Hz Frame Rate (%)	Duty cycle At 100 Hz Frame Rate (%)	Duty cycle At 50 Hz Frame Rate (%)
8×8	1	64	1.6	0.03	0.008	1.6	76%	84%	92%	96%
8×8	4	256	1.6	0.10	0.032	1.7	76%	84%	92%	96%
12×12	1	144	3.4	0.06	0.018	3.4	N/A	66%	83%	92%
12×12	4	576	3.4	0.23	0.072	3.7	N/A	66%	83%	92%
16×16	1	256	5.8	0.10	0.032	5.9	N/A	N/A	71%	86%
16×16	4	1024	5.8	0.41	0.128	6.3	N/A	N/A	71%	86%
32×32	1	1024	21.8	0.41	0.128	22.3	N/A	N/A	N/A	N/A
32×32	4	4096	21.8	1.64	0.512	23.9	N/A	N/A	N/A	N/A

Table 70: Read, Processing, and Transfer Times, and Duty Cycle at Different Frame Sample Rates and Frame Sizes of the ODGW for Readout Speed of 200 kHz.

ODGW Frame Size	Num. of H2RGs	Total Pixels	CDS Read Time at 200 kHz (ms)	Processing time at 10 instructions per pixel at 40ns per instruction (ms)	Transfer Time up 12.5 Mpixel/s Link (ms)	Total Cycle Time (ms)	Duty cycle At 500 Hz Frame Rate (%)	Duty cycle At 300 Hz Frame Rate (%)	Duty cycle At 200 Hz Frame Rate (%)	Duty cycle At 100 Hz Frame Rate (%)
8×8	1	64	0.8	0.03	0.008	0.8	80%	88%	92%	96%
8×8	4	256	0.8	0.10	0.032	0.9	80%	88%	92%	96%
12×12	1	144	1.7	0.06	0.018	1.8	N/A	75%	83%	92%
12×12	4	576	1.7	0.23	0.072	2.0	N/A	75%	83%	92%
16×16	1	256	2.9	0.10	0.032	3.0	N/A	N/A	71%	86%
16×16	4	1024	2.9	0.41	0.128	3.4	N/A	N/A	71%	86%
32×32	1	1024	10.9	0.41	0.128	11.4	N/A	N/A	N/A	N/A
32×32	4	4096	10.9	1.64	0.512	13.0	N/A	N/A	N/A	N/A

9.5 SDSU Controller Options Explored

9.5.1 Communication Interface Boards

Two interface board combinations were investigated for the SDSU-2 controller design. The 2.5 Mpixel/s VME interface/timing board that was used for NIFS and the new 12.5 Mpixel/s PMC interface board/timing board that will be used for the MCAO detector system. The PMC interface board plugs into one of the PMC slots of the IOC VME processor board. Table 71 compares pixel period time and read times for the two board combinations using slow 100 kHz readout mode. The highlighted rows are combinations of interface speed, number of outputs utilized, and readout speeds that achieve a CDS read time < 10 s. Clearly the 2.5 Mpixel/s VME interface/timing board combination is inadequate. Consequently, the baseline design uses the 12.5 Mpixel/s PMC interface board/timing board combination.

Table 71: Comparison of Readout Speed, Pixel Period Time, and Read Times for VME and PMC Interface Boards for Different Number of Outputs per Detector using 100 kHz Slow Readout Mode.

Readout Speed (kHz)	Number of Outputs per Detector	Pixel Period Time (μs)	CDS Read Time (s)	Required Interface Speed (Mpixel/s)
100	1	10.0	84.0	0.4
200	1	5.0	42.0	0.8
300	1	3.3	28.0	1.2
100	4	10.0	21.0	1.6
200	**4**	**5.0**	**10.5**	**3.2**
300	**4**	**3.3**	**7.0**	**4.8**
100	**32**	**10.0**	**2.6**	**12.8**
200	**32**	**5.0**	**1.3**	**25.6**
300	**32**	**3.3**	**0.9**	**38.4**

9.5.2 IR Video Processor Boards

There are three different IR video boards available for use with the SDSU-2 controller. The three boards are the Dual Channel IR Video Board (Dual Channel board), the Quad Channel Coadder IR Video Board (Quad Channel board), and the Octal Channel IR Video Board (Octal Channel board). The Dual Channel board and Quad Channel boards have essentially identical analog video processing chains. They have a differential front end followed by video offset subtract and gain stages. The maximum data rate for these two boards is 1 MHz. The Octal Channel board has a similar differential front end followed by video offset subtract and gain stages. However, after the front end, the Octal Channel board has a resettable two time constants (standard 1 μs and 4 μs) integrator to provide programmable bandwidth followed by a programmable gain 500 kHz maximum data rate ADC. The programmable gain is implemented by changing the ADC upper reference voltage. This voltage is set by a 12-bit DAC in the same way as the biases are set. The Quad Channel board also has image-processing capability using a Motorola DSP56002 DSP and 1 Mword of SRAM. Further differences are that the Dual Channel board has 6 programmable biases and the Octal Channel board has 7 programmable biases A comparison of the features of the three boards is presented in Table 72.

The baseline design is implemented using two Octal Channel IR Video Boards for the following reasons. First, no data processing will be done in the controller so the data processing of the Quad Channel board is not required and will add unnecessary complexity. Second, the Octal Channel board is the cheapest solutions. Third, the seven biases on each of the Octal Channel boards will have lower noise than biases generated by a clock board (Bob Leach, priv. comm.) and thus can be used for the more sensitive detector biases such as DSUB, VRESET, and CELLDRAIN. Fourth, the programmable bandwidth and gain control of the video channel of the Octal Channel board will allow the optimization of several different readout speeds.

Table 72: Comparison of Features of the Three SDSU-2 IR Video Processor Boards

Features	Dual Channel IR Video Board	Quad Channel Coadder IR Video Board	Octal Channel IR Video Board
Number of channel	2	4	8
Analog input	Differential front end	Differential front end	Differential front end
Programmable Bandwidth	No	No	Resettable integrator with two programmable time constants (1 μs and 4 μs)
ADC data rate (max.)	1 MHz	1 MHz	500 kHz
Number and type of biases	6	0	7
Image-processing capability	None	Motorola DSP56002 DSP and 1 Mword of SRAM	None
Costs per board	$5,000	$10,000	$6,000
Cost per channel	$2,500	$2,500	$750

9.5.3 Bias Generators

For each H2RG, Table 68 shows that 9 biases are required for 100 kHz slow readout mode and an additional 7 biases are required for 5 MHz fast readout mode. For the mosaic, a total of 36 biases are required for the baseline 100 kHz slow readout mode. A total of 64 will be required if the design is upgraded to the 5 MHz fast readout mode. In the baseline design, the two Octal Channel video boards (§9.5.2) will provide fourteen biases. Therefore, an additional 22 bias generators will be needed.

Two options were explored; a custom-built RSAA Bias Board or a SDSU clock board. The custom-built RSAA Bias Board will provide 24 ultra low noise and high stability biases. The SDSU clock board will provide 24 biases. The stability of the biases generated by SDSU clock board has been a concern during the NIFS design (NIFS CDR §6.7) and detector testing and is a concern to the IfA (priv. communications Ev Irwin and Don Hall) during their testing of the HAWAII-1R. The noise reduction filter time constants of the SDSU clock board are too short and will need to be increased to 20 row readout times (20 rows × 512 pixel/row × 5 μs ~ 50 ms) in order to effectively attenuate 1/*f* noise on the biases during a row read. Subtracting reference pixels should attenuate 1/*f* noise with a period greater than one row.

To reduce the risk of not meeting the stability requirement, a RSAA custom-built bias board will provide the baseline bias generators. As the testing of the NIFS detector system and IfA testing of the H2RG continues, a better understanding of the stability requirements of the bias generators and the performance of the bias generators on the SDSU clock board will be developed.

9.6 Other Controllers Explored

9.6.1 Redstar3

Peter Onaka is currently developing the Redstar3 detector controller for the Gemini Near Infrared Coronograph Imager (NICI) and Infrared Telescope Facility (IRTF) NFCAM. A comparison of features and performance between Redstar3 and the SDSU-2 detector controller design is shown in Table 73.

The Redstar3 detector controller was not adopted for GSAOI for the following reasons: RSAA has considerable experience with SDSU controllers and none with Redstar3. Consequently, RSAA can produce a GSAOI SDSU controller system more quickly than a Redstar3 system. The Redstar3 detector controller is developmental so systems are not available with known delivery times. The Redstar3 controller will be

bulkier with larger (double Eurocard) boards and more of them than the SDSU controller. The Redstar3 controller housing is an open double Eurocard subrack that will be difficult to water cool and mount on the cryostat. The Redstar3 controller is designed to be mounted inside the Gemini thermal enclosures, thus necessitating separate preamplifiers at the cryostat wall or inside the cryostat. The Redstar3 pre-amplifier has only one video offset for eight channels, so adjusting the video offset may be difficult if two devices have different offset requirements. The Redstar3 video channel has fixed gain and no programmable bandwidth control making it difficult to implement a multiple readout speed system. Finally, the Redstar3 does provide advantages in sampling rate and interface speed, but the sampling rate and interface speed of the SDSU controller are more than sufficient to meet the requirements.

Table 73: Comparison of Features and Performance Between Baseline SDSU and Redstar3

Parameter	Redstar3	SDSU Baseline	Notes
Physical			
Size	16 slot double Eurocard standard housing	12 slot single Eurocard custom housing	
Total Number of Boards	12-14 boards	8 board	
Suitability to mount to cryostat and water cool	Not suitable	Very suitable	
Clocks			
Clocks per board	8	24	
Boards Required (40 clocks)	5	2	Boards required to drive four H2RG.
Generation	Programmable 12 bit DAC	Programmable 12 bit DAC	
DAC	Analog Device AD767	Analog Device DAC8420	
DAC Stability	±5ppm/ºC (typ)	±10ppm/ºC (typ)	
Output Range	-10V to +10V	0V to 3.3V	
Biases			
Biases per board	16	48	
Boards Required (36 biases)	2	1	Boards required to drive four H2RG. With SDSU controller, 14 biases are provided by the two video boards
Generation	Programmable 12 bit DAC	Programmable 12 bit DAC	
DAC	Analog Device AD767	Analog Device DAC8420	
DAC Stability	±5ppm/ºC (typ)	±10ppm/ºC (typ)	
Output Range	-10V to +10V	0V to 3.3V	
Video Processor			
Type	Two board set; preamplifier and ADC	Complete video chain on board	
Channels per Board	4 (8/2)	8	
Boards Required	4	2	16 video channels required
Input Pre-amplifier			
Type	Fully differential	Fully differential	
Amplifier Used	Analog Device	Analog Device	

Parameter	Redstar3	SDSU Baseline	Notes
	AD797	AD8002	
Noise	0.9 nV/√Hz	2.0 nV/√Hz	
Offset Control	One global offset per board	One offset per channel	
Gain Control	Fixed	Settable by 12 bit DAC	
Bandwidth Control	Fixed 2nd order Bessel filter	Programmable two time constant resettable integrator	
16 bit ADC	Analogic ADC4322	Linear Technology LTC1608	
Stability	±15 ppm/ºC	±15 ppm/ºC	
Signal-to-(noise+Distortion)	87 dB	84 dB	
Speed	2 Msamples/sec	0.5 Msamples/sec	
Sequencer	Ipengine1 48 MHz + Altera FPGA EP6016	Motorola DSP56002 50 MHz	
Size			
Resolution	145 ns	40 ns	
Data Link			
Max. Data Throughput	120 Mpixel/sec	12.5 Mpixel/sec	
Host Interface			
Supported Buses	VME/PMC/PCI/ CompactPCI	PCI/PMC	

9.7 Other ASIC Communication Interfaces Explored

The ASIC detector controller design (§5.2.6) uses an ASIC communications interface that is custom-built by RSAA. By the time the decision is made to use either a SDSU controller or ASICs, other ASIC communication interfaces may be available. Two options have been identified; one from Rockwell and the other from Peter Onaka of IfA.

9.7.1 Rockwell ASIC Communication Interface

Rockwell states that they will develop an ASIC host computer interface board that plugs into a PCI slot of a PC. Its features and availability at present are undefined. Rockwell states that it will support most of the ASIC communication modes and may possibly support several ASICs. The cost of the interface board will be between $10,000 and $20,000. The interface can be plugged into either a PC-based DC IOC or a PC front end to a VME-based DC IOC. Whichever PC option is chosen, placing a PC in the thermal enclosure would increase cable lengths for the LVDS signals and therefore decrease their maximum reliable data rate.

An alternative is to use a small water-cooled industrial compact PC (smaller than a SDSU 6 slot housing) mounted on the GSAOI cryostat close to the detector hermetic connector. The PC would be populated with the Rockwell interface board, a VMIPCI-5588 PCI Reflective Memory board[16] to transfer ODGW data to the A&G system, and a PCI Gigabit fiber-optic Ethernet adapter to provide communication with the DC IOC or the DHS. This option would provide ohmic isolation between the cryostat electronics and the electronics in the thermal enclosure. The cost of the PC system would be under $2000, excluding the cost of the Reflective Memory board and the Rockwell interface board.

[16] http://www.vmic.com/products/reflectivememory/index.html

A design based on a Rockwell interface board was not chosen for the baseline design because the specifications of Rockwell interface board are undefined and there is no certainty that it will support four ASICs. This decision may be reconsidered when more information about the Rockwell interface board becomes available.

Figure 125: Industrial compact PC with three PCI slots and 1x 5.25" disk bay.

9.7.2 Peter Onaka ASIC Communication Interface

Peter Onaka may develop an ASIC communication interface as part of his Redstar3 controller development for IRTF NFCAM if ASICs become available on a timescale to enable NFCAM to be completed by mid-2003. The requirements of NFCAM is to interface to one ASIC. As yet, there are only preliminary design ideas. The proposed design will have an architecture similar to the proposed RSAA baseline design. A communication box will mount on the cryostat near the detector hermetic and communicates through fiber-optic links to an interface board in the DC IOC. However, the system differs from the RSAA design in that two fiber-optic links will be used. The first is the data link implemented using Systran FibreXtreme[17] SL240 fiber-optic boards. It consists of a Front Panel Data Port (FPDP) board mounted in the communication box and a PCI board plugged in a PC-based IOC. The second fiber-optic link is a command/response 10 Mbaud Ethernet fiber-optic link from the DC IOC to an ipEngine[18] processor module in the communication box. The Altera EPF6016 FPGA on the ipEngine processor will provide the interface to the FPDP Systran board and a Xilinix FPGA on a custom board will provide the interface to the ASIC.

This design has issues such as latency problems associate with the ability of the Systran fiber-optic link to transmit both large amounts of imager data and small amounts of ODGW data. In addition, the Systran device driver has a limitation in that it does not support interrupts to efficiently readout data in the receive FIFO.

The Peter Onaka design was not chosen for the baseline design because of the uncertainty of its development, its inability to handle four ASICs, and the data performance issues discussed above. Peter Onaka is happy to consider accommodating our requirement to drive four ASICs in his design or consider a joint develop of an ASIC communication interface. The development of the design will be monitored and further discussion of a joint development will continue.

9.8 PCB Layout Guidelines for ASIC LVDS Serial Link

The LVDS serial link between the ASICs and host interface board feature fast edge rates. Therefore, the interconnect between transmitters and receivers will act as a transmission line. The PCB traces that form this interconnect must be designed with care. The following general guidelines[19] will be adhered to:

- Hand route or review very closely auto-routed traces. Locate the transmitters and receivers close to the connectors to minimize PCB trace length for off PCB applications.
- LVDS traces should be designed for differential impedance control (space between traces needs to be controlled). See AN-905[20] for equations.

[17] http://www.systran.com
[18] http://www.brightstareng.com
[19] National Semiconductor Application Note AN-1108 (http://www.national.com/an/AN/AN-1108.pdf)

- Minimize the distance between traces of a pair to maximize common mode rejection.
- Place adjacent LVDS trace pairs at least twice as far away (as the distance between the conductors of the pair).
- Place TTL/CMOS (large *d*V signals) far away from LVDS, at least three times away or on a different signal layer.
- Match electrical length of all LVDS lines.
- Keep stubs as short as possible.
- Avoid crossing slots in the ground plane.
- Avoid 90° bends (use two 45s).
- Minimize the number of via on LVDS traces.
- Maintain equal loading on both traces of the pair to preserve balance.
- Match impedance of the PCB trace to connector to media (cable) to termination in order to minimize reflections (emissions) for cabled applications (typically 100 Ω differential mode impedance).
- Select a termination resistor to match the differential mode characteristic impedance of the interconnect, 2% tolerance is recommended.
- Locate the termination within 1/2 (<1) inch of the receiver inputs if not using a fly-by termination method.
- Use surface mount components to minimize parasitic L and C for bypass caps and termination resistors.

9.9 Shorter Readout Time Upgrade

The specification for the baseline design is to readout the imager detector in < 10 s using four amplifiers per H2RG at 200 kHz in 100 kHz slow readout mode. The major reason for this decision is the inability of the current DHS to receive a full mosaic frame in this time. It is also true that pushing faster than is planned for NGST increases development risk and increases the time needed to design faster wiring and characterize the detector at faster speeds. Faster readout requires faster signals (clocks, outputs, LVDS serial communication link) with accompanying higher power dissipation in the H2RG and ASIC. This increases the risk of glow and bias stability problems.

Nevertheless, the duty cycle for short integration is significantly increased if the detector read out time is reduced, even if the data transfer time remains fixed. Designs having a shorter readout time have been considered for this reason (Table 74). There are two ways to shorten the readout time; increase the readout speed and/or increase the number of outputs. The following sections investigate both options for the SDSU baseline controller, the ASIC controller, and the Redstar3 controller.

[20] National Semiconductor Application Note AN-905 (http://www.national.com/an/AN/AN-905.pdf).

Table 74: Various Options of Readout Speed, Number of Outputs per Detector, and Serial Links per ASIC.

Readout Mode	Number of Outputs per Detector	Readout Speed (kHz)	Pixel Period Time (μs)	CDS Read Time (s)	DC IOC Interface speed (Mpixel/s)	Single link per ASIC Serial Link Speed (Mbaud)	Four links per ASIC Serial Links Speed (Mbaud)
Fast (5 MHz)	4	1000	1.0	2.1	8	80	20
Fast (5 MHz)	4	1000	1.0	2.1	16	80	20
Fast (5 MHz)	4	2000	0.5	1.0	32	160	40
Fast (5 MHz)	4	5000	0.2	0.4	80	400	100
Fast (5 MHz)	1	5000	0.2	1.7	20	100	25
Fast (5 MHz)	**1**	**2500**	**0.4**	**3.4**	**10**	**50**	**12.5**
Slow (100 kHz)	4	300	3.3	7.0	4.8	24	6
Slow (100 kHz)	4	200	5.0	10.5	3.2	16	4
Slow (100 kHz)	4	100	10.0	21.0	1.6	8	2
Slow (100 kHz)	**32**	**100**	**10.0**	**2.6**	**12.8**	**64**	**16**

9.9.1.1 SDSU-2 Detector Controller

There is no cost-effective way to reduce the CDS read out time of the SDSU-2 detector controller design.

The slowest that the 5 MHz output amplifiers will operate is ~ 1 MHz. The associated read noise is expected to be ~ 50/√5 = 22 e. This readout rate is faster than can be accommodated with a SDSU-2 controller. Consequently, this option requires the development of a new detector controller. This is seen as being incompatible with the fast-tracked, low-risk nature of the instrument.

Alternatively, each HAWAII-2RG can be read out at 100 kHz through 32 amplifiers for a total of 128 amplifiers by providing an additional 14 Octal Channel IR Video Processor Boards. However, such a system will be very complex, require multiple synchronized SDSU controllers, and be expensive.

9.9.2 Redstar3 Controller

The Redstar3 controller video boards have a maximum video rate of 2 MHz. A Redstar3 controller could be used to shorten the readout time by reading out through four outputs per H2RG at a rate of 2.0 MHz using 5 MHz fast readout mode. Table 74 shows that such a system has a potential readout time of 1.0 s. However, the Redstar3 controller still remains unattractive for the reasons stated in §9.6.1; size, mounting position, uncertain availability, and high cost and risk.

9.9.3 ASIC Controller

The ASIC supports all operating modes of the H2RG including 100 kHz slow readout mode and 5 MHz fast readout mode for 1, 4, or 32 outputs. Therefore it is possible to shorten the readout time with an ASIC-based controller by either increasing the readout speed or increasing the number of outputs.

Increasing the readout speed of the ASIC controller is unattractive for the following reasons. Using 5 MHz fast readout mode has higher risk because of the increased performance requirements. There is also considerable uncertainty in the performance that will be achieved, as indicated by the wide spread in the goal-to-offer read noise specification of 20 e to 100 e. Science performance will be affected if read noise performance close to the goal value is not achieved. More seriously, the ASIC 5 MHz ADCs have only 12

bits , which gives a dynamic range of only 4096. This would compromises our ability to digitize the read noise correctly and simultaneously achieve a full-well depth of 100,000 e. Finally, if the imager is read out using fast readout mode and the ODGW is read out using 100 kHz slow readout mode, the ODGW is likely not to achieve its optimum read noise.

Increasing the number of outputs of the ASIC controller is more attractive because it has lower risk. The 100 kHz slow readout mode can be used, as in the baseline NGST design. The performance using this readout mode will be more certain and it will have a more attainable low read noise (15/10 e). However, this approach still has risks. More outputs produce more power dissipation in both the H2RG and the ASIC and increase the number of potential glow centers. The NGST package only brings out 4 outputs so either the ASIC detector package or the 32-output non-ASIC detector package will be required. The ASIC will be mounted on the motherboard, as in the baseline ASIC design, if the 32-output non-ASIC detector package is used. Funding for both packages is uncertain. However, recent information is that the 32-output non-ASIC detector package may be funded.

There are many combinations of number of output amplifiers and readout speed possible using ASICs.

Combinations with communication interface needs that can be met by minor upgrades to the ASIC baseline design will be discussed first. The data rate of the proposed ASIC baseline design is limited by the 12.5 Mpixel/sec fiber-optic link. Table 74 shows two combinations that require < 12.5 Mpixel/sec data rate. The first increases the readout speed by reading out through one output per H2RG at a rate of 2.5 MHz using the 5 MHz fast readout mode. The second increases the number of outputs by reading out through 32 output per H2RG at a data rate of 100 kHz using 100 kHz fast readout mode. Both options shorten the readout time to between 2.5 to 3 seconds.

The costs to upgrade the existing baseline ASIC design should also be considered. The communication link between the ASIC and ASIC Communication Board will need to be upgraded from one to four ASIC LVDS serial data links in order to limit the maximum serial link data rate to < 20 Mbaud. Increasing the number of serial links to four will required a more complex design for the FPGA on the ASIC communication board and additional wiring for the extra 12 LVDS serial data links. In addition, the 32 outputs per H2RG option will require the use of the 32-output non-ASIC detector packages, which may have a cost penalty. The ASIC motherboard will also be much more complex so additional time will be required for its design and layout.

A faster communication interface to the DC IOC will be required to achieve shorter readout times. This could be provide by either using the Rockwell interface boards to a networked PC (§9.7.1) or using a faster fiber-optic link such as the one proposed by Peter Onaka (§9.7.2). At these rates, a parallel interface will be required between the ASIC and the communication interface. This upgrade path has a lot of uncertainty.

9.10 Readout Methods

Three readout methods were considered for the imager; correlated double sampling, Fowler sampling (Fowler & Gatley 1990, ApJ, 353, L33), and linear fitting. Garnett & Forrest (1993, SPIE, 1946, 395) provide a full analysis of the three sampling schemes for different observing situations. Fowler sampling and linear fitting are superior to CDS in read noise limited situations (assuming that the read noise is dominated by white noise). Both provide ~ $\sqrt{n_{\text{samples}}}$ improvement over CDS. Fowler sampling performance is a function of its duty cycle, which is the ratio of the time spent sampling to the total observing time. Fowler sampling achieves its best performance at a duty cycle of 2/3, i.e., sampling the "pedestal" and "signal" level each for 1/3 of the total observing time. At this optimum duty cycle, Fowler sampling is ~ 6% inferior to linear fitting. In the background-limited case, the best theoretical signal-to-noise ratio is achieved with CDS.

The read noise of the imager detector is ~ 14 e using a 200 kHz readout speed and ~ 10 e using a 100 kHz readout. From Table 9 of Vol. 1, the imager will be background-limited in all filters including narrow band filters in integration times > 150 s. Since the imager will be background-limited, CDS is the optimal

readout method. However, Fowler sampling can be implemented with minimal additional effort, so it we will take the opportunity to offer it as well.

9.11 Lake Shore Model 340 Temperature Controller Specifications

The specifications of the Lake Shore Model 340 Temperature Controller are described in Table 75.

Table 75: Lake Shore Model 340 Temperature Controller Specifications

Thermometry	
Number of Inputs	Two included (additional inputs optional)
Measurement Type	4-lead Differential
A/D Resolution	24-bit analog-to-digital
Update Rate	Up to 20 readings/second on an input, 40 readings/second on all inputs
Control	
Control Loops	Two
Control Type	Digital PID with manual output
Heater Output (Loop 1 Only)	
Heater Output Type	Variable DC current source
Heater Output Resolution	18-bit digital-to-analog converter
Max Heater Output Power	100 W
Max Heater Output Current	2 A
Current Limit Settings	2 A, 1 A, 0.5 A, 0.25 A
Heater Output Compliance	50 V
Heater Output Ranges	5 decade steps in power
Heater Connector	Three banana plugs (Hi, Lo, Shield)
Heater Load Type	Resistive
Heater Noise	50 μV + 0.001% of output voltage
Heater Output (Loop 2 Only)	
Output	Analog Output 2
Heater Output Type	Variable DC voltage 0 to 10 V
Heater Output Resolution	1.25 mV
Max Heater Output Current	100 mA
Max Heater Power (100ohm load)	1 W
Heater Connector	BNC
Heater Load Type	Resistive
Heater Load Range	Greater than 100 ohm, 100 ohm for max heater power
PID Control Settings	
Gain (Proportional)	0-1000 with 0.1 setting resolution
Reset (Integral)	1-1000 with 0.1 setting resolution
Rate (Derivative)	1-1000 s with 1 s resolution
Rate (Derivative)	1-1000 s with 1 s resolution
Zone Control Mode	10 temperature zones with control parameters
Ramping	Setpoint ramping at user specified rate
Front Panel	
Number of Input Displays	One to eight
Display units	Temperature in K, C, or sensor units
Display Resolution Input Temperature	0.0001 K below 10 K, 0.001 K above 10 K
Heater Output Display	Numeric display in percent of full scale for

	power or current. Bar graph display of Heater Output available
Interfaces	
IEEE-488.2 Interface	SH1, AH1, T5, L4, SR1, RL1, PP0, DC1, DT0, C0, E1
Serial Interface	RS-232C electrical format, 19,200 baud, RJ-11 connector
General	
Ambient Temperature Range	20-30 C (68-86 F) for specified accuracy; 15-35 C (59-95 F) for reduced accuracy
Power Requirements	100, 120, 220, 240 VAC (+ 5%, -10%), 50 or 60 Hz; 200 VA
Enclosure Type	Full 19-inch rack mount
Size	431.8 mm × 88.9 mm × 381 mm (17" × 3.5" × 15")
Weight	11.4 kilograms (25 pounds)

9.12 Lake Shore Model 340 Temperature Controller Components

Table 76 lists the Lake Shore Model 340 Temperature Controller components that will be required.

Table 76: Temperature Controller Components.

Item	Description
Model 340	Temperature controller
3462 Dual Standard Input Option Card.	Adds two standard inputs to Model 340. The card has separate ADCs and excitation for each sensor. A microprocessor on the card manages the ADC and communication with Model 340. The card allows the Model 340 to read four sensors and use any of the sensors as a control sensor.
3003 Heater Output Conditioner	Unit that provides passive filtering to reduce the heater output noise. The typical insertion loss is 20 dB at or above line frequency and > 40 dB at or above double line frequency. A 144 mm × 72 mm × 165 mm panel mount enclosure houses this option, and it weighs 1.6 kg.
RM-1 Rack Mounting Kit	Mounting brackets, ears, and handles for 19" rack mounting.

9.13 Baseline Design of the Test Cryostat

The baseline design of the test cryostat will consists of the following:

1. A cryocooler-cooled cryostat with sufficiently large cold work surface to accommodate the imager focal plane assembly,and flex circuits.
2. A filter wheel with a blocked position for doing darks, an open position, and photometric *J*, *H*, and *K* to filters. The filter wheel will be manually rotated to move from one position to the next.
3. Imaging optics so that the detectors do not look out through a wide angle at 300 K and hence do not saturate.
4. Temperature control system consisting of a Lakeshore model 340 temperature controller, three temperature sensor diodes, internal cryostat wiring, and external cabling. The temperature control system will be required to regulate the temperature of the focal plane assemby, and to monitor various temperatures inside the cryostat.

5. Two test image generators. One for projecting hot spots to one quadrant of the detector for testing cross-talk, and the other for projecting lines to test spatial characteristics.
6. Infrared LEDs mounted inside the cryostat for projecting flats onto the detector. The LEDs will be driven by constant current sources.

This page is left blank intentionally.